

NOV 26 1975

761116

# Nuclear Cross Sections and Technology Volume II

Proceedings of a Conference  
Washington, D.C.  
March 3-7, 1975

Edited by

R. A. Schrack and C. D. Bowman

Center for Radiation Research  
National Bureau of Standards  
Washington, D.C. 20234



U.S. DEPARTMENT OF COMMERCE, Rogers C. B. Morton, Secretary

U.S. NATIONAL BUREAU OF STANDARDS, Ernest Ambler, Acting Director

Issued October 1975

# NEUTRON-INDUCED FISSION CROSS SECTIONS OF $^{233}\text{U}$ , $^{234}\text{U}$ , $^{236}\text{U}$ , AND $^{238}\text{U}$ WITH RESPECT TO $^{235}\text{U}^*$

J. W. Behrens, G. W. Carlson, and R. W. Bauer  
Lawrence Livermore Laboratory, University of California  
Livermore, California 94550

Ratios of the neutron-induced fission cross sections of  $^{233}\text{U}$ ,  $^{234}\text{U}$ ,  $^{236}\text{U}$ , and  $^{238}\text{U}$  relative to  $^{235}\text{U}$  and of  $^{238}\text{U}$  relative to  $^{233}\text{U}$  were measured with fission ionization chambers at the LLL 100-MeV electron linear accelerator. The time-of-flight technique was used to measure the cross section ratios as a function of neutron energy from 0.1 to 30 MeV, except for the  $^{233}\text{U}:$  $^{235}\text{U}$  and  $^{238}\text{U}:$  $^{233}\text{U}$  ratios, which were measured from 0.001 to 30 MeV, and 1 to 30 MeV, respectively. The continuous energy spectrum of the neutron source allowed us to cover the entire energy range of each ratio in one measurement. The threshold cross section method was used to normalize the ratios independent of other cross section measurements. Typical energy resolutions of the data are 5% at 20 MeV and 1.5% at 1 MeV. Most of the data have counting uncertainties smaller than 4%. Systematic errors are discussed, and current results are compared with previous measurements.

(Fission cross section ratios; uranium isotopes —  $^{233}\text{U}$ ,  $^{234}\text{U}$ ,  $^{235}\text{U}$ ,  $^{236}\text{U}$ ,  $^{238}\text{U}$ ;  
0.001 to 30 MeV; linear accelerator; time-of-flight technique)

## Introduction

The history of neutron-induced fission cross section measurements in the keV and MeV range on the relatively long-lived isotopes of uranium ( $^{233}\text{U}$ ,  $^{234}\text{U}$ ,  $^{235}\text{U}$ ,  $^{236}\text{U}$ , and  $^{238}\text{U}$ ) spans more than 20 years.<sup>1-17</sup> In spite of the large effort that has been expended, there are still gaps in the MeV energy range where experimental data for some of the isotopes are lacking. For the isotopes measured, there are regions of inconsistencies where different data sets disagree. The most complete and accurate set of cross sections for this group of isotopes is for  $^{235}\text{U}$ .

We measured the ratios of the fission cross sections of  $^{233}\text{U}$ ,  $^{234}\text{U}$ ,  $^{236}\text{U}$ , and  $^{238}\text{U}$  relative to  $^{235}\text{U}$ . The continuous energy spectrum of neutrons produced by the LLL 100-MeV linac made it possible to use the time-of-flight technique in the energy range from 0.001 to 30 MeV in one continuous measurement. Data for the threshold isotopes  $^{234}\text{U}$ ,  $^{236}\text{U}$ , and  $^{238}\text{U}$  are usable only above 0.1 MeV. The  $^{238}\text{U}:$  $^{233}\text{U}$  ratio was measured from 1 to 30 MeV to provide part of the normalization for the  $^{233}\text{U}:$  $^{235}\text{U}$  ratio. Our ratios fill gaps where no data existed. These data will provide better definition of the cross section vs energy curves.

The normalization is a probable cause of many discrepancies between different sets of cross section ratio data. A related problem, which can seriously limit the accuracy of the final results, is the determination of the relative masses of fissionable samples.

To normalize our ratios we followed a procedure we call the threshold cross section method. In this method determination of the normalization is an integral part of the measurement and can provide results with uncertainties less than 1% for each ratio involving a threshold isotope.

## Experiment

### Neutron Source and Detectors

The ratio measurements were made with fission chambers at the 34.25-m station of the 250-m time-of-flight tube at the LLL 100-MeV linac. The linac was operated at 1440 Hz with an electron pulse width of 10 ns to produce neutrons in a water-cooled-tantalum target.

Our fission detectors are parallel plate ionization chambers of modular design placed back-to-back in a pressure vessel with the foils oriented perpendicular to the incident neutron beam. Table 1 gives the areal densities and isotopic compositions of the fissionable materials used in the chambers.

Details of the fission chambers, electronics, and data acquisition system have been reported.<sup>18-20</sup>

TABLE 1. ISOTOPIC COMPOSITIONS AND AREAL DENSITIES OF FISSIONABLE MATERIALS.

Isotope	Isotopic Composition Mass Number (at.%)					Areal Density (g/m <sup>2</sup> )
	233	234	235	236	238	
$^{233}\text{U}$	99.99+			0.001		2.7
$^{234}\text{U}$	0.005	99.84	0.10	0.05	0.01	3.0
$^{235}\text{U}$		0.03	99.91	0.02	0.04	2.9
$^{236}\text{U}$			0.0025	99.99+		1.9
$^{238}\text{U}$			0.0006		99.99+	3.1
$^{235}\text{U}$ , $^{234}\text{U}$		60.16	39.78	0.04	0.06	2.2
$^{235}\text{U}$ , $^{236}\text{U}$		0.01	30.44	69.51	0.04	3.0
$^{235}\text{U}$ , $^{238}\text{U}$		0.01	25.35	0.01	74.63	3.8
$^{233}\text{U}$ , $^{238}\text{U}$	12.69				87.31	3.8

\*Work performed under the auspices of the U. S. Energy Research & Development Administration.

The gamma flash from the tantalum target was our main timing reference. Gamma rays cause signals with a pulse height distribution similar to the distribution for neutron-induced fission. Some of the signals arise from photo-fission events. The similarity of the two distributions means that the gamma- and neutron-induced signals cross the discriminator level at almost the same average time relative to the starting times of the signals. We located the center time of the gamma flash to within  $\pm 1.5$  ns for each fission chamber by splitting its counts evenly between two time-of-flight channels. We verified the gamma flash timing to within about 10 ns by measuring the location of the 2.079-, 2.819-, and 6.295-MeV resonances of carbon.<sup>21</sup>

The resolution of our experiment is determined by the resolution of the fission chamber system ( $\leq 9$  ns) and the pulse width of the electron pulses striking the tantalum target ( $\sim 10$  ns). Taken in quadrature, these two components result in a resolution of about 13 ns. Data are reported with a minimum time per channel of 16 ns, which corresponds to 5.4% energy resolution at 20 MeV and 1.5% at 1 MeV at the 34.25-m time-of-flight station. Uncertainty in flight path and finite target and detector thickness result in a loss of resolution that is small compared to the above two components. Our time-to-energy conversion includes the relativistic correction.

#### Threshold Cross Section Method

We use the term threshold cross section method to describe the way we obtained the normalization for our fission cross section ratios of threshold to non-threshold isotopes.<sup>22</sup> In this method the nonthreshold isotope is mixed with the threshold isotope to make the fissionable coating for one chamber. This mixed chamber is measured and compared to the measurements of a chamber containing the pure nonthreshold isotope. The resulting ratio may be written as:

$$R(E) = \frac{\beta_m N_t}{\beta_p N_{nt}} \left( \frac{\sigma_t(E)}{\sigma_{nt}(E)} + \eta \right),$$

where  $R(E)$  is the ratio of fission counts as a function of neutron energy from the two chambers,  $\beta_m$  and  $\beta_p$  are the efficiencies of the mixed and pure fission chambers,  $N_t$  is the number of atoms of the threshold isotope,  $N_{nt}$  is the number of atoms of the nonthreshold isotope in the pure chamber,  $\eta$  is the ratio of atoms of the nonthreshold isotope to threshold isotope in the mixed chamber, and  $\sigma_t(E)$  and  $\sigma_{nt}(E)$  are the fission cross sections whose ratio is to be determined.

At energies where the ratio  $\sigma_t(E)/\sigma_{nt}(E)$  is negligible, the ratio of counts  $R(E)$  is a constant  $Q$ . This constant, together with the measured value of  $\eta$ , gives the ratio of effective numbers of atoms, i.e.,  $(\beta_m N_t)/(\beta_p N_{nt}) = Q/\eta$ . This ratio normalizes the cross section ratio as follows:

$$\frac{\sigma_t(E)}{\sigma_{nt}(E)} = \eta \left( \frac{R(E)}{Q} - 1 \right). \quad (1)$$

Corrections are made for the nonzero fission cross sections of the threshold isotopes in determining  $Q$ .

We used four mixed chambers in the experiment. The atom ratios were determined by groups at Livermore and Los Alamos Scientific Laboratory using mass spectrometric methods. These measured atom ratios are compared in Table 2. An accuracy of  $\pm 0.25\%$  has been determined for each of the values of  $\eta$ .

These mixed fission chambers allow us to determine the  $^{238}\text{U}:^{235}\text{U}$ ,  $^{236}\text{U}:^{235}\text{U}$ ,  $^{234}\text{U}:^{235}\text{U}$ , and  $^{238}\text{U}:^{233}\text{U}$  ratios as a function of neutron energy without normalizing to other cross section measurements. For normalization purposes we chose energy intervals for each cross section ratio and formed averages by weighting the values of the individual ratios in their 16-ns time-of-flight channels with the energy width of the channel. Table 3 gives the threshold method ratios, the energy intervals over which they were averaged, and the contributions to the uncertainty from  $\eta$ ,  $Q$ , and  $R$  as defined in Eq. (1). In each case the statistical errors of  $R$  and  $Q$  are larger than the uncertainty in the atom ratio  $\eta$ .

The basic limitation of the threshold method is that the ratios obtained have large uncertainties when the ratio becomes small compared to the mixed chamber atom ratio. Therefore the  $^{234}\text{U}:^{235}\text{U}$ ,  $^{236}\text{U}:^{235}\text{U}$ , and  $^{238}\text{U}:^{235}\text{U}$  ratios were also measured with a chamber containing a pure sample of the threshold isotope.

All of the pure chamber data were normalized to the values shown in Table 3, which were obtained from the mixed chambers. In all cases the shapes of the data from the pure chambers and mixed chambers agreed within the experimental accuracy.

#### Corrections and Errors

Most of our data have statistical counting errors of less than 4%. A number of effects contributed

TABLE 2. MASS SPECTROMETER MEASUREMENTS OF  $\eta$ .

Main Isotopes	LLL		LASL		$\eta \pm \delta\eta$
	Samples Analyzed	Average $\eta$	Samples Analyzed	Average $\eta$	
$^{235}\text{U}, ^{234}\text{U}$	4	0.6603	3	0.6621	$0.6611 \pm 0.0017$
$^{235}\text{U}, ^{236}\text{U}$	5	0.4378	3	0.4384	$0.4380 \pm 0.0011$
$^{235}\text{U}, ^{238}\text{U}$	7	0.3397	5	0.3391	$0.3395 \pm 0.0008$
$^{233}\text{U}, ^{238}\text{U}$	3	0.1455	3	0.1451	$0.1453 \pm 0.0004$

TABLE 3. NORMALIZATION VALUES OBTAINED USING THE METHOD OF THRESHOLD CROSS SECTIONS.

Ratio	Energy Range (MeV)	Threshold Method Ratio	Breakdown of Uncertainties		
			$\eta$	$Q$	$R$
$^{234}\text{U}:^{235}\text{U}$	0.50-2.50	$1.089 \pm 0.012$	0.0030	0.0098	0.0068
$^{236}\text{U}:^{235}\text{U}$	0.90-2.50	$0.5707 \pm 0.0064$	0.0012	0.0047	0.0042
$^{238}\text{U}:^{235}\text{U}$	1.75-4.00	$0.4405 \pm 0.0040$	0.0010	0.0022	0.0032
$^{238}\text{U}:^{233}\text{U}$	1.75-4.00	$0.3005 \pm 0.0025$	0.0008	0.0016	0.0017



systematic errors to our experimental results. These effects are summarized in Table 4. The estimate of energy dependence in detector efficiency was obtained from a study of the pulse height distributions of the detectors as functions of energy.<sup>20</sup>

TABLE 4. SYSTEMATIC ERRORS IN THE RATIOS EXPERIMENT.

Effect	Error Size	Correction Made	Resultant Uncertainty in Ratios
Electronic deadtime	2% max	Yes	<0.01% (negligible)
Accidental coincidences between detectors	1% max	Yes	<0.2%
Neutron scattering in aluminum foils etc.	4% max 0.4% typical	Yes	0.8% max 0.08% typical
Out-of-time neutron background (measured by black resonance absorber technique)	<0.1%	No	<0.1%
Time independent background from amplifier noise and alpha pileup	~15% max <0.1% typical	Yes	0.6% max <0.01 typical
Energy-dependent detector efficiency	<0.5%	No	<0.5%
Impurities in isotopic samples	~10% max effect in $^{238}\text{U}/^{235}\text{U}$ ratio at 0.1 MeV	Yes	5% in $^{238}\text{U}/^{235}\text{U}$ ratio at 0.1 MeV, negligible almost everywhere else

### Results and Comparisons

#### $^{238}\text{U}/^{235}\text{U}$ Ratio

The data of Meadows<sup>16</sup> (0.898 to 5.33 MeV) agree well with our results for the  $^{238}\text{U}/^{235}\text{U}$  ratio (Figs. 1, 2, and 3). There is also good agreement with the data of White and Warner<sup>10</sup> at their three points (2.25, 5.4, and 14.1 MeV) and with the data of Poenitz and Armani<sup>15</sup> at 2.0, 2.5, and 3.0 MeV. Furthermore, our data are in general agreement with the value of Jarvis<sup>1</sup> at 2.5 MeV and the data of Grundl<sup>11</sup> (1.68 to 8.07 MeV). The data of Stein, Smith, and Smith<sup>12</sup> (1.50 to 5.00 MeV) follow the shape of our data, but they have a normalization about 4% lower than ours. The original data of Lamphere<sup>2</sup> (0.7 to 3.0 MeV) have a different shape than our data and are 5% higher from 2 to 3 MeV. Below 1.5 MeV, the Lamphere data dip below our values; however, the data of Meadows<sup>16</sup> are in general agreement with our results in this same region.

#### $^{236}\text{U}/^{235}\text{U}$ Ratio

In Fig. 4, the  $^{236}\text{U}/^{235}\text{U}$  ratio data of Lamphere<sup>2</sup> agree with our results; however, the data of Stein, Smith, and Smith<sup>12</sup> are about 4% lower than our results. The White and Warner<sup>10</sup> values (1 to 14 MeV) are also lower than our ratios.

#### $^{234}\text{U}/^{235}\text{U}$ Ratio

Our data for the  $^{234}\text{U}/^{235}\text{U}$  ratio (Fig. 5) are in good agreement with White, Hodgkinson, and Wall<sup>8</sup> at 0.127, 0.312, and 0.505 MeV, Lamphere<sup>2</sup> (0.5 to 3 MeV), Lamphere<sup>7</sup> (0.050-1.326 MeV), and White and Warner.<sup>10</sup>

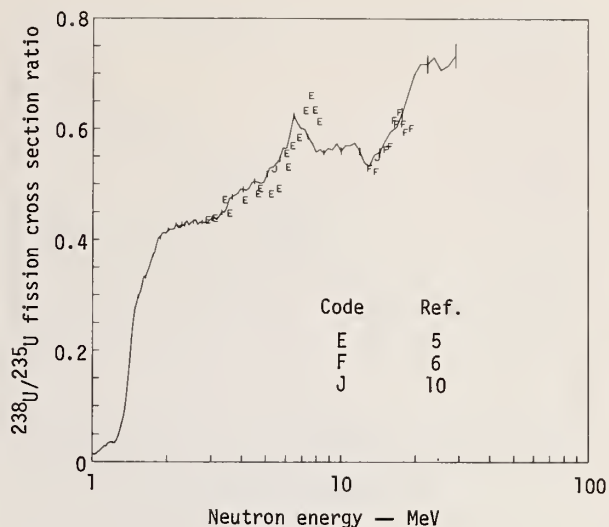


Fig. 1. Ratio of the  $^{238}\text{U}$  to  $^{235}\text{U}$  fission cross sections in the energy range 1 to 30 MeV. Present work is shown by the line that has segments connecting the individual points. Statistical error bars are shown on every fourth point.

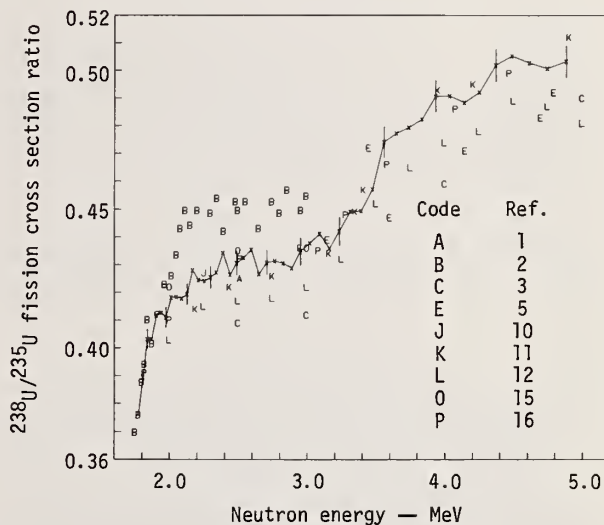


Fig. 2. Ratio of the  $^{238}\text{U}$  to  $^{235}\text{U}$  fission cross sections in the energy range 1.75 to 5.00 MeV. Present work is given by x's which are connected by line segments to guide the eye. Some of the statistical error bars are included.

#### $^{233}\text{U}/^{235}\text{U}$ Ratio

Our results (Figs. 6, 7, and 8) agree well with those of Pfletschinger and Kappeler<sup>14</sup> for the

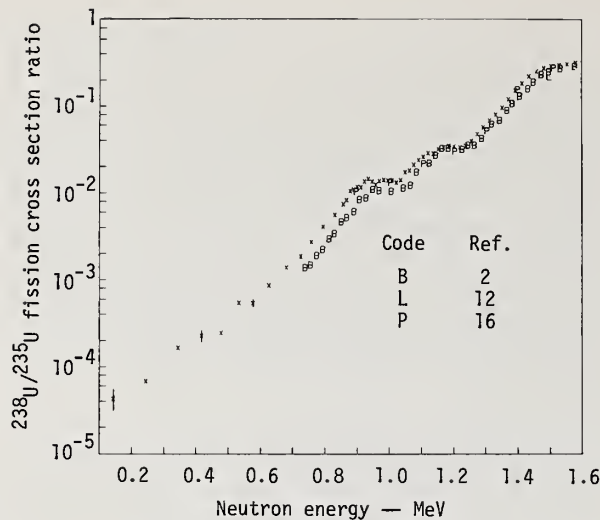


Fig. 3. Ratio of the  $^{238}\text{U}$  to  $^{235}\text{U}$  fission cross sections in the energy range 0.1 to 1.6 MeV. Present work is given by x. Some of the statistical error bars are included.

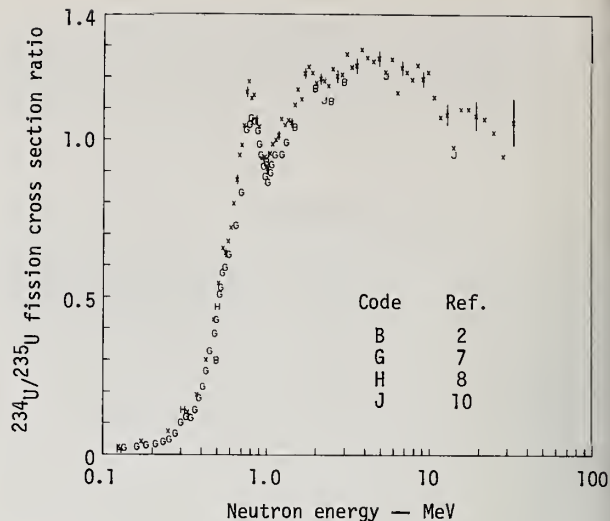


Fig. 5. Ratio of the  $^{234}\text{U}$  to  $^{235}\text{U}$  fission cross sections in the energy range 0.1 to 30 MeV. Present work is given by x. Some of the statistical error bars are included.

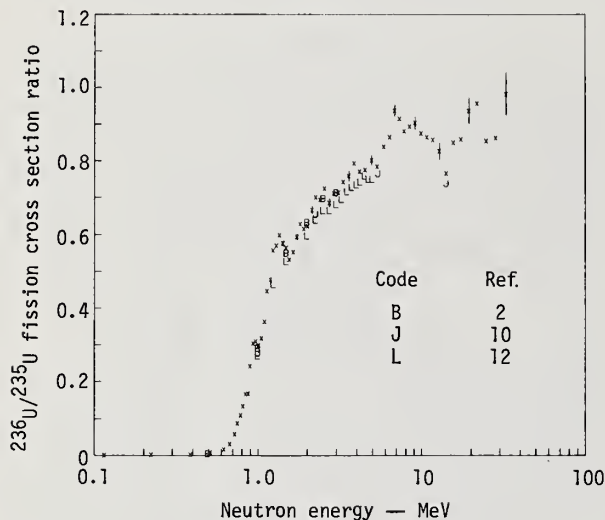


Fig. 4. Ratio of the  $^{236}\text{U}$  to  $^{235}\text{U}$  fission cross sections in the energy range 0.1 to 30 MeV. Present work is given by x. Some of the statistical error bars are included.

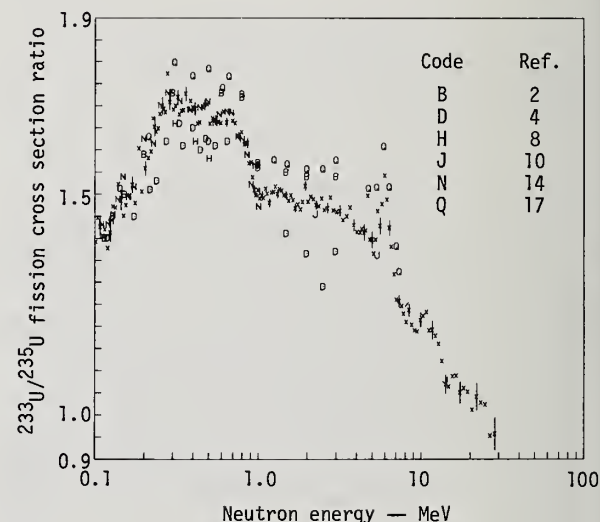


Fig. 6. Ratio of the  $^{233}\text{U}$  to  $^{235}\text{U}$  fission cross sections in the energy range 0.1 to 30 MeV. Present work is given by x. Some of the statistical error bars are included.

$^{233}\text{U} : ^{235}\text{U}$  ratios over the range of their experiment (0.005 to 1 MeV). We also agree well with White and Warner.<sup>10</sup> The results of Meadows<sup>17</sup> (0.144 to 7.1 MeV) follow the shape of our data, but have a normalization about 5% higher than ours. From 0.001 to 0.02 MeV we find structure in the ratio which, in part, is from  $^{235}\text{U}$ . It appears very difficult to get a detailed  $^{233}\text{U}$  cross section from  $^{233}\text{U} : ^{235}\text{U}$  ratio measurements in this region.

As a consistency check the  $^{233}\text{U} : ^{235}\text{U}$  ratio was also obtained by computer fitting smooth curves to our

$^{238}\text{U} : ^{235}\text{U}$  and  $^{238}\text{U} : ^{233}\text{U}$  results and forming the ratio of these smooth curves. This ratio is compared to the  $^{233}\text{U} : ^{235}\text{U}$  data in Fig. 8.

#### $^{238}\text{U} : ^{233}\text{U}$ Ratio

Our results for the  $^{238}\text{U} : ^{233}\text{U}$  ratio (Fig. 9) agree very well with those of Smith, Henkel, and Nobles.<sup>3</sup> The data of Allen and Ferguson<sup>4</sup> fall 5 to 10% lower than our values.

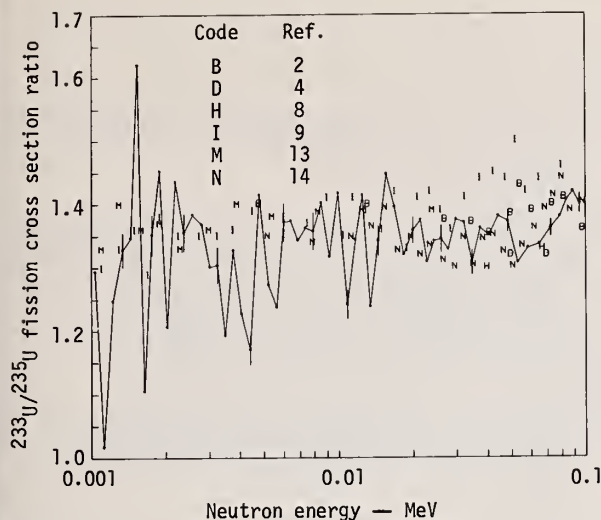


Fig. 7. Ratio of the  $^{233}\text{U}$  to  $^{235}\text{U}$  fission cross sections in the energy range 0.001 to 0.1 MeV. Present work is shown by the line of segments connecting the individual points. Statistical error bars are shown on every fourth point.

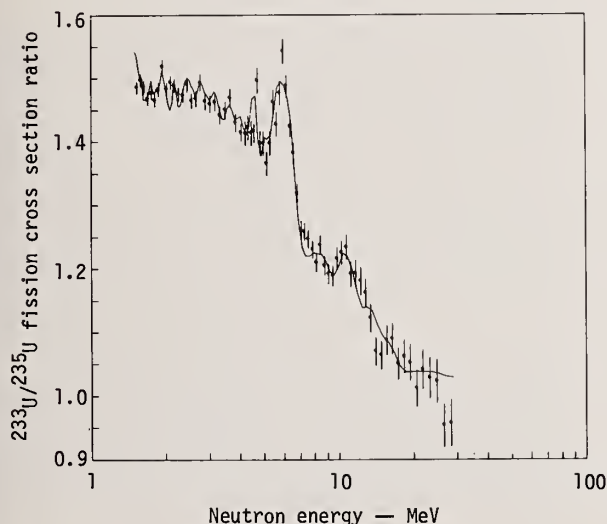


Fig. 8. Ratio of the  $^{233}\text{U}$  to  $^{235}\text{U}$  fission cross sections in the energy range 1.5 to 30 MeV. Present work is given by points. The statistical error bars are shown on each point. The line is the  $^{233}\text{U}$  to  $^{235}\text{U}$  ratio obtained by computer fitting smooth curves to our  $^{238}\text{U}$  to  $^{235}\text{U}$  results (Figs. 1 through 3) and  $^{238}\text{U}$  to  $^{233}\text{U}$  results (Fig. 9) and forming the ratio of these smooth curves.

#### Summary

Figures 1 through 9 present our results for the neutron-induced fission cross section ratios involving

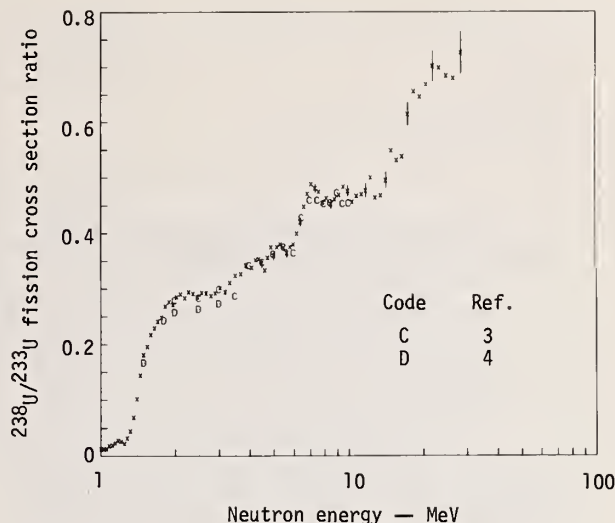


Fig. 9. Ratio of the  $^{238}\text{U}$  to  $^{233}\text{U}$  fission cross sections in the energy range 1 to 30 MeV. Present work is given by x. Some of the statistical error bars are included.

five isotopes of uranium ( $^{233}\text{U}$ ,  $^{234}\text{U}$ ,  $^{235}\text{U}$ ,  $^{236}\text{U}$ , and  $^{238}\text{U}$ ) measured continuously over a relatively wide energy range. Normalization of our ratios was obtained by applying the threshold cross section method. The comparison of our results with previous data sets demonstrates the advantage of a continuous measurement over a wide energy range in defining the cross section ratios as a function of energy.

The results presented in this paper supersede those reported in our preliminary report.<sup>19</sup> Data in tabular form will be made available upon request.

#### Acknowledgments

We wish to acknowledge the continued interest in our experiments expressed by R. L. Wagner, J. D. Anderson, and C. D. Bowman. We are indebted to E. Ables, A. Watanabe, and K. Kramer for their efforts in constructing the experimental apparatus; to J. W. Magana and J. C. Walden for handling the high purity isotopes; and to R. S. Newbury of Livermore and J. H. Capps of Los Alamos Scientific Laboratory for the mass spectrometric analyses.

#### References

1. G. A. Jarvis, Fission Comparison of  $\text{U}^{238}$  and  $\text{U}^{235}$  for 2.5 MeV Neutrons, Rept. LA-1571, Los Alamos Scientific Laboratory (1953).
2. R. W. Lamphere, Phys. Rev. **104**, 1654 (1956).
3. R. K. Smith, R. L. Henkel, and R. A. Nobles, Bull. Am. Phys. Soc. **2**, 196 (1957).
4. W. D. Allen and A. T. G. Ferguson, Proc. Phys. Soc., London, **70A**, 573 (1957).



5. S. P. Kalinin and V. M. Pankratov, in Proc. 2nd U.N. Int. Conf. on P.U.A.E., vol. 16, 1958, p. 136.
6. B. Adams, R. Batchelor, and T. S. Green, J. Nucl. Energy **14**, 85 (1961).
7. R. W. Lamphere, Nucl. Phys. **38**, 561 (1962).
8. P. H. White, J. G. Hodgkinson, and G. J. Wall, in Proc. Symp. Physics and Chemistry of Fission, Salzburg, vol. 1, 1965, p. 219.
9. R. D. Albert, Phys. Rev. **142**, 778 (1966).
10. P. H. White and G. P. Warner, J. Nucl. Energy **21**, 671 (1967).
11. J. A. Grundl, Nucl. Sci. Eng. **30**, 39 (1967).
12. W. E. Stein, R. K. Smith, and H. L. Smith, in Phys. Soc. Conf. Neutron Cross Section Techn., Washington, D.C., Rept. CONF-680307, 1968, p. 627.
13. W. K. Lehto, Nucl. Sci. Eng. **39**, 361 (1970).
14. E. Pfletschinger and F. Kappeler, Nucl. Sci. Eng. **40**, 375 (1970).
15. W. P. Poenitz and R. J. Armani, J. Nucl. Energy **26**, 483 (1972).
16. J. W. Meadows, Nucl. Sci. Eng. **49**, 310 (1972).
17. J. W. Meadows, Nucl. Sci. Eng. **54**, 317 (1974).
18. J. W. Behrens, Preparation of Fission Foils for Fission Ionization Chambers Using A Painting Technique, Rept. UCRL-51476, Lawrence Livermore Laboratory (1973).
19. J. W. Behrens and G. W. Carlson, High-Energy Measurements of Neutron-Induced Fission Cross Section Ratios Involving  $^{233}\text{U}$ ,  $^{235}\text{U}$ ,  $^{238}\text{U}$ , and  $^{239}\text{Pu}$  Using the Method of Threshold Cross Sections, Rept. UCID-16548, Lawrence Livermore Laboratory (1974, preliminary).
20. G. W. Carlson, M. O. Larson, and J. W. Behrens, Measurements of the Energy Dependence of the Efficiency of Fission Chambers, Rept. UCRL-51727, Lawrence Livermore Laboratory (1974).
21. H. T. Heaton II, J. L. Menke, R. A. Shrack, and R. B. Schwartz, Nucl. Sci. Eng. **56**, 27 (1975).
22. J. W. Behrens, Determination of Absolute Fission Cross Section Ratios Using the Method of Threshold Cross Sections, Rept. UCRL-51478, Lawrence Livermore Laboratory (1973).

#### NOTICE

"This report was prepared as an account of work sponsored by the United States Government. Neither the United States nor the United States Atomic Energy Commission, nor any of their employees, nor any of their contractors, subcontractors, or their employees, makes any warranty, express or implied, or assumes any legal liability or responsibility for the accuracy, completeness or usefulness of any information, apparatus, product or process disclosed, or represents that its use would not infringe privately-owned rights."

R. B. Perez and G. de Saussure

Oak Ridge National Laboratory  
Oak Ridge, Tennessee 37830

Recent measurements of the  $^{238}\text{U}$  neutron capture cross section show large fluctuations in the unresolved resonance region. To test whether or not the observed long-range fluctuation of the neutron capture represent departures from the compound nuclear model, the Wald-Wolfowitz runs and correlation tests were applied to the  $^{238}\text{U}$  neutron capture data obtained at ORELA. The Wald-Wolfowitz runs test deals with the statistic,  $R$ , which is the number of unbroken sequences of data points above or below a given reference line. This statistic is to be compared with the expected value of runs  $E(R) \pm \sigma(R)$  arising from randomly distributed data. In the correlation test we have computed the first serial correlation coefficient of the data as well as its expected value and variance for a set of random data. In both tests one computes the probability,  $P$ , for the given statistical entity to depart from its expected value by more than  $\epsilon$  standard deviations. Both tests confirm the presence of intermediate structure between 5 and 100 keV. The range of the structure far exceeds the width of the experimental resolution and level widths.

(  $^{238}\text{U}$  capture cross section; intermediate structure; doorway states)

### Introduction

There is considerable experimental evidence of large fluctuations of the  $^{238}\text{U}(n,\gamma)$  cross section in the unresolved resonance region.<sup>1,2</sup> Similar structure was first reported by Kopsh, Cierjacks, and Kirouac<sup>3</sup> in the total  $^{238}\text{U}$  neutron cross section between .5 and 4.35 MeV. These observed fluctuations are wider than the sharp resonances associated with the compound nucleus levels and narrower than the broad structure due to the energy dependence of the penetration coefficients. They represent departures from the statistical nuclear model in localized energy regions, hence forming an intermediate structure, rather unexpected in the framework of the compound nucleus model.

Intermediate structure in the fission cross section of various fissile nuclei is by now well known,<sup>4-7</sup> as well as its interpretation<sup>8,9</sup> in terms of Strutinsky's double humped barrier.<sup>10</sup>

Although subthreshold fission yields have been found in the case of the  $^{238}\text{U}$  nucleus,<sup>11</sup> The fact that both the capture and total  $^{238}\text{U}$  cross sections exhibit intermediate structure leads one to hypothesize that the observed structure is indeed due to nuclear dynamics phenomena in the entrance (neutron) channels, such as "doorway" states.

The problem of extracting the intermediate structure from the observed cross section has been given considerable attention in the past.<sup>13</sup> James<sup>14</sup> and Moore<sup>15</sup> were the first to introduce the use of nonparametric statistics<sup>16</sup> for the detection of intermediate structure in the fissile nuclei. Extensive studies in this field have been also performed by Baudinet-Robinet and Mahaux.<sup>17</sup> We present here the results of some statistical tests performed on the  $^{238}\text{U}(n,\gamma)$  cross section in which the Wald-Wolfowitz<sup>16</sup> nonparametric statistics were utilized.

### Statistical Treatment of the $^{238}\text{U}$ Capture Cross Section

The Wald-Wolfowitz<sup>16</sup> runs and correlation tests were applied to the  $^{238}\text{U}$  neutron capture data obtained at ORELA.<sup>1</sup> The Wald-Wolfowitz runs test deals with the statistic,  $R$ , which is the number of unbroken sequences of data points above or below a given reference line. This test evaluates the expected number of runs  $E(R)$  from randomly distributed data, as well as the corresponding variance  $\sigma^2(R)$ . It is then shown that the ratio

$$\epsilon_R = [|R - E(R)| - 1/2]/\sigma(R)$$

follows a normal probability distribution. The evaluation of the test proceeds by computing the probability,  $P(\epsilon_R)$ , that a ratio equal or larger than  $\epsilon_R$  could arise from the sampling of random data.

The Wald-Wolfowitz correlation test is based on the computation of the usual autocorrelation function of the data with some modification, so that "end effects" are mitigated. Wald and Wolfowitz also give the distribution of the correlation function for random data. The end result of this test is the ratio  $\epsilon_c$ , between the particular serial correlation coefficient obtained from the actual data and its value for a set of random data, as well as the probability  $P(\epsilon_c)$ .

The  $^{238}\text{U}(n,\gamma)$  cross section obtained at ORELA (40 m flight station) was averaged over energy intervals varying from 600 eV up to 3 keV in the region between 5 and 100 keV. The lower value of 600 eV is about six times the total experimental and Doppler resolution of the measurement at 100 keV. These data were then fitted to an average cross section (with s-wave and p-wave contributions) according to the expression

$$\begin{aligned} \langle \sqrt{E} \sigma_\gamma(E) \rangle &= g_1 \frac{A_0}{\langle \Gamma_0(E_n) \rangle} R_{0n}^\gamma(E_n) + \left( \frac{\rho^2}{1 + \rho^2} \right) \\ &\times A_1 \left[ g_1 \frac{R_{1n}^\gamma(E_n)}{\langle \Gamma_1(E_n) \rangle} + g_2 \frac{R_{2n}^\gamma(E_n)}{\langle \Gamma_2(E_n) \rangle} \right] \end{aligned} \quad (2)$$

where

$$A_0 = (4.125 \times 10^6) \langle \Gamma_\gamma \rangle S_0$$

( $S_0$  = s-wave strength function)

$$A_1 = (4.125 \times 10^6) \langle \Gamma_\gamma \rangle S_1$$

( $S_1$  = p-wave strength function)

$$\langle \Gamma_0(E_n) \rangle = \langle \Gamma_\gamma \rangle + (E_n)^{1/2} \langle \Gamma_{0n}^0 \rangle$$

$$\langle \Gamma_1(E_n) \rangle = \langle \Gamma_\gamma \rangle + \left( \frac{\rho^2}{1 + \rho^2} \right) (E_n)^{1/2} \langle \Gamma_{1n}^0 \rangle$$

$$\langle \Gamma_2(E_n) \rangle = \langle \Gamma_\gamma \rangle + \left( \frac{\rho^2}{1 + \rho^2} \right) (E_n)^{1/2} \langle \Gamma_{2n}^0 \rangle$$

$$\rho = 1.8473 \times 10^{-3} (E_n)^{1/2}, \text{ and}$$

$g_0, g_1, g_2$  = statistical weight factors.



Table 1. Input Nuclear Parameters for the Average Cross Section Calculation and the Resulting s-wave and p-wave Strength Functions.

J	$\ell$	$g_J$	$\Gamma_{0n}^{(a)}$ (eV)	$\Gamma_{1n}^{(a)}$ (eV)	$\Gamma_{2n}^{(a)}$ (eV)	Strength Function ( $\times 10^{-4}$ )
1/2	0	1	.0021	-	-	1.31
1/2	1	1	-	.00298	-	1.72
3/2	1	2	-	-	.00164	1.72

<sup>a</sup>ENDF/B-IV values (ref 19) with  $\langle \Gamma_Y \rangle = .0235$  eV.

The average radiation width,  $\langle \Gamma_Y \rangle$ , and the neutron widths for the s-wave and p-wave components,  $\langle \Gamma_{0n} \rangle$ ,  $\langle \Gamma_{1n} \rangle$ , and  $\langle \Gamma_{2n} \rangle$ , are given in Table 1. The statistical fluctuation factors  $R_{0n}^Y$ ,  $R_{1n}^Y$ , and  $R_{2n}^Y$  (ref 18) were computed at each neutron energy. The values obtained for the  $S_0$  and  $S_1$  strength functions are also given in Table 1. These values are higher than the ENDF/B-IV<sup>19</sup> values of  $S_0 = 1.05 \times 10^{-4}$  and  $S_1 = 1.57 \times 10^{-4}$  reflecting the higher values for the  $^{238}\text{U}$  capture cross section obtained at ORELA and the assumed  $\langle \Gamma_Y \rangle = .0235$  eV.

The fit obtained from Eq. (2) is shown in Fig. 1 (with some statistical error flags at selected points). Also shown in the figure is the mock-up  $^{238}\text{U}(n, \gamma)$  cross section computed by Monte-Carlo techniques on the basis of the ENDF/B-IV<sup>19</sup> average resonance parameters and s-wave strength function. The mock-up cross section data were also fitted by Eq. (2) with only the s-wave contribution. Inspection of Fig. 1 already reveals quite a deal of structure of the cross section about its average value for the experimental data, as compared with the "good" fit in the case of the capture cross section computed on the basis of the statistical nucleus model.

The average cross section fit was utilized as the reference line for the Wald-Wolfowitz runs test. For the correlation test the data were divided through by the average fit to remove the correlation bias introduced by the energy dependence of the s-wave and p-wave penetration factors.

The results of the statistical tests are given in Table 2. Both tests show that there is a probability of less than  $10^{-5}$  for the average ratio  $\langle \epsilon_c \rangle = 5.1$  and less than  $10^{-4}$  for the average ratio  $\langle \epsilon_R \rangle = 4.1$  to occur from the sampling of random data. Essentially, the Wald-Wolfowitz nonparametric statistics test whether or not a given sample exhibits longer correlations than the expected from a set of random data. When applied to the mock-up cross section and averaged over energy intervals larger than the level widths, the results of Table 2 merely indicate that the compound nuclear model behaves from the viewpoint of correlation length similarly to a set of random data. Hence, the present results are to be interpreted as showing the presence of long-range correlations which represent departures from the compound nucleus model.

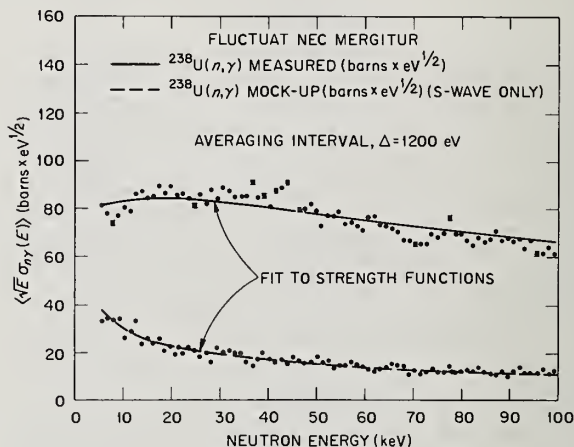


Fig. 1. Fit of the  $^{238}\text{U}(n, \gamma)$  Cross Section Measured and Mocked-up to the strength functions.

Table 2. Results of the Wald-Wolfowitz Correlation and Runs Tests for the Measured and Mockup  $^{238}\text{U}$  Capture Cross Section

Width (keV)	Capture (Measured)				(Capture (Mockup))			
	$\epsilon_c$	$P(\epsilon_c)$	$\epsilon_R$	$P(\epsilon_R)$	$\epsilon_c$	$P(\epsilon_c)$	$\epsilon_R$	$P(\epsilon_R)$
.6	5.9	$<10^{-5}$	4.5	$<10^{-5}$	.52	.60	.03	.98
.9	6.1	$<10^{-5}$	3.9	$2.7 \times 10^{-3}$	.20	.60	.96	.34
1.0	5.9	$<10^{-5}$	4.6	$<10^{-5}$	.37	.71	.68	.50
1.2	6.2	$<10^{-5}$	5.6	"	.65	.52	.34	.73
1.5	5.3	$<10^{-5}$	4.8	"	.31	.76	.002	.99
1.8	2.2	$2.7 \times 10^{-2}$	3.6	$<2.7 \times 10^{-3}$	.97	.33	1.11	.27
2.0	4.9	$<10^{-5}$	3.8	"	.22	.82	1.2	.23
3.0	3.9	$2.7 \times 10^{-3}$	1.8	$7.2 \times 10^{-2}$	1.1	.27	.006	.99

## Theoretical Interpretation

The fact that intermediate structure has been observed in both the  $^{238}\text{U}$  capture and total cross sections strongly favors the "door-way" states hypothesis. These short-lived states at the entrance channel interact via a residual interaction with the compound nucleus states. It can be shown<sup>20</sup> that the  $(n,\gamma)$  T-matrix component is given by

$$T_{n\gamma} = i \sum_{\lambda} \frac{g_{\lambda n} \Gamma_{\lambda\gamma}^{1/2}}{D_{\lambda}(E) - \phi_{\lambda}(E)}, \quad (3)$$

with the complex neutron width given by

$$g_{\lambda n} = \Gamma_{\lambda n}^{1/2} \left[ 1 - \sum_{\mu} \left( \frac{\Gamma_{\mu n}}{\Gamma_{\lambda n}} \right)^{1/2} \left( \frac{W_{\lambda\mu}}{D_{\mu}} \right) \right], \quad (4)$$

and

$$\phi_{\lambda}(E) = \sum_{\mu} \frac{|W_{\lambda\mu}|^2}{D_{\mu}}, \quad (5)$$

where

$$D_{\lambda} = (E_{\lambda} - E) + \frac{i}{2} \Gamma_{\gamma}, \quad (6)$$

$$D_{\mu} = (E_{\mu} - E) + \frac{i}{2} \Gamma_{\mu}, \quad (7)$$

$$W_{\lambda\mu} = \text{residual interaction (eV)}, \quad (8)$$

and the other symbols have the usual meaning. The sub-index,  $\lambda$ , goes over the compound nucleus states, and the subindex,  $\mu$ , classifies the "doorway" states.

On the basis of the previous results (valid only for  $|W_{\lambda\mu}/D_{\mu}| \ll 1$ ) the average cross section is again given by Eq. (2) in which the s-wave and p-wave strength functions are multiplied by the energy-dependent "modulation" factors  $M_0(E)$  and  $M_1(E)$ , respectively, where

$$M_{\ell}(E) = \left( 1 + \sum_{\mu} |D_{\mu}|^{-4} A_{\mu}^{\ell} \right) / \left( 1 + \sum_{\mu} |D_{\mu}|^{-2} B_{\mu}^{\ell} \right) \quad (9)$$

$$A_{\mu}^{\ell} = \frac{1}{2} \left[ \Gamma_{\mu}^{(\ell)} \right]^2 \Gamma_{0\mu n}^{(\ell)} \left\langle \frac{|W_{\lambda\mu}|^2}{\Gamma_{\lambda n}^{(\ell)}} \right\rangle_{\text{compound nucleus}} \quad (\text{eV}^4) \quad (10)$$

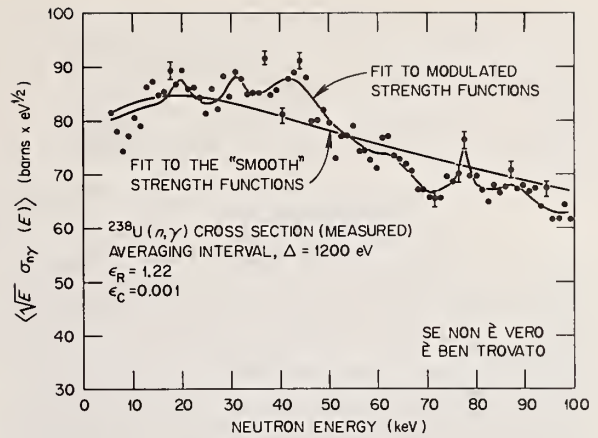


Fig. 2. Fit of the  $^{238}\text{U}(n,\gamma)$  Cross Section Measured to the Modulated Strength Function.

$$B_{\mu}^{\ell} = \Gamma_{\mu}^{(\ell)} \left\langle \frac{|W_{\lambda\mu}|^2}{\Gamma_{\lambda}^{(\ell)}} \right\rangle_{\text{compound nucleus}} \quad (\text{eV}^2) \quad (11)$$

$\ell = 0, 1$

and the brackets indicate an average over the compound nucleus states. The neutron widths  $\Gamma_{0\lambda n}^{(\ell)}$  and  $\Gamma_{0\mu n}^{(\ell)}$  are reduced neutron widths and the total level widths  $\Gamma_{\lambda}^{(\ell)}$  and  $\Gamma_{\mu}^{(\ell)}$  are computed at the level energies.

These modulation factors arise from the fact that the interaction between the compound nucleus states and the doorway states "modulates" both the neutron widths and the average level spacing.

A cavalier attempt has been made to extract the main features of the intermediate structure by fitting the average cross section of Eq. (2) with "modulated" strength functions. Although one expects both the s-wave and p-wave strength functions to be modulated, we arbitrarily changed only the s-wave contribution. The results of this procedure are shown in Fig. 2 together with the "smooth" strength function fit. The goodness of fit, expressed in terms of the chi-square test, improved by a factor close to 100 between the "smooth" and "modulated" fits. The modulated fit was then used as the reference line for the Wald-Wolfowitz runs test. For the correlation test, the data were divided by the modulated fit. The results of both statistical tests are given in Table 3 and indicate that the intermediate

Table 3. The Wald-Wolfowitz Runs and Correlation Tests for the  $^{238}\text{U}(n,\gamma)$  Cross Section After Removal of the Intermediate Structure.

Width (keV)	$\epsilon_R$			$\epsilon_c$		
	Mock-up	Exp. (a)	Reduced (b)	Mock-up	Exp. (a)	Reduced (b)
.6	.03	4.5	.40	.52	5.9	.64
.9	.96	3.9	.60	.20	6.1	.15
1.0	.68	4.6	.03	.37	5.9	.44
1.2	.34	5.6	.001	.65	6.2	1.22
1.5	.002	4.8	.72	.31	5.3	.15
1.8	1.11	3.6	1.64	.97	2.2	.08
2.0	1.2	3.8	.003	.22	4.9	.64
3.0	.006	1.8	.006	1.1	3.9	1.1

<sup>a</sup>Measured  $^{238}\text{U}(n,\gamma)$  cross section.

<sup>b</sup>Measured  $^{238}\text{U}(n,\gamma)$  cross section after removal of the intermediate structure.

structure had been adequately described. The assignment of the doorway levels to the s-wave strength function only prevents one from giving too much credibility to the level parameters obtained for the intermediate structure. The present results tend, however, to indicate an average level spacing of around 9 keV and reduced neutron widths averaging 40 eV.

### Conclusions

The two statistical tests applied to the measured  $^{238}\text{U}(n,\gamma)$  cross sections give, with a high significance level, strong support to the presence of intermediate structure in the neutron capture of the  $^{238}\text{U}$  nucleus. Although we cannot exclude the possibility for at least a fraction of this structure originating from sub-threshold fission phenomena, the presence of large local fluctuations in the  $^{238}\text{U}$  total cross section<sup>3</sup> gives support to the presence of doorway states in the reaction entrance channel.

From the theoretical results referred to here, one concludes that the intermediate structure [see Eq. (9)] is due not only to local enhancements of the reaction widths, but also to rapid fluctuations of the average level spacing.

The Wald-Wolfowitz correlation and runs tests are also valuable in connection with the fitting of the intermediate structure as they can be used as an "added" goodness of fit test.

As we have discussed earlier, not too much physical significance can be attached to the level locations and widths of the detected doorway levels. However, fits, like the ones described here, do afford a method of representing the average behavior of the  $^{238}\text{U}$  capture cross section in the unresolved region. This may prove valuable for reactor calculations.<sup>21</sup>

Studies similar to this should be applied to high resolution measurements of capture cross section in other elements such as thorium, gadolinium, and other nonfissile uranium isotopes, in order to ascertain whether there is a systematics that can be deduced regarding intermediate structure phenomena. In this regard one should mention the work of Macklin<sup>22</sup> who also showed the presence of intermediate structure in the gold capture cross section.

### Acknowledgment

The authors would like to thank Professor H. Feshbach for several illuminating discussions.

### References

- \* Research sponsored by the Energy Research and Development Administration under contract with the Union Carbide Corporation.
- <sup>1</sup>G. de Saussure *et al.*, *Nucl. Sci. Eng.* 51, 385 (1973).
- <sup>2</sup>R. R. Spencer and F. Kappeler, *Proc. Specialist Meeting on Resonance Parameters of Fertile Nuclei,  $^{232}\text{Th}$ ,  $^{238}\text{U}$ ,  $^{240}\text{Pu}$ , and  $^{239}\text{Pu}$* , Saclay, May 1974 (to be published).
- <sup>3</sup>D. Kopsch, S. Cierjacks, and G. J. Kirouac, *Sec. Conf. on Nuclear Data for Reactors*, vol. 2, 1970, IAEA.
- <sup>4</sup>D. Paya *et al.* *Proc. Dubna Conf.*, 1968, SMNF 624/68.
- <sup>5</sup>E. Migneco and J. P. Theobald, *Nucl. Phys.* A112, 603 (1968).
- <sup>6</sup>B. H. Patrick *et al.*, *J. Nucl. Energy* 24, 269 (1970).
- <sup>7</sup>C. D. Bowman *et al.*, *Sec. Conf. on Nuclear Data for Reactors*, vol. 2, 1970, IAEA.
- <sup>8</sup>H. Weigmann, *Zeitschrift fur Physik* 214, 7 (1968).
- <sup>9</sup>J. E. Lynn, AERE-R5891, Sept. 1968.
- <sup>10</sup>V. M. Strutinsky, *Nucl. Phys.* A95, 420 (1967).
- <sup>11</sup>M. G. Silvert and D. W. Bergen, *Phys. Rev. C* 4, 200 (1971). Also R. C. Block *et al.* *Phys. Rev. Letters* 31, 247 (1973).
- <sup>12</sup>H. Feshbach, A. K. Kerman, and R. H. Lemmer, *Ann. Phys.* (N. Y.) 41, 230 (1967).
- <sup>13</sup>R. B. Perez *et al.*, *Symp. Phys. and Chemistry of Fission*, SM-122/21, p. 283, 1969, IAEA.
- <sup>14</sup>G. D. James, *Nucl. Phys.* A170, 308 (1971).
- <sup>15</sup>M. S. Moore, *Statistical Properties of Nuclei*, ed. J. B. Garg, Plenum, New York, 1972, p. 55.
- <sup>16</sup>A. Wald, and J. Wolfowitz, *Annals Math. Stat.* 11, No. 2 (1940). Also Documenta Geigy, Scientific Tables, Geigy Pharmaceuticals, ed. K. Diem, Ardsley, New York.
- <sup>17</sup>Y. Baudinet-Robinet and C. Mahaux, *Phys. Rev. C*, 9, 723 (1974).
- <sup>18</sup>J. J. Schmidt, KFK120 (EANDC-E-35U), B43 (1966).
- <sup>19</sup>CSEWG, ENDF/B-IV completed in July 1974.
- <sup>20</sup>R. B. Perez and G. de Saussure, work in preparation.
- <sup>21</sup>C. R. Weisbin, private communication, 1975.
- <sup>22</sup>R. L. Macklin *et al.*, *Phys. Rev. C*, to be published, April 1975.



A DIRECT COMPARISON OF DIFFERENT EXPERIMENTAL TECHNIQUES FOR MEASURING  
NEUTRON CAPTURE AND FISSION CROSS SECTIONS FOR  $^{239}\text{Pu}^*$

R. Gwin, L. W. Weston, J. H. Todd, R. W. Ingle, and H. Weaver

Oak Ridge National Laboratory  
Oak Ridge, Tennessee 37830

A comparison of the results of two different experimental methods of measuring the neutron absorption and fission cross sections for  $^{239}\text{Pu}$  is made. These measurements were normalized at thermal energy and extend to 200 keV. The ratio of the neutron capture to fission cross section for  $^{239}\text{Pu}$  derived in these two experiments is shown to be in good agreement.

( $^{239}\text{Pu}$ ; fission, absorption; measurement; comparison; cross sections)

### Introduction

Measurements of the neutron absorption  $\sigma_a$  and neutron fission  $\sigma_f$  cross sections, and thereby the neutron capture  $\sigma_c$  cross section, have been performed at ORNL using two different techniques. These experiments covered the neutron energy region from 0.02 eV to 200 keV and represent a part of the experimental program on  $^{239}\text{Pu}$  at ORNL. Two different techniques were used to serve as a guide for further experimentation at ORNL and to provide a measure of confidence in the measurements of  $\sigma_c/\sigma_f$ .

Several aspects of the two experiments were essentially the same, such as the measurement of the neutron flux; however, the performance and analysis of these experiments were independent as well as the techniques for observing fission and absorption events. The values  $\sigma_a$ ,  $\sigma_f$ , and  $\sigma_c/\sigma_f$  derived in these experiments are given in this paper along with the respective values from ENDF/B-IV MAT-1264.<sup>1</sup> Also included are the values  $\sigma_c/\sigma_f$  for  $^{239}\text{Pu}$  from the evaluation of Sowerby and Konshin.<sup>2</sup>

### Similarities in the Two Experiments

Both of the experiments described in this paper were performed at ORNL using the Oak Ridge Electron Linear Accelerator (ORELA) to produce the source of neutrons in bursts from 5 to 30 nsec wide. The energy of the neutrons was measured by the time-of-flight technique. The neutron flux was measured in each experiment using a parallel plate (pulse) ionization chamber filled with  $\text{BF}_3$ . The prescription for the  $^{10}\text{B}(n,\alpha)$  cross section used to extract the energy dependence of the neutron flux was that given in ENDF/B-III and was the same as that suggested by Sowerby and Patrick.<sup>3</sup> The energy range 0.02 eV to 200 keV was covered in one run in both experiments; this approach eliminates the problems encountered in internormalizing runs obtained under different experimental conditions and which cover a common but narrow energy interval. Normalization of the present data sets was performed in the thermal energy region using values of  $\sigma_f$  and  $\sigma_a$  from ENDF/B-III for  $^{239}\text{Pu}$ .

### Description of the Two Experimental Methods

One experiment (method 1) was performed flight path of about 20 m. A 3-in. diameter  $^{239}\text{Pu}$  sample having a mass of 0.24 g/cm<sup>2</sup> was used. Fission events were recorded using pulse-shape discrimination to detect fission neutrons and a separate detector "total energy detector" (similar to a Moxon-Rae detector) was used to measure the prompt gamma rays following neutron absorption in the sample. In the other experiment (method 2), the  $^{239}\text{Pu}$  (0.03 g/cm<sup>2</sup>) was contained in a multi-plate pulse ionization chamber. A large liquid scintillator was used with a 40 m flight

path to detect the prompt gamma rays resulting from neutron absorption in the sample, and pulses from this scintillator system in coincidence with pulses from the fission chamber were defined as fissions.

Auxiliary experiments were performed to test various features of the experiments. For example, the neutron (pulse-shape discrimination) detector was run in coincidence with the  $^{239}\text{Pu}$  fission chamber in a series of measurements.<sup>4</sup> Also, measurements of the neutron flux were made using  $^6\text{Li}$  glass.

### Presentation of the Data

The table shows the average values of  $\sigma_a$ ,  $\sigma_f$ , and  $\sigma_c/\sigma_f$  derived from the two independent experiments. Also shown are the cross sections from ENDF/B-IV and the values  $\sigma_c/\sigma_f$  for  $^{239}\text{Pu}$  taken from the evaluation of Sowerby and Konshin. In comparing the data shown in the table an average difference refers to the sum over a number of energy intervals of the percent difference between the values divided by the number of intervals. In the cases shown in the table where explicit results for  $\sigma_c$  and  $\sigma_f$  are not given values of  $\sigma_c/\sigma_f$  for larger intervals than those in the table are obtained using  $\sigma_a$  from ENDF/B-IV along with the appropriate  $\sigma_c/\sigma_f$  to yield  $\sigma_c$  and  $\sigma_f$  for each subinterval. These latter values of  $\sigma_c$  and  $\sigma_f$  are then averaged over the large interval. The uncertainties shown for  $\sigma_f$  and  $\sigma_a$  in the table for method 2 represent the precision of the experiments. For  $\sigma_c/\sigma_f$  the uncertainties shown include the known uncertainties except those due to errors in the cross sections below 0.4 eV used in the normalization. An examination of the table shows that the results  $\sigma_c/\sigma_f$  from the two experiments overlap within their uncertainties, and in fact about 70% of the results for method 1 fall within the uncertainty shown for method 2.

The results of two experiments for  $\sigma_f$  and  $\sigma_a$  agree within 0.7% and 0.3%, respectively, for the neutron energy range from 0.1 to 1.0 keV, and the average difference between the two results for  $\sigma_f$  and  $\sigma_a$  are 1.9% and 2.9%, respectively. Above 1 keV the neutron cross sections obtained in method 1 are about 4% lower than those derived in method 2. This is thought to be due to difficulties in the measurement of the neutron flux for method 1 at the time of these experiments.

For the 28 intervals shown in the table, the present two experimental values of  $\sigma_c/\sigma_f$  have an average difference of about 6%. A comparison of the average values of  $\sigma_c/\sigma_f$  obtained in the present experiments for the intervals 0.1 to 1, 1 to 10, and 10 to 100 keV shows that they differ by 2.3, 1.5, and 2.3%, respectively, and the results for method 2 are higher in each

Average Neutron Cross Sections for  $^{239}\text{Pu}$ , 0.1 to 200 keV

$$\bar{\sigma} = \frac{\int_{E1}^{E2} \sigma(E) dE}{E2 - E1}$$

E1 - E2 (keV)	Method 2 (a)				Method 1 (b)				Sowerby and Konshin		ENDF/B-IV Mat 1264	
	$\bar{\sigma}_f$ barns	$\bar{\sigma}_a$ barns	$\bar{\sigma}_c/\bar{\sigma}_f$ (d)	$\bar{\sigma}_c/\bar{\sigma}_f$ (d)	$\bar{\sigma}_f$ barns	$\bar{\sigma}_a$ barns	$\bar{\sigma}_c/\bar{\sigma}_f$ (d)	$\bar{\sigma}_c/\bar{\sigma}_f$ (d)	$\bar{\sigma}_f$ barns	$\bar{\sigma}_a$ barns	$\bar{\sigma}_c/\bar{\sigma}_f$ (d)	$\bar{\sigma}_c/\bar{\sigma}_f$ (d)
0.1 - 0.2	17.96 ± .04	33.66	0.87 ± .015	.871 ± .052	18.41	34.45	.871 ± .052	.845 ± .077	18.20	34.97	.845 ± .077	.92
0.2 - 0.3	17.90 ± .05	34.69	0.94 ± .010	.927 ± .056	17.77	34.24	.927 ± .056	.912 ± .094	17.50	34.67	.912 ± .094	.98
0.3 - 0.4	8.48 ± .03	18.31	1.16 ± .014	1.15 ± .069	8.43	18.12	1.15 ± .069	1.15 ± .099	8.54	18.07	1.15 ± .099	1.12
0.4 - 0.5	9.40 ± .05	13.56	0.44 ± .013	.426 ± .026	8.47	13.50	.426 ± .026	.483 ± .058	9.67	14.04	.483 ± .058	.45
0.5 - 0.6	15.46 ± .09	26.54	0.72 ± .040	.718 ± .043	15.64	26.87	.718 ± .043	.704 ± .069	15.73	27.10	.704 ± .069	.72
0.6 - 0.7	4.55 ± .03	11.57	1.54 ± .040	1.488 ± .089	4.38	10.90	1.488 ± .089	1.673 ± .133	4.57	11.29	1.673 ± .133	1.47
0.7 - 0.8	5.34 ± .07	10.52	0.97 ± .017	.890 ± .053	5.54	10.47	.890 ± .053	.973 ± .087	5.55	10.68	.973 ± .087	.93
0.8 - 0.9	5.10 ± .03	9.30	0.82 ± .025	.790 ± .047	5.02	8.99	.790 ± .047	.778 ± .101	5.20	9.50	.778 ± .101	.83
0.9 - 1.0	7.83 ± .14	13.23	0.70 ± .026	.675 ± .041	8.02	13.43	.675 ± .041	.717 ± .077	8.11	13.81	.717 ± .077	.70
1 - 2	4.52 ± .02	8.31	0.84 ± .013	.802 ± .048	4.45	8.02	.802 ± .048	.927 ± .093	4.60	8.37	.927 ± .093	.82
2 - 3	3.32	6.63	1.00	.972 ± .058	3.25	6.41	.972 ± .058	1.108 ± .103	3.40	6.76	1.108 ± .103	.99
3 - 4	3.04	5.24	0.72 ± .066	.738 ± .043	2.95	5.13	.738 ± .043	.895 ± .086	3.08	5.42	.895 ± .086	.76
4 - 5	2.37 ± .01(e)	4.44	0.87 ± .040	.831 ± .050	2.35	4.30	.831 ± .050	.821 ± .079	2.41	4.88	.821 ± .079	.86
5 - 6	2.32 ± .02(e)	4.23(e)	0.82 ± .046(e)	.807 ± .048	2.13	3.85	.807 ± .048	.867 ± .084	2.27	4.14	.867 ± .084	.82
6 - 7	2.05 ± .02	3.68	0.79 ± .040	.745 ± .045	2.01	3.51	.745 ± .045	.816 ± .086	2.06	3.65	.816 ± .086	.77
7 - 8	2.11 ± .01	3.45	0.64 ± .022	.642 ± .038	2.03	3.33	.642 ± .038	.629 ± .073	2.09	3.44	.629 ± .073	.65
8 - 9	2.28 ± .01	3.51	0.54 ± .022	.537 ± .032	2.06	3.17	.537 ± .032	.575 ± .064	2.17	3.35	.575 ± .064	.54
9 - 10	1.92 ± .02	2.97	0.55 ± .022	.606 ± .036	1.76	2.83	.606 ± .036	.617 ± .067	1.95	3.08	.617 ± .067	.58
10 - 20	1.78 ± .02	2.63	0.48 ± .022	.486 ± .029			.486 ± .029	.466 ± .05	1.77	2.64	.466 ± .05	.50
20 - 30	1.64 ± .02	2.22	0.35 ± .018	.347 ± .049			.347 ± .049	.373 ± .04	1.67	2.26	.373 ± .04	.36
30 - 40	1.61 ± .01	2.09	0.30 ± .041	.254 ± .051			.254 ± .051	.296 ± .03	1.61	2.07	.296 ± .03	.28
40 - 50	1.54 ± .02	1.94	0.26 ± .020	.246 ± .049			.246 ± .049	.242 ± .03	1.59	2.01	.242 ± .03	.27
50 - 60	1.66 ± .01	2.03	0.23 ± .020	.220 ± .044			.220 ± .044	.206 ± .03	1.62	2.06	.206 ± .03	.26
60 - 70	1.62 ± .03	1.99	0.23 ± .025	.215 ± .043			.215 ± .043	.182 ± .025	1.61	1.99	.182 ± .025	.23
70 - 80	1.64 ± .04	1.95	0.19 ± .025	.200 ± .040			.200 ± .040	.165 ± .025	1.63	1.97	.165 ± .025	.21
80 - 90	1.52 ± .02	1.85	0.22 ± .030	.138 ± .028			.138 ± .028	.159 ± .03	1.56	1.88	.159 ± .03	.21
90 - 100	1.54 ± .06	1.80	0.17 ± .045					.160 ± .03	1.57	1.82	.160 ± .03	.16
100 - 200	1.61 ± .02	1.86	0.15 ± .010	.148 ± .030			.148 ± .030	.170 ± .028	1.53	1.74	.170 ± .028	.14

(a) Fission chamber plus large liquid scintillator.

(b) Solid sample, "total energy detectors," and fast-neutron detection.

(c) Experimental precision,  $S^2 = \frac{1}{N(N-1)} \sum_{i=1}^N (x_i - \bar{x})^2$

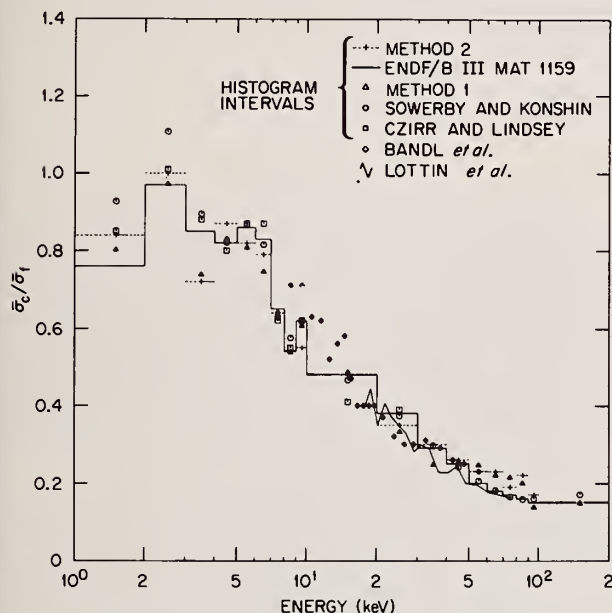
(d) Includes all known experimental errors.

(e) The aluminum resonance at 5.9 keV perturbs the measurement at this energy.



interval. The ENDF/B-IV values for  $^{239}\text{Pu}$ , MAT 1264 were based in part upon the data obtained in the present two experiments.

The relation of the present results for  $\bar{\sigma}_c/\bar{\sigma}_f$  for  $^{239}\text{Pu}$  and other experimental data can be summarized by comparing them with the results obtained in the evaluation of Sowerby and Konshin. From 0.1 to 40 keV the average difference between the present values (either set for  $\bar{\sigma}_c/\bar{\sigma}_f$  of  $^{239}\text{Pu}$  and those of Sowerby and Konshin is about 7%. For the energy intervals 1 to 10 keV and 50 to 100 keV, the present average values of  $\bar{\sigma}_c/\bar{\sigma}_f$  are 10% lower and 17% higher, respectively, than those obtained by Sowerby and Konshin.



Ratio of  $\bar{\sigma}_c/\bar{\sigma}_f$  for  $^{239}\text{Pu}$ , 1.0 to 200 keV.

The figure shows a plot of  $\bar{\sigma}_c/\bar{\sigma}_f$  for  $^{239}\text{Pu}$  obtained in the present two experiments along with those derived by Sowerby and Konshin. Experimental values measured by Czirr and Lindsey,<sup>5</sup> Bandl et al.,<sup>6</sup> and Lottin et al.<sup>7</sup> are also shown on the figure. Values from ENDF/B-III, MAT 1159 are also shown in the figure. Note that the earlier version (III) of ENDF/B shown in the figure follows very closely the results of the evaluation of Sowerby and Konshin above 10 keV and both of these data sets are systematically lower than the results of the present two experiments. These two above evaluations follow the experimental values of Lottin above 50 keV. Earlier measurements of  $\bar{\sigma}_c/\bar{\sigma}_f$  by Hopkins and Diven<sup>8</sup> (not shown in the figure) yield a value of .15 for  $\bar{\sigma}_c/\bar{\sigma}_f$  for  $^{239}\text{Pu}$  at about 60 keV, which supports the two evaluations shown in the figure. The data of Bandl et al. were normalized in the energy region from 40 to 50 keV and thus provide information on the energy dependence of  $\bar{\sigma}_c/\bar{\sigma}_f$  only.

#### Summary

The neutron cross sections  $\bar{\sigma}_f$  and  $\bar{\sigma}_a$  and especially the ratio  $\bar{\sigma}_c/\bar{\sigma}_f$  for  $^{239}\text{Pu}$  obtained by these two experiments agree to within a few percent over the

energy range of the experiments. In addition, these two results for  $\bar{\sigma}_c/\bar{\sigma}_f$  for  $^{239}\text{Pu}$  have been shown to be in good accord with the results of other measurements as reflected in the evaluation by Sowerby and Konshin.

Many factors influence the choice of detector systems for the simultaneous measurement of neutron capture and fission cross sections. The authors conclude that for the pursuit of high accuracy measurements of  $\bar{\sigma}_c/\bar{\sigma}_f$  on  $^{239}\text{Pu}$  a fission chamber used in

conjunction with total energy detectors represents a logical choice at ORELA. The total energy detectors are small and can be easily moved from one flight station to another in order to optimize the experimental conditions. Although the detection efficiency of the large liquid scintillator is larger (about a factor of 10 to 20 in the present case) than that of the total energy detector, a gain in the efficiency of the total energy detector system can be made by using additional detectors.

In the present experiments the signal-to-time-dependent background ratio for the large liquid scintillator system is about a factor of 2 to 10 less than that observed for the total energy detector system. Some of the background in the large liquid scintillator can be reduced by the dividing of the tank into optically separated sections and requiring that at least two of these sections detect the event; however, this makes the detector more sensitive to changes in the capture gamma-ray cascade with neutron energy and it also decreases the efficiency of this detector. The design and mode of use of the total energy detector minimizes possible changes in its response as the capture gamma cascade changes.

A fission chamber is preferred for use because the fission detection efficiency can approach unity (~95% efficiency). As the efficiency for fission detection approaches unity, all the fission events are identified and capture is measured directly.

The direct measurement of the neutron capture rate simplifies the normalization of  $\bar{\sigma}_c$  and eliminates a large part of the uncertainty in  $\bar{\sigma}_c/\bar{\sigma}_f$  when this ratio departs from that used in the normalization. In order to achieve the large efficiency (~95%) for fission fragment detection, the thickness of the fissile isotope is limited to about 100  $\mu\text{g}/\text{cm}^2$  and for  $^{239}\text{Pu}$  considerations of the alpha particle decay rate limit the total amount of the isotope that can be used with a single detector system. The present fission chamber contained a total of 1.4 g of  $^{239}\text{Pu}$  and had an efficiency of about 50%. Investigations of signal-to-background ratios with the total energy detector show that measurements of  $\bar{\sigma}_c/\bar{\sigma}_f$  for  $^{239}\text{Pu}$  using 0.1 g quantities of the isotope are feasible.

#### References

\* Research sponsored by the Energy Research and Development Administration under contract with the Union Carbide Corporation.

<sup>1</sup>Evaluated Nuclear Data File (ENDF/B) of the National Neutron Cross Section Center. A detailed list of the evaluators for the particular isotope (defined with a Mat number, Mat 1159 for  $^{239}\text{Pu}$ , ENDF/B, Version III) is given in File 1 of the data tape. The ENDF/B data tape is available from National Neutron Cross Section Center. The average neutron cross sections from the ENDF/B tape used in the present work were obtained using the processing code SUPERTOG, R. Q. Wright et al., "SUPERTOG: A Program to Generate Five-Group Constants and Pu Scattering Matrices from ENDF/B," ORNL-TM-2679 (1969).



<sup>2</sup>M. G. Sowerby and V. A. Konshin, Atomic Energy Review 10, No. 4, 453 (1972).

<sup>3</sup>M. G. Sowerby et al., Proc. Conf. Nuclear Data for Reactors, vol. 1, p. 161 (1970), IAEA.

<sup>4</sup>L. W. Weston and J. H. Todd, Phys. Rev. C 10, 4, 1402 (1974).

<sup>5</sup>J. B. Czirr and J. S. Lindsey, Proc. Conf. Nuclear Data for Reactors, vol. 1, p. 331 (1970), IAEA.

<sup>6</sup>R. E. Bandl, H. Miessner, and Frohner, Nucl. Sci. Eng. 48, 329 (1972).

<sup>7</sup>A. Lottin et al., Proc. Conf. Fast Critical Experiments and Their Analysis, ANL-7320, Argonne, p. 22 (1966).

<sup>8</sup>J. C. Hopkins and B. C. Diven, Nucl. Sci. Eng. 12, 169 (1962).

The  $^{232}\text{Th}(n,f)$  and  $^{238}\text{U}(n,f)$  cross sections have been measured relative to that of  $^{235}\text{U}$  up to 6 MeV. The best energy resolution was 3 keV at 1.6 MeV. Below the fission threshold of  $^{238}\text{U}$ , intermediate structures are observed. In the  $^{232}\text{Th}(n,f)$  cross section, the broad vibrational resonances located above 1 MeV are resolved into sharp structures which are interpreted as rotational states. The angular anisotropy of fission fragments has been also measured in the same energy range. Thereby, values of  $K$  and  $J$  have been determined for each structure. The moment of inertia of  $^{233}\text{Th}$  in shape isomeric deformation has been deduced.

### Introduction

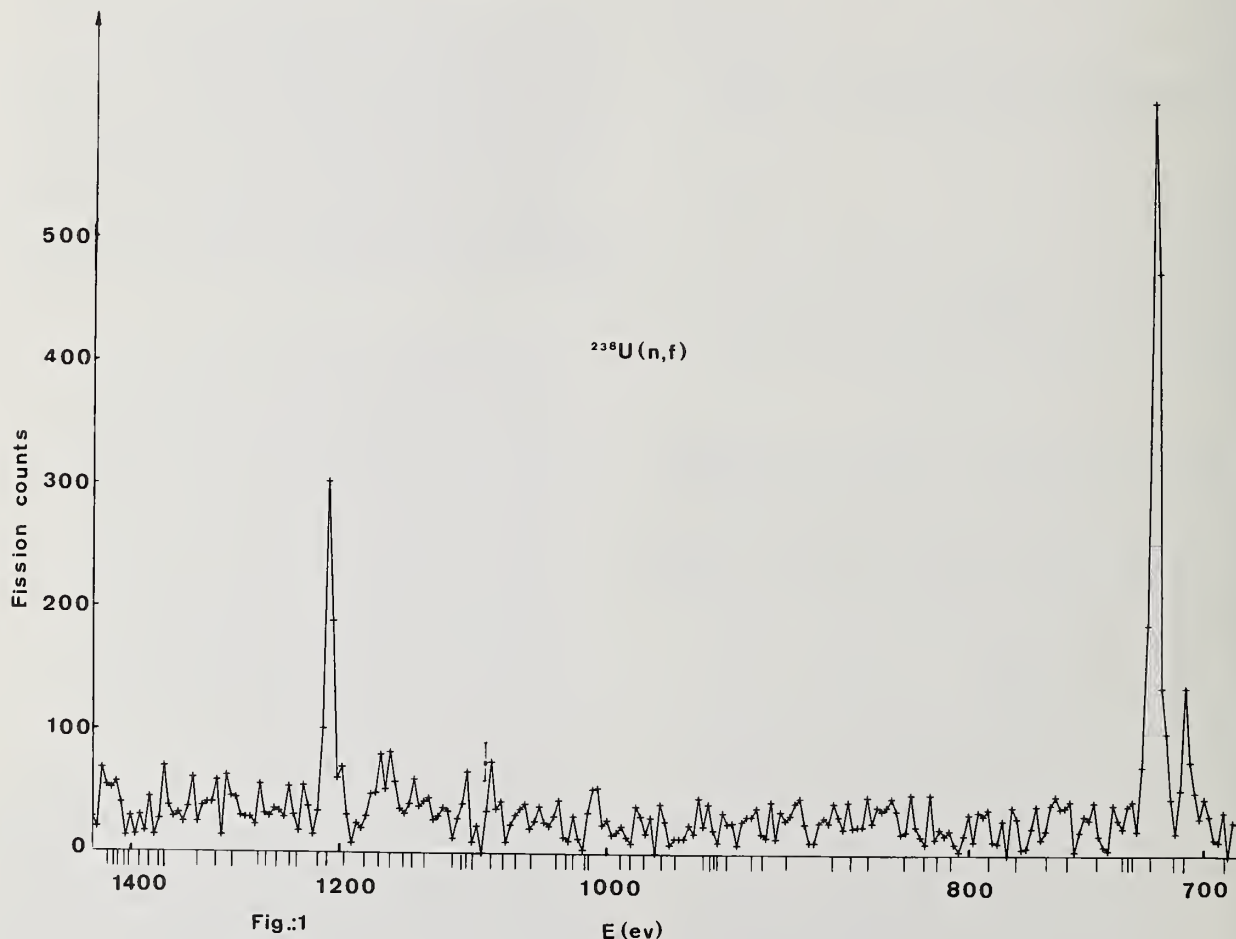
The last neutron measurements obtained with the 60 MeV Saclay linear accelerator before its closure, were used to determine fission cross sections of  $^{232}\text{Th}$ ,  $^{238}\text{U}$ ,  $^{243}\text{Am}$ ,  $^{237}\text{Np}$  and  $^{239}\text{Pu}$  relative to that of  $^{235}\text{U}$ , up to an energy of 6 MeV. The detector was a gas scintillator<sup>1</sup> divided into six optically independent cells containing a deposit of the isotope under study. In addition, one cell was equipped with an aluminium grid placed close by a layer of  $^{232}\text{Th}$ . The role of the grid was to stop the fission fragments emitted at an angle greater than  $\theta = 30^\circ$ , relative to the neutron direction, in order to measure the anisotropy of the fragments by comparison with a cell without grid. The transmission factor of the grid was 1/32.

Two sets of measurements were made : one, with a nominal resolution of 0.16 ns/m (51.9 m flight path) and one, with a nominal resolution of 0.27 ns/m (22.4 m flight path). The corresponding resolutions at 1.6 MeV were 3 keV and 6 keV respectively.

The data analysis is not completed yet. In this paper we will restrict ourselves to some outstanding features observed in the  $(n,f)$  cross sections of  $^{238}\text{U}$  and  $^{232}\text{Th}$ .

### Intermediate structure in $^{238}\text{U}(n,f)$

Block and al.<sup>2</sup> have reported an intermediate structure in the  $^{238}\text{U}$  fission cross section at 721 eV and 1211 eV. This effect is confirmed as seen in fig. 1. In the same figure we have indicated the position of



the neutron resonances. Although the statistics are barely sufficient, one observes about half of the known neutron resonances in this region. It can be seen also that the intermediate structure is not spread over many resonances as it is the case for  $^{237}\text{Np}$  or  $^{240}\text{Pu}$ . This would indicate that the widths of the class II states are of the same order or less than, the spacings of the levels in the first well. Other resonances are observed at 1684 eV, 2285 eV, 3230 eV, 4125 eV, 5250 eV, 7400 eV, 10710 eV, and 15140 eV.

In the threshold region many resonant structures appear, mainly at 337 keV, 618 keV, 793 keV, 899 keV, 921 keV, 960 keV and 1125 keV. The width of these structures is of the order of 20 keV, much larger than the ones observed in the resonance region. It is likely that many more structures exist around 1 MeV, but only those which are at energies where the cross-section does not increase very fast can be seen.

The near threshold fission of  $^{232}\text{Th}$

The  $^{232}\text{Th}$  fission cross section is known to present a broad resonance at 1.6 MeV and a smaller one at 1.7 MeV. Like in  $^{230}\text{Th}(n,f)$  cross section<sup>3</sup> it was anticipated that the shape of these resonances would be due to a rotational band built on a vibrational level but the previous attempt to resolve any fine structure has failed.<sup>4</sup> In our measurement with a 3 keV resolution, one observes, in particular, four well separated peaks at around 1.6 MeV and three others around 1.7 MeV (fig. 2). The angular anisotropy of the fragments has also been measured and is shown in fig. 3 where the number of fissions detected in the cell with

the grid, relative to the number of fissions detected in the cell without grid, is plotted versus the neutron energy. The ratio has been corrected for the transmission coefficient of the grid. In fig. 3, one also indicates the calculated values of the ratio :

$$a(K,J) = \frac{\int_0^{30^\circ} W(K,J;\theta) \sin \theta d\theta}{\int_0^{90^\circ} W(K,J;\theta) \sin \theta d\theta}$$

where  $W(K,J;\theta)$  is the angular distribution corresponding to the quantum numbers  $K$  and  $J$ .

Resonances at 1.4 and 1.7 MeV have  $K = 1/2$  and resonances at 1.5 and 1.6 MeV have  $K = 3/2$  values. The following table gives the energies of the fine structures, as obtained by a least square fit on the cross section.

$\epsilon_o(J,K)$ (MeV)	1.415	1.429	1.444	1.504	1.517	1.534	1.556
J	1/2	3/2	5/2	3/2	5/2	7/2	9/2
K	1/2			3/2			
$\epsilon_o(J,K)$ (MeV)	1.579	1.592	1.609	1.637	1.711	1.724	1.748
J	3/2	5/2	7/2	9/2	1/2	3/2	5/2
K	3/2				1/2		

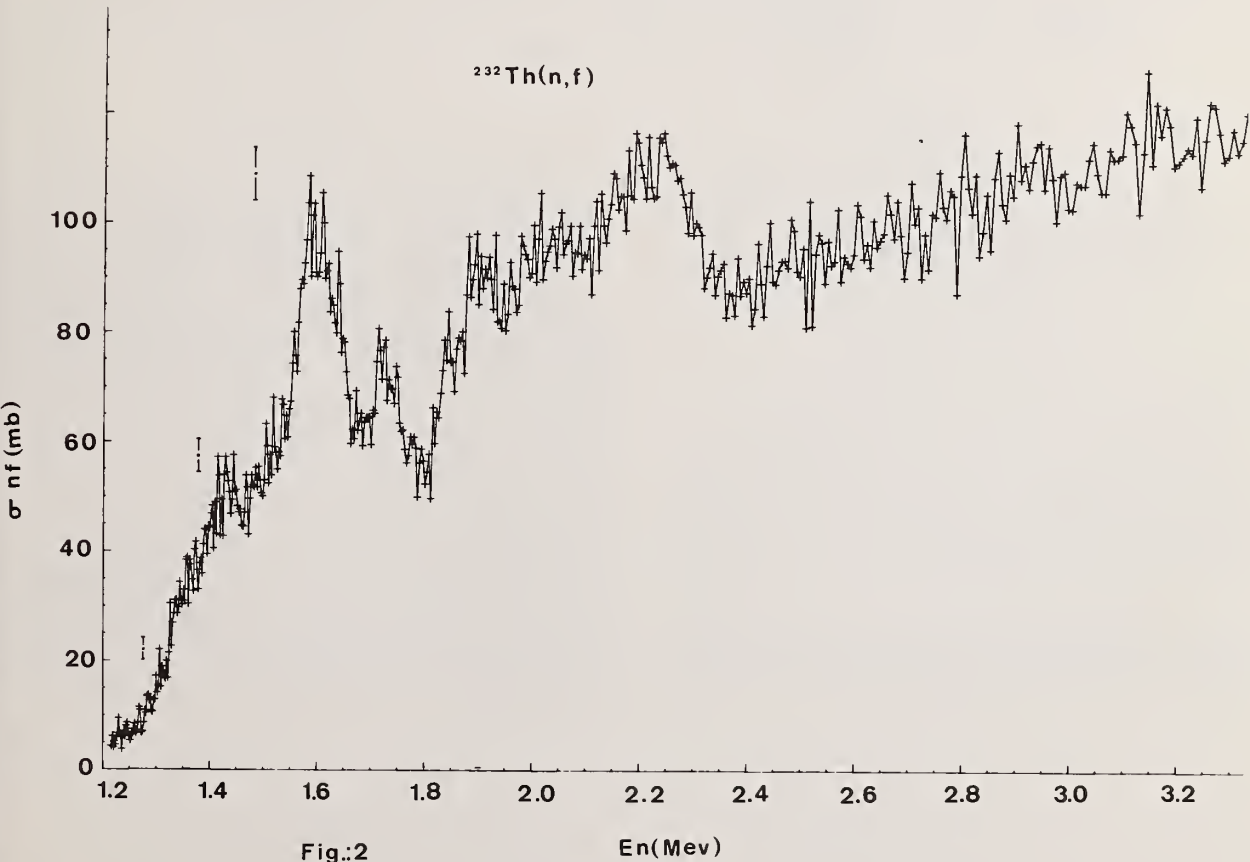


Fig.:2

En(Mev)



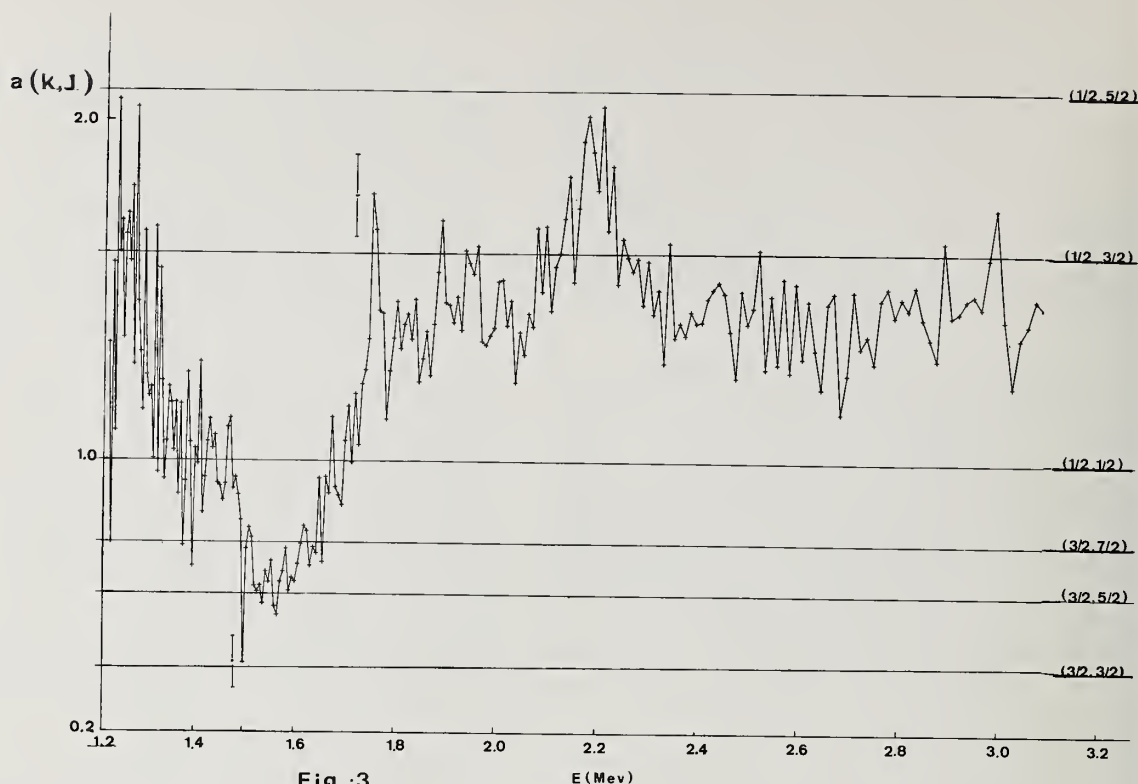


Fig.:3

These energies are in excellent agreement with the standard form for rotational bands :

$$\epsilon_o(J, K) = \epsilon_{oK} + \frac{\hbar^2}{2\mathcal{I}} |J(J+1) - K(K+1)| + \delta_{1/2, K} a(-1)^{J+1/2} (J+1/2)$$

where  $a$  is the decoupling parameter for  $K = 1/2$ .

The moment of inertia  $\mathcal{I}$  can be deduced from the energies of the rotational levels. For the  $K = 3/2$  bands, values of 2.5 and 2.8 are found for the parameter  $A = \hbar^2/2\mathcal{I}$  which is less than half of the usual value in the first well. For the  $K = 1/2$  bands, the effective moment of inertia is smaller with  $A = 3.9$  and 4.5, the decoupling parameters being  $a = 0.2$  and  $\sim 0.1$ .

The rotational levels can be fitted, both in position and in width, by the transmission coefficients of a double humped barrier, with reasonable parameters. For example, with the following parameters :

$$\begin{aligned} V_A &= 7.2 \text{ MeV} & \hbar\omega_A &= 0.8 \text{ MeV} \\ V_{II} &= 4.55 \text{ MeV} & \hbar\omega_{II} &= 0.5 \text{ MeV} \\ V_B &= 6.9 \text{ MeV} & \hbar\omega_B &= 0.56 \text{ MeV} \end{aligned}$$

The transmission coefficient shows a very broad peak at 1973 keV, a second one (10 keV wide) at 1612 keV and a third one (less than 1 keV wide) 430 keV lower. Around 1.1 MeV our statistic is too poor, but at 1306 keV, 1319 keV and 1343 keV we see three peaks with the same energy intervals as the three peaks of the rotational band located 405 keV above. In fig. 4 we have compared the fission-cross section with a calculated sum of transmission coefficients  $\sum_n a_n T_n(E)$  for a series of double humped barriers deduced from the one described above by translation along the  $V$  axis. The  $a_n$  coefficients have been chosen so that the shape of cross section is reproduced below 2 MeV. Although a more quantitative fit requires the use of the compound nucleus cross section, which is energy dependent, it is anticipated that, over a small energy range, the shape of the cross section is governed mainly by the transmission coefficients. As shown on fig. 4 a good qualitative agreement can be obtained.

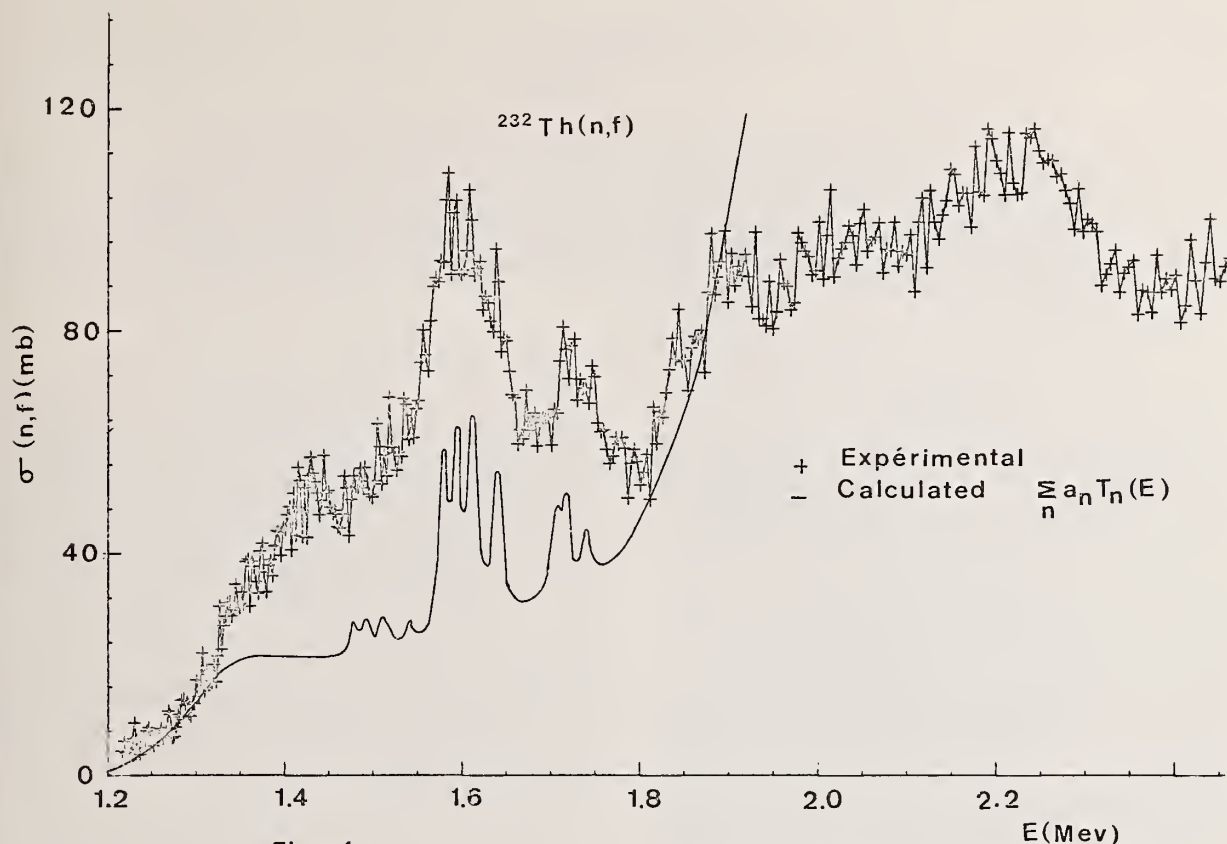


Fig.:4

#### Conclusion

Due to good energy resolution, we have been able to resolve many fine structures in the  $^{238}\text{U}(n,f)$  and  $^{232}\text{Th}(n,f)$  cross sections near the fission threshold. For  $^{232}\text{Th}$ , these fine structures have been identified as rotational bands built on vibrational levels. In the resonance region, intermediate structures have been observed for  $^{238}\text{U}$ . These measurements are intended to provide accurate fission cross sections up to 6 MeV. Data processing is in progress and the results will be published in the near future.

#### References

- 1 J. BLONS et al. Rev. Phys. appl. 4 (1969) 287.
- 2 R.C. BLOCK et al. Phys. Rev. Lett. 31 (1973) 247.
- 3 J.E. LYNN et al. AERE. R 6901 (1971).
- 4 E. KONECNY et al. Z. Physik, 251, (1972) 400.

MODEL CALCULATIONS AS ONE MEANS OF SATISFYING THE  
NEUTRON CROSS SECTION REQUIREMENTS OF THE CTR PROGRAM\*

Donald G. Gardner  
Lawrence Livermore Laboratory  
Livermore, CA 94550

A large amount of cross-section and spectral information for neutron-induced reactions will be required for the CTR design program. To undertake to provide the required data through a purely experimental measurement program alone may not be the most efficient way of attacking the problem. It is suggested that a preliminary theoretical calculation be made of all relevant reactions on the dozen or so elements that now seem to comprise the inventory of possible construction materials to find out which are actually important, and over what energy ranges they are important. A number of computer codes for calculating cross sections for neutron induced reactions have been evaluated and extended. These will be described and examples will be given of various types of calculations of interest to the CTR program.

[Cross-section calculations; statistical model codes; fast neutron reactions;  
radiation widths; gamma-ray production; isomers; applications to CTR.]

### Introduction

In a recent document<sup>1</sup> of the U.S. Nuclear Data Committee, entitled "Compilation of Requests for Nuclear Data", there are some 587 requests for information on various nuclear cross sections, of which over 100 came specifically from the AEC's Division of Controlled Thermonuclear Research (DCTR). In our opinion, only a small fraction of these requests will be satisfied in any reasonable length of time through an experimental program alone. Furthermore, these requests do not always specify the most important reactions or the most appropriate energy ranges. Finally, neutron reactions involving low abundance stable isotopes or even unstable species such as long-lived isomers or radioactive daughter products may be important in certain design considerations, and such reactions are inaccessible to normal experimental measurement in the laboratory.

It seems to us that the only approach that will get the job done is to make a preliminary theoretical calculation of all relevant reactions to find out which ones are actually important, and over what energy ranges they are important. This would then be followed by an experimental program to carefully measure only those reactions which are critical.

For certain engineering studies the calculated cross sections themselves might be sufficiently accurate, at least for preliminary evaluations, without further recourse to experiment. In a situation where there is a choice between otherwise comparable structural materials, calculations might show which material would cause the least problems. The calculated cross sections, when folded against estimated neutron flux histories from a CTR reactor, can show if unstable isotopes or isomers are important and to what extent deleterious daughter products will be produced and burned up. With regard to the experimental measurement program, the cross-section calculation can be used as a guide so that manpower is not wasted measuring relatively unimportant reactions and that important reactions are not overlooked.

### Nuclear Cross Section Codes

There are many different codes at Livermore of use in calculating nuclear reaction cross sections; however, we will restrict our discussion to the codes that we now have and are developing in Radiochemistry Division. Only the nuclear reaction codes will be discussed; no mention will be made of programs, such as nuclear structure codes, that may supply input information for our main programs.

\* Work performed under the auspices of the United States Atomic Energy Commission.

Our present codes comprise COMNUC<sup>2</sup> and CASCADE<sup>2</sup>, which are, respectively, a statistical model program and a program to calculate in detail the particle emission and fission competition occurring in a gamma-ray cascade; UHL<sup>3</sup>, another statistical model code used to compute isomer ratios; and FOURPLUS<sup>4</sup> and JUPITOR<sup>5</sup> which are coupled-channel, direct reaction codes. The codes were acquired during the past four-year period, and some have been extensively modified with the guidance of the original authors. Although we are still continuing the development of the codes, we feel at this time that they represent an exceptional facility for computing neutron-induced reaction cross sections in the neutron energy region from overlapping resonances up to perhaps 20 MeV.

Because of the exceptionally fine computer system at Livermore we are able to include in our calculations details and refinements that often are omitted. For example, the first compound nucleus population is computed for each  $J\pi$  spin and parity state, using optical model transmission coefficients, and the decay of each  $J\pi$  state is followed separately through all subsequent nuclei. At low energies, where only a few exit channels are available, the decay back to the target nucleus through the entrance channel is enhanced in COMNUC with a "correlation" correction, and again each  $J\pi$  state is considered separately. At each nucleus the gamma-ray emission in competition with particle decay and fission is considered. A combination constant temperature and Fermi gas level density may be used, and a simple yrast model is included so that unrealistically high spin states are not produced at low energies. Discrete nuclear levels may be included in all nuclei, as well as discrete fission channels where appropriate. This is vital for accurate calculations because level-density formulations cannot adequately represent the first 20 or so levels. In addition, the UHL code incorporates precompound evaporation of particles from the first compound nucleus. Both the UHL and the COMNUC - CASCADE codes calculate in great detail gamma-ray cascades. They are, to our knowledge, unexcelled in calculating reactions leading to isomers and reactions where gamma-ray cascades may be terminated by particle emission or fission before reaching the ground state.

Whenever the target nucleus is deformed it is necessary to calculate and correct for direct inelastic scattering reactions using the coupled-channel codes. The COMNUC code will accept reduced transmission coefficients from direct reaction codes, in order to properly compute the spin distribution in the first compound nucleus. The code will also accept



direct inelastic scattering cross sections and Legendre coefficients, and combine them with the compound nucleus evaporation results to give the complete inelastic scattering cross sections and angular distributions.

The codes COMNUC and UHL are compared in Table I. While they are both statistical model evaporation codes and while there are a number of differences between them they tend to complement each other. Neither code can do all calculations of interest to us, and each code was designed to do certain types of calculations better than the other code.

Table I. Comparison of current versions of statistical model codes at Livermore

Comment	COMNUC	UHL
1. Hauser-Feshbach with correlation correction	Yes	No
2. Moldauer's compound elastic "Q" correction	Yes	No
3. Built-in optical model program	Yes	No
4. Computes shape elastic and total cross sections	Yes	No
5. All possible cross sections always calculated	Yes	No
6. Entrance channel always neutrons	Yes	No
7. Level density formulation	Constant temperature plus Fermi gas	
8. Simple yrast level model	Yes	Yes
9. Discrete states in all nuclei considered	Yes	Yes
10. Computes angular distribution for discrete neutron channels	Yes	No
11. Calculates spectra of emitted particles	No	Yes
12. Precompound evaporation allowed	No	Yes
13. Gamma-ray competition with each compound nucleus	Yes	Yes
14. Maximum number of compound nuclei in evaporation sequence	3	6
15. Calculates gamma-ray spectra and gamma-ray production cross sections	No	Yes
16. Weisskopf and/or Brink-Axel energy dependence of the radiation width	Yes	Yes
17. Fission competition allowed	Yes	No
18. Direct and semi-direct neutron capture	Yes	No
19. Computes isomer populations	No	Yes
20. Accepts input from direct reaction codes	Yes	No

#### Cross-Section Calculations for the CTR Program

In a thermonuclear reactor the first wall material will face an incredibly intense, sustained radiation environment, and so radiation damage is likely to be a controlling engineering consideration in the reactor design. For the first wall this damage will be due mainly to elastic and inelastic neutron scattering and  $(n,2n)$  reactions from fast neutrons, while for low energy neutrons the  $(n,\gamma)$  reaction will be the main source of damage. For most first wall materials under consideration,  $(n,p)$  and  $(n,\alpha)$  reactions play a lesser role in displacement production, although blister production and embrittlement by hydrogen, and in particular by helium, may be a serious problem in the blanket components as well as the first wall. However, when it comes to heat deposition, in the cryogenic materials for example, it is the  $(n,p)$  and  $(n,\alpha)$  reactions, along with neutron capture, that become of major importance. Tritium production in the CTR is vital and this will be accomplished via neutron reactions on  ${}^6\text{Li}$ . However, only one neutron is produced per D-T reaction, which means that neutron multiplication through  $(n,2n)$  reactions is required. Shielding from both neutrons and gamma rays will be necessary to protect components and also to satisfy biological requirements. And then there is the problem of radioactivity produced in the reactor components. Here reliable data are essential for engineering, processing and storage design, not to mention the environmental aspects and public acceptance.

#### $(n,p)$ and $(n,\alpha)$ Reactions

With regard to the problems of hydrogen and helium embrittlement and energy deposition in structural materials, one could compute the excitation functions of these reactions for various materials such as niobium, vanadium or stainless steel, and point out which materials will cause the greatest problems. In Fig. 1 we compare an old calculation of an  $(n,\alpha)$  reaction on  ${}^{40}\text{Ca}$  with an experimental excitation function<sup>6</sup> measured about one year after the calculation was made. The agreement is quite satisfactory.

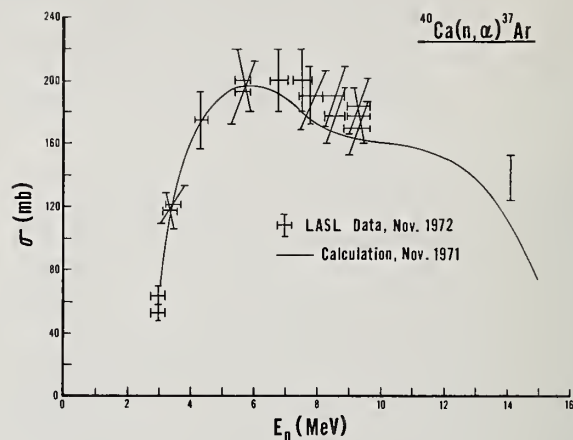


Fig. 1. Calculated and experimental values for the  ${}^{40}\text{Ca}(n,\alpha){}^{37}\text{Ar}$  reaction.

It often happens that around 14 MeV in light materials the  $(n,pn)$  and  $(n,np)$  reactions are comparable to the  $(n,p)$  reaction in magnitude. Hence, measuring only the  $(n,p)$  reaction isn't sufficient. What one needs is the cross section for proton production by whatever means possible. To a lesser extent this is also true for  $\alpha$ -particle production, since  $(n,\alpha n)$  and  $(n,\alpha\alpha)$  reactions must often be considered as well as the  $(n,\alpha)$  reaction. Figs. 2 and 3 show rough calculations for proton and alpha-particle production from neutron reactions on the ground state of  ${}^{93}\text{Nb}$ . The calculations were made two years ago using global parameters for radiation widths, level densities and transmission coefficients. No attempt was made to adjust any parameters to fit experimental data. Similar calculations for  ${}^{51}\text{V}$  show that around 14 MeV the  $(n,p)$  and  $(n,pn)$  cross sections are quite similar, while the  $(n,np)$  cross section is about a factor of two greater than the sum of the  $(n,p)$  and  $(n,pn)$  cross sections.

Another common occurrence in such light materials is that neighboring isotopes of an element will have quite sizeable differences in the Q-values for  $(n,p)$  and  $(n,\alpha)$  reactions. For instance  ${}^{54}\text{Fe}$  and  ${}^{56}\text{Fe}$  have high thresholds for  $(n,p)$  and  $(n,\alpha)$  reactions whereas unstable  ${}^{55}\text{Fe}$  will undergo these reactions with thermal neutrons. The isotope  ${}^{50}\text{V}$  has considerably higher cross sections than does  ${}^{51}\text{V}$  for  $(n,p)$  and  $(n,\alpha)$  reactions for neutrons of a few MeV and lower. Therefore, the importance of rare stable isotopes or unstable species will depend on the energy spectrum and the fluence of neutrons to which they are exposed. Structural materials will be exposed to a sea of scattered,

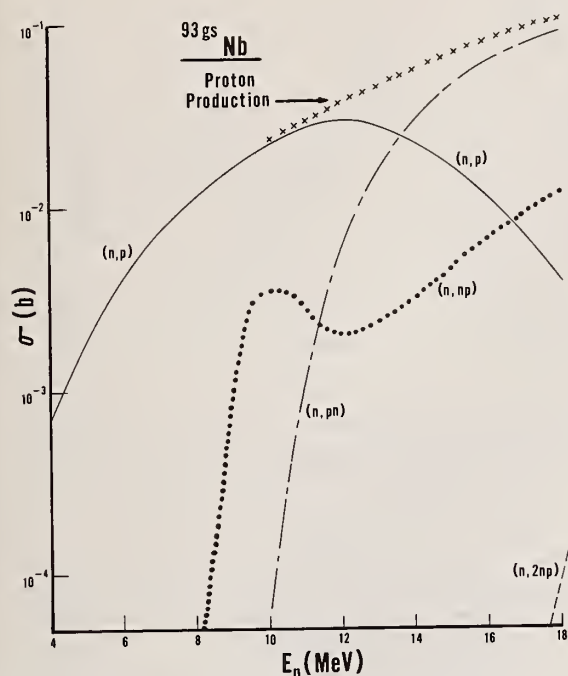


Fig. 2. Estimated proton production induced by neutrons on  $^{93}\text{Nb}$  ground state.

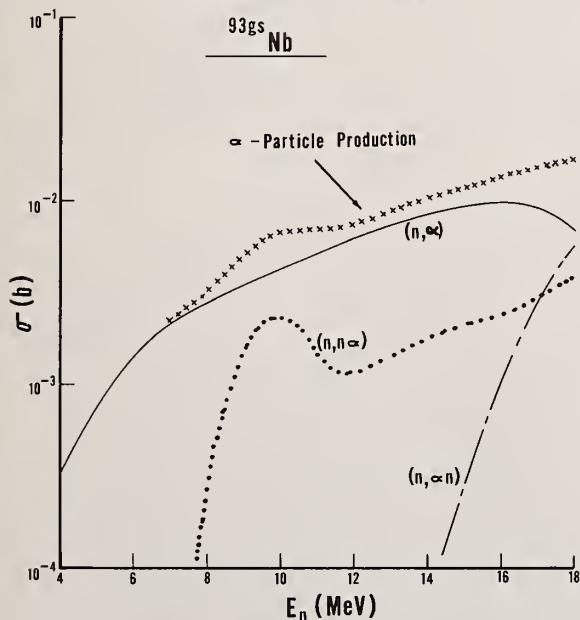


Fig. 3. Estimated helium production induced by neutrons on  $^{93}\text{Nb}$  ground state.

lower energy neutrons in addition to the primary spectrum of neutrons emitted by the plasma. Furthermore, the primary flux will tend to be normal to the surface of the first wall, while the scattered flux will have a full selection of incident angles and thus have a longer average path in the wall and other structural components. Hence, realistic calculations should be made over all neutron energies, not just at 14 MeV, to see if such rare or unstable species are important.

#### Gamma-Ray Production and Shielding

Gamma-ray production cross sections and the energy spectrum of the emitted gamma rays following most particle reactions can be computed, particularly in the gamma-ray energy regions below one MeV and above 5 MeV where the greatest experimental difficulties are encountered. In the latter range it is the transmission of the gamma-ray flux through shielding that is of concern, whereas for low-energy gamma rays it is usually the local deposition of energy resulting in ionization or heat that is important. To assist in local heating calculations one can also compute the conversion-electron, production cross section and energy spectrum.

Recently we have made calculations for  $^{181}\text{Ta}$  for neutrons up to 20 MeV in energy, and for  $^{197}\text{Au}$  for neutrons in the keV region. Fig. 4 presents some of our  $^{181}\text{Ta}$  results compared with experimental measurements from Oak Ridge.<sup>7</sup> Fig. 5 compares the calculated conversion electron spectrum following thermal neutron capture with some unpublished, relative measurements.<sup>8</sup> The latter were arbitrarily normalized at the point

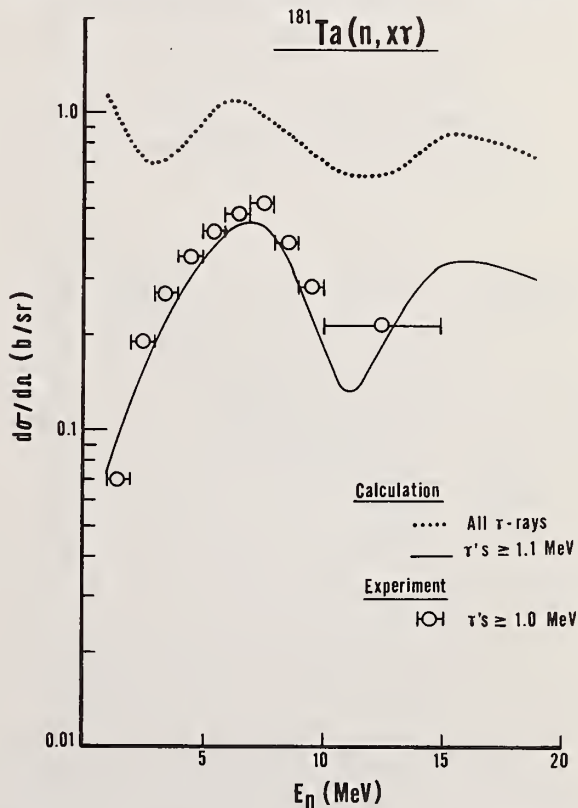


Fig. 4. Calculated and experimental values for gamma-ray production induced by neutrons on  $^{181}\text{Ta}$ .

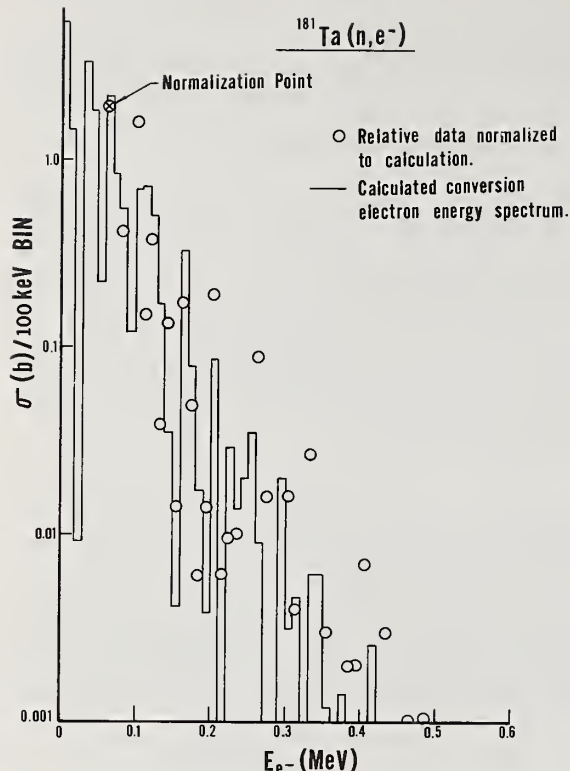


Fig. 5. Calculated conversion electron spectrum following thermal neutron capture on  $^{181}\text{Ta}$ , compared with normalized, relative experimental measurements.

shown so that the general trend of the data could be compared with the calculations. The calculated transitions have been grouped in 100-keV bins for clarity.

As an example of a calculation of the gamma-ray energy distribution following neutron capture, we show in Fig. 6 some recent results for  $^{197}\text{Au}$ . The calculation is in terms of photons/100 captures, and hence is quite insensitive to the magnitude of the radiation width employed. The data is that of Orphan.<sup>9</sup> We show the original, unnormalized data, and disregard the measurements for gamma rays below 2 MeV in energy. The EI gamma-ray strength function required to fit both the energy spectrum and the  $(n, \gamma)$  excitation function shown in Fig. 7 is displayed in Fig. 8. The general shape and magnitude agree with the strength functions extracted from other experimental data.<sup>10</sup> To obtain the indicated shape it was necessary to assume that the energy dependence of the radiation width corresponded to about 60% Brink-Axel, with a large, sharp decrease in the tail of the giant dipole resonance around 4 MeV, together with 40% "pigmy" resonance around 2.9 MeV. An almost equally good fit could be obtained with a combination of 30% Brink-Axel (with the same step) and 70% Weisskopf single particle energy dependence.

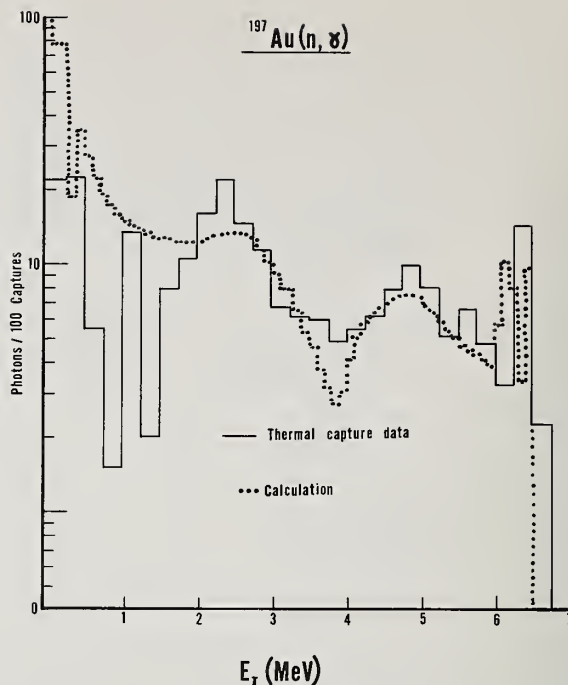


Fig. 6. Calculated and experimental values for the gamma-ray energy spectrum following thermal neutron capture by  $^{197}\text{Au}$ .

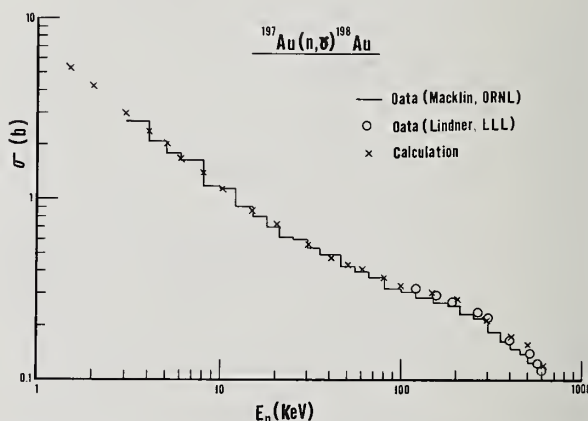


Fig. 7. Calculated and experimental values for the capture cross section of  $^{197}\text{Au}$ .

The step in the giant dipole tail amounted to about 95% decrease, and was necessary to reproduce the "excess" high-energy gamma rays in the capture spectrum. The same step is responsible for the fact that "excess" high-energy gamma rays do not appear in the spectrum following neutron inelastic scattering. When the same strength function is assumed for  $^{197}\text{Au}$  as was determined for  $^{198}\text{Au}$ , the results shown in Fig. 9 are obtained for the  $^{197}\text{Au}(n, n'\gamma)$  reaction. Even at



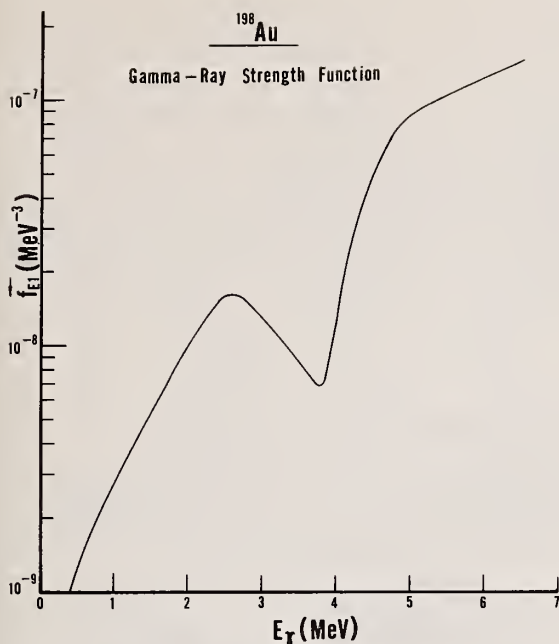


Fig. 8. Deduced gamma-ray strength function for  $^{198}\text{Au}$ .

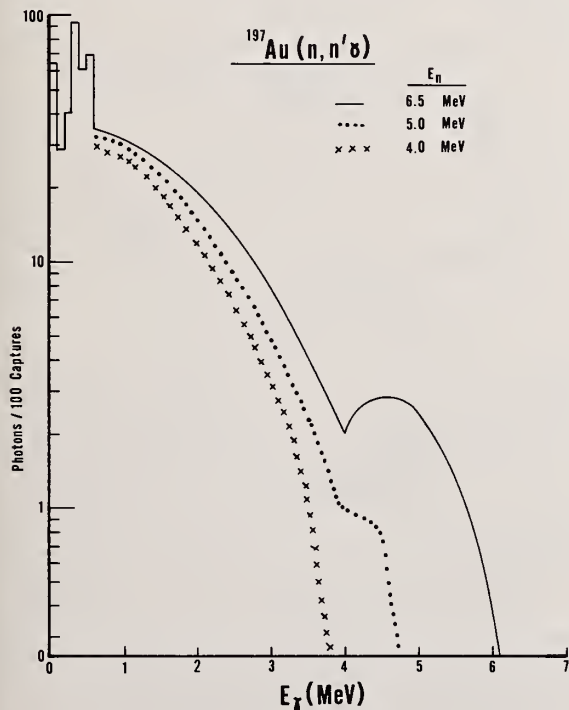


Fig. 9 Calculated gamma-ray spectrum following the inelastic scattering reaction on  $^{197}\text{Au}$ .

6.5 MeV, which corresponds to the neutron separation energy in  $^{198}\text{Au}$ , the high-energy bump is barely noticeable. The reason is that the  $(n,n')$  reaction will populate states in the target nucleus from zero up to

the center-of-mass energy of the incident particle. Only those states higher in energy than the step in the strength function can produce the high-energy bump, and it is only a small fraction of these states that actually will emit the required high-energy gamma rays. Clearly, the  $(n,n')$  gamma-ray spectrum will always be more skewed towards lower-energy transitions than the capture spectrum at an equivalent energy.

In the past we have used the approach of Stolovy and Harvey<sup>11</sup> to estimate unknown radiation widths. They suggest the semi-empirical relation

$$\overline{\Gamma}_\gamma = K A^{2/3} U^\alpha [D(U)]^\beta, \quad (1)$$

where  $A$  is the mass,  $U$  is the excitation energy corrected for pairing effects, and  $D(U)$  is the level spacing per spin state.

We have obtained values<sup>12</sup> for the constants  $K$ ,  $\alpha$ , and  $\beta$  by fitting 83 experimental radiation widths for nuclei from  $^{59}\text{Co}$  to  $^{246}\text{Cm}$ . For energies and level spacings in MeV units and for radiation widths in millivolts, good results are obtained with  $K = 0.0916$ ,  $\alpha = 3.50$ , and  $\beta = 0.256$ . Actually a slight improvement is effected if smaller ranges of elements are fitted separately. Our current parameter values are given in Table II, and the calculated radiation widths are compared with experiment in Fig. 10. The error flags merely indicate the spread in the reported experimental values for a few nuclei.

Table II. Parameter Values for the Stolovy-Harvey Radiation Width Expression.

Range	$K$	$\alpha$	$\beta$
$\leq 43$	0.19241	2.9955	0.20397
44-83	0.19745	2.9297	0.23454
$\geq 84$	0.087102	1.9449	0.052733

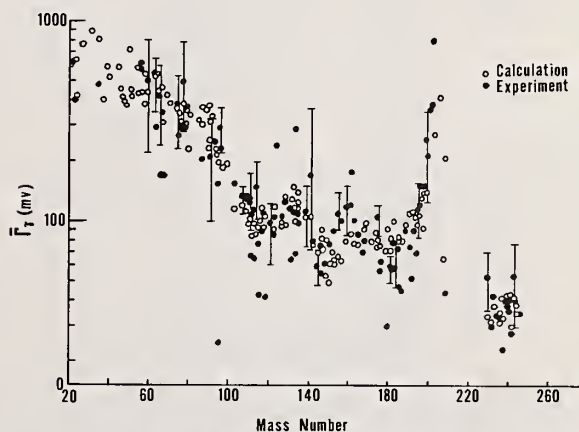


Fig. 10. Calculated and experimental values for average radiation widths.

We now feel, however, that it may be easier to develop systematics for estimating unmeasured gamma-ray strength functions, rather than the radiation widths themselves. This appears to be true at least for medium weight to heavy nuclei.

Some of the most accurate kinds of calculations that we can make involve neutron elastic and inelastic scattering reactions. For these we can compute the cross-sections, angular distributions, and the energy spectrum of the emitted neutron. Such information is of interest, for example, because these reactions are major producers of recoil target atoms, which, in turn, produce an important portion of the radiation damage in materials. Furthermore, the information is required for neutron shielding calculations, and for the estimation of radioactivity produced in structural materials.

As an example, we present some recent calculations made on  $^{235}\text{U}$ . The general situation is illustrated in Fig. 11, using the single-hump fission barrier approximation. In order to compute the inelastic scattering properly it is necessary to compute concurrently all reactions that can compete, and all calculations must be satisfactory. In this case the fission and gamma-ray competition are critically important, and because  $^{235}\text{U}$  is deformed the direct inelastic scattering to the ground state band must be

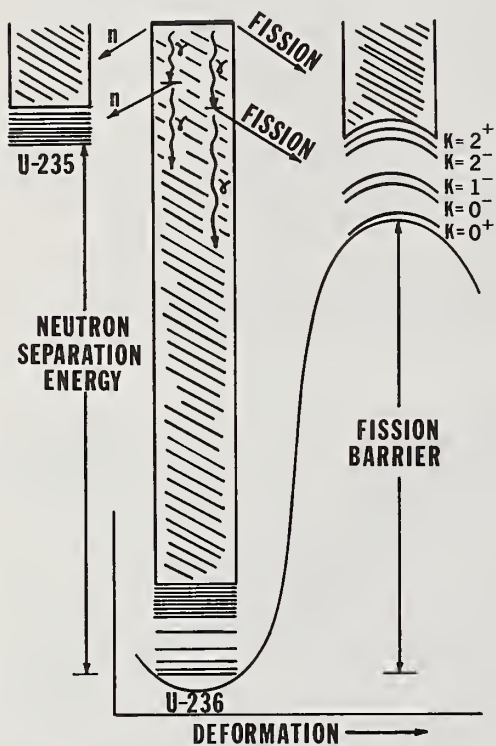


Fig. 11. Gamma-ray and fission competition to neutron inelastic scattering on  $^{235}\text{U}$ .

included. Nineteen discrete levels were included for  $^{235}\text{U}$ , twenty-five for  $^{236}\text{U}$ , and twenty discrete fission channels were used. Beyond these in each case a continuum of levels and fission channels was assumed. The discrete fission channels were taken as rotational bands built upon the vibrational bandheads shown in Fig. 11. The positions of these bandheads were

taken from the work of Britt, et al.,<sup>13</sup> and adjusted slightly to improve the fit to the ENDF/B-IV and the ENDF<sup>14</sup> evaluations. Moldauer's optical model parameters<sup>15</sup> were used to produce the neutron transmission coefficients. The total and fission cross sections appear in Fig. 12, while the elastic scattering and capture cross sections are given in Fig. 13. The angular distributions for the elastic scattering reaction, computed with a spherical potential for incident neutron energies of 0.2 and 0.5 MeV, are shown in Fig. 14. Finally, in Fig. 15 we present the calculated total inelastic scattering excitation function together with those for two of the levels in  $^{235}\text{U}$ .

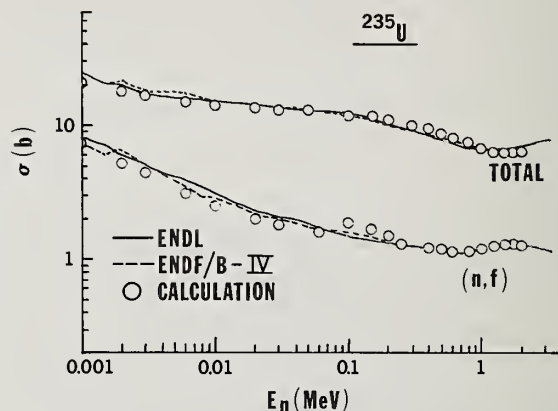


Fig. 12. Calculated and evaluated excitation functions for the neutron total and (n,fission) reactions on  $^{235}\text{U}$ .

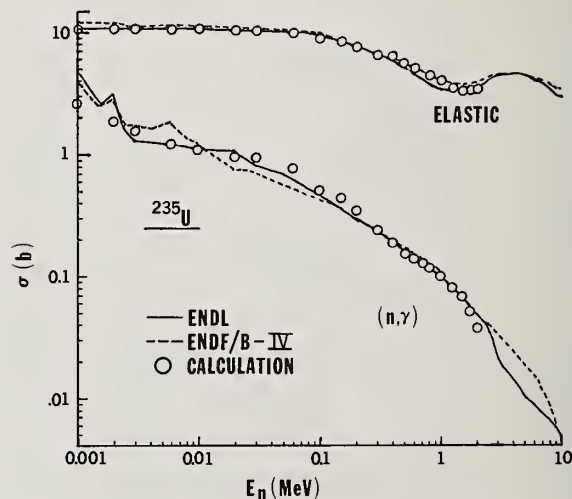


Fig. 13. Calculated and evaluated excitation functions for the neutron elastic scattering and capture reactions on  $^{235}\text{U}$ .

#### Radioactivity in Structural Materials

Radioactivity will be built up in the materials comprising a fusion reactor. Since the components must be replaceable when their damage approaches unsafe levels, it is important to know what levels of radioactivity may be anticipated in the various

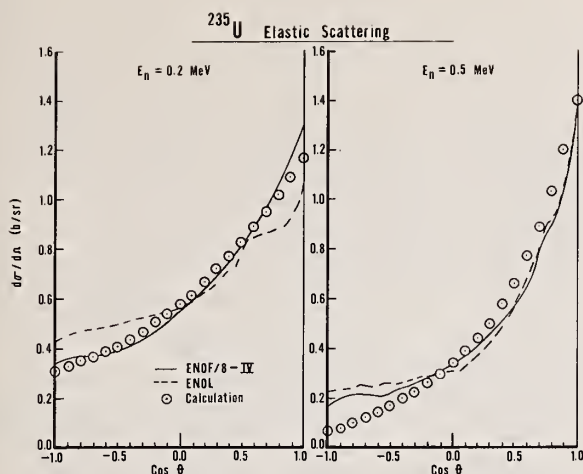


Fig. 14. Calculated and evaluated angular distributions for elastically scattered neutrons, at 0.2 and 0.5 MeV initial energy, on  $^{235}\text{U}$ .

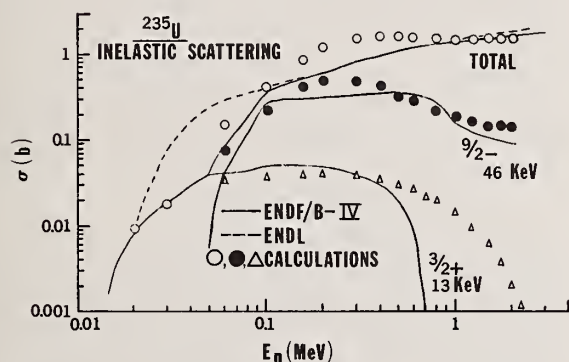


Fig. 15. Calculated and evaluated excitation functions for the total inelastic scattering reaction on  $^{235}\text{U}$ , and to two specific target levels.

components. Some components, such as the first wall, might have to be replaced every other year, while others might last 30 years or the anticipated life of a fusion reactor. Hence, not only the amount of radioactivity, but the activity as a function of operating time must be estimated.

The fast neutron flux from a fusion reactor will emphasize the importance of  $(n,2n)$  reactions, particularly where medium weight and heavy elements are involved. A relatively recent calculation for  $^{169}\text{Tm}$  is shown in Fig. 16, along with some Livermore measurements.<sup>16</sup> The high energy tail of the inelastic scattering reaction is due to precompound neutron evaporation plus the direct inelastic scattering.

Sometimes the radioactivity produced is due primarily to only one isomer in the daughter nucleus. In this case the gamma-ray cascade leading to the production of the isomer must be considered. Fig. 17 shows an old calculation for the production of the 4.5-hour isomer in  $^{115}\text{In}$ . The high-energy tail results from the assumption that the precompound evaporation of neutrons builds up to about 4% of the total

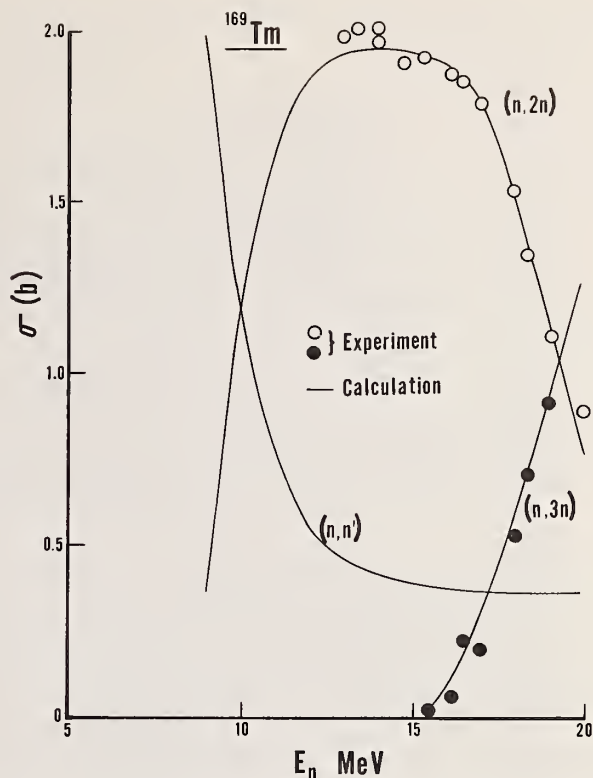


Fig. 16. Calculated and experimental values for the  $(n,2n)$  and  $(n,3n)$  reactions on  $^{169}\text{Tm}$ .

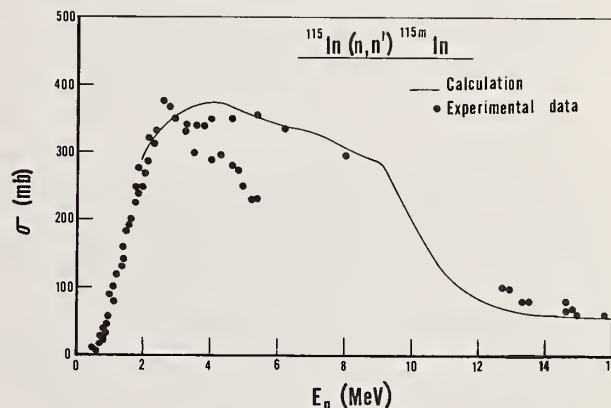


Fig. 17. Calculated and experimental values for the  $^{115}\text{In}(n,n')^{115m}\text{In}$  reaction.

neutron evaporation.

In many instances the amount of radioactivity likely to be produced could limit the choice of construction materials. For example, the 6-second positron emitter  $^{26m}\text{Al}$  produced by the  $(n,2n)$  reaction on  $^{27}\text{Al}$  might cause a problem in aluminum-based electrical insulators. Unfortunately there is about a factor of 30 discrepancy in the available experimental data. We have recently made the calculation, and in Fig. 18 we present our results both for the total  $(n,2n)$  reaction and for that fraction leading to the isomer. Our calculations are in fair agreement with the ENDF/B-IV estimate for the total  $(n,2n)$  reaction, and agree



better for the isomer production with Mani, *et al.*<sup>17</sup> than with Arnold.<sup>18</sup>

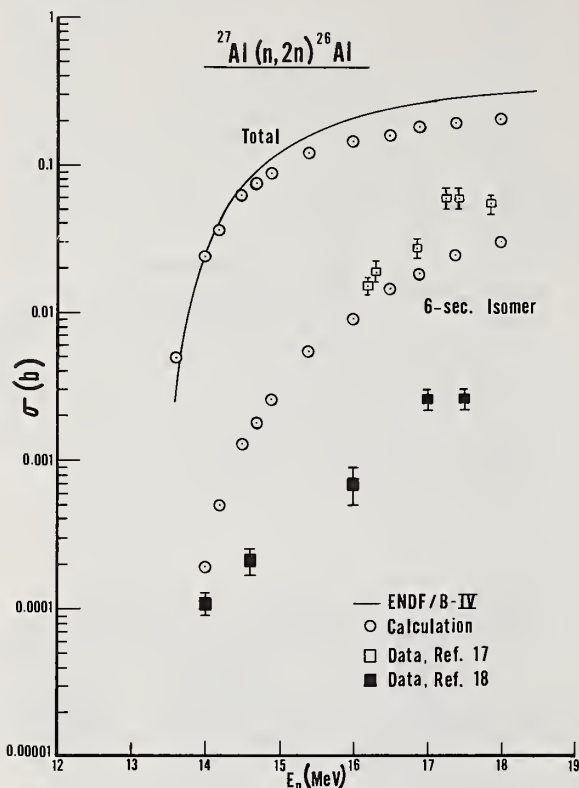


Fig. 18. Calculated excitation functions for the total (n,2n) reaction on  $^{27}\text{Al}$ , and for the production of the 6-second isomer in  $^{26}\text{Al}$ .

#### Accuracy of the Calculations

It is difficult to be quantitative about the accuracy that may be expected in any given case, because different reactions require different kinds of physical parameters as input. Our philosophy is that all reactions that occur concurrently must all be calculated satisfactorily before any of them can be trusted. If some information is available on any of the competing reactions, this will improve the accuracy of all calculations. Some reactions are inherently more difficult to calculate, and certain mass regions present more problems than others. However, a few rough generalizations may be made.

1. The total and elastic scattering reactions depend on optical model parameters. There are good sets available, for a spherical potential, that have been so adjusted to represent even deformed nuclei rather well. Finding parameters to be used with a deformed potential is far more difficult, but this is less important because the correction for direct inelastic scattering is usually less than 20% of the compound nucleus formation cross-section.
2. Inelastic scattering and (n, $\gamma$ ) reactions are dependent upon a good estimate of the first 15-25 levels in the target nucleus. We always use theoretical estimates of these levels to supplement the available experimental information. The levels in the A + 1

nucleus are of less importance, particularly for medium and heavy nuclei. However, for light nuclei, where most or all of the levels may be of one parity, the inclusion of these levels can affect the apparent energy dependence of the radiation width as the different partial waves come in. We always include precompound evaporation for neutron energies above a few MeV, although the effect is relatively small. The radiation width and its energy dependence can be estimated fairly well, and there is hope that this can be done even better with gamma-ray strength functions.

3. The (n,2n) reaction can usually be well represented, particularly for medium weight and heavy nuclei not susceptible to fission. For deformed nuclei the enhancement of the inelastic scattering at the expense of the (n,2n) reaction must be included.

4. For (n,p) and (n, $\alpha$ ) reactions at low energies it is more difficult to find satisfactory optical model parameters. Discrete level information is again quite important, and in the case of (n,p) reactions with light nuclei the precompound evaporation is very important.

5. Perhaps the most difficult situation involves fission. At low energies a shift in position of a discrete band of fission channels can be quite significant. Usually the density of fission channels at the saddle point exceeds the normal level density, and by as much as a factor of two in some cases. At high energies it becomes necessary to consider individually the (n,n' fission) and the (n,2n fission) reactions with gamma-ray and neutron competition. Except for fission isomers and subthreshold resonances related to levels in the second minimum, it is often adequate to use the single-hump barrier approximation in fission calculations.

#### Acknowledgments

We are particularly indebted to C. Dunford and M. Uhl, who supplied the original statistical model codes and guided their further development. At Livermore many people have contributed to the development of our codes and calculations. The assistance of the following people is gratefully acknowledged: J. Brownlee, A. Delucchi, C. Gatrousis, R. Lanier, N. Smith, G. Struble and J. Ferguson

#### References

1. L. Stewart, *et al.*, editors, LA-5252-MS (USNDC-6), 1973.
2. C. L. Dunford, AI-AEC-12931 (July, 1970).
3. M. Uhl, Acta Physica Austriaca **31** (1970) 245.
4. C. L. Dunford, unpublished computer program.
5. T. Tamura, ORNL-4152 (August, 1967).
6. Private communication, R. Prestwood, LASL.
7. G. L. Morgan, *et al.*, ORNL-TM-3702 (February 8, 1972).
8. P. Goudsmit, Thesis, Amsterdam University, 1969, NUIS-18536.
9. V. Orphan, *et al.*, GA-10248 (July 31, 1970).
10. G. Bartholomew, *et al.*, Advances In Nuclear Physics, Vol. 7, Chapter 4, Plenum Press, New York, 1973.
11. A. Stolovy and J. Harvey, Phys. Rev. **108** (1957) 353.
12. D. Gardner and C. Gatrousis, unpublished results.
13. H. Britt, *et al.*, Phys. Rev. **175** (1968) 1525.
14. R. Howerton, Lawrence Livermore Laboratory.
15. P. Moldauer, Nuclear Physics **47** (1963) 65.
16. D. Nethaway, private communication.
17. G. Mani, *et al.*, Nuclear Physics **19** (1960) 535.
18. D. Arnold, thesis, Dissertation Abstracts **26** (1965) 3525.

T. A. Tombrello  
California Institute of Technology  
Pasadena, California 91125

The copious production of neutrons in the "standard" CTR fuels has led to a renewed interest in proposals that various "exotic" fusion fuels be investigated. These fuels invariably involve reactions on lithium, beryllium, or boron isotopes in which most of the energy is liberated in the form of charged particles. Obtaining reaction cross sections at the appropriate energies or extrapolating the yield into inaccessible energy regions is, however, not always a straightforward procedure; and each reaction may require the development of new techniques. By means of selections from among such "exotic" fuel reactions, I shall show examples of experimental techniques for charged particle cross-section measurements at low energies and some techniques for extrapolation to still lower energies.

(NUCLEAR REACTIONS Discussion of the use of the  $d+d$ ,  $d+t$ ,  $d+{}^3\text{He}$ ,  $p+{}^6\text{Li}$ ,  $d+{}^6\text{Li}$ ,  $p+{}^9\text{Be}$ , and  $p+{}^{11}\text{B}$  reactions for CTR energy production.)

### Introduction

It is my intention in this paper to provide a brief survey of current ideas, problems, and data needs related to the use of nuclear reactions in controlled thermonuclear reactors. Though I shall be mainly concerned with questions related to nuclear reaction cross sections; problems of fuel cost, energy yield, build-up of radioactivity, etc. must be considered simultaneously to achieve a balanced perspective.

The present status of both magnetic confinement and laser driven fusion indicates that we are somewhere between two and three orders of magnitude away from the temperatures, densities, or confinement times that are necessary for useful CTR's. Thus, our current problems lie entirely in achieving these goals, thereby making the subject of this paper seem extremely premature. However, the construction of new fusion research facilities to test our current ideas involves lead times of 10-20 years; thus, even though we cannot see beyond the nearby obstacles, we need to face in parallel other difficulties that arise from radiation damage processes and fuel availability. Only if we have the required nuclear cross-section data in hand can we evaluate potential fuels and fuel cycles far enough in advance that decisions on second generation facilities can be made at an opportune time.

### Criteria for Fusion Fuels

It is quite clear that what one ultimately chooses as the optimum fusion fuel will represent a trade-off of many competing factors. A primary requirement is that one can find an exoergic nuclear reaction that has a high cross section at very low bombarding energies. From our knowledge of stellar element formation we know, however, that this requirement may also imply relative rarity. Thus, we must immediately think in terms of the cost of procuring this fuel and consider the possibility that it must be separated from other common isotopes of the same element.

Going beyond the questions of reaction rate and fuel cost, the nature of the reaction products of the fuel-burning reactions must also be taken into account. Obviously, we would like to minimize both the production of long term radioactivities and the structural damage that occurs through sputtering or through the interaction of fast neutrons with the reactor components. Such requirements involve a detailed study of the rate of radiation damage and the development of procedures by which radioactive by-products may be

safely handled. To use a currently fashionable analogy: we must consider not only the initial fuel cost but also the fuel's impact on the environment of the reactor.

Though the major part of the energy release is expected to occur at quasiequilibrium (equilibrium implying a well-defined temperature), one expects that non-equilibrium processes are also involved. Such processes arise mainly from nuclear reaction products that interact with the fuel before they are thermalized. Such effects play a large role in making possible some of the so-called "exotic" fuels. However, it is also expected that these processes allow the build up of unwanted radioactive species and thus must be evaluated from both points of view.

Because of the need for a high cross section at low temperature, we are necessarily limited in our choice of fuels to elements of low atomic number. This arises, of course, because of the Coulomb barrier between the charged particles in the fuel-burning reactions. This limitation also occurs due to rapid increase in the bremsstrahlung yield with atomic number. Cooling of the fuel by the escape of these x-rays requires that not only must the fuel be of low atomic number but also one must avoid the build-up of high-Z reaction products or contaminants. In magnetic confinement devices the major problem in the latter regard lies in the sputtering of metal ions from the reactor walls by energetic neutral atoms from the plasma; in laser-driven devices the shell of the pellet or microballoon must be chosen with this criterion in mind.

To summarize these points; our fuel and fuel reactions should be chosen to best reflect the following criteria:

- (1) The reaction cross section should be high at low energy and the reaction should have an appreciable energy release.
- (2) The fuel should be relatively cheap, require a minimum of preparation and be easily handled.
- (3) Reaction products should not lead to structural damage or to the buildup of long-lived radioactivities.
- (4) Elements with higher atomic numbers should be avoided because of their enhanced bremsstrahlung losses.

\*Supported in part by the National Science Foundation [GP-28027 and GP-43585].



Since we may for many years be limited to ignition temperatures corresponding to ion energies of 1-10 keV, criterion (1) takes on a special significance. Thus, you will hear no real enthusiasm from the people responsible for CTR development for any reaction other than  $d + t \rightarrow n + \alpha$  ( $Q = 17.6$  MeV). Because of the s-wave resonance at a center-of-mass energy of 60 keV and the lowest possible values of  $Z$ , this reaction has a rate that is orders of magnitude greater than its nearest competitor.<sup>1</sup> (See Fig. 1.) However, it is quite clear that an enormous price has been paid in terms of criteria (2) and (3). The tritium must be produced in nuclear reactors and it may be too expensive to consider as a fuel for anything but initial testing of first generation fusion reactors. In addition, tritium is radioactive and represents a significant handling problem. The neutrons from the reaction carry away 80% of the energy — leading to structural damage and further problems with induced radioactivity.

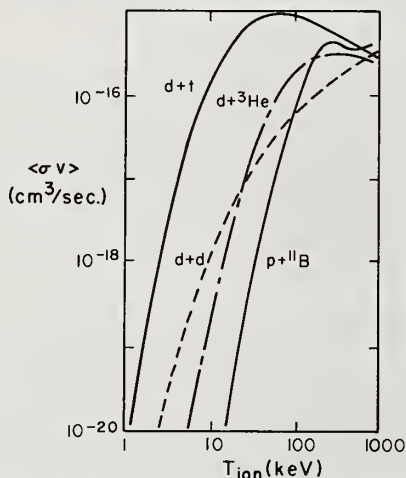
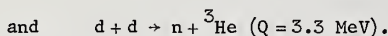
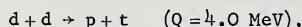


Fig. 1. The values of the reaction rate averaged over the Maxwell-Boltzmann distribution for the reactions induced by  $d + t$ ,  $d + d$ ,  $d + {}^3\text{He}$ , and  $p + {}^{11}\text{B}$ . The rate is plotted versus the temperature (in keV) of the interacting ions. (Taken from ref. 1.)

No one would seriously consider  $d + t$  as a fuel reaction unless the product neutrons were used to breed more tritium through  $n + {}^6\text{Li} \rightarrow t + \alpha$  ( $Q = 4.8$  MeV). Most present plans, however, consider an eventual shift to a pure deuterium fuel. This involves the primary reactions:

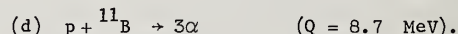
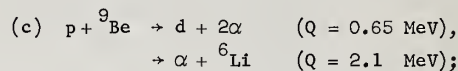
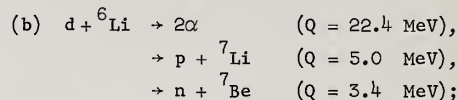
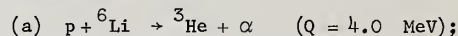


Subsequently, the tritium and  ${}^3\text{He}$  formed would also burn through  $d + t \rightarrow n + \alpha$  ( $Q = 17.6$  MeV) and  $d + {}^3\text{He} \rightarrow p + \alpha$  ( $Q = 18.4$  MeV). As shown in Fig. 1 the combined rate of the  $d + d$  reactions is very low compared to  $d + t$ , but at low energies  $d + d$  wins easily over other competitors. Though the same problems occur as with  $d + t$ , copious neutron production and the presence of tritium, neither is as serious for  $d + d$ .

$d + {}^3\text{He}$  would be a possible alternative to  $d + d$  if it were not for the cost of  ${}^3\text{He}$ . There is no breeding feature to this reaction and thus tritium would still

have to be separately produced to obtain more  ${}^3\text{He}$  fuel.

As the present technical difficulties are overcome we would expect that criteria (2) and (3) will assume increasing importance — especially when ignition temperatures above 100 keV can be attained. With this in mind, several proposals for second generation "exotic" fuels have been suggested.<sup>1-5</sup> The best possibilities appear to be:



Though  ${}^6\text{Li}$ ,  ${}^9\text{Be}$ , and  ${}^{11}\text{B}$  are all extremely rare in a cosmological sense, i.e., their large reaction cross sections insure their rapid destruction in stellar environments, they are relatively common on earth. For reasons of clarity, I have not put the curves for  ${}^6\text{Li}$  and  ${}^9\text{Be}$  in Fig. 1; for energies above 100 keV they are similar in form to that shown for  ${}^{11}\text{B} + p$ . For these temperatures (d) is better than (a), which in turn is better than (b) and (c). However, all have disadvantages: (d) has the highest bremsstrahlung losses and ignition temperature; (c) produces a deuteron which usually will produce a neutron in turn; (b) has a high neutron yield and a radioactive product,  ${}^7\text{Be}$ ; and (a) and (b) require the less common isotope of lithium.

It is obvious that with the possible exception of (d), there are many side reactions possible among the reaction products that also liberate energy and which must be carefully considered in a detailed evaluation. In addition, one must pay attention to reactions with other isotopes present. For example,  ${}^{10}\text{B}(p, \alpha){}^7\text{Be}$  ( $Q = 1.1$  MeV) will produce a radioactive product and thus the isotopic purity of the fuel may also have to be considered.<sup>6</sup>

#### Relevant Cross-Section Measurements

I shall not be able to discuss all these reactions, but shall choose examples that are typical of the techniques that may be required. With the exception of the small fraction of nonthermal processes, the nuclear reactions occur at energies that are low compared to the Coulomb barrier between the interacting ions. In this energy range the cross section is very energy dependent and can be written quite simply:

$$\sigma = \frac{S(E)}{E} \exp(-2\pi\eta),$$

where  $E$  is the center-of-mass energy and  $\eta = \frac{Z_1 Z_2 e^2}{\hbar v}$ .

The incident ions have mass numbers  $A_1$  and  $A_2$  and atomic numbers  $Z_1$  and  $Z_2$ . Removing the Gamow factor in this way usually leads to an  $S(E)$  that is slowly varying and which can be easily extrapolated to still lower energies. Often a slightly modified form of  $S$  is introduced that may further smooth its variation:

$$S(E) = \tilde{S}(E) \exp(-gE),$$



where 
$$g = \frac{2}{3\hbar} \left( \frac{2A_1 A_2}{(A_1 + A_2)} \frac{R^3}{Z_1 Z_2 e^2} \right)^{1/2} \quad \text{and}$$

R is the sum of the radii of the interacting ions.

Because the reaction cross section is varying rapidly, an accurate knowledge of its value can be obtained only if the beam energy and target energy loss are known very accurately. For this reason target thickness and composition, carbon build-up and absolute beam energy calibration are of crucial importance. One must include, for example, the variation of the cross section at different depths even in very thin targets.

For many years the measurements of the lithium reactions were notoriously unreliable because of the varying composition of the chemically active lithium targets. The solution adopted by Spinka et al.<sup>7</sup> was to use a differentially-pumped methane (CH<sub>4</sub>) target and a lithium beam. In this way a thin target of known density and composition could be obtained, and they could eliminate the uncertainties that plagued many of the earlier attempts. A cross sectional view of their scattering chamber is shown in Fig. 2, and the values of  $\tilde{S}(E)$  found for  ${}^6\text{Li}(p, {}^3\text{He}){}^4\text{He}$  are shown in Fig. 3 for data from refs. 7 and 8. In viewing this figure it would be very easy to assume that Spinka et al.<sup>7</sup> had been wasting their time because Gemeinhardt et al.<sup>8</sup> had more extensive data of comparable accuracy. However, before Spinka et al. established a reliable absolute cross section, there was no way to tell which of the many previous measurements were correct. (These previous data varied by a factor of at least two on both sides of the correct value.<sup>9</sup>)

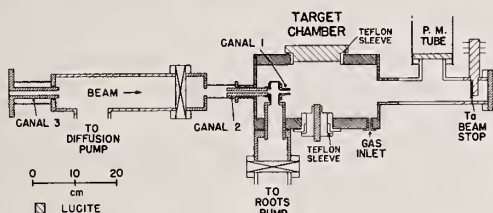


Fig. 2. The differentially-pumped target chamber of ref. 7. In this experiment the CH<sub>4</sub> target gas was bombarded with beams of  ${}^6\text{Li}$  and  ${}^7\text{Li}$ .

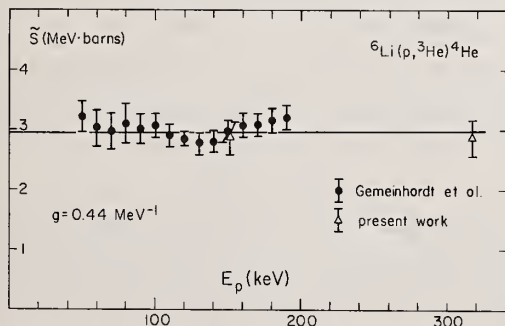


Fig. 3. The values of  $\tilde{S}$  versus proton bombarding energy for the  ${}^6\text{Li}(p, {}^3\text{He}){}^4\text{He}$  reaction. The Gemeinhardt et al. data are from ref. 8; the data labeled "present work" are from ref. 7. The quantities  $g$  and  $\tilde{S}$  are defined in the text.

Similar measurements have been made by Dwarakanath and Winkler for  ${}^3\text{He}({}^3\text{He}, 2p){}^4\text{He}$  using a recirculating,

differentially-pumped target.<sup>10</sup> Though the present low energy  ${}^6\text{Li}+d$  data look reasonable,<sup>11-13</sup> the accuracy of the absolute cross section could be established by using a recirculating, differentially-pumped deuterium target and a  ${}^6\text{Li}$  beam.

The  ${}^9\text{Be}+p$  reactions have recently been carefully measured for bombarding energies down to 30 keV.<sup>14</sup> Over the energy range of 300 keV to 30 keV the total cross section falls by five orders of magnitude, which required careful attention to target condition and the beam energy calibration. Fig. 4 shows the angular distribution coefficients for the  ${}^9\text{Be}(p, d){}^8\text{Be}$  reaction versus bombarding energy. Contrary to the usual expectation, the angular distributions become increasingly anisotropic as the energy is reduced. In ref. 14 this effect is attributed to interference between the 330-keV resonance and a level just below the  $p+{}^9\text{Be}$  threshold. However, an alternative (and perhaps more appealing) explanation is that a Coulomb pickup process provides the interfering amplitude instead of the bound state.<sup>15,16</sup> It is, of course, quite interesting that some nontrivial aspects of nuclear reaction theory survive in the few keV region.

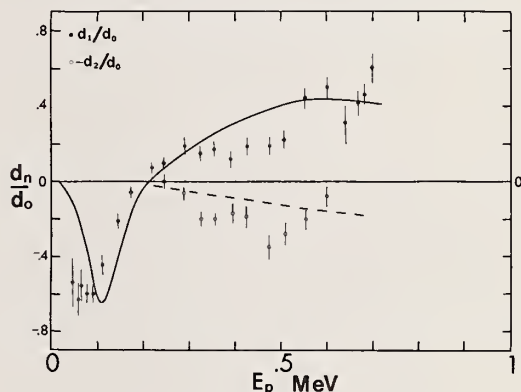


Fig. 4. The coefficients of a Legendre polynomial expansion of the deuteron center-of-mass angular distributions from  ${}^9\text{Be}(p, d){}^8\text{Be}(\text{g.s.})$  plotted versus proton bombarding energy.  $\sigma(\theta) = d_0 + d_1 P_1(\cos\theta) + d_2 P_2(\cos\theta)$ . The solid and dashed lines are R-matrix fits to the data (ref. 14).

The S-factor for the  ${}^9\text{Be}+p$  reactions is given in Fig. 5, clearly showing the utility of extrapolating  $S$  instead of the cross section. The five decades of variation in  $\sigma$  have been reduced to a mere factor of five. Note that the presence of the tail of the 330-keV resonance requires a more elaborate extrapolation than that described at the beginning of this section; in the case of ref. 14 this was done using the R-matrix formalism.

The measurement of accurate total cross sections for the  ${}^{11}\text{B}(p, 3\alpha)$  reaction is made difficult not only by all the effects mentioned earlier but also by the fact that most of the yield involves the broad, first excited state of  ${}^8\text{Be}$ .<sup>17</sup> Thus, the alpha-particle spectrum is continuous and one must accurately determine the number of low energy reaction products. For the data shown in Fig. 6 this problem was overcome by RF pulsing the incident proton beam, which permitted the reaction products to be identified by comparing their energies and flight times from the target. Again, one should take note of the relevant energy range in which

the cross section must be measured. Even at the lowest energies shown, we are still talking about effective temperatures for a CTR that lie uncomfortably far in the future.

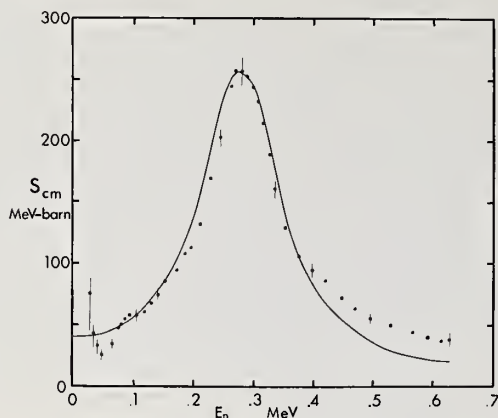


Fig. 5. The values of  $S$  for the sum of the  ${}^9\text{Be}(p,d)$  and  ${}^9\text{Be}(p,\alpha)$  reactions. The solid line corresponds to an R-matrix fit (ref. 14).

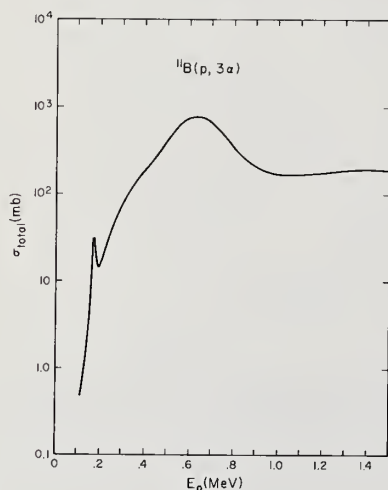


Fig. 6. The total cross section for  ${}^{11}\text{B}(p,3\alpha)$ . A smooth curve has been drawn through the many data points.

There is an interesting nonequilibrium process related to this reaction that serves as an excellent example of where cross-section measurements at higher energies may be important. In  ${}^{11}\text{B}(p,\alpha){}^8\text{Be}^*$  the decay of the 3 MeV, first excited state of  ${}^8\text{Be}$  produces many alpha particles with energies around 1.5 MeV. With this in mind we should look at the  ${}^{11}\text{B}(\alpha,p){}^{14}\text{C}$  ( $Q=0.8$  MeV) reaction, for it may represent an important contribution to the build-up of a long-lived radioactive product. Fig. 7 shows the total cross section for  ${}^{11}\text{B}(\alpha,p){}^{14}\text{C}$ . As luck would have it, there is a resonance near 1.5 MeV — just where it will do considerable harm.<sup>18,19</sup>

Another type of important nonequilibrium effect is caused by elastic scattering. For example, if one of the high energy alphas from  ${}^{11}\text{B}(p,3\alpha)$  strikes a proton, the recoiling proton will have a long range

and plenty of chance to interact at higher energies where the cross section is much larger. Thus, not all nonequilibrium effects are detrimental and in this case the burning of the fuel is enhanced.<sup>20</sup>

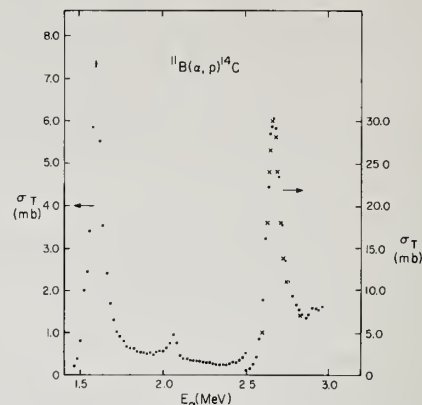


Fig. 7. The total cross section for  ${}^{11}\text{B}(\alpha,p){}^{14}\text{C}$  versus the alpha-particle bombarding energy. The dots are the data of ref. 18; the crosses are data from ref. 19.

### Cross Section Needs

Probably more important to the reader than all my examples are the cases where the existing data should be improved. Some of the reactions I'll list are already under investigation in our laboratory, but much still remains to be done.

- 1) Of the primary fuels, the  ${}^6\text{Li}+d$  reactions are the least accurately known — especially for energies below 500 keV.
- 2) The cross section for  ${}^{10}\text{B}(p,\alpha){}^7\text{Be}$  stands in need of improvement for energies between 100 and 500 keV.
- 3) The low energy elastic scattering cross sections are in a sad state. Differential cross sections are needed for 0.5 to 3 MeV alpha particles and 0.5 to 2 MeV protons and deuterons on  ${}^6\text{Li}$ ,  ${}^9\text{Be}$ , and  ${}^{11}\text{B}$  targets. These data would be especially useful in determining the exact role played by nonequilibrium reactions.

It must be emphasized that the most frequently neglected region is that below 500 keV — but that is just the region where the data are relevant for application to CTR problems.

### Acknowledgments

The author greatly appreciates the generosity of J. R. McNally, Jr. and T. A. Weaver for making available to him preprints of much of their recent work. Permission to include the preliminary data of R. Dayras and M. Lowry is also gratefully acknowledged.

### References

1. T. Weaver, G. Zimmerman, and L. Wood, UCRL-74938 (1973)
2. R. F. Post, Nucl. Fusion Suppl., Part 1, 119 (1962).
3. J. R. McNally, Jr., *Nuclear Data in Science and Technology II*, IAEA, Vienna (1973) p. 41.
4. J. R. McNally, Jr., Nucl. Fusion **11**, 187, 554 (1971).

5. A. J. Elwyn, J. E. Monahan, and J. P. Schiffer, Nucl. Fusion 11, 551 (1971).
6. T. Weaver, G. Zimmerman, and L. Wood, URCL-74191 (1972).
7. H. Spinka, T. Tombrello, and H. Winkler, Nucl. Phys. A164, 1 (1971).
8. W. Gemeinhardt, D. Kamke, and C. von Rhöneck, Z. Phys. 197, 58 (1966).
9. J. Audouze and H. Reeves, Astrophys. J. 158, 419 (1968).
10. M. R. Dwarakanath and H. Winkler, Phys. Rev. C4, 1532 (1971).
11. C. C. Lee, J. Korean Phys. Soc. 2, 1 (1969).
12. F. Ajzenberg-Selove and T. Lauritsen, Nucl. Phys. A227, 1 (1974).
13. C. R. McClenahan and R. E. Segel, Phys. Rev. C11, 370 (1975).
14. A. J. Sierk and T. A. Tombrello, Nucl. Phys. A210, 341 (1973).
15. J. P. Schiffer, private communication (1973).
16. D. Novikoff, A. Sierk, and T. Tombrello, unpublished work (1974).
17. M. Lowry, M. Dwarakanath, and P. Batay-Csorba, work in progress.
18. R. Dayras and Z. E. Switkowski, Bull. Am. Phys. Soc. 20, 85 (1975).
19. L. L. Lee and J. P. Schiffer, Phys. Rev. 115, 160 (1959).
20. J. J. Devaney and M. L. Stein, Nucl. Sci. and Engin. 46, 323 (1971).



Sources of fast-neutrons and their spectra are discussed briefly. A critical survey of experimental techniques employed in studies of nuclear reactions (excluding fission) at  $E_n \geq 14$  MeV is presented. The recent experimental cross-section data are described concisely. Special attention is paid to the case of low-yield reactions, such as processes with trinucleon emission. A review of recently discussed cross-section systematics together with an outline of some of the theoretical implications is given.

(Fast neutrons; sources and spectra; non-elastic interactions; nuclear reactions; cross-section measurements; cross-section data and systematics; excitation functions)

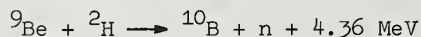
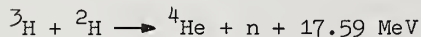
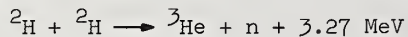
### Introduction

Measurements at various incident neutron energies of the total and scattering cross sections, together with the yield, energy spectrum and angular distribution of the emitted particles, yield useful information on nuclear forces, nuclear structure, reaction mechanisms etc. and provide a good way to test the applicability of various nuclear models. Furthermore, fast-neutron induced reaction cross-section data are finding increasing applications in several fields. The neutron data at 14 MeV are of prime interest for fusion technology.

This paper gives a brief survey of recent studies in the field of neutron cross-section measurements at 14 MeV and higher energies. The discussion is limited to the various components of the non-elastic interactions (excluding fission). Keeping in mind the need of data for applied purposes, in this survey the emphasis lies on experimental techniques and analysis of systematic trends in the data rather than on reaction theories and nuclear structure etc.

### Sources of Fast-Neutrons and their Spectra

The most intense available neutron sources are fission reactors and electron linear accelerators in which neutrons are produced by fission and photonuclear reactions, respectively. The average energies of the neutrons from both these sources, however, are well below 10 MeV. Fast neutrons can also be produced in the interactions of high-energy protons with various materials. The spectra of such neutrons extend to quite high energies. However, the most effective means of producing high-energy neutrons is the interaction of deuterons with deuterium, tritium and beryllium, giving rise to the following three nuclear reactions:



The neutron production cross sections in the forward direction for deuteron energies up to about 20 MeV, as summarized by Barschall<sup>1</sup>, are given in Fig. 1 and the average energies of the produced neutron<sup>1</sup> for various deuteron

bombarding energies in Fig. 2. It is evident that at low bombarding energies only the  $^3\text{H}(^2\text{H},n)^4\text{He}$  reaction has a large cross section. At higher energies the reaction  $^9\text{Be}(^2\text{H},n)^{10}\text{B}$  gives the highest yield. The increase with bombarding energy in the cross sections, and the decrease in the average neutron energy for the reaction  $^3\text{H}(^2\text{H},n)^4\text{He}$  is caused by the start of deuteron break-up which becomes the dominant mode above a deuteron energy of about 6 MeV.

Technology seems to be now sufficiently advanced to allow production of low-energy deuterons or tritons with ion currents up to a few amperes. However, the problem of dissipating hundreds of kW in a target of deuterium or tritium as well as maintaining a constant supply of neutrons are enormous. It seems that whereas the present day sources of fast-neutrons may suffice for many nuclear physics experiments, more intense sources are needed to study low-yield reactions and radiation damage phenomena similar to those anticipated in fusion reactor structural materials. The main efforts in overcoming these problems have been recently reviewed by Barschall<sup>1</sup>, and Csikai<sup>2</sup> has summarized the total neutron yields using various target compositions. The insulated core transformer system with a rotating tritium target at Livermore as well as the Los Alamos proposal of collisional interaction between intersecting beams of tritium ions and a supersonic jet of deuterium molecules are very promising. Construction of a high intensity neutron source at Jülich is also under discussion.

With low-energy deuterons only the  $^3\text{H}(^2\text{H},n)^4\text{He}$  reaction yields neutrons of energies above 13 MeV. This reaction in principle gives rise to monoenergetic neutrons whose energy depends on the energy of the accelerated deuterons as well as on the emission angle to the direction of bombarding deuterons, the anisotropy being less than 20 % at  $E_d < 400$  keV. If  $E_d = 200$  keV, at 90° the energy of the neutron is  $14.0 \pm 0.1$  MeV and the total angular variation of energy is  $E_n \sim 2$  MeV. In practice, however, due to scattering effects etc. in the immediate vicinity of the target, the spectra show much more spreads. Such effects have been recently estimated<sup>3-5</sup> in detail and it has been shown<sup>3</sup> that the calculated energy of neutrons from a sealed neutron generator tube depends also on the assumed  $^2\text{H}-^3\text{H}$  distribution ratio in the target.

Using deuterons of energies up to 4 MeV, neutrons of energies in the range of 13 to 19 MeV, depending on the angle of emission, can be obtained. Monoenergetic neutron beams above 19 MeV are difficult to get because deuterons of energies above 4 MeV show considerable break-up. This difficulty can be overcome by accelerating tritons rather than deuterons. However, due to health hazards associated with the acceleration of radioactive tritium, it has till now been only sparsely employed.

For the production of neutrons of energies above 10 MeV via  ${}^2\text{H}({}^2\text{H},n){}^3\text{He}$  and  ${}^9\text{Be}({}^2\text{H},n){}^{10}\text{B}$  reactions high energy deuterons are needed.

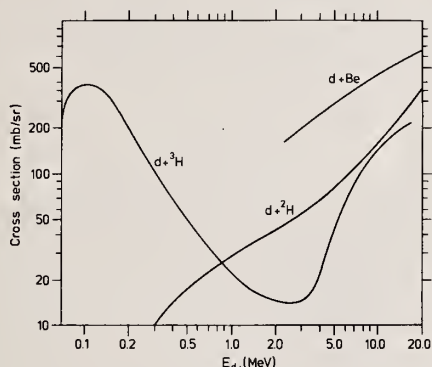


Fig. 1. Neutron production cross sections in the forward direction as a function of incident deuteron energy

However, since with increasing deuteron energy the break-up mode dominates, the neutron spectra cover a very broad range of energies. The energy spectra of the forward neutrons produced in bombardments of beryllium with deuterons of different energies, as given by Krivan and Münzel,<sup>6,7</sup> are reproduced in Fig. 3. The maximum intensity of the neutrons occurs at about one half of the incident deuteron energy. In the low-energy part of the spectrum an additional small peak occurs (not shown in Fig. 3) and is due to neutrons produced via evaporation effects. Elements other than Be have also been investigated but the neutron

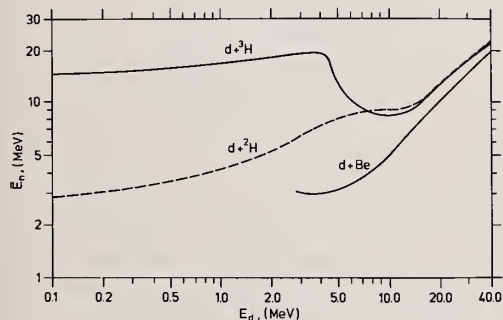


Fig. 2. Average energy of the neutrons from bombardments of thin targets with deuterons of varying energies

yields have been found to be much lower. In spite of the continuous shape of the neutron spectrum, using a high resolution time-of-flight spectrometer, such as the one at Karlsruhe,<sup>8,9</sup> it is possible to sort out neutrons of various energy groups and thus to determine the excitation functions with fairly good accuracies.

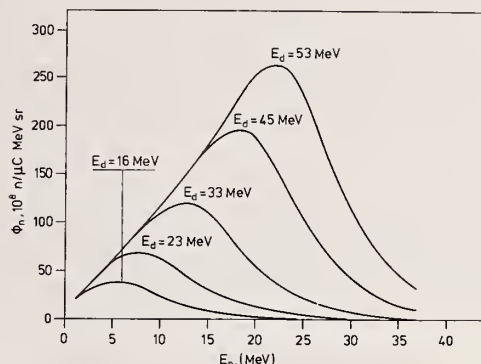


Fig. 3. Energy spectra of the forward neutrons produced in bombardments of beryllium with deuterons of different energies

#### Relative Contributions of Nuclear Reactions at 14 MeV

The relative contributions of the major components of the non-elastic interactions for elements with  $A > 40$  at 14 MeV, excluding fission which competes in the case of heavier nuclei, are roughly sketched out in Fig. 4. It is evident that the most common nuclear reactions are  $(n,\gamma)$ ,  $(n,n'\gamma)$ ,  $(n,2n)$ ,  $(n,p)$  and  $(n,\alpha)$ . Most of the studies so far have

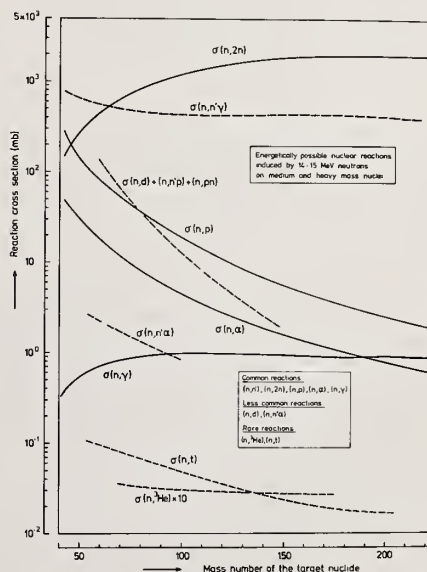


Fig. 4. Relative contributions of nuclear reactions induced by 14 MeV neutrons



concentrated in the investigation of those reactions. Certain less common reactions, however, like  $(n,n'p)$  and  $(n,n'\alpha)$  also have relatively high cross sections but still have not been looked for in any detail. The other reactions like  $(n,t)$ ,  $(n,^3\text{He})$ ,  $(n,2p)$ , and in heavier mass nuclei  $(n,3n)$ , are also energetically possible but are rare and need detailed investigations. A full discussion on the state of our knowledge on these reactions is given later but it seems appropriate here to mention that whereas in the lighter nuclei charged particle and neutron emission compete with each other, in the heavier mass region neutron emission is by far the most dominating process;  $(n, \text{charged particle})$  reactions in the heavy mass region are therefore difficult to investigate. At incident neutron energies higher than 14 MeV many more reaction channels are energetically possible, causing thereby high background problems. In general at higher energies the  $(n,xn)$  processes play the most dominating role.

### Techniques of Cross-Section Measurements

In cross-section measurements extensive use has been made both of the activation and spectrum methods. As discussed below, the two techniques have their own merits and limitations and are often complementary to each other.

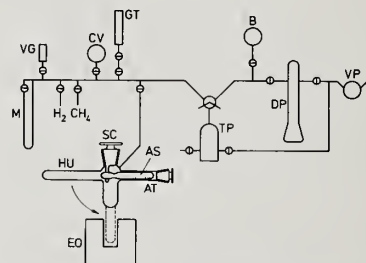
#### The Activation Method

The activation technique consists of off-line identification and quantitative determination of the reaction products by radiometric methods. In the case of stable and very long-lived products, if the cross section is very high, for the identification of the product mass spectrometric method may be applied.<sup>10</sup> In fast-neutron work, however, since the cross sections are not very high and the neutron sources are not very intense, this procedure so far has not been used. One relies therefore on the measurement of the radioactivity. Although all types of counting methods have been employed, in recent years with the use of high-resolution  $\text{Ge(Li)}$  detectors,  $\gamma$ -ray spectrometry is almost superseding all the other methods of counting (cf. 11-17). In work on elements consisting of several isotopes, use of enriched isotopes<sup>12,15,18,19</sup> and chemical separations<sup>15,18</sup> has led to higher precision.

The activation method is a relatively slow process and yields only an integral value of the cross section. No information on the differential cross sections or on the reaction mechanism is obtained. Nonetheless, in the case of simple reactions, like  $(n,p)$  and  $(n,\alpha)$ , the technique has a slight advantage over the spectrum method in that the contributions of  $(n,n'p)$  and  $(n,n'\alpha)$  reactions have not to be corrected for. The method is of special advantage in investigations of low-yield nuclear reactions like  $(n,t)$ ,  $(n,^3\text{He})$  etc., since the spectrum method is not sensitive enough to identify the low-abundance emitted particles. In this direction most of the studies in recent years have been carried out at Debrecen,<sup>20</sup> Jülich,<sup>21-25</sup> and Zagreb.<sup>26,27</sup> In particular at the Jülich Institute of Nuclear Chemistry extensive use of modern

radiochemical separations has been made.

A slight modification of the activation technique consists of accumulation and integral determination of the emitted particles rather than the reaction product; thus, for example,  $(n,\alpha)$  reaction on steel with reactor fast neutrons has been studied<sup>28</sup> using a high sensitivity gas mass spectrometric technique for the estimation of generated helium. Similarly in the case of  $(n,t)$  reactions, the emitted tritium was accumulated and identified off-line.<sup>20,25,29</sup> Separation of tritium was carried out by Qaim et al.<sup>29</sup> using the apparatus shown in Fig. 5. Quantitative estimation of tritium was effected using gas counting either in an anticoincidence circuit<sup>29</sup> or by a pulse shape discrimination procedure.<sup>30</sup>



Vacuum apparatus for the extraction of tritium from targets irradiated with fast neutrons

M	Manometer	EO	Electric oven
VG	Vacuum gauge	B	Bulb for carrier $\text{H}_2$
CV	Calibrating volume	TP	Taper pump
GT	Gas counting tube	DP	Hg-Diffusion pump
AT	Tube for introducing ampoule	VP	Vacuum pump
AS	Ampoule containing irradiated sample	SC	Stopcock with eccentric rod
HU	Heating unit		

Fig. 5. Sketch of vacuum apparatus used for isolation of tritium

#### The Spectrum Method

In this method the techniques employed differ from one reaction to another. Various types of reactions are therefore discussed individually.

**Radiative Neutron Capture.** For work with 14 MeV neutrons spherical telescopic scintillation pair spectrometer,<sup>31</sup> coincidence anti-coincidence pair spectrometer<sup>32</sup> as well as time-of-flight techniques<sup>33,34</sup> have been used. The fast neutron capture cross section is obtained by integrating the spectrum over the whole  $\gamma$ -ray energy. A drawback of the method appears to be that only transitions to the bound states are considered; the possible  $\gamma$ -ray branches to particle unstable states, which can subsequently decay by a further  $\gamma$ -ray transition, are not taken into consideration. It may, however, be added that, due to the smallness of the  $\gamma$ -ray widths compared to particle widths, the branching to unstable states should be relatively small.

**Neutron Inelastic Scattering and the  $(n,2n)$  Reaction.** For investigating neutron emission, time-of-flight techniques are employed in combination with large liquid scintillators as neutron detectors. At 14 MeV the  $(n,n')$  and  $(n,2n)$  reactions, and at higher energies



(n,xn) reactions, contribute to the spectrum, the relative contributions of which can be resolved by determining the angular correlations <sup>35,36</sup> between the various outgoing neutrons. At Livermore an extensive programme of work is underway on neutron spectra from bombardment of a variety of materials with pulsed 14 MeV neutron beams.<sup>36</sup> For the measurement of (n,2n) cross sections a watertank-method <sup>37</sup> has also been used. In this method the emitted neutrons are all thermalised prior to identification.

The (n,n'γ) reaction has also been investigated via the characterization of the associated prompt γ-lines.<sup>38,39</sup> The prompt γ-radiation and the neutrons emitted from the target irradiated with a pulsed 14 MeV neutron source are separated from each other using a short flight path and a Ge(Li) detector. Using a somewhat similar technique investigations up to a neutron bombarding energy of about 30 MeV have also been performed.<sup>9</sup>

(n,charged particle) Reactions. In studies on (n,p), (n,d), (n,t) and (n,α) reactions somewhat similar techniques have been employed. In order to minimize the absorption of the emitted charged particles thin targets have to be used and special shielding is needed for reducing the background. Although for the detection of charged particles nuclear emulsions,<sup>40,41</sup> thin CsI(Tl) crystals <sup>42,43</sup> as well as small semiconductor detectors <sup>44</sup> have been used, the more common technique seems to employ a counter telescope <sup>45-49</sup> consisting in general of two dE/dx proportional counters for measurement of the specific energy loss and one E scintillation or semiconductor detector for measuring the residual energy. At Tübingen, however, in studies of (n,α) reactions parallel plate avalanche counters have also been employed. A schematic diagram of such a telescope <sup>47</sup> is given in Fig. 6 and consists of two ΔE-parallel plate counters (PC 1 and PC 2), one Si-semiconductor detector (SD), and a third parallel plate counter (Veto) in front of the target which operates in anticoincidence to reduce the background.

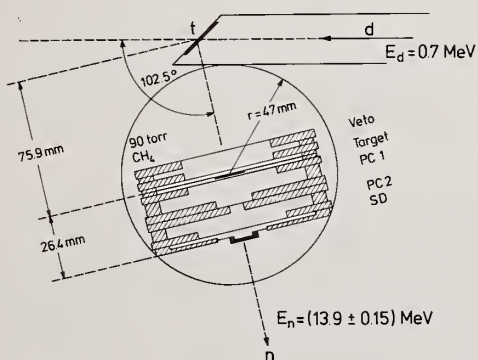


Fig. 6. Schematic diagram of a counter telescope employing parallel plate avalanche counters

At Karlsruhe a semiconductor telescope in combination with the time-of-flight facility is used for such studies. A typical spectrum

of the charged particles <sup>50</sup> from the neutron interaction with <sup>9</sup>Be is given in Fig. 7. The x-axis of the figure is defined by the relation

$$D = (E/\text{MeV} + 2)^{1.75} - (E_R/\text{MeV} + 2)^{1.75}$$

The helium nuclei <sup>4</sup>He and <sup>6</sup>He are separated completely and the hydrogen isotopes to better than 97 % for particles with energy distributions as given in the insert of Fig. 7. It is thus a very useful technique for investigating the energy and angular distributions of the emitted charged particles over the neutron energy range of 8 to 30 MeV.

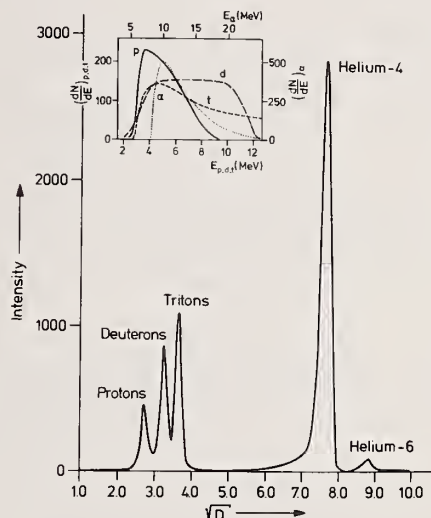


Fig. 7. Spectrum of charged particles from the neutron interaction with <sup>9</sup>Be measured in a Si-semiconductor detector telescope. The energy distributions of the charged particles involved are given in the insert

#### Experimental Cross-Section Data

Within the last few years a large number of measurements, mostly by the activation method at 14 - 15 MeV, have been reported. Due to the limited space available it is not possible to enumerate all of them here, hence only some selected works are discussed.

#### Cross-Section Data at 14 MeV

(n,2n), (n,p) and (n,α) Data. The data on these reactions in the energy range 13.9 to 15.1 MeV till January 1972 have been reviewed <sup>51-55</sup> and recommended cross-section values <sup>53-55</sup> have been given. Since then several measurements in various mass regions, including radioactive isotopes,<sup>56-60</sup> have been carried out. Among the works<sup>12,16-19,61-71</sup> on (n,2n) reactions, the investigations at Jülich <sup>16-19</sup> dealt with more than 55 nuclides of various elements, many of them being potential structural materials in fusion technology. The information published on (n,p) cross sections has been comparatively smaller.<sup>4,12,14,15,18,19,45,61,66,67,70,72-74</sup>

Some measurements on  $(n, \alpha)$  cross sections<sup>4,18,19</sup> have been carried out by the activation method. More extensive investigations, however, have been performed on the angular and energy distributions of the emitted  $\alpha$ -particles, e.g. on light nuclei at Tübingen,<sup>47,75</sup> on light and medium mass nuclei at Hamburg<sup>42,43</sup> and Rawalpindi,<sup>41</sup> and on heavy nuclei at Warsaw.<sup>44</sup> In the heavy mass region the spectrum of  $\alpha$ -particles<sup>44</sup> seems to be significantly shifted in the forward direction.

**(n,  $\gamma$ ) Data.** Recent measurements by the spectrum method have been carried out by Drake et al.,<sup>76</sup> Stamatelatos et al.,<sup>32</sup> Rigaud et al.,<sup>33</sup> Bergqvist et al.,<sup>34</sup> and Potokar et al.<sup>31</sup> Furthermore, in order to clarify the discrepancy between the results of activation and spectrum methods, activation measurements with improved target-sample arrangements have been repeated. Some of the authors<sup>77-80</sup> claim to have found good agreement between the results of two methods whereas Petö et al.<sup>81</sup> believe that the activation method definitely yields higher values except in the region of closed shells. A linear dependence of the apparent activation cross section on the target and sample thickness has been demonstrated<sup>81</sup> but according to Petö et al.<sup>81</sup> this does not explain the discrepancy fully.

**(n, n'  $\gamma$ ) Data.** Cross sections for the formation of several metastable states, with half-lives on the order of a few seconds, have been measured by the activation technique. These, however, are only partial cross sections. Using the spectrum method cross sections for several  $(n, n' \gamma)$  reactions have been obtained.<sup>35,36,38,39</sup>

**(n, d), (n, n' p) and (n, n'  $\alpha$ ) Data.** A survey of  $(n, d)$  reactions on very light nuclei has been given.<sup>82</sup> Very little information has been published on  $(n, n' p)$  and  $(n, n' \alpha)$  reactions. Cross sections have been measured using the activation technique for  $(n, n' p)$  reactions<sup>18,19,83</sup> on  $^{56}\text{Ni}$ ,  $^{84}\text{Sr}$ ,  $^{91,92}\text{Zr}$ ,  $^{92,96}\text{Mo}$ ,  $^{96}\text{Ru}$ ,  $^{106}\text{Cd}$ ,  $^{112}\text{Sn}$ ,  $^{142}\text{Ce}$  and  $^{183,184,186}\text{W}$ , and for  $(n, n' \alpha)$  reactions<sup>18</sup> on  $^{65}\text{Cu}$ ,  $^{70}\text{Zn}$ ,  $^{74}\text{Ga}$ ,  $^{76}\text{Ge}$  and  $^{99}\text{Tc}$ . The cross sections lie in the mb region.

**(n, t), (n,  $^3\text{He}$ ) and (n, 2p) Data.** Studies of  $(n, t)$  reactions on light nuclei have been carried out<sup>48,84,85</sup> by the spectrum method, mostly at Zagreb.<sup>48,84</sup> The angular distributions of tritons<sup>84</sup> from the  $(n, t)$  reactions on  $^{14}\text{N}$  and  $^6\text{Li}$  are shown in Fig. 8 and suggest that significant contributions from direct reactions, probably deuteron pick-up, are present. In the case of medium and heavy mass nuclei the information available till March 1972 has been summarized by Qaim and Stöcklin<sup>23</sup> who also reported<sup>18,23</sup> very careful measurements of a large number of  $(n, t)$  cross sections by activation and activity determination. Diksic et al.<sup>27</sup> later reported a few  $(n, t)$  cross sections and Biro et al.<sup>20</sup> investigated several  $(n, t)$  reactions by separation and  $\beta$ -counting of tritium. Although there are discrepancies in certain individual cases, the general conclusion from these studies is that the  $(n, t)$  cross sections for medium and heavy mass nuclei are quite small and amount to between 10 and 100  $\mu\text{b}$ .

The published information on  $(n, ^3\text{He})$  reactions till March 1973 has been reviewed

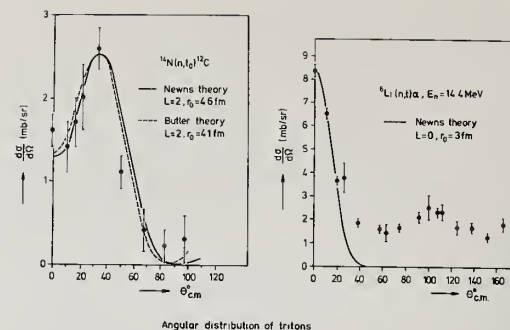


Fig. 8. Angular distributions of tritons produced in  $(n, t)$  reactions on  $^6\text{Li}$  and  $^{14}\text{N}$  at 14 MeV

by Qaim<sup>24</sup> who has described the first systematic study<sup>22,24</sup> on these reactions. Diksic et al.<sup>27</sup> have also reported a few  $(n, ^3\text{He})$  cross sections. In general the  $(n, ^3\text{He})$  cross sections at 14 MeV amount to a few  $\mu\text{b}$ .

In the case of  $(n, 2p)$  reactions, since the investigations of Lulic et al.<sup>26</sup> no further work has been reported.

#### Excitation Functions

The excitation functions of  $(n, 2n)$ ,  $(n, p)$  and  $(n, \alpha)$  reactions, mostly over the incident neutron energy up to 20 MeV, have been compiled by Bormann et al.<sup>55</sup> Some recent excitation function measurements over the energy range of 13 to 15 MeV deal with fast-neutron flux standards,<sup>86,87</sup>  $(n, 2n)$ ,  $(n, p)$  and  $(n, \alpha)$  reactions on medium and heavy mass nuclei,<sup>15,88</sup> and  $(n, 2n)$  reactions on heavy radioactive nuclei.<sup>58-60</sup> Excitation functions over the energy range up to about 20 MeV have been reported for  $(n, n' \gamma)$  reactions<sup>89</sup> on  $^{113}\text{In}$  and  $^{204}\text{Pb}$ ,  $(n, 2n)$  reactions<sup>68,71,89</sup> on  $^{46}\text{Ti}$ ,  $^{66}\text{Zn}$ ,  $^{113,115}\text{In}$  and  $^{197}\text{Au}$ , and  $(n, \alpha)$  reaction<sup>90</sup> on  $^{51}\text{V}$ . Using the time-of-flight technique excitation functions for a few  $(n, x)$  reactions over the energy range 11 to 30 MeV have also been measured.<sup>9,50</sup> In spite of these recent measurements the total available information on the excitation functions of reactions induced by neutrons above 15 MeV energy is still rather scanty and further measurements are needed.

#### Cross-Section Data with Break-up Neutrons

Krivan and Münzel<sup>6,7</sup> investigated on several nuclides  $(n, p)$ ,  $(n, \alpha)$  and  $(n, 2n)$  reactions induced with neutrons produced in the break-up of 33 and 53 MeV deuterons and constructed excitation functions empirically. With a view to investigating  $(n, t)$  reactions at a rather high reaction energy, Qaim et al.<sup>29</sup> recently carried out a systematic study employing radiochemical isolation and gas phase counting of tritium. In this work neutrons produced in the break-up of 53 MeV deuterons were used. Evidently the total information available in this field is still rather small.

#### Evaluated Cross-Section Data

In connection with reaction mechanism studies several theoretical methods have been



reported which describe the cross-section data more or less satisfactorily; e.g. semi-direct capture theory in the case of  $(n,\gamma)$  reactions, and statistical model calculations in the case of  $(n,n'\gamma)$ ,  $(n,2n)$ ,  $(n,p)$  and  $(n,\alpha)$  reactions. In the case of  $(n,p)$  and  $(n,\alpha)$  reactions contributions from pre-equilibrium emission processes have also been taken into account. On rare nuclear reactions like  $(n,t)$  and  $(n,^3\text{He})$ , especially in the medium and heavy mass regions, very little theoretical work has been done. Using the Hauser-Feshbach method Qaim et al<sup>91</sup> recently calculated  $(n,t)$  cross sections at 14.6 MeV on nuclei with  $A = 32 - 45$ . The dominant mode seems to be the statistical process.

Several formalisms and codes have been developed which are very successful in evaluating and predicting cross-section data. In this direction the work at Brookhaven and Livermore is worth mentioning.<sup>92,93</sup> In addition to these methods certain phenomenological formulae have been suggested as well as some systematic trends in cross sections have been analysed. The latter two methods are rather empirical but they do allow a quick estimation of unknown cross sections, although not with very high accuracies.

### Systematics of Reaction Cross Sections

#### Systematics of Cross-Section Data at 14 MeV

Although the systematics of reaction cross sections at 14-15 MeV have been investigated by several groups, in recent years most extensive investigations have been carried out at Jülich. It should, however, be mentioned that these studies are rather empirical since the cross-section data are not normalised to a constant reaction energy. Nonetheless, they are very useful for practical purposes and provide a method for quick prediction of unknown cross sections, in the case of common reactions like  $(n,2n)$ ,  $(n,p)$  and  $(n,\alpha)$ , where the data are relatively abundant, with errors of about 20 to 30 %, but for less common and rare reactions with lesser accuracies. A summary of the systematic trends observed in cross sections of various nuclear reactions is given below.

Systematics of  $(n,\gamma)$  Reaction Cross Sections. Using the method of Cvelbar et al<sup>94</sup> the total radiative neutron capture cross sections are shown as a function of  $A$  in Fig. 9. The results of the spectrum measurements show that the cross section increases up to a mass number of about 80 beyond which it is almost constant and approximately equal to 1 mb. Whereas in the region of magic neutron numbers the agreement between the results of activation and spectrum measurements is generally good, in between closed shells the discrepancies are maximum. Recent activation measurements with improved methods, however, tend to show that the discrepancies are not so high as in earlier works.

Systematics of  $(n,n'\gamma)$  and  $(n,2n)$  Reaction Cross Sections. The compilation of Csikai<sup>2</sup> on  $(n,n'\gamma)$  cross sections was updated and the total  $(n,n'\gamma)$  cross sections are plotted as a function of the asymmetry parameter  $(N-Z)/A$  in Fig. 10. Partial cross sections are omitted. Due to the paucity of data any detailed systematic trends

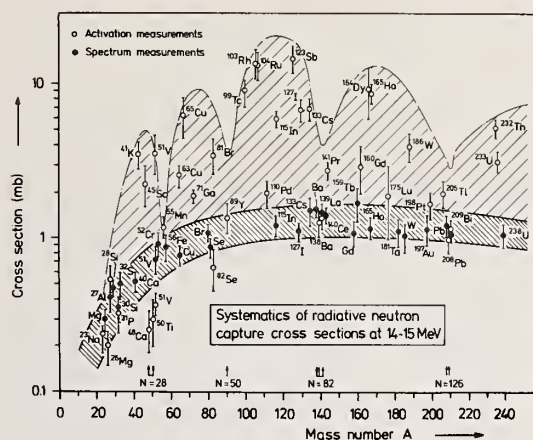


Fig. 9. Systematics of radiative neutron capture cross sections at 14 MeV

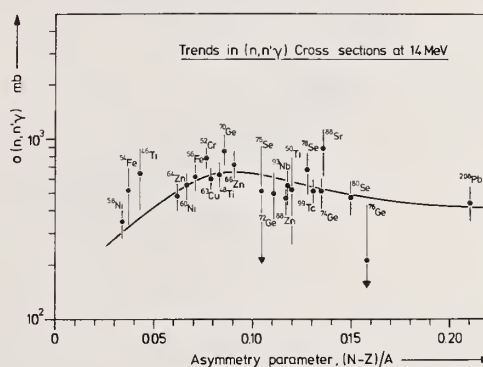


Fig. 10. Trends in  $(n,n'\gamma)$  cross sections at 14 MeV

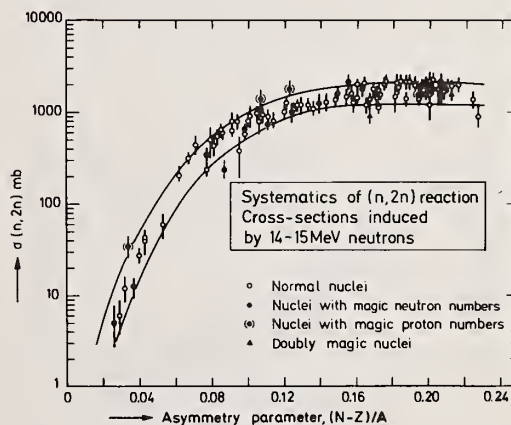


Fig. 11. Systematics of  $(n,2n)$  cross sections at 14 MeV

are difficult to discern. After a slight initial rise (presumably due to decreasing contribution from charged particle emission



with increasing  $(N-Z)/A$  the cross section decreases slowly, possibly due to increasing competition from  $(n,2n)$  reaction.

The systematics of  $(n,2n)$  cross sections as described by Qaim<sup>16</sup> are given in Fig. 11. The steep rise in cross sections for nuclides with small  $(N-Z)/A$  is probably due to the decreasing thresholds for  $(n,2n)$  reactions on those nuclides. For nuclides with  $(N-Z)/A \geq 0.1$  the cross section increases only gradually till in the medium and heavy mass regions the  $(n,2n)$  reaction becomes the most dominating process.

Systematics of  $(n,p)$  and  $(n,\alpha)$  Reaction Cross Sections. The  $(n,p)$  cross-section data as a function of residual nuclear charge  $Z_R$  are shown<sup>95</sup> in Fig. 12. Apart from even-odd effects in the case of light nuclei, no systematic variations can be seen. In the case of

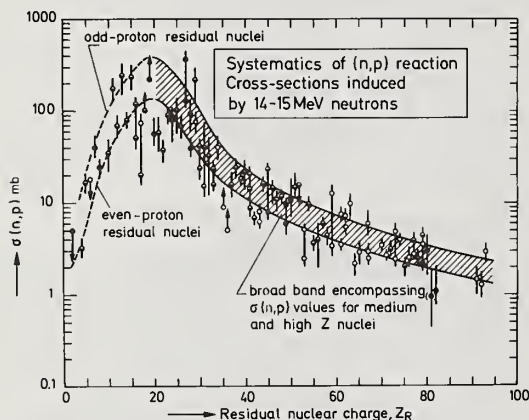


Fig. 12. Plot of 14 MeV  $(n,p)$  cross sections against proton number of the residual nucleus,  $Z_R$

$(n,\alpha)$  reactions no even-odd effects are found. The trend in  $(n,\alpha)$  cross sections for medium and heavy mass nuclei (Fig. 13) is similar to that for  $(n,p)$  cross sections. In the medium

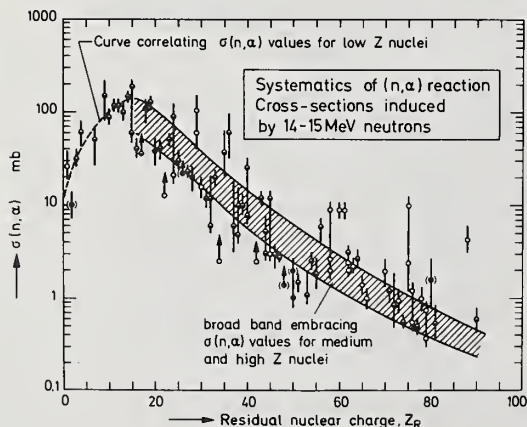


Fig. 13. Plot of 14 MeV  $(n,\alpha)$  cross sections against proton number of the residual nucleus,  $Z_R$

and heavy mass regions both the  $(n,p)$  and  $(n,\alpha)$  reaction cross sections decrease<sup>21,96</sup> with the increasing relative neutron excess  $(N-Z)/A$  of the target nucleus (Figs. 14 and 15).

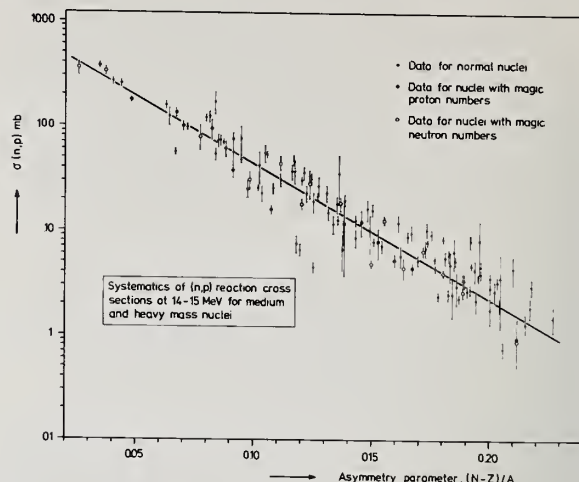


Fig. 14. Systematics of  $(n,p)$  cross sections at 14 MeV for medium and heavy mass nuclei

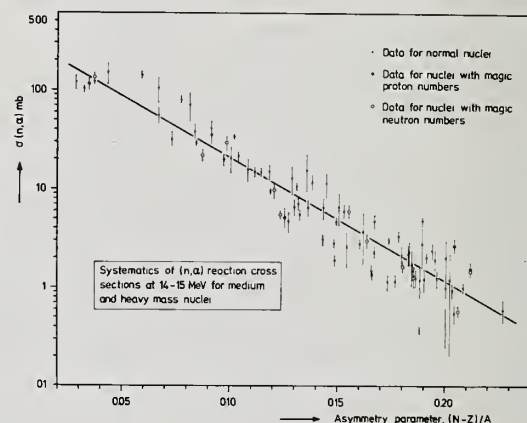


Fig. 15. Systematics of  $(n,\alpha)$  cross sections at 14 MeV for medium and heavy mass nuclei

This decrease in cross section with increasing  $(N-Z)/A$  is due to the increasing competition between charged particle and neutron emission.

Systematics of  $(n,t)$  and  $(n,^3\text{He})$  Reaction Cross Sections. The systematics of  $(n,t)$  cross sections, as described by Qaim and Stöcklin,<sup>18,21,23</sup> are shown in Fig. 16. The data based on both  $\gamma$ -spectrometric measurements<sup>18,23</sup> and  $\beta$ -counting of tritium<sup>20</sup> are shown. For medium and heavy mass nuclei the data which appeared to be very erroneous were discarded. For light nuclei the cross sections are rather high due to cluster formation which facilitates direct processes like deuteron pick-up and triton knock-out. In the case of elements with  $Z > 22$  the  $(n,t)$  cross sections decrease<sup>21-23</sup> with the increasing  $(N-Z)/A$

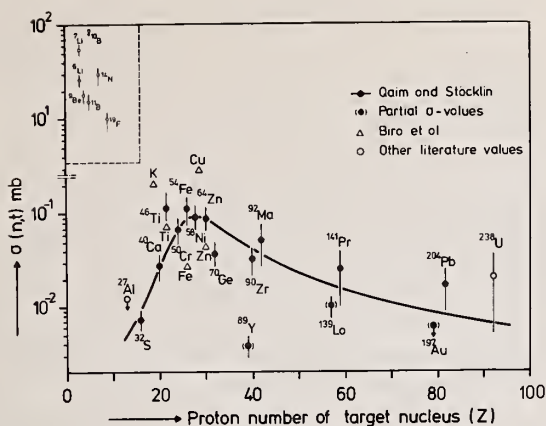


Fig. 16. Systematics of (n,t) cross sections at 14 MeV

and can be fitted with the empirical equation<sup>22</sup> given in Fig. 17. A somewhat similar trend is observed in the case of (n,<sup>3</sup>He) reactions (Fig. 18) though the decrease with increasing (N-Z)/A is less marked which suggests more contribution from direct processes.

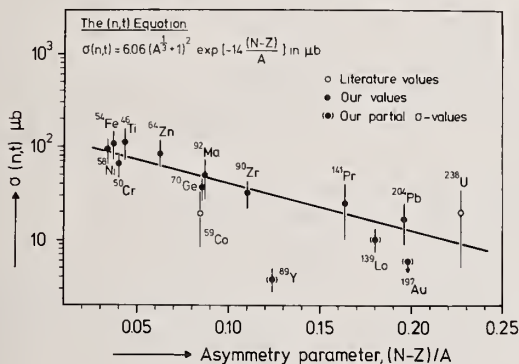


Fig. 17. 14 MeV neutron induced (n,t) reaction cross sections as a function of (N-Z)/A of target nuclei with Z > 22

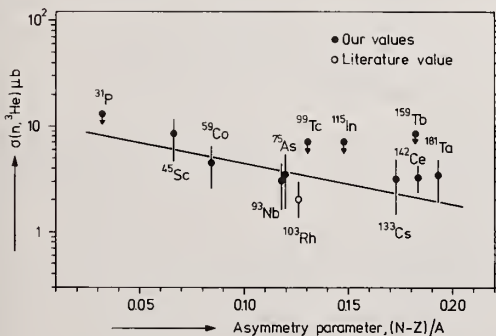


Fig. 18. (n,<sup>3</sup>He) reaction cross sections at 14 MeV for medium and heavy mass elements as a function of (N-Z)/A of the target nuclei

Trends in Cross Sections for Other Reactions. A survey of (n,d) reactions on light nuclei has been carried out<sup>82</sup> but no systematic trends in cross sections were reported. In the case of [(n,d)+(n,n'p)+(n,pn)] reactions Lu and Fink<sup>83</sup> noted that the cross section for the lightest isotope of each element decreases linearly with the increasing atomic number. Qaim and Graca<sup>19</sup> have shown recently that for adjacent isotopes of tungsten the cross section shows a dependence on (N-Z)/A. No further detailed analysis of trends in cross sections for this reaction or for (n,2p) and (n,n'α) reactions has been reported.

#### Systematics of (n,t) Reaction Cross Sections at $E_n \approx 22.5$ MeV

Qaim et al<sup>29</sup> investigated the systematics of tritium formation cross sections with fast neutrons produced via break-up of 53 MeV deuterons on Be. The cross sections lie between 3.5 and 5.5 mb for all the elements investigated over the Z range of 20-83. Only a slightly decreasing trend with the increasing Z of the target element has been observed.

#### Systematics of Excitation Functions

Krivan and Münzel<sup>6</sup> analysed some systematic trends in the excitation functions for (n,2n), (n,p) and (n,α) reactions. These are summarized in Fig. 19. Whereas with increasing Z the maximum cross section for the (n,2n) and (n,α) reaction increases, that for the (n,p) and (n,α) reaction decreases (Fig. 19 (A)). As is evident from Fig. 19 (B), for (n,2n) reactions the energy in excess of the Q-value at which the maximum of the excitation function occurs decreases only slightly with increasing Z. In the case of (n,p) and (n,α) reactions, on the other hand, this energy value increases, presumably due to increasing Coulomb barriers.

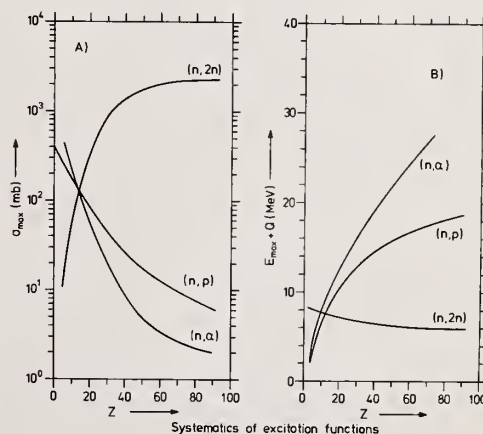


Fig. 19. Systematics of excitation functions of (n,2n), (n,p) and (n,α) reactions



## Conclusions

The techniques of cross-section measurements appear to be sufficiently advanced but more intense neutron sources are needed to study low-yield nuclear reactions and radiation damage phenomena similar to those anticipated in fusion reactor structural materials. Most of the reported cross-section data have been obtained at 14 MeV and deal mainly with  $(n, \gamma)$ ,  $(n, n'\gamma)$ ,  $(n, 2n)$ ,  $(n, p)$  and  $(n, \alpha)$  reactions. The latest data seem to attain the precision needed for fusion technology. The total information available on reactions like  $(n, d)$ ,  $(n, n'p)$ ,  $(n, n'\alpha)$ ,  $(n, t)$ ,  $(n, {}^3\text{He})$  etc. is rather small. The excitation functions in energy ranges in excess of 15 MeV have been investigated only in a few cases. The various calculational codes give data in good agreement with the experiment and the systematic trends discussed allow a quick estimation of unknown cross sections.

## Acknowledgements

It is a pleasure to thank G. Stöcklin, the Director of this Institute, for his active support of this research programme. The author is indebted to S. Bederka, M. Bormann, S. Cierjacks, J. Csikai, R. Haight, W. Herr, R.J. Howerton, S.E. Hunt, B. Karlik, N.A. Khan, V. Krivan, R.W. Loughheed, R. Michel, S. Mubarakmand, H. Münzel, D.R. Nethaway, A. Paulsen, O. Schult, I. Slaus, G. Staudt, H. Vonach, J. Walker and Z. Wilhelm for providing the author with the latest published and unpublished works from their labs.

## References

- <sup>1</sup> H.H. Barschall, in "Nuclear Structure Study with Neutrons" (Editors J. Erö and J. Szücs, Plenum Press, London, 1974), p. 289.
- <sup>2</sup> J. Csikai, Atomic Energy Review 11, 415 (1973).
- <sup>3</sup> J. Wieldraaijer and H.R. Hoogerbrug, Nucl. Instr.Meth. 95, 119 (1971).
- <sup>4</sup> M. Schmidt-Hönow and W. Herr, Radiochim. Acta 17, 142 (1972).
- <sup>5</sup> R. Michel and H. Weigel, Radiochim.Acta, in press
- <sup>6</sup> V. Krivan and H. Münzel, J.inorg.nucl.Chem. 34, 2093, 2989 (1972).
- <sup>7</sup> V. Krivan and H. Münzel, J.Radioanalyt. Chem. 15, 575 (1973).
- <sup>8</sup> S. Cierjacks, in "Nuclear Structure Study with Neutrons" (Editors J. Erö and J. Szücs, Plenum Press, London, 1974), p. 299.
- <sup>9</sup> S. Cierjacks, KFK 1857 (1973).
- <sup>10</sup> H. Michael, A. Neubert and H. Nickel, Int. J.Appl.Rad.Isotopes 25, 183 (1974).
- <sup>11</sup> V.N. Levkovskii and O.I. Artem'ev, Sov.J. Nucl.Phys. 13, 525 (1971).
- <sup>12</sup> A.K. Hankla and R.W. Fink, Nucl.Phys. A180, 157 (1972).
- <sup>13</sup> D.R. Nethaway, Nucl.Phys. A190, 635 (1972).
- <sup>14</sup> W. Struwe and G. Winkler, Nucl.Phys. A222, 605 (1974).
- <sup>15</sup> T. Mavaddat, S.A. Rao and P.K. Kuroda, J.inorg.nucl.Chem. 36, 953 (1974).
- <sup>16</sup> S.M. Qaim, Nucl.Phys. A185, 614 (1972).
- <sup>17</sup> S.M. Qaim, Nucl.Phys. A224, 319 (1974).
- <sup>18</sup> S.M. Qaim and G. Stöcklin, Proc. 8th Symposium on Fusion Technology, Noordwijkerhout (The Netherlands) EUR 5182e, 939 (1974).
- <sup>19</sup> S.M. Qaim and C. Graca, Nucl.Phys., in press
- <sup>20</sup> T. Biro, S. Sudar and J. Csikai, Proc.Conf. Nucl.Structure Study with Neutrons, Budapest (1972), p. 130.
- <sup>21</sup> S.M. Qaim, R. Wölflle and G. Stöcklin, Proc. Conf. Chemical Nuclear Data, Canterbury, BNES (1971), p. 121.
- <sup>22</sup> S.M. Qaim, Proc.Conf. Nuclear Structure Study with Neutrons, Budapest (1972), p. 25.
- <sup>23</sup> S.M. Qaim and G. Stöcklin, J.inorg.nucl.Chem. 35, 19 (1973).
- <sup>24</sup> S.M. Qaim, J.inorg.nucl.Chem. 36, 239 (1974).
- <sup>25</sup> S.M. Qaim, R. Wölflle and G. Stöcklin, J.Radioanalyt.Chem. 21, 395 (1974).
- <sup>26</sup> S. Lulic, P. Strohal and I. Slaus, Nucl. Phys. A154, 273 (1970).
- <sup>27</sup> M. Diksic, P. Strohal and I. Slaus, J.inorg. nucl.Chem. 36, 477 (1974).
- <sup>28</sup> N.D. Dudey, S.D. Harkness and H. Farrar IV, Nuclear Applications and Technology 9, 700 (1970).
- <sup>29</sup> S.M. Qaim, R. Wölflle and G. Stöcklin, J.inorg.nucl.Chem. 36, 3639 (1974).
- <sup>30</sup> S. Sudar, L. Vas and T. Biro, Nucl.Instr. Methods 112, 399 (1973).
- <sup>31</sup> M. Potokar, A. Likar, F. Cvelbar, M. Budnar and E.R. Hodgson, Nucl.Phys. A213, 525 (1973).
- <sup>32</sup> M. Stamatelatos, B. Lawergren and L.J. Lidofsky, Nucl.Sci.Eng. 51, 113 (1973).
- <sup>33</sup> F. Rigaud, J.L. Irigaray, G.Y. Petit, G. Longo and F. Saporetti, Nucl.Phys. A176, 545 (1971).
- <sup>34</sup> I. Bergqvist, D.M. Drake and D.K. McDaniels, Nucl.Phys. A191, 641 (1972); A231, 29 (1974).
- <sup>35</sup> O.A. Sal'nikov, G.N. Lovchikova, G.V. Kotel'nikova, V.S. Nesterenko, N.I. Fetisov and A.M. Trufanov, Sov.J.Nucl. Phys. 12, 620 (1971).
- <sup>36</sup> L.F. Hansen, J.D. Anderson, P.S. Brown, R.J. Howerton, J.L. Kammerdiener, C.M. Logan, E.F. Plechaty and C. Wong, Nucl.Sci.Eng. 51, 278 (1973).
- <sup>37</sup> M. Häring, H. Vonach and E.J. Feicht, Z.Physik 244, 352 (1971).
- <sup>38</sup> W. Breunlich, G. Stengel and H. Vonach, Z.Naturf. 26a, 451 (1971).
- <sup>39</sup> F.S. Dietrich, M.C. Gregory and J.D. Anderson, Phys.Rev. C9, 973 (1974).
- <sup>40</sup> B. Antolkovic, Nucl.Instr.Meth. 100, 211 (1972).



- 41 N.A. Khan, S. Mubarakmand and M. Ahmad, Nucl.Phys. A202, 123 (1973) and (private communication).
- 42 M. Bormann, W. Schmidt, V. Schröder, W. Scobel and U. Seebeck, Nucl.Phys. A186, 65 (1972).
- 43 M. Bormann, D. Kaack, V. Schröder, W. Scobel and L. Wilde, Z.Physik 258, 285 (1973).
- 44 M. Jaskola, J. Turkiewicz, L. Zemlo and W. Osakiewicz, Acta Phys. Polonica B2, 521 (1971).
- 45 K.R. Alvar, Nucl.Phys. A195, 289 (1972).
- 46 M. Brendle, M. Möricke, G. Staudt and G. Steidle, Nucl.Instr.Meth. 81, 141 (1970).
- 47 H.J. Brede, Z.Physik 254, 364 (1972).
- 48 D. Miljanic, V. Valkovic, D. Rendic and M. Furic, Nucl.Phys. A156, 193 (1970).
- 49 J.P. Perroud, Ch. Sellem and J.F. Loude, Nucl.Instr.Meth. 115, 357 (1974).
- 50 L. Kropp and P. Forti, Nucl.Instr.Meth. 104, 381 (1972).
- 51 G. Eder, G. Winkler and P. Hille, Z.Physik 253, 335 (1972).
- 52 Z.T. Bödy, INDC (HUN)-10 (1973).
- 53 Z.T. Bödy and J. Csikai, Atomic Energy Review 11, 153 (1973).
- 54 V.L. Levkovskii, Sov.J.Nucl.Phys. 18, 361 (1974).
- 55 M. Bormann, H. Neuert and W. Scobel, in "Handbook on Nuclear Activation Cross Sections", Technical Reports Series No. 156, IAEA, Vienna (1974), p. 87.
- 56 S.M. Qaim, J.inorg.nucl.Chem. 35, 3669 (1973).
- 57 J.G. Kuhry and G. Bontems, Radiochem.Radio-analyt.Letters 15, 29 (1973).
- 58 J.R. Landrum, R.J. Nagle and M. Lindner, Phys.Rev. C8, 1938 (1973).
- 59 C.K. Paulson and E.J. Hennelly, Nucl.Sci. Eng. 55, 24 (1974).
- 60 R.W. Loughheed, Livermore (private communication).
- 61 S.S. Hasan, R. Prasad and M.L. Seghal, Nucl. Phys. A181, 101 (1972).
- 62 R. Mogharrab and H. Neuert, Atomkernenergie 19, 107 (1972).
- 63 A.A. Druzhinin, N.I. Ivanova and A.A. Lbov, Sov.J.Nucl.Phys. 14, 383 (1972).
- 64 D.V. Viktorov and V.L. Zyablin, Sov.J.Nucl. Phys. 15, 608 (1972).
- 65 G.N. Salaita and P.K. Eapen, J.inorg.nucl. Chem. 35, 2139 (1973).
- 66 J. Janczyszyn and L. Gorski, J.Radioanalyt. Chem. 14, 201 (1973).
- 67 S. Hlavac, J. Kristiak, P. Oblozinsky and I. Turzo, Int.Symp. Neutron Induced Reactions, Smolenice, Czechoslovakia (Sept. 1974).
- 68 S.K. Ghorai, R. Vos, J.R. Cooper and W.L. Alford, Nucl.Phys. A223, 118 (1974).
- 69 T.H. Kao and W.L. Alford, Nucl.Phys. A237, 11 (1975).
- 70 W. Mannhart and H. Vonach, Z.Physik, in press
- 71 A. Paulsen, Geel (private communication).
- 72 T. Tuurnala and V. Pursiheimo, Physica Scripta 5, 183 (1972).
- 73 N.C. Dyer and J.H. Hamilton, J.inorg.nucl. Chem. 34, 1119 (1972).
- 74 P. Holmberg, R. Rieppo, J.K. Keinänen and M. Valkonen, J.inorg.nucl.Chem. 36, 715 (1974).
- 75 H.J. Brede, Z.Physik 254, 375 (1972).
- 76 D. Drake, I. Bergqvist and D.K. McDaniels, Phys.Lett. 36B, 557 (1971).
- 77 M. Valkonen and J. Kantele, Nucl.Instr. Meth. 103, 549 (1972).
- 78 J. Vuletin, P. Kulisic and N. Cindro, Lett. Nuovo Cim. 10, 1 (1974).
- 79 K. Ponnert, G. Magnusson and I. Bergqvist, Physica Scripta 10, 35 (1974).
- 80 F. Rigaud, M.G. Desthuilliers, G.Y. Petit, J.L. Irigaray, G. Longo and F. Saporetti, Nucl. Sci.Eng. 55, 17 (1974).
- 81 G. Petö, J. Csikai, K.D.V. Long, S. Mukerjee, J. Banhalmi and Z. Miligy, Int.Symp. Neutron Induced Reactions, Smolenice, Czechoslovakia (Sept. 1974).
- 82 D. Miljanic and V. Valkovic, Nucl.Phys. A176, 110 (1971).
- 83 W. Lu and R.W. Fink, Phys.Rev. C4, 1173 (1971).
- 84 D. Rendic, in "Few Body Problems, Light Nuclei and Nuclear Interactions", Vol. II, Gordon and Beach, New York (1968), p. 485
- 85 J.P. Perroud and Ch. Sellem, Nucl.Phys. A227, 330 (1974).
- 86 R.A. Jarjis and S.E. Hunt, J.Radioanalyt. Chem. 16, 611 (1973).
- 87 R.A. Jarjis and S.E. Hunt, Int.J.Appl.Rad. Isotopes, in press
- 88 Y. Kanda, Nucl.Phys. A185, 177 (1972).
- 89 P. Decowski, W. Grochulski, J. Karolyi, A. Marcinkowski, J. Piotrowski, E. Saad and Z. Wilhelmi, Nucl.Phys. A204, 121 (1973).
- 90 A. Paulsen, R. Widera and H. Liskien, Atomkernenergie 22, 291 (1974).
- 91 S.M. Qaim, A. Fäßler, H.V. Klapdor and H. Reiss, to be published
- 92 R.J. Howerton, UCID-16376 (1973); UCRL-50400 Vol. 15, to be published
- 93 D.G. Gardner, Livermore (private communication).
- 94 F. Cvelbar, A. Hudoklin and M. Potokar, Nucl.Phys. A158, 251 (1970).
- 95 S.M. Qaim, Z.Naturf. 25a, 1977 (1970).
- 96 E. Havlik, Acta Physica Austriaca 34, 209 (1971).

S. A. W. Gerstl, D. J. Dudziak, and D. W. Muir  
Theoretical Division  
Los Alamos Scientific Laboratory  
University of California  
Los Alamos, New Mexico 87544

A computational method to quantitatively determine cross section requirements is described and applied to a particular CTR design project. In order to provide a rational basis for the priorities assigned to new cross section measurements or evaluations, this method includes a quantitative assessment of the uncertainty of currently available data, the sensitivity of important nuclear design parameters to selected cross sections, and the accuracy desired in predicting nuclear design parameters. Perturbation theory is used to combine estimated cross section uncertainties with calculated sensitivities to determine the variance of any nuclear design parameter of interest. Selected computational results are presented for a model of the Tokamak Fusion Test Reactor.

(Sensitivity, uncertainties, perturbation theory, fusion reactors, cross sections)

### Introduction

Upon applying nuclear data developed for fission reactor, nuclear weapon, or accelerator applications to fusion reactors, a need for more accurate neutron cross sections in the MeV range becomes immediately apparent.<sup>1</sup> Due to the large number of cross section data needed for fusion reactor design calculations it is clear that not all deficient data can be improved within a short time frame. Therefore, some reasonable criterion is sought to provide a rational basis for programmatic priority assignments for new cross section measurements or evaluations. We feel that such a criterion should be based on a quantitative assessment of the uncertainties of currently available data, the sensitivity of important nuclear design parameters to such cross sections, and the accuracy desired in predicting nuclear design parameters at various stages of an evolving fusion reactor design. The development of such a quantitative criterion for priority assignments to new cross section measurements and evaluations is an integral part of a CTR cross section assessment program now being pursued at LASL within the framework of recommendations of the CTR-Subcommittee of the U.S. Nuclear Data Committee.

It is obvious that the importance of a specific cross section for a specific fusion reactor design depends strongly on that particular design. Also, the accuracy of an existing cross section set may be fully satisfactory for the calculation of a certain design parameter  $R_A$  in a reactor design (A), while the same design parameter in another design (B),  $R_B$ , may be extremely sensitive to this particular cross section in question, so that its errors may introduce an unacceptably large uncertainty in  $R_B$ . This demonstrates that every cross section assessment task must be seen within the context of a given reactor design, and that any statement about the quality of a given cross section set must be related to its application. Such applications, however, may cover a generic class of designs. In this study we concentrate on cross section requirements for the presently highest priority CTR construction project, the Tokamak Fusion Test Reactor (TFTR), for which a preliminary design concept was made available by the Princeton Plasma Physics Laboratory<sup>2</sup> and Westinghouse.<sup>3,4</sup> The objective of the study is to identify any data deficiencies for TFTR nuclear design calculations early enough so that necessary new cross section measurements or evaluations can be performed in time to be available for final design calculations. The purpose of this paper is to demonstrate the application of this new, quantitative method to assess the cross section requirements for the TFTR project.

### Method of Analysis

Our goal is to calculate the effect of a given cross section uncertainty  $\Delta\Sigma$  on a specific nuclear design parameter of interest  $R$ ; or in other words, to predict the uncertainty  $\Delta R$  of a calculated integral parameter due to a given cross section uncertainty  $\Delta\Sigma$ . In the following we assume that the application of first-order perturbation theory is adequate.

Following a derivation by Perey,<sup>5</sup> we denote with  $(\Sigma_i)$  a set of group cross sections and with  $R$  any design parameter of interest which is calculated as the result of some transport calculation which uses the group cross sections  $(\Sigma_i)$ . Then we can write

$$R = R(\Sigma_i) \quad (1)$$

and calculate any change in  $R$  due to small changes  $\delta\Sigma_i$  in  $\Sigma_i$  as

$$\delta R \approx \sum_i \frac{\partial R}{\partial \Sigma_i} \delta \Sigma_i, \quad (2)$$

by using first-order perturbation theory. However, what we really want is the standard deviation of  $R$  derived from the statistical population of possible cross section values, which is defined as

$$\Delta R = \sqrt{E\{\delta R^2\}} = \sqrt{\text{Var}(R)}, \quad (3)$$

where  $\text{Var}(R)$  denotes the variance of the calculated parameter  $R$ .  $\text{Var}(R)$  is formally obtained as the expectation value of  $\delta R^2$  and may be written as

$$\begin{aligned} \text{Var}(R) &= E\{\delta R^2\} \\ &= E\left\{\sum_{i,j} \frac{\partial R}{\partial \Sigma_i} \frac{\partial R}{\partial \Sigma_j} \delta \Sigma_i \delta \Sigma_j\right\}, \end{aligned} \quad (4)$$

using Eq. (2). Since  $\partial R/\partial \Sigma_i$  and  $\partial R/\partial \Sigma_j$  are constants over the considered statistical ensemble, we can rewrite Eq. (4) as

$$\text{Var}(R) = \sum_{i,j} \frac{\partial R}{\partial \Sigma_i} \frac{\partial R}{\partial \Sigma_j} E\{\delta \Sigma_i \delta \Sigma_j\}. \quad (5)$$

The expectation value of the product of  $\delta \Sigma_i$  and  $\delta \Sigma_j$  is the definition of a matrix element of the covariance matrix for cross sections  $\Sigma_i$  and  $\Sigma_j$  over a joint probability density function  $f(\Sigma_i, \Sigma_j)$ :

$$\text{Cov}(\Sigma_i, \Sigma_j) \equiv E\{\delta \Sigma_i \delta \Sigma_j\}$$

\*Work performed under the auspices of the U. S. Energy Research and Development Administration.



$$= \iint_{-\infty}^{+\infty} f(\Sigma_i, \Sigma_j) \cdot (\Sigma_i - \hat{\Sigma}_i) (\Sigma_j - \hat{\Sigma}_j) d\Sigma_i d\Sigma_j, \quad (6)$$

where  $\hat{\Sigma}_i$  and  $\hat{\Sigma}_j$  are the expectation values of  $\Sigma_i$  and  $\Sigma_j$ , respectively. Inserting this definition (6) into Eq. (5) we obtain our final result

$$\text{Var}(R) = \sum_{i,j} \frac{\partial R}{\partial \Sigma_i} \frac{\partial R}{\partial \Sigma_j} \text{Cov}(\Sigma_i, \Sigma_j), \quad (7)$$

which is the basis for our quantitative data assessment program.

The diagonal elements of the covariance matrix,  $\text{Cov}(\Sigma_i, \Sigma_i)$ , are the usual (uncorrelated) cross section uncertainties expressed as the variance of  $\Sigma_i$ :

$$\begin{aligned} \text{Cov}(\Sigma_i, \Sigma_i) &= \text{Var}(\Sigma_i) \\ &\equiv E\{\delta \Sigma_i^2\} \\ &= \Delta \Sigma_i^2. \end{aligned} \quad (8)$$

Cross section variances have been compiled recently for a wide variety of CTR materials by the CTR Subcommittee of the USNDC.<sup>6</sup> The off-diagonal terms of the covariance matrix indicate correlations between the cross sections  $\Sigma_i$  and  $\Sigma_j$ .

The quantities  $\partial R / \partial \Sigma_i$  in Eq. (7) are the sensitivity coefficients which result from a sensitivity analysis of the particular transport problem of interest.<sup>7-9</sup> It is convenient and useful to define a relative sensitivity coefficient

$$P_{\Sigma_i} = \frac{(\partial R / R)}{(\partial \Sigma_i / \Sigma_i)}, \quad (9)$$

which is called a sensitivity profile for cross section  $\Sigma_i$  when  $i$  is the group index of a multigroup cross section set ( $\Sigma_i$ ).  $P_{\Sigma_i}$  can be interpreted as the fractional (percentage) change of the design parameter  $R$  per fractional (percentage) change of cross section  $\Sigma_i$ . The sensitivity profile for cross section  $\Sigma_i$  can be calculated from

$$P_{\Sigma_i} = \frac{\langle \phi^*, L_{\Sigma_i} \phi \rangle_i}{R}, \quad (10)$$

where  $\phi$  and  $\phi^*$  are the forward and adjoint angular fluxes of the problem in consideration, and  $L_{\Sigma_i}$  denotes that portion of the Boltzmann transport operator which contains the cross section  $\Sigma_i$ . The symbol  $\langle, \rangle_i$  indicates integrations over all angles and all spatial zones containing  $\Sigma_i$ . While the sensitivity profile for a certain cross section contains much valuable detailed information, it is also convenient to define an integral cross section sensitivity

$$S_{\Sigma} = \sum_i P_{\Sigma_i}, \quad (11)$$

which reduces the sensitivity information about the whole cross section set ( $\Sigma_i$ ) to one number.  $S_{\Sigma}$  can be interpreted as the percentage change of the design parameter of interest,  $(\partial R / R)$ , resulting from a simultaneous 1% increase of the group cross sections  $\Sigma_i$  in all energy groups  $i$  (assuming full correlation, i.e., a correlation coefficient of +1).

For convenience we transform our basic Eq. (7) into a form containing only fractional quantities. Inserting Eq. (9) into Eq. (7) and using Eq. (3) we obtain

$$\left(\frac{\Delta R}{R}\right)^2 = \sum_{i,j} P_{\Sigma_i} P_{\Sigma_j} \frac{\text{Cov}(\Sigma_i, \Sigma_j)}{\Sigma_i \Sigma_j}. \quad (12)$$

In Eq. (12) all cross section uncertainty information is contained in the relative covariance matrix elements  $\text{Cov}(\Sigma_i, \Sigma_j) / \Sigma_i \Sigma_j$  and all sensitivity information in the product of the profiles  $P_{\Sigma_i} P_{\Sigma_j}$ . It is seen from Eq. (10) that a sensitivity profile is highly problem-dependent and specific for a particular cross section  $\Sigma_i$  as well as a particular design parameter  $R$ . Hence, Eq. (12) combines the problem-dependent cross section sensitivities of a particular nuclear design with the basic cross section error information into a design-oriented quantity  $\Delta R / R$  which is of immediate use for the designer.

The predicted uncertainty  $\Delta R / R$  for a calculated design parameter  $R$  due to given uncertainties of a multigroup cross section set ( $\Sigma_i$ ) may be compared to a specified design criterion requiring a certain confidence limit for the parameter  $R$ . Such a confidence limit may be described as a maximum allowable standard deviation for the design parameter  $R$ ; say  $(\Delta R / R)_{\max, \text{crit.}}$ . Then three cases are possible:

$$a) \quad \Delta R / R < (\Delta R / R)_{\max, \text{crit.}} \quad (13a)$$

$$b) \quad \Delta R / R \approx (\Delta R / R)_{\max, \text{crit.}} \quad (13b)$$

$$c) \quad \Delta R / R >> (\Delta R / R)_{\max, \text{crit.}} \quad (13c)$$

For case (a) we conclude that the cross section set ( $\Sigma_i$ ) is adequate for the calculation of this particular design parameter in the underlying design, while in cases (b) and (c) we have identified situations where the cross section set is either marginal or grossly inadequate for this application. After such a deficient cross section set has been found, an inspection of the sensitivity profile  $P_{\Sigma_i}$  reveals in which energy range a cross section improvement should be attempted to contribute must to a reduction of  $\Delta R / R$ .

#### Upper Limits for $\Delta R / R$

In cases where no complete error files are available but rough error estimates can be obtained for the cross sections of interest, it is useful to determine upper limits for  $\Delta R / R$  based on calculated sensitivities and such rough error estimates. The term "rough" should indicate that either cross section correlations or energy dependencies or both are neglected when errors are estimated. Then certain conservative assumptions can be made about such correlations or energy dependencies to obtain upper limits for resulting response uncertainties  $\Delta R / R$ .

#### 1. Uncorrelated Cross Section Uncertainties

If cross sections  $\Sigma_i$  are assumed to be uncorrelated, then their uncertainties will also be uncorrelated, with the result that all off-diagonal elements of the covariance matrix vanish:

$$\text{Cov}(\Sigma_i, \Sigma_j)_{\text{uncorr.}} = \text{Cov}(\Sigma_i, \Sigma_j) \delta_{ij}. \quad (14)$$

Inserting Eq. (14) into Eq. (12) allows us to reduce the double sum to a single summation and we obtain with Eq. (8)

$$\left(\frac{\Delta R}{R}\right)_{\text{uncorr.}}^2 = \sum_i \left( P_{\Sigma_i} \frac{\Delta \Sigma_i}{\Sigma_i} \right)^2. \quad (15)$$

#### 2. Fully Correlated Cross Section Uncertainties

A more conservative assumption about group-wise cross sections  $\Sigma_i$  than being uncorrelated is to assume



a correlation of +1. This means that when a cross section in one specific energy group is increased by a certain amount, then the cross sections in all other groups are also increased by the same amount. Under this assumption all off-diagonal elements of the covariance matrix are fully determined by the diagonal elements alone:<sup>14</sup>

$$\text{Cov}(\Sigma_i, \Sigma_j)_{\text{corr.}(+1)} = \sqrt{\text{Cov}(\Sigma_i, \Sigma_i)} \sqrt{\text{Cov}(\Sigma_j, \Sigma_j)} \quad (16)$$

Inserting this into Eq. (12) and using again the notation of Eq. (8), we obtain

$$\left(\frac{\Delta R}{R}\right)_{\text{corr.}(+1)} = \left| \sum_i P_{\Sigma_i} \frac{\Delta \Sigma_i}{\Sigma_i} \right| \quad (17)$$

### 3. Energy Independent Cross Section Error Estimates

The simplest possible and most conservative error specification is to assume that all uncertainties in an entire cross section set are equal to the largest uncertainty in any of the individual cross sections, i.e.,

$$\frac{\Delta \Sigma_i}{\Sigma_i} = \text{const.} = \left(\frac{\Delta \Sigma}{\Sigma}\right)_{\text{max.}} \quad (18)$$

If we further assume the group-by-group errors to be fully correlated, we obtain the most conservative upper limit for  $\Delta R/R$ . Using a new definition for an always positive integral sensitivity [in contrast to  $S_{\Sigma}$  defined in Eq. (11)]:

$$\hat{S}_{\Sigma} = \sum_i |P_{\Sigma_i}| \quad (11a)$$

and inserting Eq. (18) into Eq. (17) we obtain

$$\left(\frac{\Delta R}{R}\right)_{\text{max.}} = \hat{S}_{\Sigma} \cdot \left(\frac{\Delta \Sigma}{\Sigma}\right)_{\text{max.}} \quad (19)$$

As long as the sensitivity profile  $P_{\Sigma_i}$  does not change sign (which is always the case in this study), it can be shown by comparing Eqs. (12), (17), and (19) that

$$\left(\frac{\Delta R}{R}\right) \leq \left(\frac{\Delta R}{R}\right)_{\text{corr.}(+1)} \leq \left(\frac{\Delta R}{R}\right)_{\text{max.}} \quad (20)$$

Then the largest upper limit for  $\Delta R/R$  is given by  $\left(\frac{\Delta R}{R}\right)_{\text{max.}}$ , if  $\left(\frac{\Delta \Sigma}{\Sigma}\right)_{\text{max.}}$  is the largest error expected in any group of the entire energy region of interest.  $\left(\frac{\Delta R}{R}\right)_{\text{corr.}(+1)}$  weighs the energy-dependent error estimates with the energy-dependent sensitivities, and  $\left(\frac{\Delta R}{R}\right)_{\text{uncorr.}}$  replaces the strong assumption of full correlation by the weaker assumption of no correlation at all. The last step to  $\Delta R/R$  via Eq. (12) allows individual terms of the double sum to have differing signs and thereby account for the possible cancellation or cumulation of errors. Therefore, while  $\left(\frac{\Delta R}{R}\right)_{\text{max.}}$  and  $\left(\frac{\Delta R}{R}\right)_{\text{corr.}(+1)}$  are real upper limits for  $\Delta R/R$ , the special case  $\left(\frac{\Delta R}{R}\right)_{\text{uncorr.}}$  does not constitute any limit to the real  $\Delta R/R$  from Eq. (12). The utility of the two different upper limits for  $\Delta R/R$  is recognized when a numerical comparison is made with the design criterion  $\left(\frac{\Delta R}{R}\right)_{\text{max, crit.}}$ . If it is found that Eq. (13a) is satisfied already with one of the upper limits for  $\Delta R/R$ , then a further uncertainty evaluation of that cross section set is not urgent for the design problem considered.

### Application and Results

The methodology outlined in the previous section has been applied to the nuclear design of the TFTR.<sup>4</sup> A preliminary one-dimensional computational model for neutronics calculations has been supplied by the

Princeton Plasma Physics Laboratory<sup>2</sup> and Westinghouse,<sup>3</sup> and is shown in Fig. 1, where  $R$  is the radial distance from the plasma centerline. Since the main objective of the TFTR is to demonstrate the scientific feasibility of a Tokamak fusion reactor, it is not required to breed tritium, and therefore does not employ a lithium blanket. The reactor is expected to operate in a pulsed mode yielding a maximum of 1 000 pulses per year, generating a maximum neutron fluence of  $1.4 \times 10^{15}$  fusion neutrons per  $\text{cm}^2$  per year on the first wall. Due to this low neutron fluence, radiation damage or nuclear heating problems are not of major concern. However, the activation of magnet coils, structural materials, and instruments is considered a major neutronics problem area, in particular the generation of long-living radioactive isotopes. Therefore, and for biological shielding reasons, a radiation shield is provided as close to the plasma as possible (Fig. 1). In cooperation with Princeton and Westinghouse we selected several threshold activation reactions in the structural steel (zones 9 and 11 in Fig. 1) and the main copper coil (zone 10 in Fig. 1) as important nuclear design parameters of interest (cf. Table I). Our objective is to estimate the uncertainties introduced in the calculation of these activation rates due to estimated errors in the neutron cross sections of the system. Of particular interest are uncertainties in the cross sections of the shield-zone 7, the composition of which is given in Table II.

TABLE I  
ACTIVATION REACTIONS OF INTEREST  
("Response")

1. In Steel:
  - $A_1 = \text{Fe54}(n,p)\text{Mn54}, \quad t_{1/2} = 303 \text{ d}$
  - $A_2 = \text{Mn55}(n,2n)\text{Mn54}, \quad t_{1/2} = 303 \text{ d}$
  - $A_3 = \text{Fe56}(n,p)\text{Mn56}, \quad t_{1/2} = 2.6 \text{ h}$
  - $A_4 = \text{Ni58}(n,p)\text{Co58}, \quad t_{1/2} = 71 \text{ d}$
2. In Copper:
  - $A_5 = \text{Cu65}(n,2n)\text{Cu64} \quad t_{1/2} = 12.9 \text{ h}$

In order to calculate the sensitivity coefficients  $\partial R / \partial \Sigma_i$  for Eq. (7) or, equivalently, the sensitivity profiles  $P_{\Sigma_i}$  for Eq. (12), we performed a forward transport calculation for the TFTR model of Fig. 1 and an adjoint for each of the 5 activation reactions listed in Table I, saving the angular fluxes  $\phi$  and  $\phi^*$ . All transport calculations were performed with the one-dimensional  $S_N$  code DTF-IV<sup>10</sup> in an  $S_8$  approximation using 20-group  $P_3$  neutron cross sections. This cross section set was generated from the first 20 groups of

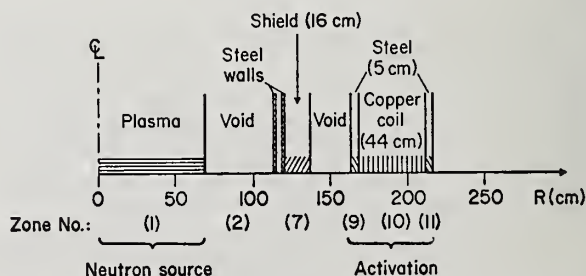


Fig. 1. One-dimensional computational model for TFTR cross section sensitivity analysis.

TABLE II  
SHIELD COMPOSITION  
("Perturbed Cross Section")

Lead-Borated-Polyethylene,  $\rho = 4.2 \text{ g/cm}^3$

Element	weight - %	at/barn'cm
H	1.8	0.0455
C	10.7	0.0225
Pb	80.0	0.0098
B	1.0	0.0023
$\emptyset$	6.5	0.0103

the DLC-2E 100-group set distributed by RSIC.<sup>11</sup> It covers neutron energies between 2.02 and 14.92 MeV, which is sufficient for the considered activation reactions. Cross sections for the activation reactions listed in Table I were taken from Ref. 12. The stored angular fluxes  $\phi$  and  $\phi^*$  from the transport calculations were then read into the LASL sensitivity code SENSIT-1D<sup>13</sup> to evaluate Eqs. (10), (11), and (12), and plot the sensitivity profiles of interest. In order to combine the sensitivity information with the cross section uncertainties, according to Eq. (12), the covariance matrices for the cross sections of interest ("perturbed cross sections") must also be read into SENSIT-1D. However, at present complete covariance matrices are available in ENDF/B only for three materials: N, O, and C. Therefore, cross section uncertainties had to be estimated for most of the materials in our design model and these estimates are still incomplete. We selected a few partial cross sections for which estimated covariance matrices have been produced and which serve here as illustrative samples.

As a basis for such selection we calculated the integral sensitivities, Eq. (11), of all five activation reactions to the total cross sections of all materials in the system and tabulate them in Table III. It is noted that all sensitivities are negative (except for

TABLE III

INTEGRAL SENSITIVITIES,  $S$ , OF THE RESPONSES,  $A_k$  (ACTIVATION REACTIONS), TO THE NEUTRON CROSS SECTIONS OF CERTAIN MATERIALS IN CERTAIN ZONES

Perturbed Cross Section	in Zone	RESPONSE				
		$A_1$ in Zone 9	$A_2$ in Zone 9	$A_3$ in Zone 9	$A_4$ in Zone 9	$A_5$ in Zone 10
$C_{Tot}$	7	-0.76	-0.67	-0.69	-0.68	-0.55
$C(n,n'3\alpha)$	7	-0.10	-0.12	-0.11	-0.09	-0.09
$Pb_{Tot}$	7	-1.30	-1.11	-1.14	-1.14	-0.91
$Pb(n,2n)$	7	-0.42	-0.46	-0.45	-0.39	-0.38
$\emptyset_{Tot}$	7	-0.26	-0.24	-0.24	-0.23	-0.19
$R_{Tot}$	7	-1.00	-0.70	-0.76	-0.82	-0.58
$Fe_{Tot}$	9	-0.72	-0.47	-0.53	-0.57	-0.88
$Fe_{incl. cont.}$	9	-0.09	-0.12	-0.14	-0.11	-0.22
$Cr_{Tot}$	9	-0.20	-0.13	-0.14	-0.15	-0.23
$Ni_{Tot}$	9	-0.13	-0.09	-0.09	-0.10	-0.16
$Mn_{Tot}$	9	-0.02	-0.01	-0.02	-0.02	-0.03
$Cu_{Tot}$	10	-0.05	-0.001	-0.006	-0.02	-1.96
$Cu_{Scat}$	10	+0.14	+0.09	+0.10	+0.11	+0.82

the scattering cross section of copper in the coil-zone 10) indicating that an increase in such cross sections would cause all of the considered activations to decrease. The largest sensitivity shown in Table III is that of  $A_5$  to  $Cu_{Tot}$  (viz., -1.96), which indicates that a 1% increase in the total cross section of copper would decrease the  $^{64}Cu$ -production in the coil by 1.96%. This and the other responses are even less sensitive to the total cross sections of the radiation shield materials (zone 7), resulting from the fact that this shield is relatively thin. Indeed, a hand calculation shows that the 16 cm of shield material corresponds to only 1.8 mean-free-path for the 14-MeV fusion neutrons originating in the plasma. Nevertheless, the uncertainties in these cross sections with marginal sensitivities still could be so high as to produce an undesirably large  $\Delta R/R$ .

For this paper we shall analyse in detail only the uncertainties in two partial cross sections of Pb and C. As shown in Table III as well as Table IV, the  $Pb(n,2n)$  cross section contributes about 32% to the sensitivity of the Pb total cross section, when the activation reaction  $Fe54(n,p)Mn54$  in the first structural steel-region (zone 9) is considered. Similarly, the  $C(n,n'3\alpha)$  cross section contributes 13% to the carbon total sensitivity. Therefore, an attempt was made to generate covariance matrices for these two partial cross sections.

Table IV gives the numerical values for the various upper limits for  $\Delta R/R$ , as well as  $\Delta R/R$  according to Eq. (12), depending upon the detail of available error information.<sup>6</sup> For example, uncertainties in the  $Pb(n,2n)$  cross section are estimated to be 15 to 50% in the energy range from 8 to 15 MeV (threshold energy  $E_{thres} = 7 \text{ MeV}$ ). Therefore, if a 50% uncertainty is assumed for the entire energy range of interest ( $E_{thres}$  to 15 MeV) then a maximum uncertainty of 21% can be expected in the calculated value for the  $Fe54(n,p)Mn54$  activation in steel-zone 9. However, a more realistic error estimate is the assumption of 15% error at 15 MeV increasing linearly to 50% at the threshold energy, which reduces  $\Delta R/R$  to 7.45% if the additional assumption is made that these cross section uncertainties are fully correlated among energy groups (which is considered correct for this case). Also given in Table IV is the  $\Delta R/R$  due to the estimated uncertainty of the  $Fe54(n,p)$  activation cross section itself, which constitutes no significant neutron transport effect but contributes to the overall  $\Delta R/R$  and must therefore be considered. Figure 2 shows the measured and recommended smoothed data for this reaction cross section and demonstrates a typical situation: in about half of the energy range of interest

TABLE IV

EFFECTS OF ESTIMATED ERRORS IN SELECTED COMPONENT CROSS SECTIONS IN TFTR SHIELD-ZONE 7, ON  $Fe54(n,p)Mn54$  ACTIVATION REACTIONS IN STEEL-ZONE 9 ( $A_1$ ). Question marks indicate missing cross section error data.

Pert. Cross Section in Shield-zone 7	Integral Sensitivity of $A_1$ , $S(\% \text{ per } \%)$	$\left(\frac{\Delta R}{R}\right)_{\max}^{\%}$	$\left(\frac{\Delta R}{R}\right)_{\max}^{\%}$	$\left(\frac{\Delta R}{R}\right)_{\text{corr}(\pm 1)}^{\%}$	$\left(\frac{\Delta R}{R}\right)_{\text{uncorr.}}^{\%}$	$\left(\frac{\Delta R}{R}\right)_{\text{uncorr.}}^{\%}$
$Pb_{Tot}$	- 1.30	4	5.2	5.2	3.15	?
$Pb_{Abs}$	- $5 \times 10^{-5}$	25	0.001	0.001	$< 10^{-3}$	?
$Pb_{scat.}$	- 1.30	?	?	?	?	?
$Pb(n,2n)$	- 0.42	50	21	7.45	---	7.45
$C_{Tot}$	- 0.76	4	3.04	2.93	1.9	?
$C_{Abs}$	- 0.07	25	1.75	0.53	0.28	?
$C_{scat.}$	-0.69	?	?	?	?	?
$C(n,n'3\alpha)$	- 0.10	50	5	2.05	---	2.05
$Fe54(n,p)$	+ 1.0	25	25	25	---	?



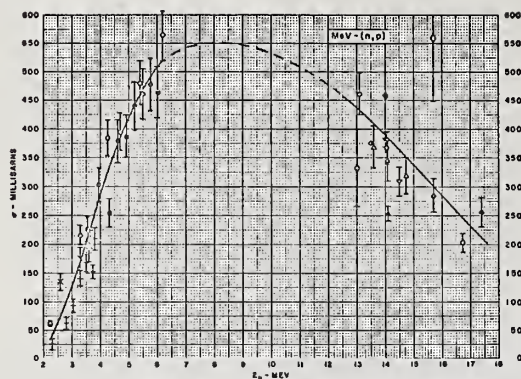
<sup>54</sup>Fe


Fig. 2. Uncertainties of measured Fe54(n,p)Mn54 reaction cross section (from BNL-325).

to our problem there exist no measured data at all. Therefore, an estimate of  $\Delta\Sigma/\Sigma = 25\%$ , fully correlated over the entire range from 2 to 15 MeV, appears realistic. This, of course, also gives a 25% uncertainty in the calculated Fe54(n,p) reaction rate, as included in Table IV. The question marks in Table IV indicate missing cross section error information.

In order to determine the cross section requirements for the entire TFTR nuclear design many tables of the type of Table IV have to be provided (for each design parameter of interest and each cross section set used in the nuclear model calculation). Then the calculated values for  $\Delta R/R$  must be compared with the specified design criterion according to Eqs. (13) to sift out those satisfying Eq. (13a). For the selected results shown in Table IV we conclude that if the Fe54(n,p)Mn54 activation rate in the first structural steel region must be predicted to better than 25% standard deviation then the accuracy of the Fe54(n,p) cross section must be improved, either by a re-evaluation or new measurements. If an even higher accuracy of the predicted activation  $A_1$  is desired (e.g., better than 7%) then the Pb(n,2n) cross section must also be improved. An improvement of the C(n,n' $\alpha$ ) cross section is only required if a very tight design criterion, e.g.,  $(\Delta R/R)_{\max, \text{crit.}} < 2\%$ , were set for  $A_1$ . In order to determine at which neutron energy a new cross section measurement should be performed to give the largest benefit to the considered design problem, we look at the sensitivity profile. Figure 3 shows the sensitivity profile for the Pb(n,2n) cross section. It indicates that 76% of the integral sensitivity is due to the cross section in the highest energy group. Although the highest accuracy of 15% was estimated for the Pb(n,2n) cross section at this energy, it still contributes 64% of the total  $\Delta R/R$  due to all Pb(n,2n) cross section uncertainties, as shown in Fig. 4. This histogram plots the group-wise contributions to  $\Delta R/R$  for the case of fully correlated uncertainties

$$\left(\frac{\Delta R}{R}\right)_{\text{corr. (+1)}}^i = P_{\Sigma_i} \cdot \frac{\Delta\Sigma_i}{\Sigma_i}, \quad (21)$$

so that, according to Eq. (17),  $(\Delta R/R)_{\text{corr. (+1)}}$  is obtained as the linear sum of all terms of Eq. (21). Hence, from Fig. 4 we can conclude that an improvement of the Pb(n,2n) cross section in the first energy group, ranging from 13.5 to 14.9 MeV, would be more beneficial for the calculation of  $A_1$  than a similar improvement at any lower energy.

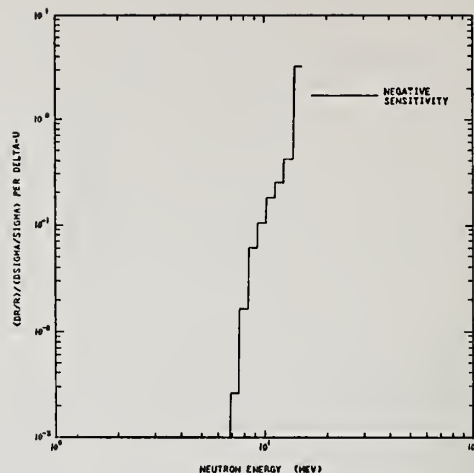


Fig. 3. Sensitivity of Fe54(n,p)Mn54-reaction rate in steel-zone 9 to Pb(n,2n) cross sections in shield-zone 7 of TFTR. The sensitivity profile is plotted per group width  $\Delta u$ . For all groups  $\Delta u = 0.1$ .

### Conclusion

We have demonstrated the applicability of a new quantitative method to assess cross section requirements by combining the results of a sensitivity analysis with estimated uncertainties of existing cross section data. The results of such quantitative assessment can be used in guiding priority assignments for new cross section measurements or evaluations. In addition, these results provide added confidence in cross section sets which have been found adequate for this application. Only selected results could be presented in this paper, partly due to the lack of complete cross section error files. Therefore, there is an immediate need for the establishment of estimated covariance data files for CTR materials. Such data are essential in order to

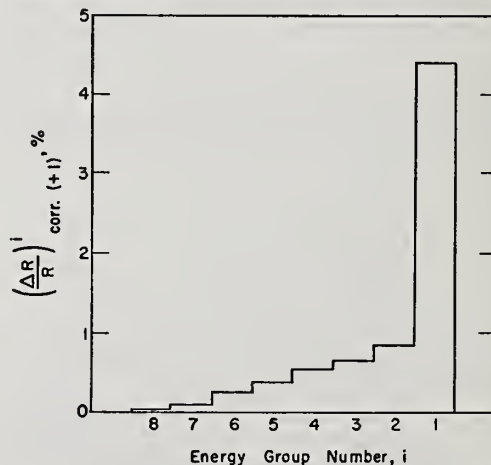


Fig. 4. Group-wise contributions to uncertainty of  $A_1$  in zone 9 due to estimated errors in Pb(n,2n) cross sections.



perform complete design-oriented cross section assessment tasks as outlined in this paper. However, the full information content as specified by the ENDF covariance file format<sup>5</sup> is not always necessary if rough, conservative error-estimates lead to acceptable upper limits of  $\Delta R/R$ . Therefore, the presently available ENDF covariance data, together with other estimated error information, have enabled us to draw some important conclusions regarding the adequacy of several existing cross section sets for TFTR applications. Many sensitivity profiles, similar to the sample shown in Fig. 3, and plotted automatically, have already added to our capability to identify areas for meaningful improvements in future cross section measurements and evaluations.

#### REFERENCES

1. D. Steiner, "Nuclear Data Needs for Fusion Reactor Design," this conference; and D. Steiner, N. D. Dudey, B. R. Leonhard, Jr., J. R. McNally, Jr., and L. K. Price, "Review of CTR Nuclear Data Requirements," Trans. Am. Nucl. Soc. 19, 457 (1974).
2. W. G. Price, Jr., Princeton University Plasma Physics Laboratory, private communication, December 7, 1974.
3. G. Gibson, Westinghouse Research and Development Center, private communication, February 6, 1975.
4. "TCT-Two-Component Torus," joint conceptual design study, performed by Plasma Physics Laboratory, Princeton, NJ, and Westinghouse Electric Corporation, Pittsburgh, PA, Vol. III, Sec. 6.1 (1974).
5. F. G. Perey, "Estimated Data Covariance Files of ENDF/B - Their Uses," presentation to the Cross Section Evaluation Working Group (CSEWG), Brookhaven, NY, June 1974.
6. D. Steiner, coordinator, "The Status of Neutron-Induced Nuclear Data for Controlled Thermonuclear Research Applications: Critical Reviews of Current Evaluations," USNDC-CTR-1 (1974).
7. S. A. W. Gerstl, "Second-Order Perturbation Theory and its Application to Sensitivity Studies in Shield Design Calculations," Trans. Am. Nucl. Soc. 16, 342 (1973); S. A. W. Gerstl and W. M. Stacey, Jr., "A Class of Second-Order Approximate Formulations of Deep Penetration Radiation Transport Problems," Nucl. Sci. Eng. 51, 339 (1973).
8. S. A. W. Gerstl, "The Application of Perturbation Methods to Shield and Blanket Design Sensitivity Analyses," AP/CTR/TM-28, Applied Physics Division, Argonne National Laboratory (1974).
9. D. E. Bartine, E. M. Oblow, and F. R. Mynatt, "Radiation-Transport Cross Section Sensitivity Analysis - A General Approach Illustrated for a Thermonuclear Source in Air," Nucl. Sci. Eng. 55, 147 (1974).
10. K. D. Lathrop, "DTF-IV, a FORTRAN-IV Program for Solving the Multigroup Transport Equation with Anisotropic Scattering," Los Alamos Scientific Laboratory report LA-3373 (1965).
11. "DLC-2/100G, 100 Group Neutron Cross-Section Data Based on ENDF/B," RSIC Data Library Collection, Radiation Shielding Information Center, HNL (1975).
12. D. W. Muir in "Applied Nuclear Data Research and Development Quarterly Progress Report, July 1 through September 30, 1974," edited by G. M. Hale, D. R. Harris, and R. E. MacFarlane, Los Alamos Scientific Laboratory report LA-5804-PR (1974).
13. S. A. W. Gerstl, "SENSIT-1D, A FORTRAN Code to Perform Cross Section and Design Sensitivity Analyses in One-Dimensional Geometries," Los Alamos Scientific Laboratory report, to be published.
14. W. C. Hamilton, "Statistics in Physical Science," Ronald Press, New York, NY, p. 31 (1964).

A SENSITIVITY STUDY OF DATA DEFICIENCIES, WEIGHTING FUNCTIONS,  
AND 14 MeV NEUTRON SOURCE SPECTRUM EFFECTS IN A  $^{238}\text{U}$  FUELED FUSION-FISSIION HYBRID BLANKET  
B. R. Leonard, Jr., U. P. Jenquin, D. L. Lessor,  
D. F. Newman and K. B. Stewart  
Battelle-Northwest  
Richland, Washington 99352

Neutronic calculations have been made for a hybrid DT fusion reactor blanket in which the initial region is fueled with depleted uranium followed by lithium and graphite. The important parameters of the blanket are the tritium production, fissions,  $^{238}\text{U}$  captures, and thermal flux in the graphite. The sensitivity of these integral parameters was studied as a function of  $^{238}\text{U}$  region thickness and the  $^{238}\text{U}$  microscopic data used. In particular, the effect of modifying some improbable secondary neutron energy distributions of  $^{238}\text{U}$  on both versions III and IV of ENDF/B was calculated. Calculations were made for multigroup data obtained by collapsing over constant and  $E^{-1}$  weighting functions below the fusion peak. Results were also obtained for a narrow DT fusion neutron peak and for neutron source distribution resulting from an essentially exact calculation of a mirror plasma driven by 100 keV neutral  $^2\text{H}$  and  $^3\text{H}$ .

(Nuclear reactions,  $^{238}\text{U}$ , (n,n'), (n,2n), (n,3n) calculated sensitivity of secondary neutron energies to fusion blanket neutronics)

### Introduction

In previous work<sup>1,2</sup> Battelle-Northwest (BNW) has reported the results of the neutronic analyses of a fission hybrid blanket designed for a mirror fusion reactor. Nuclear data from ENDF/B-III was employed in these studies. We now report on a study which was designed to define uncertainties and improved estimates of the calculated neutronic performance parameters due to nuclear data deficiencies and related data handling and physical problems. Haight and Lee,<sup>3</sup> for example, have reported significant differences in neutronics parameters for calculations of a particular hybrid blanket for calculations employing ENDF/B-III and those using Lawrence Livermore Laboratory ENDL microscopic data. These calculated differences are assumed<sup>3</sup> to be primarily due to the known differences in the descriptions of neutron energy spectra of secondary neutrons from non-elastic reactions on iron<sup>4</sup> and uranium.<sup>5</sup> It is further known that the emission spectra of neutrons above 2 MeV from iron or uranium spheres<sup>6</sup> pulsed with a central 14 MeV neutron source are calculated much better with ENDL than with ENDF/B data. Since the first region of the hybrid blanket calculated by BNW was comprised primarily of iron and  $^{238}\text{U}$ , effects due to these data differences similar to those observed by Haight and Lee<sup>3</sup> may occur. In addition, Muir<sup>7</sup> has recently pointed out that the neutron emission spectra resulting from high-temperature isotropic Maxwellian DT plasmas are quite broad in energy distribution and can have significant impacts on calculated reaction rates for reactions which have significant variation with energy near 14 MeV. The mirror fusion reactor concept in which the leaky plasma is driven by 100 keV or higher<sup>1</sup> energetic neutrals produces plasma ion-energy distributions which are very similar to Maxwellian distributions with high characteristic temperatures.<sup>8</sup> Thus, the expected broad neutron source spectrum can impact on the calculated reaction rates and associated secondary neutron spectra in the mirror hybrid blanket. The broad source spectrum also raises questions of possible effects of: 1) assumptions used in the neutron spectrum used to obtain the multigroup data set, 2) the energy multi-group structure, and 3) the neutron source distributions used in the neutron balance calculation.

### Calculational Model

#### Description of the Hybrid Blanket

In the previously reported work,<sup>1</sup> the conceptual hybrid blanket consisted of inner and outer fissile blanket regions. The inner blanket region consisted of helium-cooled, depleted-uranium oxide and was called a convertor. Leakage neutrons from this region were used to drive a slightly-enriched HTGR lattice which (for lower energy neutrons) was largely decoupled from the convertor by an intervening thickness of lithium. The effects to be studied in the present work are dominated by events in the convertor region. Thus, in this study the HTGR thermal fission lattice has been replaced by graphite. This results in a blanket configuration similar to those reported by Lee<sup>9</sup> and by Haight and Lee.<sup>3</sup> Thus, the calculated neutronic parameters can be compared with the results of these studies. The basic blanket configuration is given in Table I.

Table I. Mirror Hybrid Blanket Description

Region	Thickness	Constituents	Density (at-b <sup>-1</sup> -cm <sup>-1</sup> )
1	3.5 m rad.	DT	0
2	5.0 m rad.	Vacuum	
3	t(cm)	Helium	0.000159
		St. steel	0.009935
		Oxygen	0.025734
		$^{238}\text{U}$	0.012828
		$^{235}\text{U}$	0.0000386
4	4.5 cm	$^6\text{Li}$	0.003317
		$^7\text{Li}$	0.04139
		SS	0.002524
		He	0.0000002
5	(188.5-t)cm	C	0.08123
6	7 cm	$^6\text{Li}$	0.003317
		$^7\text{Li}$	0.04139
		SS	0.002524
		He	0.0000002

The uranium in the convertor (region 3) is 0.3%  $^{235}\text{U}$ . The initial thickness of the convertor was 8.5 cm and this thickness was varied in the sensitivity calculations at the expense of the thickness of the graphite region.

### Calculational Methods

For the reference case, ENDF/B-III data were processed into a 27 energy group structure using a constant lethargy weighting function. Effective capture and fission cross sections obtained using the



GRANIT<sup>10</sup> and EGGNIT<sup>11</sup> codes were substituted into this set to account for spectral effects. All of the calculations reported in this study were performed for room temperature. Neutron balance calculations were performed using the ANISN<sup>12</sup> code in P<sub>3</sub>, S<sub>8</sub> approximation in spherical geometry with the 14 MeV neutron source distributed uniformly in the top energy group (1.5 - 14.92 MeV).

### Sensitivity Studies

#### ENDF/B <sup>238</sup>U Data

The ENDF/B-III description of <sup>238</sup>U, MAT-1158, used evaporation formula models to describe single distribution functions for the energy of secondary neutrons from (n,2n), (n,3n) and (n,n' $\gamma$ ) reactions. These distributions have been reevaluated to significantly increase the kinetic-energy of the outgoing neutrons, relative to the available energy, and are now similar to the descriptions on ENDL.<sup>5</sup> The cross sections and resultant average neutron energies for MAT-1158 and the BNW modification are compared on Table II for 14.07 MeV incident energy. The n,n' cross section was also reduced in magnitude and the difference added to the elastic cross section.

Table II. Description of Secondary Neutrons from U-238 for an Incident Neutron of 14.07 MeV Energy

Reaction	Cross Section (b)		Average Secondary Neutron Energy (MeV)	
	MAT-1158	BNW	MAT-1158	BNW
(N,2N) E <sub>1</sub>			1.03	1.50
E <sub>2</sub>			1.03	4.70
Total	0.824	0.824	2.06	6.20
(N,3N) E <sub>1</sub>			0.61	0.50
E <sub>2</sub>			0.61	0.50
E <sub>3</sub>			0.61	1.16
Total	0.505	0.505	1.83	2.16
N,N' Cont	0.325	0.0066	1.55	1.55
E <sub>1</sub>		0.045		12.58
E <sub>2</sub>		0.0525		11.57
E <sub>3</sub>		0.0525		10.57
E <sub>4</sub>		0.035		9.57
Total		0.1916		

The results of neutron balance calculations using the BNW modified <sup>238</sup>U data compared with the reference case are summarized on Table III for the important blanket parameters

Table III. Calculated Reactions per 14 MeV Source Neutrons

	ENDF/B-III	BNW Mod.	<sup>238</sup> U
Converter Thickness (cm)	8.5	8.5	12.0
Tritium Produced	1.040	1.065	1.053
Total Fissions	0.208	0.229	0.298
<sup>238</sup> U Captures	0.440	0.443	(Lost)
Graphite Thermal Flux	2.93	3.03	2.87

The differences in the integral quantities due to the <sup>238</sup>U data alone do not, in themselves, seem very large for the 8.5 cm thick converter. However, the calculations with a 12 cm thick converter show that the converter size can be significantly increased with this data set while still breeding tritium and decreasing the graphite thermal flux by only 2% relative to the ENDF/B-III 8.5 cm thick converter.

#### Mirror Neutron Source Spectrum

In order to evaluate the DT neutron source spectrum of the mirror fusion reactor, a computer program was written to make an essentially exact calculation of the neutron emission spectrum from tabulated ion-energy distributions as well as from Maxwellian distributions. Barr, et al<sup>8</sup> have reported a calculated ion-energy distribution for a mirror device in which the average injection energy was 100 keV. The calculated ion-energy distribution closely resembles a 100 keV Maxwellian. Our calculations using this ion-energy distribution yielded a neutron-energy distribution not greatly different from that of a 100 keV Maxwellian ion-energy distribution except for truncation of the wings of the distribution. The calculated neutron-energy distribution was centered at 14.2 MeV with a FWHM of 1.70 MeV with a significant contribution of neutrons above 15 MeV energy. Since the uranium files on ENDF/B-III terminated at 15 MeV we were forced to change to ENDF/B-IV cross sections in order to make calculations using this neutron source spectrum.

#### Sensitivity Studies Using ENDF/B-IV

In the remainder of the studies, all of the nuclear data were derived from ENDF/B-IV. The ENDF/B-IV <sup>238</sup>U, MAT-1262, descriptions for the secondary neutron energy distributions from (n,2n) and (n,3n) reactions were not changed from ENDF/B-III. Thus, these files were modified to contain the descriptions of our present evaluation. The ENDF/B-IV (n,n' $\gamma$ ) secondary neutron distributions were changed from ENDF/B-III. Since they are now similar to our evaluation they were not changed.

The energy group structure used in our calculations was modified to 30 groups, extended to 18.22 MeV, and given a finer mesh over the broad mirror neutron spectrum. Most of this source spectrum is now contained in 4 groups from 12.21- to 15.88 MeV. For mirror spectrum calculations, the neutron source was distributed in 6 energy groups in the ANISN calculations according to the fraction of the total source spectrum in each energy group.

**Weighting Functions.** Reference calculations were carried out using group cross sections derived using the calculated mirror neutron spectrum joined to a constant lethargy spectrum below 12 MeV. In order to study the effect of the broad spectrum mirror neutron-source, an alternate set of group cross sections was obtained for <sup>238</sup>U only in which the broad source spectrum was replaced by a 20 keV "line" source. As a further perturbation another <sup>238</sup>U group cross section set was calculated using the "line" source with a constant-flux weighting spectrum below the source. All of the line source calculations were made with all of the source neutrons in a single energy group (13.50-14.19 MeV) in ANISN.

**Results of ENDF/B-IV Calculations.** The results of the sensitivity studies described above are summarized in Table IV for the 8.5 cm thick converter.

Table IV. Calculated Reactions per 14 MeV Source Neutron Using ENDF/B-IV Data.<sup>a)</sup>

	Line Source <sup>b)</sup>		
	Mirror Source	Const $\phi(u)$	Const $\phi(E)$
Tritium Prod.	1.107	1.097	1.102
Total Fissions	0.236	0.233	0.235
<sup>238</sup> U captures	0.456	0.451	0.451
Graphite Flux	3.25	3.20	3.24

a) <sup>238</sup>U modified from ENDF/B-IV.

b) <sup>238</sup>U only weighting changed.



**Converter Thickness.** Calculations were also made for a 12 cm thick converter for the mirror source and for the line source with constant lethargy flux weighting. The relative differences in the calculated blanket parameters were only one percent or less.

**Comparison with Other Calculations.** Lee<sup>9</sup> has reported neutronic calculations for a natural uranium dioxide mirror hybrid blanket similar to the one studied here. The major differences in the two converters are that Lee's converter region contains lithium (Li/U = 0.39), different structural materials (Fe, Ni, Nb) at relatively lower concentrations (S/U = 0.43 vs S/U = 0.77), no voids (helium), and slightly more <sup>235</sup>U. In Table V the results of Lee's calculation (Table III of Ref. 9) are compared with the results of the mirror spectrum calculations of this study. The results are tabulated in reference to the equivalent <sup>238</sup>U atoms-b<sup>-1</sup> thickness of the converter.

Table V. Comparison of Two UO<sub>2</sub> Hybrid Blankets in Reactions per Source Neutron

Converter Thickness (at-b <sup>-1</sup> <sup>238</sup> U)	Lab	Tritium Produced	Total Fissions	<sup>238</sup> U Captures
0.154	BNW	1.09	0.305	0.69
0.154	Lee <sup>9</sup>	1.36	0.309	0.50
0.257	BNW	0.92	0.417	1.21
0.308	Lee <sup>9</sup>	1.00	0.484	1.20

Comparison of the two 0.154 at-b<sup>-1</sup> <sup>238</sup>U thickness blankets indicates that there are no great differences brought about by <sup>238</sup>U data or calculational techniques. The blanket model of Lee breeds tritium better because of <sup>7</sup>Li(n,n'T) $\alpha$  reactions in the converter region essentially at the expense of <sup>238</sup>U captures. The BNW blanket performance is worse than that calculated by Lee for the thicker blankets. This may be due to greater amounts of structural material and less <sup>235</sup>U in the BNW blanket design.

#### Summary and Conclusions

The sensitivity studies of this paper clearly indicate that this type of blanket is more sensitive to the description in the data files of the energies of secondary neutrons than to broadening of the neutron source spectrum. The cumulative uncertainty in the calculated integral parameters due to neutron source spectrum description and weighting functions used to derive multigroup data appears to be less than that due to the uncertainty in the proper description of these secondary neutron energy distri-

butions. The broad neutron-energy spectrum typical of the mirror fusion reactor appears not to have much impact on the important parameters of the system studied here. This conclusion, however, might not be valid if the descriptions of (n,2n) and (n,3n) reaction shapes near 14 MeV given in these data files are not good estimates. The broad spectrum certainly is expected to impact on other features of fusion reactor blankets not considered in the present study.

#### Acknowledgment

This paper is based on work performed under USAEC Contract AT(45-1)-1830.

#### References

1. W. C. Wolkenhauer, B. R. Leonard, Jr., A. M. Sutey and R. W. Moir, Proc. First Topical Conf. on Fusion Technology, San Diego, CONF-740402-P1, 238 (1974).
2. B. R. Leonard, Jr. and W. C. Wolkenhauer, IAEA Fifth Conf. on Plasma Physics and Controlled Fusion Research, Tokyo, 1974, in Publication.
3. R. C. Haight and J. D. Lee, Proc. First Topical Conf. on Fusion Technology, San Diego, CONF-740402-P1, 271 (1974).
4. L. F. Hansen, J. D. Anderson, P. S. Brown, R. W. Howerton, J. L. Kammerdiener, C. M. Logan, E. F. Plecharty, and C. Wong, Nucl. Sci. Engr. 51, 278 (1971).
5. R. J. Howerton and M. H. MacGregor, USAEC Report UCRL-51427 (1973).
6. J. L. Kammerdiener, USAEC Report UCRL-51232 (1972).
7. D. W. Muir, Proc. First Topical Conf. on Fusion Technology, San Diego, CONF-740402-P2, 166 (1974).
8. W. L. Barr, R. J. Burleigh, W. L. Dexter, R. W. Moir and R. R. Smith, USAEC Report UCRL-74636 (1973).
9. J. D. Lee, Proc. First Topical Conf. on Fusion Technology, San Diego, CONF-740402-P1, 223 (1974).
10. C. L. Bennett, USAEC Report BNWL-1634 (1971).
11. C. R. Richey, USAEC Report BNWL-1203 (1967).
12. W. W. Engle, Jr., USAEC Report K-1693 (1967).

Should magnetic confinement of hot plasma prove satisfactory at high beta ( $\beta \approx 0.2$ ), nuclear fusion fuels other than DT will be important in future fusion reactors. The prospect of the advanced fusion fuels DD and  ${}^6\text{LiD}$  in such fusion reactors appears very promising provided the system is large, well reflected and has a sufficiently high density and temperature (high beta). Steady state burning of DD can ensue in a 60 kG field, 5m radius reactor for  $\beta \gtrsim 0.1$  and wall reflectivity  $R_w = 0.9$ . The first generation thermonuclear reactions between D and D or  ${}^6\text{Li}$  produce the very active, energy-rich fuels t and  ${}^3\text{He}$  which exhibit a high burnup probability in very hot plasmas. Steady state burning of  ${}^6\text{LiD}$  has also been demonstrated theoretically for low concentrations of  ${}^6\text{Li}$ ; however, important features of the  ${}^6\text{LiD}$  system still need to be incorporated in the calculation. In particular, there is a need for new and improved nuclear cross section data on over 80 reaction possibilities.

(Advanced-Fuels; Fusion-Dynamics; DD;  ${}^6\text{Li}$ ; Reactivity-Coefficients; I-Layer)

Recent studies of the advanced fusion fuels DD and  ${}^6\text{LiD}$ <sup>1-3</sup> indicate that under certain conditions these fuels could prove superior to the DT fueled system. The conditions include: 1). stable, high- $\beta$  plasmas such as the I-layer nuclear dynamo ( $\beta = \Sigma \mu n k T / p^2 \gtrsim 0.2$ ); 2). large, dense and well reflected systems to reduce the synchrotron radiation losses; 3). some mechanism for feeding cold fuel deep into the plasma interior; and 4). particle loss processes significantly greater than classical diffusion permits. Other scientists are beginning to recognize the importance of the high- $\beta$  I-layer;<sup>2,4</sup> "Potentially even more fruitful in actual fusion reactors could be schemes in which the necessary ring currents are carried by very high energy ions."<sup>5</sup> The present paper lists the advantages which accrue to the advanced fuel systems and details the reactivity of such high- $\beta$  plasmas.

Some of the important advantages of the advanced fuels are: 1). there would be no dependence on a tritium breeding blanket or on neutron economy; 2). there would be cheap initial (and continuing) fueling costs (initial tritium fueling costs for DT reactors are about 75M\$ for a 10 kg T inventory); 3). significantly lower equilibrium concentration of tritium will be present in the plasma (e.g., 2% vs 50%); 4). reduced environmental hazards due to tritium leaks will apply because of the grossly reduced T inventory; 5). the fast neutron (14 MeV) flux is reduced by a factor of more than two; 6). a wider latitude is permitted in the choice of structural materials from the standpoint of fast neutron damage and induced radioactive after-heat; 7). a sodium based heat exchanger instead of a lithium blanket will increase the energy release on neutron capture by  $12.6/4.8 = 2.6$ ; 8). no chemical combustion hazard exists if the heat exchanger is based on chemically fixed sodium (e.g.,  $\text{Na}_2\text{CO}_3$  or NaOH in water); 9). there is a high burnup of tritium ( $\sim 80\%$ ) in steady state, high- $\beta$  plasma systems; 10). catalyzed DD or  ${}^6\text{LiD}$  burning of unburned tritium will further reduce the total tritium inventory; 11). increased energy release in charged particles improves the burn properties; and 12). all the neutrons are "free" and can be used for breeding  ${}^{235}\text{U}$  or  ${}^{239}\text{Pu}$  fuel for fission reactors (with increased energy amplification) or for other applications.

The present plasma reactivity code is an extension of that developed by Etzweiler, Clarke and Fowler<sup>6</sup> and now includes 15 reactions of a possible 80 reactions.<sup>7</sup> The reactions presently included in the code are  $d(t,n)\alpha + 17.6$  MeV,  $d(d,n){}^3\text{He} + 3.3$  MeV,  $d(d,p)t + 4.0$  MeV,

$t(t,2n)\alpha + 11.3$  MeV,  $d({}^3\text{He},p)\alpha + 18.4$  MeV,  $t({}^3\text{He},d)\alpha + 14.3$  MeV,  $t({}^3\text{He},n){}^5\text{Li} \rightarrow p + \alpha + 12.1$  MeV,  $t({}^3\text{He},p){}^5\text{He} \rightarrow n + \alpha + 12.1$  MeV,  ${}^6\text{Li}(p,{}^3\text{He})\alpha + 4.0$  MeV,  ${}^6\text{Li}(d,p){}^7\text{Li} + 5.0$  MeV,  ${}^6\text{Li}(d,p)t + \alpha + 2.6$  MeV,  ${}^6\text{Li}(d,n){}^7\text{Be} + 3.4$  MeV,  ${}^6\text{Li}(d,n){}^3\text{He} + \alpha + 1.8$  MeV,  ${}^6\text{Li}(d,\alpha)\alpha + 22.4$  MeV and the endothermic reaction  $t(p,n){}^3\text{He} - 0.8$  MeV which is evaluated in terms of the slowing down rates for energetic protons from  $d(d,p)t$  and  $d({}^3\text{He},p)\alpha$  reactions.<sup>1</sup> The  ${}^6\text{Li}(p_{\text{fast}}, {}^3\text{He})\alpha + 4.0$  MeV reaction is also treated as a beam-plasma type process as the energetic protons slow down in the fuel mix. Averaged  $\sigma v$  values are taken from Greene<sup>8</sup> or calculated from the literature as in the case of  ${}^6\text{Li}(p,{}^3\text{He})\alpha$ . Fig. 1 shows the temperature variation of  $\langle \sigma v \rangle Q_+$  summed over all channels,

where  $Q_+$  is the energy release in charged particles. At temperatures above 100 keV the advanced fuels become very competitive with the exotic fuels DT and D-He.

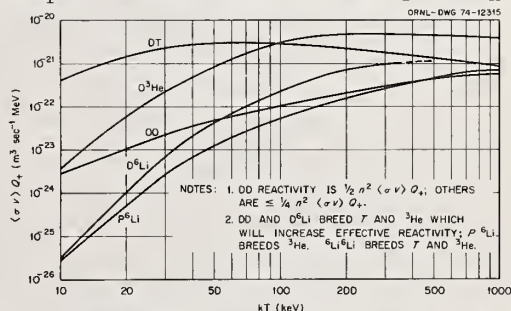


Fig. 1 Temperature dependence of reactivity parameters,  $\langle \sigma v \rangle Q_+$ , for all exothermic reaction channels. See notes for additional factors involved in evaluating reactivity of different fuels.

The particle and energy balance equations are described elsewhere<sup>1</sup> but include radiation dominated plasmas in closed (pulsed) systems and radiation damped plasmas in systems having particle losses and source feed terms. Both bremsstrahlung and synchrotron radiation terms are relativistically corrected. Except for the few beam-plasma reactions included the plasma is taken to have Maxwellianized electron and ion temperatures established by a dynamic equilibrium between the ions and the electrons resulting from the power input from the nuclear reactions, from the power



loss by radiation and particle escape and from the power loss to incoming cold-fuel feed. Synchrotron radiation is partially reduced by absorption in the plasma in large, dense and well reflected systems ( $R_\mu = 0.9$ ) and is found to be tolerable especially with "primed" fuels, i.e., fuels having a nearly equilibrium abundance of the active t and  $^3\text{He}$  such that the production rates of these energy-rich fuels are approximately equal to their burnup rates.

Fig. 2 illustrates schematically the burning characteristics of a DT fueled system. If a brute force ignition mode is used, such as injection in tokamaks, the plasma will ignite at about 6 keV and undergo a thermal runaway to the operating or burning temperature which may exceed 200 keV ( $\sim 2 \times 10^9 \text{K}$ ) at which point the charged particle nuclear power production equals the radiation (and particle power) losses. The burning temperature is then a stable operating temperature if the particle densities remain constant; however, in a closed, pulsed system the ashes eventually build up and the system gradually quenches due to the increased radiation losses as calculated for a pulsed DD system shown in Fig. 3 for which the burn time extends for about 200 sec.

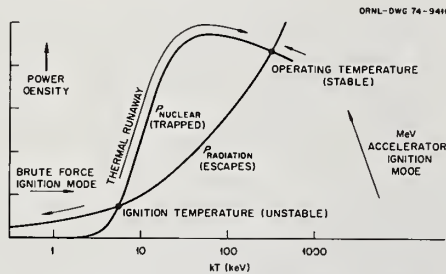


Fig. 2 Illustration of the thermal runaway of a radiation-dominated DT reactor above its ignition temperature of about 6 keV. Operating temperature is a "stable" operating point in terms of its negative temperature coefficient (but see text on positive density coefficient). Accelerator ignition mode discussed in Ref. 2.

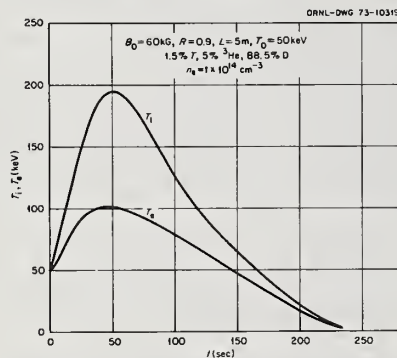


Fig. 3 Burn characteristics of a radiation dominated, pulsed burn, closed DD reactor.

Three new features have been recently introduced into the evaluations; namely, 1). the inclusion of an approximate nuclear elastic scattering energy flow correction, 2). the incorporation of a magnetic field correction to the Coulomb logarithm which reduces the electronic stopping power on the fast ions and, 3). the addition of catalyzed burning of t and  $^3\text{He}$  (feed

of cold t and  $^3\text{He}$  equal to their loss rates).

Figs. 4 and 5 illustrate the energy loss rate in a  $10^{20} \text{m}^{-3}$  density deuterium plasma due to the nuclear elastic collisions of different fast ions with deuterons.<sup>9</sup> Arbitrarily taking all nuclear elastic collision energy loss rates to be continuous rather than discrete functions one has  $dW/dt \approx -0.13 \times 10^{-20} W_1 n_2$ .

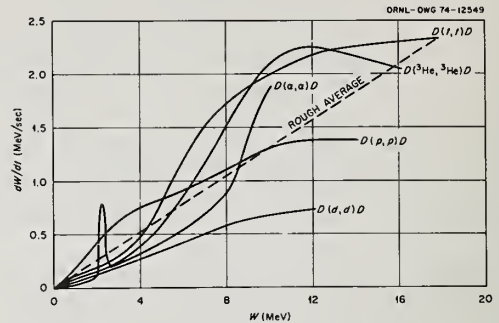


Fig. 4 Nuclear elastic collisional energy loss rate vs fast particle energy (after Devaney and Stein<sup>9</sup>). Deuteron density  $n_D = 10^{20} \text{m}^{-3}$ .

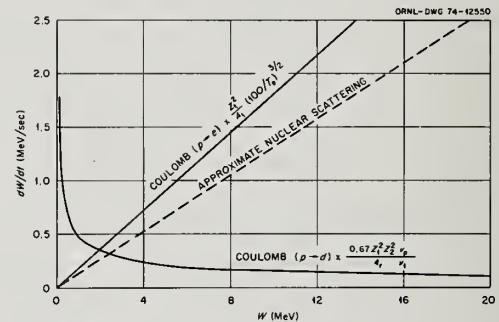


Fig. 5 Energy loss rates of fast particles due to nuclear elastic collisions with ions and due to Coulomb collisions with ions and electrons. An average curve is used for nuclear elastic collisions to give simple analytic expression for  $f_e$  (see text).

Plasma density:  $n_D = n_e = 10^{20} \text{m}^{-3}$

This gives for the energy flow from fast reaction products to plasma ions and electrons (see Ref. 10):

$$\frac{dW}{dt} = -\frac{2.5 W_1 Z_1^2}{\tau_s A_1} [1 + \gamma] - 0.13 \times 10^{-20} W_1 n_2$$

where  $W_1$  is the fast ion energy in keV,  $n_2$  is the total density of all plasma ions in  $\text{m}^{-3}$ ,  $Z_1$  and  $A_1$  are the charge and atomic number of the test ion. Following Rose,<sup>10</sup> one obtains for the fraction of the fast ion energy delivered to the plasma electrons,

$$f_e = \frac{\ln A_1 e}{30(1+NS)} \int_0^{\infty} \frac{1+NS+\gamma}{\gamma} \left[ \frac{(1+NS+\gamma)e^{-x} - \gamma}{1+NS} \right]^{2/3} dx$$



where

$$\tau_s = 1.25 \times 10^{18} \left( \frac{20}{\ln \Lambda_{1e}} \right) \frac{T_e^{3/2}}{n_e}$$

$$NS = 5.2 \times 10^{-22} \tau_s n_2 A_1 / Z_1^2$$

$$\gamma = \frac{57}{n_e} \sum_2 \frac{Z_2^2 n_2}{A_2} \frac{\ln \Lambda_{1i}}{\ln \Lambda_{1e}} \left( \frac{T_e A_1}{W_{10}} \right)^{3/2} \frac{A_1 + \bar{A}_2}{A_1} \frac{10}{6.5}$$

where  $\bar{A}_2$  is the average atomic mass number of the field ions and  $10(A_1 + \bar{A}_2)/6.5 A_1$  represents a slight reduced mass correction to Rose's  $\gamma$ .<sup>10</sup> The Coulomb logarithms are of the form  $\ln \Lambda = \ln (\lambda_D m v_t^2 2\alpha c / Ze^2 v_t)$ , where

$\lambda_D$ , the Debye length, is  $2.3 \times 10^4 \sqrt{T(\text{keV})/n(\text{cm}^{-3})}$ ,  $v_t$  is the velocity of the test particle, and  $\alpha = 1/137$ .

The effect of the magnetic field on the Coulomb logarithm<sup>11</sup> has been included by using  $v_t/\sqrt{2}\omega_{ce}$  (where  $\omega_{ce} = eB/mc$  = electron gyro-frequency) when it is less than  $\lambda_D$ . This reduction in the Coulomb logarithm results from long range binary collisions between fast ions and electrons because the electrons execute an  $E \times B$  drift about the test ion trajectory rather than a "free-fall" towards the test ion. The effect is more important for test ions than for test electrons ( $v_e \gg v_t$ ) and leads to a larger disparity between ion and electron temperatures. Fig. 6 shows the effects of including both nuclear elastic scattering corrections and Coulomb logarithm corrections in a magnetic field on a pulsed DD reactor "primed" with some initial  $t$  and  $^3\text{He}$  approximately equal to their concentrations during the burn period. The ignition temperature is taken as 50 keV. The peak ion temperature is about 80 keV higher when both nuclear elastic and  $\ln \Lambda(B)$  corrections are included.

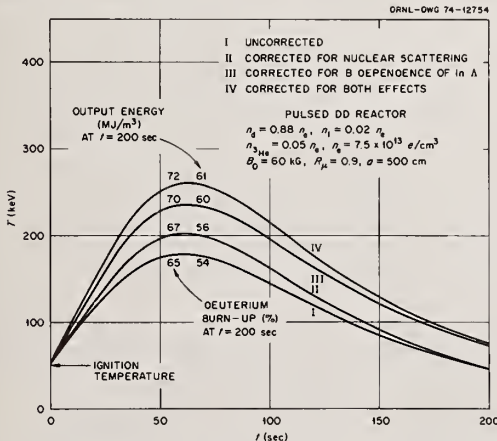


Fig. 6 Effects of nuclear elastic collisions and magnetic field corrected Coulomb logarithm on reactivity of a pulsed DD fusion reactor.

Figs. 7 and 8 illustrate the variation in the peak ion and electron temperatures as a function of the density of radiation-dominated, pulsed DD or  $D^6\text{Li}$  plasmas. Also given are the burn time to reach the peak ion temperature as well as the associated  $\beta (= \Sigma 8\pi n_k T / B^2)$ , the radiation power ( $P_{\text{RAD}}$ ), and the power in neutrons and blanket energy release ( $P_{\text{NAB}}$ ).

The important feature of Figs. 7 and 8 is that they reveal a positive density coefficient for a fusion

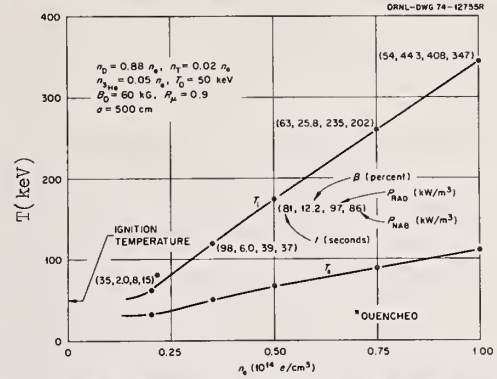


Fig. 7

Peak temperatures and other parameters as a function of the density of radiation-dominated, pulsed, closed DD fusion reactors ignited at 50 keV.  $R_\mu$  = wall reflectivity in infrared and microwave region,  $a$  = plasma radius.

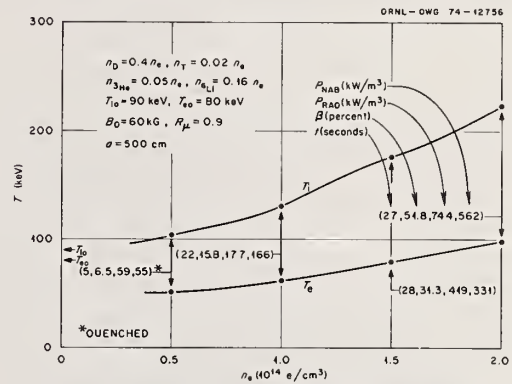


Fig. 8

Peak temperatures and other parameters as a function of the density of radiation-dominated, pulsed, closed  $D^6\text{Li}$  fusion reactors ignited at about 90 keV.

reacting plasma, i.e., any increase of density increases the net reactivity (the reaction power input goes as  $n^2$  whereas the synchrotron radiation losses vary only as  $n^{1/2}$ ). Thus, a fuel leak into such a system can lead to a nuclear excursion if cold fuel feed is realizable - this must then be compensated for by a positive feedback loop probably tied to the magnetic field since particle diffusion losses should increase with reduced magnetic confining field. Impurity feed such as ordinary hydrogen feed could also be used to control the plasma reactivity.

Note that at low densities which give beta's in the tokamak range ( $\leq 0.10$ ) these pulsed reactors will quench or just barely ignite. At high densities, and hence higher beta's the "primed" reactors ignite and burn very well. Both DD and  $D^6\text{Li}$  plasmas generate interesting power levels for pulsed mode operation at high beta's ( $\geq 0.20$ ). These high  $\beta$  values would necessitate a closed magnetic mirror configuration such as the proton E-layer<sup>12</sup> or the I-layer,<sup>2,4</sup> and possibly the ELMO Bumpy Torus,<sup>13</sup> all of which permit high average beta's. In the ion layers the magnetic mirror is closed by the self magnetic field produced by a transparent proton or ion ring-current perpendicular to the applied magnetic field.<sup>2,5,12</sup>

The I-layer nuclear dynamo system should also permit axial fuel feed deep into the plasma along the

magnetic axis as well as provide a strong divertor action outside the region of the closed flux lines.<sup>4,14</sup> Divertor action is necessary in steady state reactors for the removal of any impurities as well as the ashes and some of the unburned plasma. It may also provide a partial separation of electrical charges leading to the prospects of some direct energy conversion or even thrust.<sup>4,14</sup>

Steady state operation of the advanced fuel fusion reactors is now considered. The actual particle loss processes in fusion reactors are not well understood and may be weak (pseudo-classical losses), strong (Bohm or trapped particle losses) or perhaps controllable (charge exchange losses). To evaluate whether a fusion reactor might operate, in principle, as a steady state system we have provided for cold D or <sup>6</sup>LiD fuel feed in such a way as to maintain the plasma electron density and the deuteron density constant without specifying the actual physical nature of the loss or feed mechanisms.

Catalyzed burning is also included by eliminating any net tritium or <sup>3</sup>He losses, i.e., the source feed rates of cold t and <sup>3</sup>He are set equal to their hot particle loss rates. The effect of including source and loss terms is illustrated in Fig. 9 for which the source and loss terms were introduced at t = 30 sec in such a way as to maintain n<sub>e</sub> and n<sub>d</sub> constant. The plasma shifted quickly to a lower-temperature, steady-state operation with T<sub>e</sub> ≈ 81 keV, T<sub>i</sub> ≈ 186 keV and the plasma β = 27%. The particle confinement (or replacement) time required to maintain this steady state is 22.2 seconds. It should be noted that the feed of cold fuel ions and associated electrons and the loss of hot plasma ions and electrons cools the plasma but it does not cool it below an ignition temperature. Thus, from Fig. 1 the operating (or burning) temperature remains above the ignition (or quench) temperature even with cold particle feed and losses and a steady state burn behavior is ensured. The particle confinement time of 22.2 seconds for the case illustrated in Fig. 9 is many orders of magnitude shorter than classical or pseudo-classical particle diffusion times; thus, a strong instability-driven loss mechanism or controlled charge exchange losses can not only be permitted but is essential to steady state operation. Whether an appropriate loss process may exist in such high β systems must await careful experimentation and theoretical analysis.

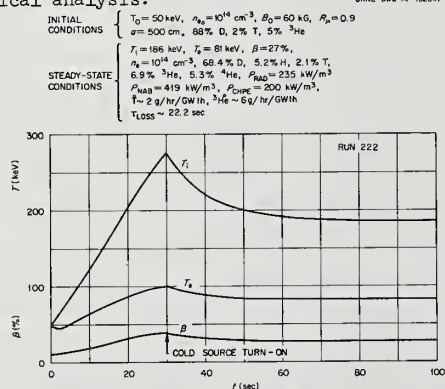


Fig. 9 Effect of turn-on of a source of cold D<sup>0</sup> feed and fixed losses 30 seconds after ignition of a DD fusion reactor. Source and losses are defined so as to maintain n<sub>e</sub> and n<sub>d</sub> constants. Catalyzed burning of T and <sup>3</sup>He ( $S_T = L_{nT}$ ;  $S_{\text{He}} = L_{n\text{He}}$ ;  $L = 1/\tau_{\text{LOSS}}$ ).

Note that in the steady-state, catalyzed DD reactor of Fig. 9 the equilibrium tritium concentration is only 2.1% whereas <sup>3</sup>He is at 6.9%. The power output in neutron energy release and blanket energy release (assumed only 4.8 MeV/n) is P<sub>RAD</sub> which with the radiation power output, P<sub>RAD</sub>, and NAB the leakage escape power in charged particles, P<sub>CHPE</sub> [= 1.5nk(T<sub>i</sub>+T<sub>e</sub>)/τ], gives 0.85 MW/m<sup>3</sup>, a quite respectable figure. Thus, a 5m radius spherical reactor of this type would then give P<sub>OUT</sub> ~ 400 MW (thermal) and a wall loading of P/A ~ 1.3 MW/m<sup>2</sup> at the plasma surface (5m) or ~ 0.7 MW/m<sup>2</sup> at 7m. Higher power production could be attained by increase of the plasma density (see Fig. 7).

The prospects of direct conversion of the charged particle escape power to electricity may be rather modest since it would involve only about 23% of the total energy release - the 77% fraction would require a thermal cycle. Thus, for 70% direct electrical conversion of the 23% for P<sub>CHPE</sub> the total thermal efficiency would be of order 23(0.70) + 77(0.35) ~ 43%.

Perturbation studies of the steady state, DD fueled reactor of Fig. 9 indicate that it has a negative temperature coefficient, which is very desirable; however, as mentioned earlier it does have a positive density coefficient which must be controlled by a positive feedback system involving power output sensors which control the magnetic field (or the feed of impurity atoms). It should be emphasized that the startup of any fusion reactor will necessitate very careful controls on the reactivity level since the walls may well be loaded with excess D and some T. Any thermal excursion of the plasma would lead to a thermal loading of the walls with a concomitant increase in gas release which may enhance the thermal runaway.

The prospects for steady state operation of D<sup>6</sup>Li fusion reactors are beginning to emerge at the present time and steady state D<sup>6</sup>Li reactors containing up to at least 21% <sup>6</sup>Li appear feasible (see Table I). The further improvement of the reactivity codes and the inclusion of many more reaction combinations may well reveal the operation of steady-state D<sup>6</sup>Li fueled plasmas having even higher concentration of <sup>6</sup>Li. It should be noted that stripped ions of <sup>6</sup>Li should have a high affinity for charge exchange with any H<sup>0</sup>, D<sup>0</sup> or T<sup>0</sup> atoms which enter the plasma and hence the <sup>6</sup>Li<sup>3+</sup> would help purge the plasma of the bound electrons since the Li<sup>2+</sup> so formed would be rapidly ionized.<sup>15</sup> There is an urgent need for the evaluation and accurate (~15%) measurement of the nuclear reaction cross sections for the many charged particle nuclear reactions involving <sup>6</sup>Li (and <sup>7</sup>Li and <sup>7</sup>Be) (see Price<sup>7</sup>). The production of a large I-layer type plasma will probably require a major development program on multi-MeV accelerators with steady state current outputs in excess of 10 mA (see Ref. 2).

I am greatly indebted to R. D. Sharp of the Computer Sciences Division at ORNL for many improvements to the Etzweiler, Clarke and Fowler code.



Table I. Plasma Parameters of Two Possible Steady-State, Advanced Fuel, Catalyzed Fusion Reactors\* ( $B = 60$  kG,  $a = 500$  cm,  $R_p = 0.90$ )

Parameter	$\frac{DD}{D^6Li}$	$\frac{D^6Li}{D^6Li}$
$n_e$	$1.0 \times 10^{14} \text{ e/cm}^3$	$2.0 \times 10^{14} \text{ e/cm}^3$
$T_i$	186 keV	150 keV
$T_e$	81 keV	75 keV
$\beta$	27%	40%
$n_p/n_e$	5.2%	4.2%
$n_d/n_e$	68.4%	44.0%
$n_t/n_e$	2.1%	1.4%
$n_{^3He}/n_e$	6.9%	5.6%
$n_\alpha/n_e$	5.3%	5.1%
$n_{^6Li}/n_e$	---	9.3%
$n_{^7Li}/n_e$	---	0.4%
$n_{^7Be}/n_e$	---	0.1%
$P_{RAD}$	$235 \text{ kW/m}^3$	$514 \text{ kW/m}^3$
$P_{NAB}^{**}$	$419 \text{ kW/m}^3$	$765 \text{ kW/m}^3$
$P_{CHPE}$	$200 \text{ kW/m}^3$	$190 \text{ kW/m}^3$
$\tau$ (Conf. Time)	22.2 sec	18.9 sec
D thrupt	48 gms/hr/GWth	47 gms/hr/GWth
T thrupt	1.8 gm/hr/GWth	1.8 gm/hr/GWth
$^3He$ thrupt	6.0 gm/hr/GWth	7.2 gm/hr/GWth
14 MeV n rate	$1.1 \times 10^{20} \text{ n/s/GWth}$	$1.2 \times 10^{20} \text{ n/s/GWth}$
Total n rate	$2.5 \times 10^{20} \text{ n/s/GWth}$	$2.6 \times 10^{20} \text{ n/s/GWth}$

\* Presumes cold fuel feed and fixed losses to maintain  $n_e$  and  $n_d$  constant.

\*\* Assumes average 4.8 MeV/n energy release on neutron capture in blanket.

\*\*\* 1 gm tritium  $\sim 10^4$  Curies. Maximum permissible losses to atmosphere  $\sim 10$  Curies/day.

## References

- 1) J. Rand McNally, Jr., "Reactivity of Advanced Fusion Fuels," USAEC Report ORNL-TM-4647 (1974).
- 2) J. Rand McNally, Jr., "Fusion Chain Reactor Prospects and Problems," USAEC Report ORNL-TM-4575 (1974).
- 3) J. Rand McNally, Jr., "Advanced Fuels for Nuclear Fusion Reactors," Third Conference on Application of Small Accelerators, North Texas State University, Oct., 1974 (to be published).
- 4) J. Rand McNally, Jr., "Conjectures on Fusion Chain Reaction Cycles and the I-layer Configuration," USAEC Report ORNL-CF-64-8-9 (1964).
- 5) N. Rostoker and K. Moses, "The Application of High Current Relativistic Electron Beams in Controlled Thermonuclear Research," USAEC Report WASH-1286 (1974).
- 6) J. F. Etzweiler, J. F. Clarke, and R. H. Fowler, "Effect of Fuel Injection of a Cyclic  $\beta$ -limited Radiation Dominated Fusion Reactor," USAEC Report ORNL-TM-4083 (1974).
- 7) L. K. Price, "Nuclear Data Requests," USAEC letter to Fusion Technology Group, May 9, 1974.
- 8) S. L. Greene, Jr., "Maxwell Averaged Cross Sections for Some Thermonuclear Reactions on Light Isotopes," USAEC Report UCRL-70522 (1967).
- 9) J. J. Devaney and M. L. Stein, Nuclear Science and Engineering 46, 323 (1971).
- 10) D. J. Rose, Nuclear Fusion 9, 183 (1969).
- 11) J. Rand McNally, Jr., submitted to Nuclear Fusion.
- 12) Nicholas C. Christofilos, "Proton E-layer Astron for Producing Controlled Thermonuclear Reactions," U. S. Government Patent 3, 664, 921 (1972).
- 13) R. A. Dandl, H. O. Eason, A. C. England, G. E. Guest, C. L. Hedrick and J. C. Sprott, "The Elmo Bumpy Torus Experiment," USAEC Report ORNL-TM-3694 (1971).
- 14) J. Rand McNally, Jr., "Speculations on the Configurational Properties of a Fusing Plasma," Nuclear Fusion 12, 265 (1972).
- 15) J. Rand McNally, Jr., "Neutral Injection Heating of Tokamaks," USAEC Report ORNL-TM-4363 (1973).

\* Research sponsored by the U. S. Atomic Energy Commission under contract with the Union Carbide Corporation.

# A STUDY OF THE ${}^6\text{Li}(n,\alpha)\text{t}$ REACTION BETWEEN 2-10 MeV\*

C. Murray Bartle\*\*  
University of Wisconsin,  
Madison 53706, U.S.A.

Absolute  ${}^6\text{Li}(n,\alpha)\text{t}$  cross section measurements are reported between 2.16 and 9.66 MeV. The results agree with the Pendlebury evaluation. The possibility of unfolding angular distributions from the pulse-height distributions in  ${}^6\text{LiI}(\text{Eu})$  is investigated.

( ${}^6\text{Li}(n,\alpha)\text{t}$ ; 2-10 MeV; angular distribution)

## Introduction

A review of the  ${}^6\text{Li}(n,\alpha)\text{t}$  reaction below  $E_n = 1.7$  MeV was recently made by Uttley et al<sup>1</sup>. Above 1.7 MeV the total cross section has been evaluated by Pendlebury<sup>2</sup> and Uttley et al<sup>3</sup>. The reaction is employed as a primary standard for neutron flux measurement<sup>4</sup> and has important applications in the nuclear engineering field. These include the development of a  ${}^6\text{Li}$ -sandwich detector<sup>5</sup> to measure neutron spectra in fast-breeder reactors<sup>6,7</sup> and tritium breeding for the proposed D-T fusion reactors<sup>8</sup>. Therefore accurate cross sections for the reaction up to 14 MeV are needed.

At the present time there are serious discrepancies in previous data for neutron energies above 1 MeV. The recent evaluation of the total cross sections made by Uttley et al<sup>3</sup> is in very poor agreement with the earlier-obtained Pendlebury evaluation<sup>2</sup> which is the accepted data source<sup>9</sup>. Here, an attempt has been made to produce data of improved reliability through the utilization of the proven associated particle system developed at the University of Wisconsin<sup>10-13</sup>. A feature of this system is that the sources of experimental error are reduced through the inherent simplicity of the procedures involved. Strictly absolute neutron flux measurements are obtained through electronic techniques which involve counting the recoiling associated  ${}^3\text{He}$  ions within a carefully chosen experimental geometry. In this work the  ${}^6\text{Li}$  target is a  ${}^6\text{LiI}(\text{Eu})$  scintillator which has interesting response properties which yield information about the details of the  ${}^6\text{Li}(n,\alpha)\text{t}$  angular distributions.

## Total Cross Section Measurements

### Experimental Method

The experimental system, illustrated in fig.1 and discussed in detail elsewhere<sup>10</sup>, employs a  ${}^6\text{LiI}(\text{Eu})$  scintillator measuring 2.5cm in diameter and 1.3cm in depth#. This scintillator is positioned to encompass the electronically-collimated neutron beam following measurements of the beam profile<sup>14,15</sup>.

### Experimental Spectra

Typical spectra which show the broad  ${}^6\text{Li}(n,\alpha)\text{t}$  distribution are shown in fig.2. These events occur in time coincidence with the detected  ${}^3\text{He}$  ions. The timing resolution is typically 2ns. The timing constraint greatly reduces the observed experimental background, such as would arise, for example, from the

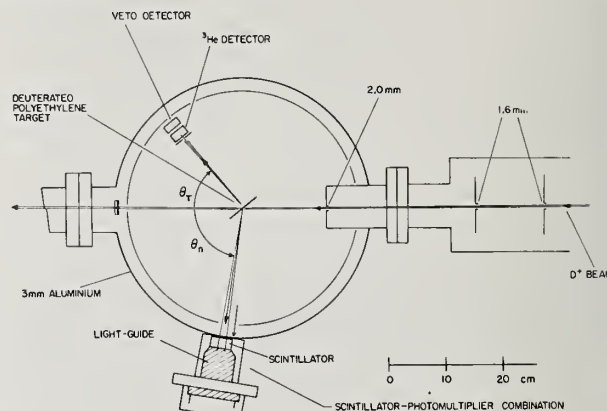


Fig.1. The experimental system. Typical experimental parameters are: beam current, 0.3μA; target thickness, 100μg/cm<sup>2</sup> and neutron flux, 100 /s.

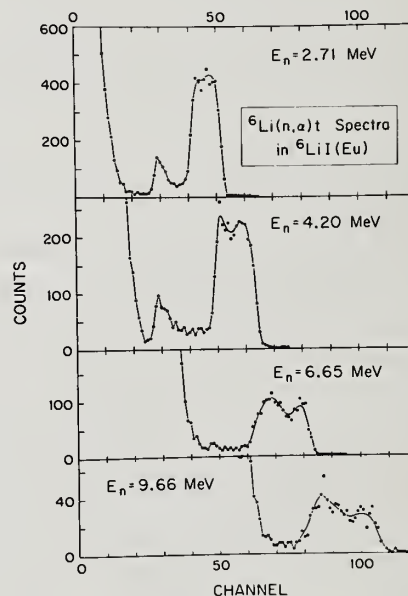


Fig.2. Typical spectra for monoenergetic neutrons incident on  ${}^6\text{LiI}(\text{Eu})$ .

\* Work supported in part by the U.S. Atomic Energy Commission.

\*\*AINSE Fellow - present address: School of Physical Sciences, ANU, A.C.T. 2600, Australia.

# Manufactured by Harshaw Chemical Co., Cleveland, Ohio.



reactions of thermal neutrons unavoidably present in the experimental environment. Reactions produced by energy degraded neutrons in the energy region where the cross section is large produce a low energy tail on the fast-neutron distribution. Slowing-down mechanisms include the  ${}^6\text{Li}(n,n){}^6\text{Li}$  and  ${}^6\text{Li}(n,\alpha)d$  reactions.

### Analysis

Cross sections for the reaction are calculated using a standard procedure<sup>10,15</sup>. In all 24 spectra were obtained in the energy range from 2.16 to 9.66 MeV in several running periods during which the neutron energies chosen were interwoven. A feature of the experiment is the individual independence of the calculated cross sections obtained. Small corrections arise from effects of neutron elastic and non-elastic processes occurring both outside and inside the scintillator which cause the neutron beam to be partially attenuated. A typical summary is given in table 1. Allowance is made for events contributed to the broad fast-neutron distribution by the appropriate proportion of the energy-degraded neutrons produced within the scintillator.

### Errors

The total cross section measurements are shown in fig.4. Of the typical uncertainty of  $\pm 3\%$  the component uncertainties are typically:  $\pm 2\%$  due to the effective beam attenuation correction (table 1);  $\pm 2\%$  due to the counting statistics;  $\pm 0.5\%$  in counting the  ${}^3\text{He}$  ions;  $\pm 0.5\%$  in the scintillator thickness and  $\pm 0.2\%$  in scintillator edge effects.

### Discussion

In fig.3, the measurements are compared with pertinent previous data. It is clear that the results of the present experiments strongly support the previous Pendlebury evaluation<sup>2</sup>. The measurements of Clements and Rickard<sup>16</sup> which are a basis for the recent evaluation by Uttley et al<sup>3</sup> do not agree with the present measurements. Apparently, the problem in the case of the measurements of ref:16 is primarily one of normalization. Since these measurements are normalized with the data of Coates et al<sup>17</sup> in the keV region, there are possibly undetermined uncertainties in this region. It would be informative, too, to investigate

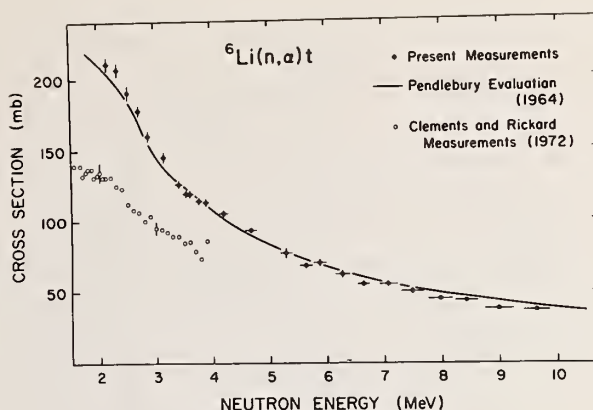


Fig.3. A comparison with earlier data. Horizontal error bars represent the energy spread of the incident neutrons. The present measurements are tabulated in Appendix 1.

the low energy tail exhibited by the fast-neutron  ${}^6\text{Li}(n,\alpha)t$  distributions from  ${}^6\text{LiI}(\text{Eu})$  with Monte Carlo methods. Such an analysis may affect the number of events attributed to the fast-neutron distribution although the adjustment should be small.

### Differential Cross Section Measurements

The difficulty in measuring  $(n,\alpha)$  differential cross sections is illustrated by the absence of data for the  ${}^6\text{Li}(n,\alpha)t$  reaction between 2.7 and 14 MeV<sup>18</sup>. Here, the possibility of unfolding angular distributions from  ${}^6\text{Li}(n,\alpha)t$  distributions in  ${}^6\text{LiI}(\text{Eu})$  is investigated.

### Resolution of the ${}^6\text{Li}(n,\alpha)t$ Distributions

As illustrated in the superimposed spectra in fig.4, the resolution of the  ${}^6\text{Li}(n,\alpha)t$  distribution for fast neutrons is much poorer than that for thermal

Table 1. Effective neutron beam attenuation

Source	4 MeV		8 MeV	
	correction (%)	error ( $\pm$ )	correction (%)	error ( $\pm$ )
Non-elastic events:				
outside scintillator	+1.1	0.6	+1.4	0.7
inside scintillator	+1.9	0.9	+1.5	0.8
Elastic events:				
inside scintillator				
(a) multiple scattering	-1.6	0.8	-1.6	0.8
(b) scattering on ${}^6\text{Li}$	+2.0	1.0	+2.0	1.0
outside scintillator	+1.7	0.2	+0.4	0.1
Net Correction	+5.1	1.7	+3.7	1.7

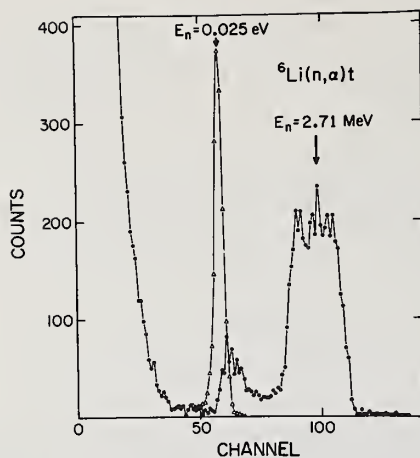


Fig. 4. Comparison of the  ${}^6\text{Li}(n,\alpha)t$  distributions produced by thermal and fast neutrons. The origin of the thermal neutrons is a Pu-Be source.

neutrons. This observation has been attributed by several groups<sup>19-21</sup> to the difference between the triton and  $\alpha$ -particle response in  ${}^6\text{LiI}(\text{Eu})$ . This is effective because, in the case of fast neutrons, large c.m. motion causes the emitted tritons and  $\alpha$ -particles to have a range of energies in the laboratory system. From reaction kinematics, the energy of each product particle is a linear function of the Cosine of the c.m. emission angle of the outgoing triton ( $\theta_{\text{cm}}$ ). Thus, if each product particle has a different linear response in  ${}^6\text{LiI}(\text{Eu})$  the total response from the simultaneous detection of both particles is in turn a linear of  $\text{Cos}(\theta_{\text{cm}})$ . Since the strength of this effect is proportional to the product of the particle and c.m. velocities the fast-neutron distributions are relatively broad as illustrated in fig. 4. Indeed, the eloquent observations made by Barschall and Kanner<sup>22</sup> and Barschall and Powell<sup>23</sup> in relation to the interpretation of recoil spectra in  ${}^4\text{He}$ -counters also apply to  ${}^6\text{Li}(n,\alpha)t$  distributions in  ${}^6\text{LiI}(\text{Eu})$ . With appropriate scaling the pulse-height distribution images the differential-cross-section curve plotted against  $\text{cos}\theta_{\text{cm}}$ .

#### Response Curves for ${}^6\text{LiI}(\text{Eu})$

Response curves are necessary to unfold the spectra. It is possible to derive these response curves by tracing the movement of the  ${}^6\text{Li}(n,\alpha)t$  distribution with neutron energy, assuming that kinematic broadening dominates the spectral width. These curves are based on the expected dominance of the response of the scintillator to the emitted triton<sup>21</sup>, particularly for forward emission. In fig. 5 the idealized line shapes corresponding to isotropic angular distributions clearly do not reproduce the experimental spectral shapes obtained. The unfolded angular distributions shown in fig. 6 exhibit a fluctuating behaviour.

#### Discussion

Preliminary results have been obtained. There are several interesting observations to be summarized here. First, for excitations of the  ${}^7\text{Li}$  system corresponding to  $E_n = 2.5$  and  $3.5$  MeV accentuated maxima and minima are observed. The agreement with the positions of the  $\frac{1}{2}^-$  and  $\frac{3}{2}^-$  states found previously<sup>24</sup> suggests a strong contribution through compound nucleus formation.

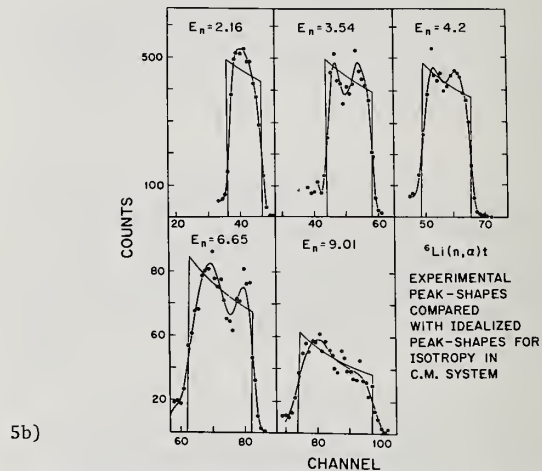
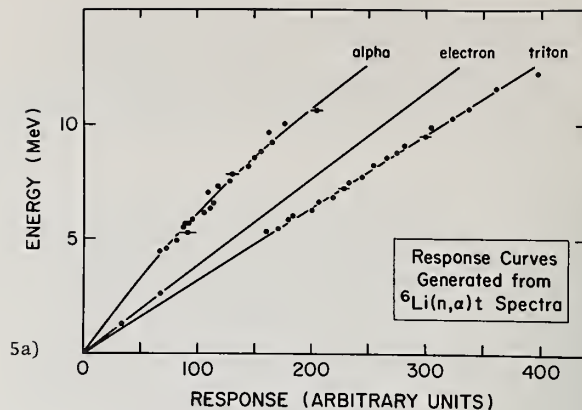


Fig. 5. Idealized spectrum shapes for isotropic triton distributions in c.m. (fig. 5b) are derived from response curves (fig. 5a) obtained from an analysis of the spectral-width of the experimental distributions

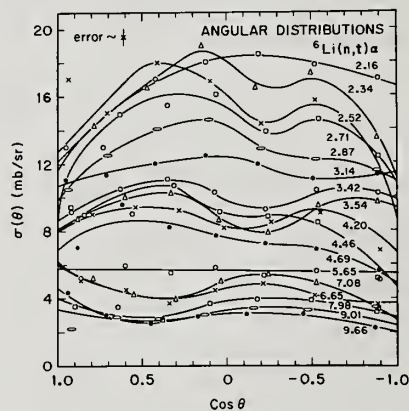


Fig. 6. Angular distributions for the emitted triton plotted in the c.m. system. Lines drawn through the points are a guide to the eye only. For clarity, other curves are not shown but are in similar agreement. The statistical error is indicated. Each point represents the average cross section over an increment of approximately 0.2 in  $\text{Cos}\theta$ .



At higher neutron energies a forward-peaked pattern is established in good agreement with the measurement of Valkovic et al.<sup>25</sup> at 14.4 MeV. Generally, the curves are in good agreement with the corresponding  ${}^6\text{Li}(p, {}^3\text{He})\alpha$  distributions<sup>26,27</sup> where the higher-energy data is described well by direct-mechanism codes<sup>27</sup>. There is a suggestion in fig.6 that there is a transition from the dominance of a compound-nucleus mechanism to a direct mechanism in the region of  $E_n = 5.65$  MeV. The study of the  ${}^6\text{Li}(n, \alpha)t$  angular distributions is continuing.

### Conclusions

A feature of the present experiment is the individual independence of the measurements which generate the  ${}^6\text{Li}(n, \alpha)t$  excitation function. Only small deviations from the predictions of the Pendlebury evaluation are found in this work. Thus, the recent evaluation of Uttley et al. which is normalized quite differently appears to be in error.

The broadening of the  ${}^6\text{Li}(n, \alpha)t$  distributions in  ${}^6\text{LiI}(\text{Eu})$  is due to a sensitivity to the reaction kinematics obtained through the differing response curves for the product particles. Angular distributions have been unfolded with apparently good reliability and provide new insight into the reaction mechanism.

### Acknowledgement

The author is indebted to Professor P.A. Quin and Dr D.T.L. Jones for their assistance during the experimental phases of this work.

### References

1. C.A. Uttley, M.G. Sowerby, B.H. Patrick and E.R. Rae, Neutron Standards and Flux Normalization (Argonne, 1971) p.80.
2. E.D. Pendlebury, AWRE 0-60/64 (1964).
3. C.A. Uttley, M.G. Sowerby and R. North, AERE-PR/NP 19 (1972).
4. D.J. Deruytter, Nuclear Data for Reactors (Helsinki, 1970) p.129.
5. I.C. Rickard, Nucl.Instr. 105 (1972) 397.
6. M.E. Lee and M.L. Awcock, Neutron Dosimetry I (Vienna, 1963) p.441.
7. S.K.I. Patterson and M.J. Stevenson, Proc. CEGB Conf.on Radiation Measurements in Nuclear Power (1966).
8. Wisconsin Tokamak Reactor Design, Univ.of Wisc., UWFD-68.
9. J.R. Stehn, NNCSC, BNL, private communication.
10. C.M. Bartle and P.A. Quin, Nucl.Instr. 121 (1974) 119.
11. C.M. Bartle and P.A. Quin, Nucl.Phys. A216 (1973) 90.
12. C.M. Bartle, Nucl.Instr. 117 (1974) 569.
13. C.M. Bartle, Nucl.Instr. in press.

14. C.M. Bartle, N.G. Chapman and P.B. Johnson, Nucl.Instr. 95 (1971) 221.
15. C.M. Bartle, P.B. Johnson and N.G. Chapman, Nucl.Phys. A220 (1974) 395.
16. P.J. Clements and I.C. Rickard, AERE-R 7075.
17. M.S. Coates, J. Hunt and C.A. Uttley, AERE-PR/NP 18 (1970/71).
18. USAEC Report BNL-400, 3rd edition.
19. B.D. Kern and W.E. Kreger, Phys.Rev., 112 (1958) 926.
20. R.B. Murray, Nucl.Instr. 2 (1958) 237.
21. T.R. Ophel, Nucl.Instr. 3 (1958) 45.
22. H.H. Barschall and M.H. Kanner, Phys.Rev., 58 (1940) 590.
23. H.H. Barschall and J.L. Powell, Phys.Rev., 96 (1954) 713.
24. F. Ajzenberg-selove and T. Lauritsen, Nucl.Phys. A227 (1974) 55.
25. V. Valkovic, I. Slaus, P. Tomas and M. Cerineo, Nucl.Phys. A98 (1967) 305.
26. J.M.F. Jeronymo, G.S. Mani and A. Sadeghi, Nucl. Phys. 43 (1963) 424.
27. M.F. Werby, M.B. Greenfield, K.W. Kemper, D.L. McShan and S. Edwards, Phys.Rev. C8 (1973) 106.

### APPENDIX

The  ${}^6\text{Li}(n, \alpha)t$  Cross Section

Mean neutron energy (MeV)	Energy width (keV) -FWHM	$\sigma_{n, \alpha}$
2.16	80	211 $\pm$ 5
2.34	100	207 $\pm$ 5
2.52	80	191 $\pm$ 5
2.71	120	178 $\pm$ 4
2.87	120	160 $\pm$ 4
3.14	120	145 $\pm$ 4
3.42	120	126 $\pm$ 3
3.54	140	119 $\pm$ 3
3.61	140	119 $\pm$ 3
3.77	140	114 $\pm$ 3
3.89	140	113 $\pm$ 3
4.20	160	105 $\pm$ 3
4.69	200	93 $\pm$ 2
5.30	240	77 $\pm$ 4
5.65	240	68 $\pm$ 2
5.89	240	70 $\pm$ 3
6.28	240	62 $\pm$ 3
6.65	240	55 $\pm$ 2
7.08	320	55 $\pm$ 2
7.51	400	50 $\pm$ 2
7.98	400	44.8 $\pm$ 1.4
8.44	400	43.2 $\pm$ 1.6
9.01	500	37.9 $\pm$ 1.4
9.66	500	36.3 $\pm$ 1.5

# ABSOLUTE CROSS SECTIONS FOR NEUTRONS FROM ${}^6\text{Li} + d$ REACTIONS AT ENERGIES BETWEEN 0.2 AND 0.9 MeV<sup>†</sup>

A. J. Elwyn, R. E. Holland, F. J. Lynch, J. E. Monahan, and F. P. Mooring  
Argonne National Laboratory, Argonne, Illinois 60439

Absolute differential and total cross sections in reactions of deuterons with  ${}^6\text{Li}$  have been measured for neutrons corresponding to the formation of  ${}^7\text{Be}$  in both its ground and its first excited state, and for the continuum neutrons involved in the breakup of  ${}^7\text{Be}$  at deuteron energies between 0.2 and 0.9 MeV. Discussion of the experimental procedure is presented. The results indicate that the breakup neutrons are a substantial portion of the total neutron production cross section in this reaction. The reaction rates of the various neutron production reactions are presented.

(Measured  $\sigma(\theta; E_d)$ ,  $\sigma_t(E_d)$  for  ${}^6\text{Li}(d, n){}^7\text{Be}$  reactions; measured  $\frac{d^2\sigma}{dE_n d\Omega}(\theta; E_d)$ ,  $\sigma_t(E_d)$  for  ${}^7\text{Be}$  breakup reaction;  $E_d = 0.2-0.9$  MeV).

## Introduction

It has been pointed out by McNally<sup>1</sup> and others<sup>2</sup> that knowledge of absolute reaction cross sections for the outgoing particles in nuclear reactions of deuterons with  ${}^6\text{Li}$  at energies between 100 keV and a few MeV is of importance to evaluate the prospects of fusion chain reactions in controlled thermonuclear research applications. Unfortunately, data for deuteron-induced reactions on the lithium isotopes reveal<sup>2</sup> substantial disagreement among the various existing measurements. For the case of neutron production in  $d + {}^6\text{Li}$  reactions only one absolute total cross section measurement (over a limited energy range) had been reported<sup>3</sup> prior to 1973.

As part of a program for determining reaction cross sections for various nuclear particles emitted in charged particle induced reactions on light nuclei we report here the results of a study of the outgoing neutrons in the bombardment of  ${}^6\text{Li}$  by 0.2–0.9-MeV deuterons. Differential and total cross sections for neutrons from the  ${}^6\text{Li}(d, n){}^7\text{Be}$  reaction, and for those associated with the breakup of  ${}^7\text{Be}$  were obtained. The present measurements supplement, in part, a recent report by McClenahan and Segel<sup>4</sup> who measured  ${}^6\text{Li}(d, n)$  cross sections from  $\sim 0.5-3.0$  MeV by a different technique.

## Experiment

The experiment was carried out at the ANL 4-MV Dynamitron accelerator equipped with a pulsed and bunched ion source. The  $\text{D}_3^+$  molecular ion beam was incident on thin ( $75-90 \mu\text{g}/\text{cm}^2$ ) targets of LiF (enriched to 99.3% in  ${}^6\text{Li}$ ) evaporated onto thick tantalum backings. The use of LiF rather than metallic lithium, which was possible since the number of neutrons that arise from  $(d, n)$  reactions on F are negligibly small for deuteron energies below 1-MeV, allowed the fabrication of very uniform stable films. The target was supported on an O-ring seal at the end of an aluminum can which also acted as a Faraday cup. A current integrator accurate to considerably better than 1% was utilized to ensure proper beam integration. A jet of compressed air cooled the target which was also rotated at about 1 rev/sec. The acceleration of the  $\text{D}_3^+$  molecular ion beam rather than the normal  $\text{D}_1^+$  ion made it possible to obtain low deuteron energies on target for the higher terminal

voltages at which more stable Dynamitron operating conditions prevailed.

In order to monitor the condition of the target during an experimental run and to measure the target thickness a thin layer of Au ( $\leq 10 \mu\text{g}/\text{cm}^2$ ) was evaporated over the LiF film and the spectrum of deuterons backscattered at  $177^\circ$  was recorded in a Si surface-barrier detector. This spectrum is shown in Fig. 1. The energy difference between the narrow peak which corresponds to deuteron scattering from the thin Au film, and the edge due to scattering from the thick tantalum backing is directly related to the energy loss of the deuteron beam in LiF. Target thicknesses obtained in this fashion agree very closely with determinations by more conventional techniques. The error of the measurement depends primarily upon the accuracy with which the rates of energy loss are known, and is probably less than 10%.

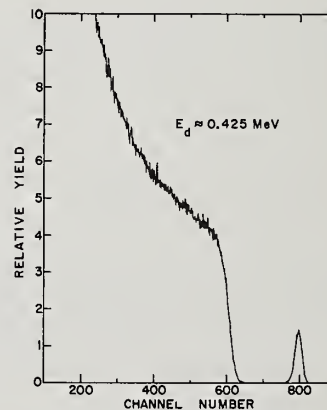


Fig. 1. Spectrum of deuterons scattered at  $177^\circ$  from "sandwich" target that consists of Au +  ${}^6\text{LiF}$  + Ta backing.

Differential cross sections for neutrons from the  ${}^6\text{Li}(d, n){}^7\text{Be}$  reaction and for those that arise from the breakup of  ${}^7\text{Be}$  into  ${}^3\text{He}$  and  ${}^4\text{He}$  were determined from time-of-flight measurements. Four detectors, each of which was a cylindrical stilbene scintillator 2.54 cm long and 5.08 cm in diameter directly coupled to an RCA-8575 photomultiplier, were used so that simultaneous measurements at four angles were possible. Each counter assembly was supported



by a wedge-shaped arm that could rotate about a pivot directly below the target position. The main features of the electronic instrumentation, which utilized pulse-shape  $\gamma$ -ray suppression, have been described previously.<sup>5</sup>

A typical time-of-flight spectrum is shown in Fig. 2. The flight path, 3.5 meters, was sufficient to resolve the neutron groups corresponding to the ground and first excited states of  $^7\text{Be}$ , the two sharp peaks on this spectrum. The broad peak corresponds to the continuous neutron distribution from the  $^7\text{Be}$  breakup reaction.

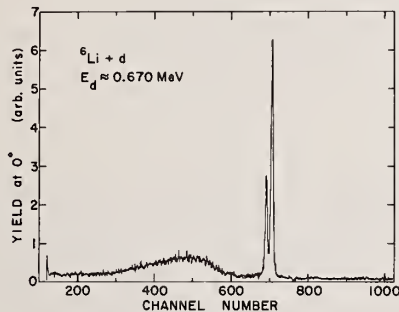


Fig. 2. Typical T.O.F. spectrum for neutrons emitted in  $d + ^6\text{Li}$  reactions at 3.5 m. flight path. Time dispersion is  $\sim 1$  ns/ch.

The absolute efficiency for one of the detectors is shown in Fig. 3. It was obtained from measurements of the  $0^\circ$  neutron yield in the  $^7\text{Li}(p,n)^7\text{Be}$  reaction for energies between 0.25 and 2.75 MeV by use of the recently published cross sections of Burke et al.<sup>6</sup> and Smith and Meadows,<sup>7</sup> and at a few higher energies (to 4 MeV) by measuring the ratio<sup>8</sup> of neutron- $^3\text{He}$  coincidences to total  $^3\text{He}$  counts in the  $\text{D}(d,n)^3\text{He}$  reaction. The solid curve of Fig. 3 represents a calculation<sup>9</sup> that takes into account the production of recoil protons by direct  $n$ - $p$  collisions in the stilbene scintillator as well as by proton collisions with neutrons scattered by one or more carbon atoms. The photomultiplier gains and other electronics settings were adjusted to give similar responses for all four detectors; differences in efficiency occurred mostly in the region of the detector threshold ( $\sim 0.3$  MeV). Accuracy of the absolute efficiencies is  $\sim 12\%$ , based predominately on the quoted<sup>6</sup> accuracy of the  $^7\text{Li}(p,n)$  cross sections and the uncertainty in target thickness.

Neutron backgrounds at the detectors were evaluated by use of a blank tantalum disc in place of the  $\text{LiF}$ -plus-tantalum targets. These measurements accounted well for beam-line related sources of neutrons. Backgrounds at the detectors associated with the  $^6\text{LiF}$  target itself were determined by intercepting the direct neutron beam with Lucite absorbers placed between the target and each detector; although such effects were small they were taken into account in the subsequent analysis of the data.

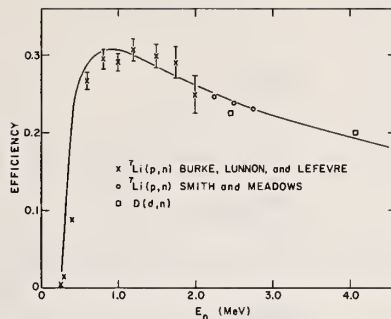


Fig. 3. Absolute neutron-detector efficiency as function of neutron energy.

The intensities of the neutron groups corresponding to the ground and first excited state of  $^7\text{Be}$  were found by summing the contents of the relevant channels and subtracting the background. Since the two groups were not completely resolved at most bombarding energies, an unfolding procedure<sup>10</sup> was used. Differential cross sections were obtained from these results after correction for detector efficiency by use of the measured target thickness and total integrated charge. Corrections for electronic dead time and other effects were determined (experimentally) or estimated to be less than 2% and were not made. For the continuum neutrons, corresponding to  $^7\text{Be}$  breakup, measured counts per channel were corrected for background and converted into differential cross section per unit energy interval. An example of such results is shown in Fig. 4. These distributions were then integrated from a neutron energy of 0.5 MeV, to the maximum neutron energy at which breakup can occur for each deuteron energy in order to obtain differential cross sections at each angle.

Angular distributions were determined at seven angles between  $0^\circ$  and  $149^\circ$  at each of a number of average deuteron energies between 0.204 and 0.880 MeV. Calibration of the energy scale of the accelerator gave deuteron energies accurate to  $\pm 0.005$  MeV.

### Results

Figures 5 shows center-of-mass differential cross sections as a function of angle at various bombarding energies for the  $^7\text{Be}$  ground state and 0.431-MeV first excited state neutrons, respectively. Total cross sections for each neutron group were obtained from the values of the coefficient  $B_0$  in an expansion of the differential cross section into a series of Legendre polynomials [i. e.

$$\frac{d\sigma}{d\Omega} = \sum_{L=0}^5 B_L P_L(\cos\theta)], \text{ and are displayed in Fig. 6 and Table I.}$$

Laboratory differential cross sections for all continuum neutrons with energy greater than 0.5 MeV are shown at a number of bombarding energies in Fig. 7. From the Legendre polynomial expansion of these, the total cross sections are obtained and displayed in Fig. 8 and Table I.

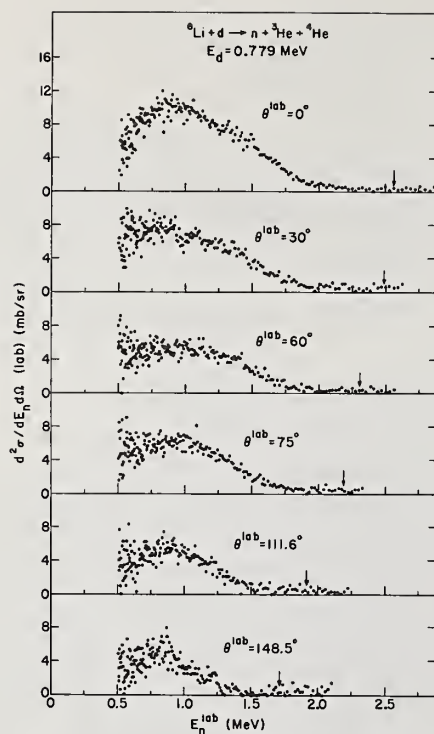


Fig. 4. Lab. differential cross sections per MeV as function of  $E_n$  at  $E_d = 0.779$  MeV for neutrons associated with  ${}^7\text{Be}$  breakup. The arrows indicate the max. value of  $E_n$  at which breakup neutrons can occur.

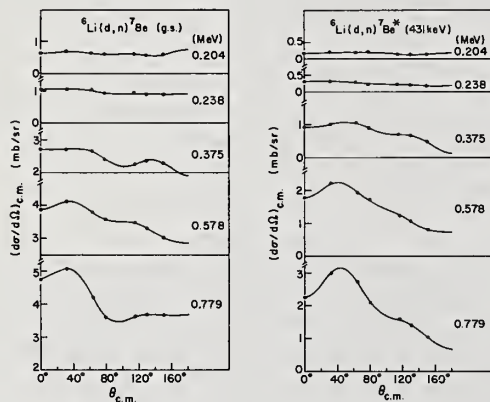


Fig. 5. C.M. differential cross sections as a function of angle for neutrons associated with the ground state and 431-keV state in the  ${}^6\text{Li}(d,n){}^7\text{Be}$  reaction at various deuteron energies. The curves represent Legendre polynomial fits.

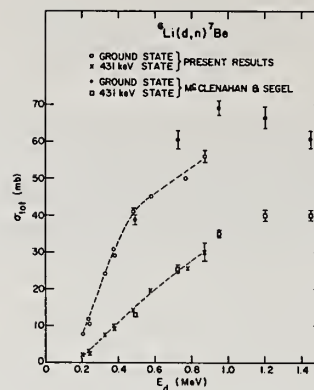


Fig. 6. Total cross section for the  ${}^6\text{Li}(d,n){}^7\text{Be}$  reaction as a function of  $E_d$ . The dashed curves are drawn to guide the eye.

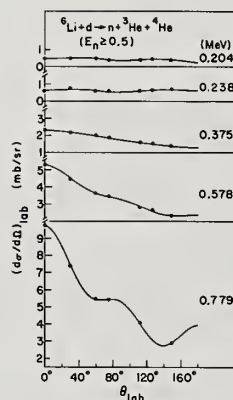


Fig. 7. Lab. differential cross sections as a function of angle for neutrons with  $E_n \geq 0.5$  MeV associated with  ${}^7\text{Be}$  breakup at various deuteron energies. The curves represent Legendre polynomial fits.

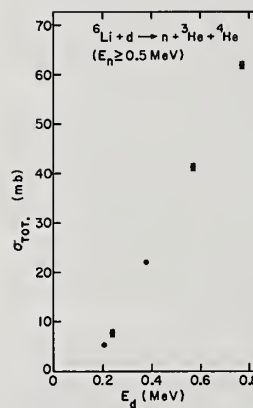


Fig. 8. Total cross section for neutrons with  $E_n \geq 0.5$  MeV associated with  ${}^7\text{Be}$  breakup as a function of  $E_d$ .

The relative uncertainties of the differential and total cross sections are indicated in Figs. 5–8 by the error bars (or the size of the data points). On the basis of the precision with which absolute efficiencies and target thicknesses were obtained, along with the statistical accuracy of the data, total cross sections for the  $(d,n)$  reaction should have absolute uncertainties of  $\sim 16\%$ . For the continuum neutrons this value



should be  $\sim 18\%$  because of larger uncertainties associated with the problems of proper background subtraction.

### Discussion

As indicated in Table I the neutrons associated with  ${}^7\text{Be}$  breakup contribute between 35 and 45% to the total neutron production cross section for  ${}^6\text{Li} + d$  reactions at deuteron energies 0.2–0.9 MeV. The importance of this contribution emphasizes the necessity of its inclusion in any quantitative evaluation of advanced fusion fuels containing  ${}^6\text{Li}$ .

This point stresses the utility of attempting to interpret the energy dependence of the measured continuum neutron distributions in terms of reaction mechanisms. While such efforts can clearly contribute to the understanding of the structure of light nuclei, a consistent interpretation of mechanisms that can produce a neutron in the final state will also allow the extrapolation from neutron detector threshold to zero neutron energy in order to obtain more complete total cross sections. In Fig. 9, the results of a preliminary calculation for a few individual contributions to three-body breakup processes are compared to the observed  $0^\circ$ -neutron distributions. As seen, the observations are qualitatively different from the spectra expected for a direct-breakup (i.e., one-step) mechanism. On the other hand, the calculation based on a sequential decay mechanism in which the s-wave Coulomb interaction between  ${}^3\text{He}$  and  ${}^4\text{He}$  in the final state is taken into account, appears quite promising. A more complete analysis, based on various final-state interactions, is currently in progress.

The reaction rate coefficients  $^{1,2} \sigma_t v$  for the  $d + {}^6\text{Li}$  reactions described in this report are shown in Fig. 10, along with the corresponding quantities for the  $d + T$  and  $d + D$  reactions. The feasibility of the use of  ${}^6\text{Li}$  as a fusion fuel should depend at least in part on the magnitude of the total reactivity for all exothermic reactions of deuterons with  ${}^6\text{Li}$ . Cross-section measurements for the charged particles emitted in these reactions at energies between 0.2 and 1.0 MeV is currently underway at ANL.

Table I

Total cross sections (in mb) for neutrons emitted in  $d + {}^6\text{Li}$  reactions.

$E_d$ (MeV)	$\sigma_t$ (g. s.)	$\sigma_t$ (431 keV)	$\sigma_t$ ( $E_n \geq 0.5$ MeV)
( $\pm 0.005$ )	( $\pm 16\%$ )	( $\pm 16\%$ )	( $\pm 18\%$ )
0.873	56.0	29.9	
0.779	49.9	25.5	61.7
0.578	45.0	19.5	41.2
0.482	41.2	14.6	
0.379	29.0	9.45	
0.375	30.4	10.1	22.1
0.328	24.3	7.78	
0.242	10.0	2.68	
0.238	11.8	3.12	7.64
0.204	7.67	2.16	5.29

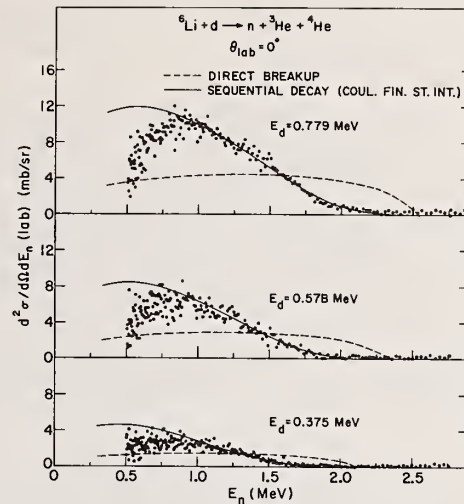


Fig. 9. Lab. differential cross sections per MeV as a function of  $E_n$  at  $\theta = 0^\circ$  for various deuteron energies compared to preliminary calculations for direct  ${}^7\text{Be}$  breakup (dashed curve) and for sequential decay with a Coulomb final state interaction between  ${}^3\text{He}$  and  ${}^4\text{He}$  (solid curve). The calculations were normalized to the data at neutron energies greater than 0.9 MeV.

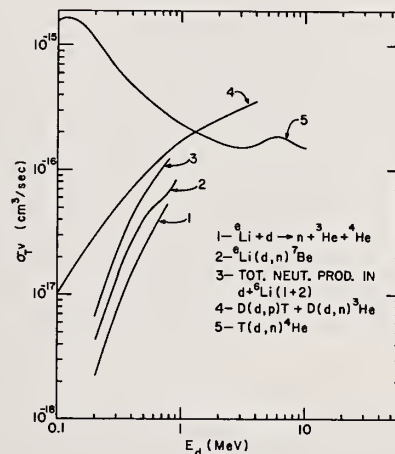


Fig. 10. Reaction rate coefficients  $\sigma_t v$ , where  $\sigma_t$  = total cross section and  $v$  = velocity of deuteron beam, as a function of  $E_d$ .

### References

<sup>†</sup>Work performed under the auspices of the U. S. Atomic Energy Commission.

<sup>1</sup>See, e.g., J. Rand McNally, Jr., "Fusion Chain Reactor Prospects and Problems," USAEC Report ORNL-TM-4575 (1974).

<sup>2</sup>V. S. Crocker, S. Blow, and C. J. H. Watson, "Nuclear Cross-Section Requirements for Fusion Reactions," Culham Laboratory Report #CLM-P240 (1970).

<sup>3</sup>F. Hirst, I. Johnstone, and M. J. Poole, Phil. Mag. 45, 762 (1954).

<sup>4</sup>C. R. McClenahan and R. E. Segel, Phys. Rev. C 11, 370 (1975).

<sup>5</sup>A. J. Elwyn, F. T. Kuchnir, J. E. Monahan, F. P. Mooring, and J. F. Lemming, Phys. Rev. C 6, 1730 (1972).

<sup>6</sup>C. A. Burke, M. T. Lunnnon, and H. W. Lefevre, Phys. Rev. C 10, 1299 (1974).

<sup>7</sup>J. W. Meadows and D. L. Smith, "Neutrons from Proton Bombardment of Natural Lithium," Argonne Nat'l. Lab. report ANL-7938 (1972).

<sup>8</sup>A. Chastel, M. B. Davis, C. M. Hoffman, M. N. Kreisler, and A. J. S. Smith, Nucl. Instrum. Methods 94, 493 (1971); R. Plasek, D. Miljanic, V. Valkovic, R. B. Liebert, and G. C. Phillips, Nucl. Instrum. Methods 111, 251 (1973).

<sup>9</sup>A. J. Elwyn, J. V. Kane, S. Ofer, and D. H. Wilkinson, Phys. Rev. 116, 1490 (1959).

<sup>10</sup>J. R. Comfort, "Manual of Data-Analysis Programs for Charged-Particle Reactions," ANL Physics Division Informal Report PHY-1970B (1970).



Investigations of proton, deuteron and helium induced reactions on  ${}^6\text{Li}$  are of importance in connection with the advantages of fusion reactor cycles involving only charged particles. The cross section data for many of these reactions are incomplete and poorly known. We report measurements of the absolute cross sections of the reactions  ${}^6\text{Li}(p,p)$ ,  ${}^6\text{Li}(p,{}^3\text{He})$  at  $E_p = 3-12$  MeV,  ${}^6\text{Li}(d,p)$ ,  ${}^6\text{Li}(d,\alpha)$  at  $E_d = 2.25-6$  MeV and  ${}^6\text{Li}({}^3\text{He},p)$  at  $E = 3-6$  MeV. Our data are combined with available information in the literature to determine reaction rate parameters as a function of the temperature of the reacting nuclei.

(NUCLEAR REACTIONS  ${}^6\text{Li}(p,p)$ ,  $(p,{}^3\text{He})$ ,  $({}^3\text{He},p)$ ,  $(d,p)$ ,  $(d,\alpha)$  measured  $\sigma(\theta)$ , deduced  $\sigma$  and  $\langle\sigma v\rangle$ )

### Introduction

Nuclear chain reactions involving only charged particles are of considerable interest at the present time in studies for controlled thermonuclear reactors.<sup>1</sup> If all the particles are charged, the reaction products may be confined magnetically thus maintaining most of the energy within the plasma. In contrast, of course, neutrons cannot be magnetically confined and much energy will be lost from a plasma in which substantial neutron production is taking place.

McNally *et al.*<sup>2</sup> have studied the reactivity of systems containing  $d$ - ${}^6\text{Li}$  and have identified the reactions among the  $p$ ,  $d$ ,  $t$ ,  ${}^3\text{He}$ ,  $\alpha$  and  ${}^6\text{Li}$  ions which are likely to make the largest contributions to energy production in the plasma. In 1970 Crocker, Blow and Watson<sup>3</sup> made a compilation of the results of a number of light mass reaction cross section measurements, including those for  ${}^6\text{Li}$  and  ${}^7\text{Li}$ . However, detailed evaluations of the performance of advanced fuel systems such as  $d$ - ${}^6\text{Li}$  are still hampered by a lack of knowledge of the absolute cross sections for reactions among the constituent ions. In this paper we summarize some recent and continuing work at Triangle Universities Nuclear Laboratory on the measurement of absolute cross sections for charged particle induced reactions on  ${}^6\text{Li}$ . In particular we report measurements for  $(p,p)$ ,  $(p,p')$ ,  $(p,{}^3\text{He})$ ,  $({}^3\text{He},p)$ ,  $(d,p)$  and  $(d,\alpha)$  reactions on  ${}^6\text{Li}$  and attempt to correlate our results with existing data in the literature. Most of these reactions have been studied in at least part of the energy range of interest, but frequently absolute cross sections were either not reported or were based on mutually inconsistent reference cross sections. We have tried to base all our absolute cross sections on one reference value; namely that for proton elastic scattering from  ${}^6\text{Li}$  at  $E_p = 6.868$  MeV and  $\theta_{\text{lab}} = 95^\circ$  as reported by Bingham *et al.*<sup>4</sup>

### Cross Section Results

#### ${}^6\text{Li}(p,{}^3\text{He})\alpha$

This reaction is of prime importance as a means of creating  ${}^3\text{He}$  in the plasma. The  $d({}^3\text{He},p)\alpha$  reaction, which is one of the main energy producing reactions in the  $d$ - ${}^6\text{Li}$  system, has a  $Q$  value of +18.4 MeV. The protons will lose energy in the plasma via elastic and inelastic collisions and one thus expects a continuum of proton energies in the system up to ~15 MeV. Our

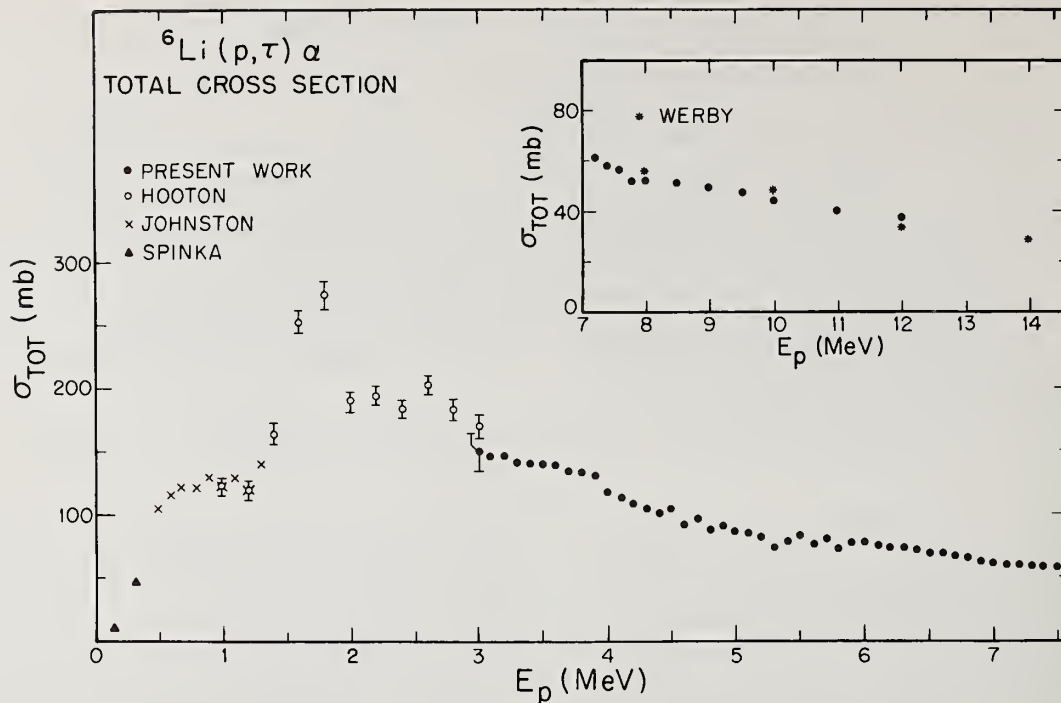
measurements<sup>5</sup> for the  ${}^6\text{Li}(p,{}^3\text{He})\alpha$  reaction extended from  $E_p = 3$  to 12 MeV and are shown in Fig. 1. The cross section has a large resonance near 1.8 MeV and our results support the contention of Hooton and Ivanovich<sup>6</sup> that the cross section in the neighbourhood of this resonance is higher than has previously been supposed. Other data in Fig. 1 are from Werby *et al.*<sup>7</sup>, Spinka and Tombrello<sup>8</sup> and, more recently, Johnston and Sargood<sup>9</sup> in the region 0.5 to 1.2 MeV. These latter data were arbitrarily normalized to those of Ref. 6 at  $E_p = 1.0$  and 1.2 MeV.

#### ${}^6\text{Li}(p,p)$ , ${}^6\text{Li}$ , ${}^6\text{Li}(p,p')$ , ${}^6\text{Li}^*$

The first excited state of  ${}^6\text{Li}$  at 2.2 MeV is particle unstable and is a potentially important source of suprathermal  $d$  and  $\alpha$  particles in the plasma. On the basis of our results in Ref. 5 we concluded that our cross sections for elastic and inelastic proton scattering were 40% higher than those of Harrison and Whitehead<sup>10</sup> and Harrison<sup>11</sup>. In fact in Ref. 11, Harrison discusses relative normalizations among different experiments and indicates that other work by Tombrello and Parker<sup>12</sup> would probably yield a more reliable absolute normalization for his proton inelastic scattering data. This alternative normalization implies his cross section should be  $25 \pm 5\%$  higher. This is in only moderate agreement with our value of a  $40 \pm 10\%$  increase but subject to the errors in the measurements is not necessarily inconsistent. In Fig. 2 we show the data of Ref. 11 for the total cross section leading to the 2.2 MeV state in  ${}^6\text{Li}$  where we have increased the values by 40% in accordance with the normalization factor discussed above.

#### ${}^6\text{Li}({}^3\text{He},p)2\alpha$

This reaction has a high positive  $Q$  value (16.9 MeV) which makes it important from the point of view of energy deposition in the plasma. The  ${}^3\text{He}$  energies in the  $d$ - ${}^6\text{Li}$  system are low however and therefore the reaction is likely to be inhibited by the effect of the Coulomb barrier in the entrance channel. The work of Schiffer *et al.*<sup>13</sup> indicated that there were no strong resonances in the energy range 0.8 - 5 MeV. The three body final state in this reaction is actually reached by three possible channels:  ${}^6\text{Li}({}^3\text{He},p){}^8\text{Be}$ ,  ${}^6\text{Li}({}^3\text{He},\alpha){}^5\text{Li}$  and direct three body break up.  ${}^8\text{Be}$  and  ${}^5\text{Li}$  are of course particle unstable and immediately break up into  $2\alpha$  or  $\alpha + p$  respectively. Only reactions proceeding to the  ${}^8\text{Be}$



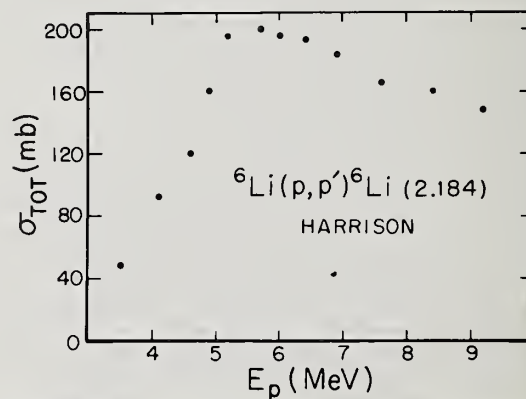
ground and first excited states yield discrete proton groups and these are the only channels for which absolute cross section measurements have been reported<sup>13,14</sup>. No estimates of the absolute magnitude of the continuum cross section have been given. Fig. 3 is a typical proton spectrum obtained at 5 MeV bombarding energy with stoppings foils in front of the detectors to remove all  ${}^3\text{He}$  and  $\alpha$  particles. As can be seen there is a substantial continuum present in the proton spectra and some care is therefore required in extracting yields to the 2.9 MeV first excited state of  ${}^8\text{Be}$ .

We parametrized the proton continuum by assuming it to be due solely to direct three body break up. The cross section is then determined by phase space considerations and is given, in the laboratory frame, by<sup>16</sup>

$$\frac{d^2\sigma}{d\Omega dE} = [E(\frac{8}{9}E_T - E_C)]^{\frac{1}{2}} \times A$$

where  $E$  is the laboratory proton energy at a laboratory angle  $\theta$ ,  $E_C$  the center of mass proton energy corresponding to  $E$ ,  $\theta$  and  $E_T$  is the total energy available in the center of mass ( $E_T = 18.9 + 0.667 \times E({}^3\text{He})$ ). The line in Fig. 3 is a best fit of the phase space expression to the experimental background and fixes the value of the quantity  $A$ . We find this

Fig. 1 Total cross section results for  ${}^6\text{Li}(p, {}^3\text{He})\alpha$  up to 14 MeV. Apart from the present work, the other measurements are from Refs. 6-9.



Erratum

Paper HA10 "Cross Section Measurements for Charged Particle Induced Reactions on  ${}^6\text{Li}$ " by C. R. Gould, J. M. Joyce, and J. R. Boyce.

"Absolute cross sections for the  ${}^6\text{Li}({}^3\text{He}, p){}^8\text{Be}$  reaction are incorrect due to a normalization error. The values shown in Fig. 4 should be increased by a factor of 2.1. The cross section results for the proton and deuteron induced reactions are not affected."



The large uncertainty in this latter case arises from the fact that the protons from reactions with the carbon backing obscure the low energy part of the proton continuum ( $E_p \leq 8$  MeV) and make it impossible to determine exactly how well the phase space expression fits the background in this region. The data of Schiffer *et al.*<sup>13</sup> and Fletcher *et al.*<sup>14</sup> are also shown in Fig. 4 and have been normalized to agree with our total cross sections at the energies where we have equivalent data. Our renormalization implies that the cross sections of Ref. 13 are about a factor three too high.

#### ${}^6\text{Li}(d,p){}^7\text{Li}$ , ${}^6\text{Li}(d,\alpha){}^3\text{He}$

The (d,p) reaction ( $Q = +5.0$  MeV) provides a means of regenerating energetic protons to continue  ${}^3\text{He}$  production via  ${}^6\text{Li}(p,{}^3\text{He})\alpha$ . The (d, $\alpha$ ) reaction has the highest  $Q$  value of all  ${}^6\text{Li}$  reactions (+22.4 MeV) and can thus be investigated simultaneously with the (d,p) reaction without the need for any particle identification. The reactions were studied in 250 keV steps from 2.25 MeV to 4 MeV and in 500 keV steps up to 6 MeV with particles detected at laboratory angles from  $20^\circ$  to  $160^\circ$ . Based on Legendre polynomial fits to the center of mass angular distributions, we obtain the total cross section results shown in Fig. 5 for the (d, $\alpha$ ) channel and for protons leading to the ground and first excited states of  ${}^7\text{Li}$ . For these deuteron induced cross section measurements, we used as our reference cross section the value of Ref. 1 quoted for  ${}^6\text{Li}(d,d)$  at 8 MeV bombarding energy and  $\theta = 70^\circ$ . We estimate the uncertainty in our cross section results to be  $\sim 15\%$ . Mclenahan and Segel<sup>17</sup> have recently studied both these reactions in some detail and have also summarized the results of previous investigations. Their absolute cross section results were determined by comparison to Rutherford scattering at very low energies and are shown in Fig. 5 as the open circles. Subject to their stated error of 15%, our values are in good agreement in the energy range 2-3.5 MeV. The (d, $p\alpha$ ) cross section results do seem to deviate systematically from each other more than the values for the other two channels however.

The (d, $\alpha$ ) reaction has two broad resonances around 1 and 4 MeV. The (d,p) reaction appears to be predominantly direct<sup>17</sup>, with both ground and first excited state cross sections decreasing smoothly at bombarding energies higher than about 1 MeV.

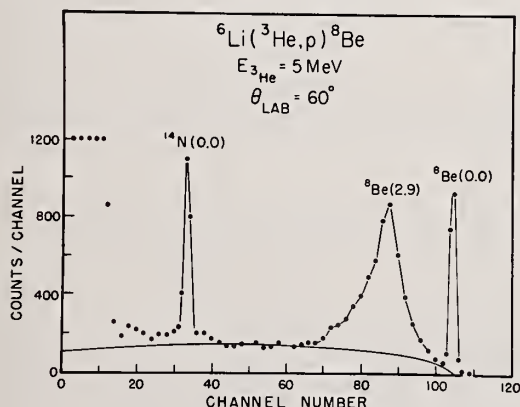


Fig. 3. The proton spectrum obtained at  $60^\circ$  for the  ${}^6\text{Li}({}^3\text{He},p){}^8\text{Be}$  reaction at 5 MeV bombarding energy. Stopping foils remove  ${}^3\text{He}$  and  $\alpha$  particles from the spectrum.

#### Summary

Cross section results for a number of charged particle induced reactions on  ${}^6\text{Li}$  have been presented and correlated where possible with existing data in the literature. Our values are based on one reference cross section value and are believed to be accurate to  $\sim 15\%$ .

In order to estimate the energy release in a plasma the quantity of interest is the Maxwell averaged reaction rate parameter  $\langle\sigma v\rangle$ , as a function of the temperature of a plasma of the reacting ions<sup>18</sup>. Calculations of  $\langle\sigma v\rangle$  for deuteron induced reactions on  ${}^6\text{Li}$  have been presented by Greene<sup>19</sup>. Fig 6 shows the results of a calculation of  $\langle\sigma v\rangle$  versus  $kT$  for  $p$ - ${}^6\text{Li}$  and  ${}^3\text{He}$ - ${}^6\text{Li}$  systems. For the  $p$ - ${}^6\text{Li}$  system, the necessary cross sections required for the calculation were obtained by interpolating smoothly between the values of Fig. 1. For the  ${}^3\text{He}$ - ${}^6\text{Li}$  system there are no cross section data below 1 MeV and we therefore assumed that the  ${}^8\text{Be}$  cross sections would fall monotonically following the  $s$  wave Gamow form<sup>20</sup>,  $\sigma = S/E \exp[-B/E^{1/2}]$ . Here  $B = 108 \text{ keV}^{1/2}$  and  $S = 6410 \text{ keV-b}$  and  $15730 \text{ keV-b}$  respectively for the ground and 2.9 MeV states respectively. A contribution from the three body break up continuum was not included and there are clearly large uncertainties in the  $\langle\sigma v\rangle$  curve for the  ${}^3\text{He}$ - ${}^6\text{Li}$  system. Nevertheless the values do imply that the contribution of this reaction to the reactivity of a  $d$ - ${}^6\text{Li}$  fuelled plasma will be small even though the energy deposition per event is considerable.

\*Work supported in part by USAEC.

\*\*Summer visitor from East Carolina University.

#### References

1. J. Rand McNally, Jr., "Nuclear Data in Science and Technology," Proc. IAEA Conf., Paris 1973, 2, 41, International Atomic Energy Agency, Vienna (1973).
2. J. Rand McNally, Jr., R. D. Sharp, R. H. Fowler and J. F. Clarke, Nucl. Fusion **14**, 579 (1974).
3. V. S. Crocker, S. Blow and C. J. H. Watson, Nuclear Data for Reactors **1**, 67 (IAEA, Vienna (1970)).

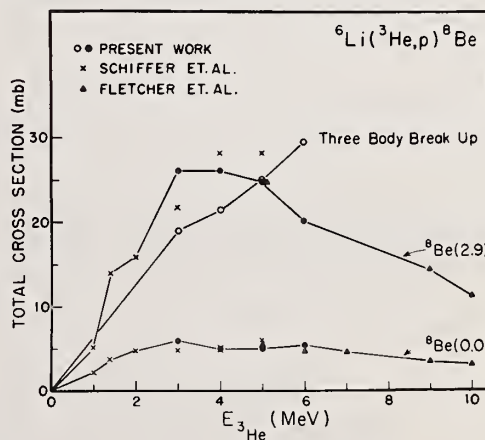


Fig. 4. Total cross section results for the  ${}^6\text{Li}({}^3\text{He},p)2\alpha$  reaction. Apart from the present work, other measurements are from Refs. 13, 14.



4. H. C. Bingham, A. R. Zander, K. W. Kemper, and N. R. Fletcher, Nucl. Phys., A173, 265 (1971).
5. C. R. Gould, R. O. Nelson, J. R. Williams and J. R. Boyce, Nucl. Sci. Eng. 55, 267 (1974).
6. B. W. Hooton and M. Ivanovich, "Neutron Physics Division Progress Report from the Period May 1, 1970-April 30, 1971," AERE-PR/NP 18, p. 37, United Kingdom Atomic Energy Authority, Harwell (1972). See also Ref. 1.
7. M. W. Werby, M. B. Greenfield, K. W. Kemper, D. L. McShan, and S. Edwards, Phys. Rev., C8, 106 (1973).
8. H. Spinka, T. A. Tombrello, and H. Winkler, Nucl. Phys. A164, 1 (1971).
9. G. P. Johnston and D. G. Sargood, Nucl. Phys. A224, 349 (1974).
10. W. D. Harrison and A. B. Whitehead, Phys. Rev. 132, 2607 (1963).
11. W. D. Harrison, Nucl. Phys. A92, 260 (1967).
12. T. A. Tombrello and P. D. Parker, Phys. Rev. 130, 1112 (1963).
13. J. P. Schiffer, T. W. Bonner, R. H. Davis and F. W. Prosser, Phys. Rev. 104, 1064 (1956).
14. N. R. Fletcher, J. D. Marshall and R. H. Davis, Nucl. Phys. 70, 471 (1965).
15. G. G. Ohlsen, Nucl. Inst. Meth. 37, 240 (1965).
16. C. R. Gould et al. (to be published).
17. C. R. Mclenahan and R. E. Segel, Phys. Rev. C11, 370 (1975).
18. D. J. Rose and M. Clark, Jr., Plasmas and Controlled Fusion, MIT Press, p. 81 Cambridge, Massachusetts (1961).
19. S. L. Greene, USAEC report UCRL-70522 (1967).
20. E. M. Burbridge, G. R. Burbridge, W. A. Fowler and F. Hoyle, Rev. Mod. Phys. 29, 548 (1957).

Fig. 6. Plot of the Maxwell averaged reaction rate parameter  $\langle\sigma v\rangle$  as a function of the temperature of the system,  $kT$ . See text for a discussion of the cross section data used.

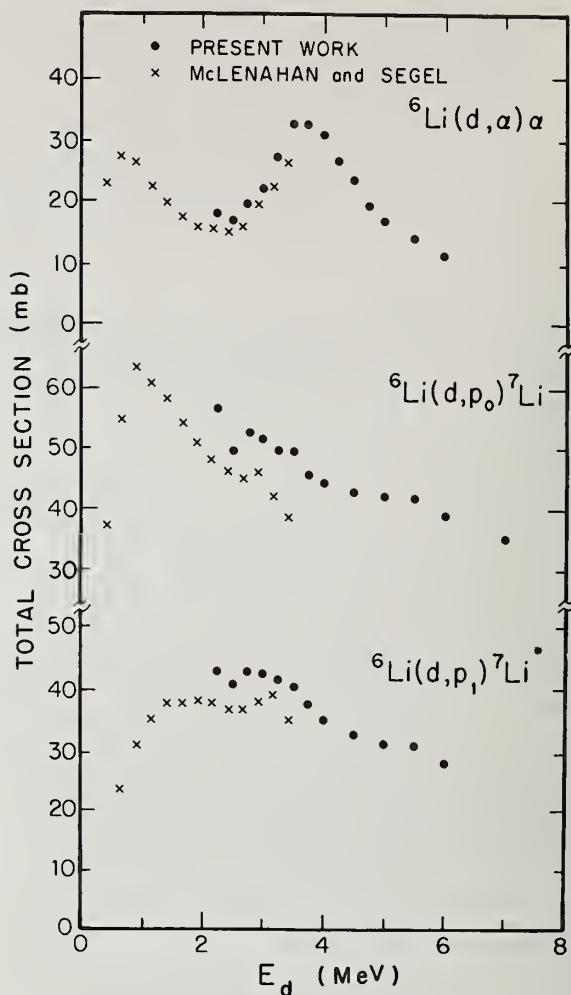
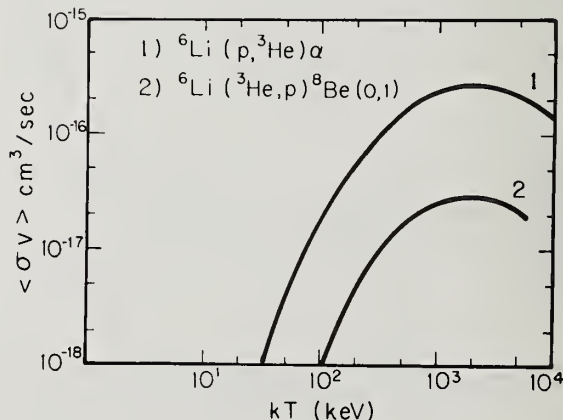


Fig. 5. Total cross section results for the (d,p) and (d,α) reactions on  ${}^6\text{Li}$  from the present work and from Ref. 17.



Explicit formulas are given for the elastic and inelastic cross sections of neutrons, deuterons, tritons and alpha particles. These formulas, obtained by a phase shift analysis, are the best fit to currently available experimental data, for all angles and energies up to 14 MeV.

(Cross sections; phase shifts; neutrons; deuterons; tritons; alpha particles)

### Introduction

Calculations on fusion in dense plasmas require a detailed knowledge of numerous elastic cross sections. Unfortunately, experimental data are often very sparse. In order to interpolate (in angle and energy) between available data, we have performed a phase shift analysis of the various elastic cross sections. No theoretical nuclear model was assumed. Our only guidelines were the following:

a) Phase shifts at each energy were usually assumed to depend only on the total spin  $S$  and orbital angular momentum  $\ell$ . However, for  $\alpha$ -D resonant scattering and  $\alpha$ -T scattering, we also introduced a  $j$ -dependence (see below).

b) At low energy, the phase shift  $\delta_\ell$  behaves as  $E^{\ell+1/2}$ . At higher energies, we write  $\text{tg} \delta_\ell = E^{\ell+1/2} f(E)$ , where  $f(E)$  is a rational function of  $E$  (usually a polynomial). It is convenient to fit  $\text{tg} \delta_\ell$ , rather than  $\delta_\ell$  itself, as a function of  $E$ , because the expressions  $e^{i\delta} \sin \delta = 1/(\cot \delta - i)$ , which appear in the cross sections, become rational functions of the parameters. This ensures considerable savings of computer time.

c) The number of partial waves needed, and the number of parameters for the energy dependence of each one, were found by trial and error. A formula was considered satisfactory when it reproduced the experimental data with errors comparable to the experimental errors. We endeavored to find "satisfactory" formulas with as few parameters as possible.

All cross sections are given in barns per steradian in the c.o.m. system as functions of  $P_\ell(\cos \theta)$ . All energies are given in MeV in the laboratory system.

### Neutron - Deuteron

The n-D cross sections are well documented.<sup>1</sup> Above the breakup threshold (3.339 MeV) the (n,2n) channel has a cross section<sup>2,3</sup>

$$\sigma_{n,2n} = (E-3.339) (5.36783 \cdot 10^{-2} - 0.115396/E - 2.07008 \cdot 10^{-3} E)$$

where  $E$  is the energy of neutron.

The differential elastic cross section can be written in terms of the doublet and quartet phase shifts  $\delta_{\ell 2}$  and  $\delta_{\ell 4}$ . Below threshold<sup>4-7</sup> ( $E < 3.339$  MeV) we have

$$\frac{d\sigma}{d\Omega} = \frac{0.155572}{E} \left[ 2 \left| \sum_{\ell=0}^2 \frac{(2\ell+1)P_\ell}{\cot \delta_{\ell 4} - i} \right|^2 + \left| \sum_{\ell=0}^2 \frac{(2\ell+1)P_\ell}{\cot \delta_{\ell 2} - i} \right|^2 \right]$$

where

$$\begin{aligned} \text{tg} \delta_{04} &= [-3.75982 - 9.18518 \cdot 10^{-1} (E-3.339)] (E/3.339)^{1/2} \\ \text{tg} \delta_{02} &= [-4.79059 \cdot 10^{-1} + 5.49062 \cdot 10^{-1} (E-3.339)] (E/3.339)^{1/2} \\ \text{tg} \delta_{14} &= [2.51485 \cdot 10^{-1} - 3.31624 \cdot 10^{-1} (E-3.339)] (E/3.339)^{3/2} \\ \text{tg} \delta_{12} &= [-5.49470 \cdot 10^{-1} - 4.64498 \cdot 10^{-1} (E-3.339)] (E/3.339)^{3/2} \\ \text{tg} \delta_{24} &= [-3.57546 \cdot 10^{-3} + 2.25043 \cdot 10^{-1} (E-3.339)] (E/3.339)^{5/2} \end{aligned}$$

$$\text{tg} \delta_{22} = [5.17095 \cdot 10^{-2} + 3.54638 \cdot 10^{-1} (E-3.339)] (E/3.339)^{5/2}$$

Above threshold<sup>8-13</sup> ( $E > 3.339$  MeV) one must introduce the inelasticity factors  $\eta_{\ell 4}$  and  $\eta_{\ell 2}$ . The formula then becomes

$$\frac{d\sigma}{d\Omega} = \frac{0.155572}{E} \left[ 2 \left| \sum_{\ell=0}^2 \frac{(2\ell+1)P_\ell}{2} \left( 1 - \eta_{\ell 4} \frac{i - \text{tg} \delta_{\ell 4}}{i + \text{tg} \delta_{\ell 4}} \right) \right|^2 + \left| \sum_{\ell=0}^2 \frac{(2\ell+1)P_\ell}{2} \left( 1 - \eta_{\ell 2} \frac{i - \text{tg} \delta_{\ell 2}}{i + \text{tg} \delta_{\ell 2}} \right) \right|^2 \right]$$

where

$$\begin{aligned} \text{tg} \delta_{04} &= [-3.75982 + 8.69252 \cdot 10^{-2} (E-3.339)] (E/3.339)^{1/2} \\ \text{tg} \delta_{02} &= [-4.79059 \cdot 10^{-1} + 4.18254 \cdot 10^{-2} (E-3.339)] (E/3.339)^{1/2} \\ \text{tg} \delta_{14} &= [2.51485 \cdot 10^{-1} - 1.46593 \cdot 10^{-2} (E-3.339)] (E/3.339)^{3/2} \\ \text{tg} \delta_{12} &= [-5.49470 \cdot 10^{-1} + 8.80116 \cdot 10^{-2} (E-3.339)] (E/3.339)^{3/2} \\ \text{tg} \delta_{24} &= [-3.57546 \cdot 10^{-3} + 2.05239 \cdot 10^{-4} (E-3.339)] (E/3.339)^{5/2} \\ \text{tg} \delta_{22} &= [5.17095 \cdot 10^{-2} - 3.62048 \cdot 10^{-3} (E-3.339)] (E/3.339)^{5/2} \end{aligned}$$

and

$$\eta_{\ell m} = [1 - X_{\ell m} (E-3.339) (E-3.85646 \cdot 10^{-2} E^2 - 2.14977)]^{1/2}$$

where

$$\begin{aligned} X_{04} &= 1.89456 \cdot 10^{-2}, \quad X_{14} = 1.74255 \cdot 10^{-2}, \quad X_{24} = -1.72691 \cdot 10^{-2} \\ X_{02} &= 2.10000 \cdot 10^{-2}, \quad X_{12} = 2.06282 \cdot 10^{-2}, \quad X_{22} = 1.14229 \cdot 10^{-2} \end{aligned}$$

Since by definition  $\eta_{\ell m} < 1$ , the  $X_{\ell m}$  should be positive. The small violation of unitarity ( $X_{24} < 0$ ) is probably due to the arbitrary truncation at  $\ell = 2$ .

### Neutron - Triton

The n-T breakup data are extremely sparse<sup>14</sup>. The  $T(n,2n)$  threshold is 8.35 MeV and the  $T(n,3n)$  threshold 11.3 MeV. At 14.1 MeV the inelastic channel has a cross section  $\sigma_{ne} = (45 \pm 5) \cdot 10^{-3}$  barn and the upper limit for  $T(n,3n)$  is  $10^{-3}$  barn.

Although the elastic scattering is more adequately documented<sup>14-19</sup> the data hardly justify the introduction of inelasticity factors above threshold. Therefore we write a single expression for the elastic scattering cross section up to 14.1 MeV:

$$\frac{d\sigma}{d\Omega} = \frac{0.092244}{E} \left[ 3 \left| \sum_{\ell=0}^1 \frac{(2\ell+1)P_\ell}{\cot \delta_{\ell 3} - i} \right|^2 + \left| \sum_{\ell=0}^2 \frac{(2\ell+1)P_\ell}{\cot \delta_{\ell 1} - i} \right|^2 \right]$$

where  $\delta_{\ell 3}$  and  $\delta_{\ell 1}$  (the triplet and singlet phase shifts)<sup>4</sup> are given by

$$\begin{aligned} \text{tg} \delta_{03} &= [-6.54134 / (10.81013 - E)] E^{1/2} \\ \text{tg} \delta_{01} &= [-2.24628 / (5.00099 - E)] E^{1/2} \\ \text{tg} \delta_{13} &= (1.736229 \cdot 10^{-1} - 1.47844 \cdot 10^{-2} E) E^{3/2} \\ \text{tg} \delta_{11} &= (1.233168 \cdot 10^{-1} - 8.81344 \cdot 10^{-3} E) E^{3/2} \end{aligned}$$



$$\text{tg}\delta_{21} = (-2.96688 \cdot 10^{-3} + 1.78526 \cdot 10^{-4} E) E^{5/2}$$

The  $\ell = 2$  triplet phase shift  $\delta_{23}$  is very poorly defined by the data. It can be put equal to zero without affecting the quality of the fit.

### Deuteron - Deuteron

The cross sections for the exothermic D-D reactions  ${}^2\text{H}(d,n){}^3\text{He}$  and  ${}^2\text{H}(d,p){}^3\text{H}$  are well documented<sup>20,27</sup>. They can be written as

$$\sigma_{d,n} = (0.182039 + 0.203408 E - 0.0083589) \exp(-1.49426/\sqrt{E})/E$$

$$\sigma_{d,p} = (0.12193 + 0.181099 E - 0.00672257) \exp(-1.41385/\sqrt{E})/E$$

At very low energy these cross sections are dominated by the Gamow factors  $\exp(-C_i/\sqrt{E})$ . The numerical coefficients  $C_i$  have been considered as variational parameters and not held fixed at their theoretical values.

No inelastic factors are included in the differential elastic scattering cross section, because they are very close to 1. Moreover, we assume that spin dependence enters only via the parity of the wave function, i.e. that singlet and quintuplet phase shifts are equal.

The expression we obtain including data<sup>28-33</sup> up to 13.80 MeV is

$$\frac{d\sigma}{d\Omega} = \frac{0.138359}{E} \left[ 2 \left| F_c(\theta) + F_c(\pi-\theta) + \sum_{\ell=0,2} \frac{2(2\ell+1)P_\ell \Psi_\ell}{\cot\delta_\ell - i} \right|^2 + \left| F_c(\theta) - F_c(\pi-\theta) + \sum_{\ell=1} \frac{2(2\ell+1)P_\ell \Psi_\ell}{\cot\delta_\ell - i} \right|^2 \right]$$

where

$$\Psi_0 = 1, \quad \Psi_1 = (1+i\eta)/(1-i\eta), \quad \Psi_2 = \Psi_1(2+i\eta)/(2-i\eta)$$

and the Coulomb amplitude is

$$F_c = -\frac{\eta}{2} [2/(1-\cos\theta)]^{1+i\eta}$$

with  $\eta = 0.223476/\sqrt{E}$ . The phase shifts are given by

$$\text{tg}\delta_0 = (-2.92914 \cdot 10^{-1} - 8.65496 \cdot 10^{-2} E) E^{1/2}$$

$$\text{tg}\delta_1 = (-4.38663 \cdot 10^{-2} + 2.20396 \cdot 10^{-3} E) E^{3/2}$$

$$\text{tg}\delta_2 = (-7.33607 \cdot 10^{-4} + 2.36004 \cdot 10^{-5} E) E^{5/2}$$

### Deuteron - Triton

In this section,  $E$  denotes the lab energy of the deuteron, the triton being initially at rest.

The cross section for the exothermic D-T reaction  ${}^3\text{H}(d,n){}^4\text{He}$  is well documented<sup>34-40</sup>. The expression that we obtain including data up to 12.3 MeV is

$$\sigma_{d,n} = \left[ 7.18593 \cdot 10^{-1} + \frac{2.74077 \cdot 10^{-1}}{(E - 7.39272 \cdot 10^{-2})^2 + 4.73695 \cdot 10^{-3}} \right] \times \exp(-1.47564/\sqrt{E})/E$$

where again the numerical coefficient in the Gamow factor was treated as a variational parameter.

Below 3.7 MeV (the threshold for deuteron breakup) we assume that the  $(d,n)$  reaction (which is the only inelastic process) occurs in the  $\ell=0$ ,  $J=3/2$  channel. Therefore in this range of energies there is only one inelastic factor

$$\eta_0 = \sqrt{1 - 1.65420 E \sigma_{d,n}}$$

With this assumption, we obtain<sup>41,42</sup> for  $E < 3.7$  MeV

$$\frac{d\sigma}{d\Omega} = \frac{0.0962127}{E} \left[ \left| F_c(\theta) + \sum_{\ell=0}^2 \frac{(2\ell+1)P_\ell \Psi_\ell}{\cot\delta_{\ell 2} - i} \right|^2 + 2 \left| F_c(\theta) + \frac{i}{2} (1-\eta_0) \frac{i - \text{tg}\delta_{04}}{i + \text{tg}\delta_{04}} + \sum_{\ell=1}^2 \frac{(2\ell+1)P_\ell \Psi_\ell}{\cot\delta_{\ell 4} - i} \right|^2 \right]$$

The expressions for  $F_c(\theta)$  and  $\Psi_\ell$  are the same as in the preceding section and the quartet and doublet phase shifts  $\delta_{\ell 4}$  and  $\delta_{\ell 2}$  are given by

$$\text{tg}\delta_{04} = (-9.55679 \cdot 10^{-1} + 2.25676 \cdot 10^{-1} E) E^{1/2}$$

$$\text{tg}\delta_{02} = (-1.38718 + 3.49639 \cdot 10^{-1} E) E^{1/2}$$

$$\text{tg}\delta_{14} = (7.39132 \cdot 10^{-2} - 4.80847 \cdot 10^{-4} E) E^{3/2}$$

$$\text{tg}\delta_{12} = (2.35300 \cdot 10^{-1} - 3.00796 \cdot 10^{-2} E) E^{3/2}$$

$$\text{tg}\delta_{24} = (-2.11482 \cdot 10^{-2} + 2.30548 \cdot 10^{-3} E) E^{5/2}$$

$$\text{tg}\delta_{22} = (-1.04178 \cdot 10^{-2} + 3.59294 \cdot 10^{-3} E) E^{5/2}$$

Above 3.7 MeV<sup>42,43</sup> inelasticity factors have to be introduced for all partial waves and the formula becomes

$$\frac{d\sigma}{d\Omega} = \frac{0.0962127}{E} \left[ 2 \left| F_c + i \sum_{\ell=0}^2 \frac{(2\ell+1)P_\ell \Psi_\ell}{2} \left( 1 - \eta_{\ell 4} \frac{i - \text{tg}\delta_{\ell 4}}{i + \text{tg}\delta_{\ell 4}} \right) \right|^2 + \left| F_c + i \sum_{\ell=0}^2 \frac{(2\ell+1)P_\ell \Psi_\ell}{2} \left( 1 - \eta_{\ell 2} \frac{i - \text{tg}\delta_{\ell 2}}{i + \text{tg}\delta_{\ell 2}} \right) \right|^2 \right]$$

where

$$\eta_{04} = \eta_0 \exp[0.593732(1 - 3.7/E)]$$

and all the other inelasticity factors are given by

$$\eta_{\ell m} = \exp[X_{\ell m}(1 - 3.7/E)]$$

where

$$\begin{aligned} X_{02} &= -1.34428 \cdot 10^{-1} \\ X_{14} &= -4.25545 \cdot 10^{-1} & X_{12} &= -2.41299 \\ X_{24} &= -3.17153 \cdot 10^{-1} & X_{22} &= 2.29534 \cdot 10^{-1} \end{aligned}$$

The phase shifts above threshold are

$$\text{tg}\delta_{04} = [-2.32132 \cdot 10^{-1} + 6.93633 \cdot 10^{-2} (E - 3.7)] (E/3.7)^{1/2}$$

$$\text{tg}\delta_{02} = [-1.79880 \cdot 10^{-1} + 2.16838 \cdot 10^{-2} (E - 3.7)] (E/3.7)^{1/2}$$

$$\text{tg}\delta_{14} = [5.13385 \cdot 10^{-1} - 2.17363 \cdot 10^{-2} (E - 3.7)] (E/3.7)^{3/2}$$

$$\text{tg}\delta_{12} = [8.82557 \cdot 10^{-1} - 6.90601 \cdot 10^{-2} (E - 3.7)] (E/3.7)^{3/2}$$

$$\text{tg}\delta_{24} = [-3.32269 \cdot 10^{-1} - 8.18759 \cdot 10^{-4} (E - 3.7)] (E/3.7)^{5/2}$$

$$\text{tg}\delta_{22} = [7.57325 \cdot 10^{-2} - 1.09782 \cdot 10^{-2} (E - 3.7)] (E/3.7)^{5/2}$$

### Triton - Triton

The total cross section for the T-T reactions up to 1.9 MeV is<sup>44,45</sup>

$$\sigma_{t,2n} = 7.62 \cdot 10^{-2} + 5.58 \cdot 10^{-2} \log_{10} E.$$

There is one single experimental paper<sup>46</sup> on T-T elastic scattering. The expression we obtain is

$$\frac{d\sigma}{d\Omega} = \frac{0.0692965}{E} \left[ \left| F_c(\theta) + F_c(\pi-\theta) + \frac{2}{\cot\delta_0 - i} \right|^2 + 3 \left| F_c(\theta) - F_c(\pi-\theta) \right|^2 \right]$$

where

$$\text{tg}\delta_0 = -5.10253 \cdot 10^{-1} E^{1/2}.$$

The expression for  $F_c(\theta)$  is the same as previously, but with  $\eta = 0.273482/\sqrt{E}$ . There was no need of higher waves, because in ref. 46 the maximum triton energy

was 2 MeV, and a single parameter could fit all the data. Clearly, further experiments at higher energies are needed.

#### Helium 4 - Deuteron

In this section, all data refer to the  $^4\text{He}$  lab energy, the deuteron being initially at rest. We have considered only energies up to 3.9 MeV since higher energies are irrelevant for fusion calculations.

The experimental results in alpha-deuteron scattering around 2.1 MeV<sup>47,48</sup> show the existence of a well defined resonance in the  $\ell=2$ ,  $J^P=3^+$  channel. The expression that we obtain including data<sup>48,49</sup> up to 3.9 MeV is

$$\frac{d\sigma}{d\Omega} = \frac{0.155325}{E} \left[ 2 \left| F_c(\theta) + \sum_{\ell=0}^1 \frac{(2\ell+1)P_{\ell}^{\Psi_{\ell}}}{\cot\delta_{\ell}-i} + \left( \frac{2}{\cot(\delta_2+\beta)-i} + \frac{3}{\cot\delta_2-i} \right) P_2^{\Psi_2} \right|^2 + 3 \left| F_c(\theta) + \sum_{\ell=0}^1 \frac{(2\ell+1)P_{\ell}^{\Psi_{\ell}}}{\cot\delta_{\ell}-i} + \left( \frac{3}{\cot(\delta_2+\beta)-i} + \frac{2}{\cot\delta_2-i} \right) P_2^{\Psi_2} \right|^2 + \left| \frac{1}{\cot(\delta_2+\beta)-i} - \frac{1}{\cot\delta_2-i} \right|^2 (25-24.5\sin^2\theta)\sin^2\theta \right]$$

where the expressions for  $F_c(\theta)$  and  $\Psi_{\ell}$  are the same as previously, but with  $\eta=0.630074/\sqrt{E}$ . The phase shifts are given by

$$\begin{aligned} \text{tg}\delta_0 &= (4.13812 \cdot 10^{-2} - 2.03203 \cdot 10^{-1}E)E^{1/2} \\ \text{tg}\delta_1 &= (-1.09999 \cdot 10^{-2} + 3.06920 \cdot 10^{-3}E)E^{3/2} \\ \text{tg}\delta_2 &= (-7.66435 \cdot 10^{-3} + 1.44385 \cdot 10^{-3}E)E^{5/2} \\ \text{tg}\beta &= 3.22039 \cdot 10^{-2} / (2.13624 - E). \end{aligned}$$

#### Helium 4 - Triton

Again,  $E$  is the  $^4\text{He}$  lab energy, the triton being initially at rest, and we considered only energies up to 3.9 MeV.

Data on elastic scattering in this range of energies are very sparse<sup>50,51</sup> (non-existent below 2 MeV), nevertheless to obtain a reasonable fit it was necessary to introduce a  $j$ -dependence. The expression that we obtain is

$$\frac{d\sigma}{d\Omega} = \frac{0.282773}{E} \left[ \left| F_c + \sum_{\ell=0}^2 \left( \frac{\ell+1}{\cot\delta_{\ell+}-i} + \frac{\ell}{\cot\delta_{\ell}-i} \right) P_{\ell}^{\Psi_{\ell}} \right|^2 + \left| \sum_{\ell=1}^2 \left( \frac{1}{\cot\delta_{\ell+}-i} - \frac{1}{\cot\delta_{\ell}-i} \right) \frac{dP_{\ell}}{d\cos\theta} \Psi_{\ell} \right|^2 \sin^2\theta \right]$$

where  $\delta_{\ell\pm}$  denotes the  $j = \ell \pm \frac{1}{2}$  wave, and where the expressions for  $F_c(\theta)$  and  $\Psi_{\ell}$  are the same as previously, but with  $\eta = 0.630074/\sqrt{E}$ .

The phase shifts are given by

$$\begin{aligned} \text{tg}\delta_{0+} &= (-1.037485 + 2.44679 \cdot 10^{-1}E)E^{1/2} \\ \text{tg}\delta_{1+} &= (-1.14880 \cdot 10^{-1} + 1.02002 \cdot 10^{-2}E)E^{3/2} \\ \text{tg}\delta_{1-} &= (-3.32005 \cdot 10^{-1} + 1.04970 \cdot 10^{-1}E)E^{3/2} \\ \text{tg}\delta_{2+} &= -5.05390 \cdot 10^{-3} E^{5/2} \\ \text{tg}\delta_{2-} &= 7.85087 \cdot 10^{-3} E^{5/2} \end{aligned}$$

#### Concluding Remarks

The formulas which we have obtained can be considered as the best interpolation between currently available data. However, we found many other inequivalent sets of phase shifts which reproduced the experimental results almost as well as these ones. Therefore our formulas should be revised when new experimental data becomes available.

#### References

1. A. Horsley, Nucl. Data A4, 321 (1968)
2. M. Holberg, Nucl. Phys. A129, 327 (1969)
3. H.C. Catron, et al., Phys. Rev. 123, 218 (1961)
4. W.D. Allen, et al., Proc. Phys. Soc. A68, 650 (1955)
5. A.J. Elwyn, et al., Phys. Rev. 128, 779 (1962)
6. R.K. Adair, et al., Phys. Rev. 89, 1165 (1953)
7. J.D. Seagrave, et al., Phys. Rev. 105, 1816 (1957)
8. E. Wantuch, Phys. Rev. 84, 169 (1951)
9. J.D. Seagrave, et al., Ann. Phys. 74, 250 (1972)
10. B.E. Bonner, et al., Nucl. Phys. A128, 183 (1969)
11. J.C. Allred, et al., Phys. Rev. 91, 90 (1953)
12. J.D. Seagrave, Phys. Rev. 97, 757 (1955)
13. A.C. Berick, et al., Phys. Rev. 174, 1105 (1968)
14. J.D. Seagrave, et al., Ann. Phys. 74, 250 (1972)
15. J.D. Seagrave, et al., Phys. Rev. 119, 1981 (1960)
16. J.H. Coon, et al., Phys. Rev. 81, 33 (1951)
17. J.M. Kootsey, Nucl. Phys. A113, 65 (1968)
18. Los Alamos Physics and Cryogenics Groups, Nucl. Phys. 12, 291 (1959)
19. V.P. Vertebnyj, Bull. Acad. Sci. USSR, Phys. Ser. 31, 334 (1967)
20. W.A. Wenzel, et al., Phys. Rev. 88, 1149 (1952)
21. R.B. Theus, et al., Nucl. Phys. 80, 273 (1966)
22. N. Ying, et al., Nucl. Phys. A206, 481 (1973)
23. J.R. Smith, et al., Can. J. Phys. 50, 783 (1972)
24. R.L. Schulte, et al., Nucl. Phys. A192, 609 (1972)
25. S.T. Thornton, Nucl. Phys. A136, 25 (1969)
26. F.S. Dietrich, et al., Nucl. Phys. A184, 449 (1972)
27. J.E. Brolley Jr., et al., Phys. Rev. 107, 820 (1957)
28. J.M. Blair, et al., Phys. Rev. 74, 1594 (1948)
29. A.S. Wilson, et al., Nucl. Phys. A126, 193 (1969)
30. J.E. Brolley, et al., Phys. Rev. 117, 1307 (1960)
31. L. Rosen, et al., Phys. Rev. 76, 1283 (1949)
32. L. Rosen, et al., Phys. Rev. 88, 431 (1952)
33. J.C. Allred, et al., Phys. Rev. 76, 1430 (1949)
34. W.R. Arnold, et al., Phys. Rev. 93, 483 (1954)
35. H.V. Argo, et al., Phys. Rev. 87, 612 (1952)
36. S.J. Bame, et al., Phys. Rev. 107, 1616 (1957)
37. J.R. Smith, et al., Nucl. Phys. A187, 433 (1972)
38. M.D. Goldberg, et al., Phys. Rev. 122, 164 (1961)
39. J.E. Brolley Jr., et al., Phys. Rev. 82, 502 (1951)
40. L.E. Stewart, et al., Phys. Rev. 119, 1649 (1960)
41. W.R. Stratton, et al., Phys. Rev. 88, 257 (1952)
42. M. Ivanovich, et al., Nucl. Phys. A100, 441 (1968)
43. J.E. Brolley, et al., Phys. Rev. 117, 1307 (1960)
44. A.M. Govorov, et al., Soviet Phys. JETP 15, 266 (1962)
45. N. Jarmie, et al., Phys. Rev. 111, 1121 (1958)
46. D.M. Holm, et al., Phys. Rev. 101, 1772 (1956)
47. T. Lawritsen, et al., Phys. Rev. 92, 1501 (1953)
48. A. Galonsky, et al., Phys. Rev. 98, 586 (1955)
49. J.M. Blair, et al., Phys. Rev. 75, 1678 (1949)
50. L.S. Chuang, Nucl. Phys. A174, 399 (1971)
51. A. Hemmendinger, Bull. Am. Phys. Soc. 1, 96 (1956)



The neutron emission spectra from <sup>238</sup>U spheres pulsed with 14-MeV neutrons have been measured from the source energy down to 10 keV and have been compared with calculations employing ENDF/B-IV and ENDL cross sections. The low energy spectra (10 keV to 1 MeV) are best described using ENDF/B-IV cross sections while the high energy spectra (2 MeV to 15 MeV) are best described using ENDL cross sections. It is concluded that use of ENDL cross sections should yield the best estimate of tritium breeding and ENDF/B-IV that of Pu breeding in a CTR fusion-fission blanket.

[<sup>238</sup>U Pulsed Sphere Measurements; spectra from 10 keV to 15 MeV compared with calculations; implications for fusion-fission blanket calculations.]

### Introduction

A recent study<sup>1</sup> has shown that the breeding of tritium and Pu in a CTR fusion-fission blanket is quite sensitive to the emission spectra from 14-MeV neutrons on <sup>238</sup>U and other structural materials in the reactor. To have confidence in the breeding calculations, it is essential that the cross sections used in the calculations describe reasonably well the neutron emission spectra from 14-MeV neutrons incident on <sup>238</sup>U. The neutron emission spectra from 0.8 and 2.8 mean-free-paths (m.f.p.) <sup>238</sup>U spheres pulsed with 14-MeV neutrons have been measured from the source energy down to 10 keV. From a comparison of these measurements with calculations, it is concluded that use of ENDL cross sections<sup>2</sup> should yield the best estimate of tritium breeding and ENDF/B-IV that of Pu breeding in a CTR fusion-fission blanket.

### Experimental Method

Figure 1 shows the 0.8 and 2.8 m.f.p. <sup>238</sup>U spheres. A conical insert was machined into the spheres in order to accommodate the low mass target assembly. A tritium loaded titanium target was located at the center of the spherical targets. A solid state silicon detector at 174° with respect to the D<sup>+</sup> beam line monitored the neutron production by counting the associated <sup>4</sup>He particle from the T(d,n)<sup>4</sup>He reaction. For measurements between 2 and 15 MeV, 5.1 cm diameter by 5.1 cm long NE 213 and Pilot B scintillators were used at 120° and 30° respectively. The flight paths were 765 cm at 30° and 977 cm at 120°. The repetition rate for the high energy measurements was 2.5 MHz and the burst width was 4 ns.

For measurements between 10 keV and 1 MeV, a 5.1 cm diameter by 1.9 cm long <sup>6</sup>Li glass scintillator was used at 26° with respect to the deuteron beam line at a flight path of 801 cm. The burst widths were 10 and 100 ns while the repetition rate was 10 KHz. A detailed description of the neutron detector packages and the collimations employed is given in ref. 3.

Standard time-of-flight electronics were used in measuring the emitted spectra. The stop pulses into the time-to-amplitude converter were generated from a capacitive beam pick-off unit. Time calibration of the system and the conversion from counts (cts)/channel to cts/ns (high energy) and cts/μs (low energy) are described in detail in ref. 3. The high energy data are presented as time-of-flight spectra while the low energy data have been converted into energy spectra.

### Experimental Results and Calculations

Figures 2 and 3 show the measured and calculated high energy time-of-flight spectra. The various spectra are identified by the <sup>238</sup>U sphere size, angle of observation and cross section library used. Figures 4, 5 and 6 show the similarly identified low energy spectra.

The high energy spectra are presented as cts (sphere in) per ns per total 14 MeV cts (sphere out). The high energy spectra calculations therefore require that the Pilot B and NE 213 detector efficiencies be folded into the Monte Carlo calculations.

The low energy spectra measurements are presented as neutron/keV/source neutron. The conversion from cts to neutrons requires a knowledge of the <sup>6</sup>Li glass detection efficiency. The detection efficiencies for the <sup>6</sup>Li glass and Pilot B, NE 213 scintillators can be found in ref. 3. The absolute source strength was required for the low energy measurement and it was obtained by calibrating the alpha counter against the 14-MeV flux as measured with the NE 213 and Pilot B scintillators. Reference 4 describes in detail the measurement and data processing of the low energy spectra. In particular, it describes the determination of the time independent background by inserting in good geometry a thick paraffin absorber between the <sup>6</sup>Li detector and <sup>238</sup>U sphere.

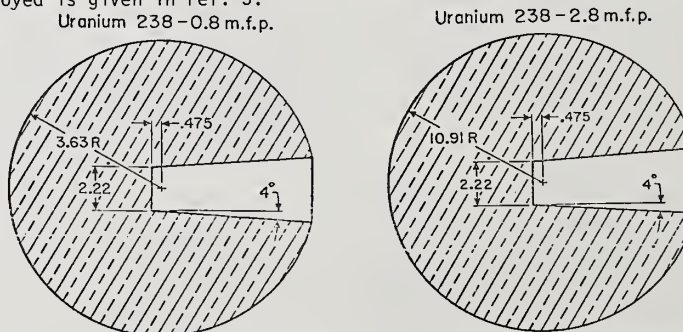


Fig. 1 Schematic drawing of the 0.8 and 2.8 m.f.p. <sup>238</sup>U spheres  
(Dimensions are in centimeters)



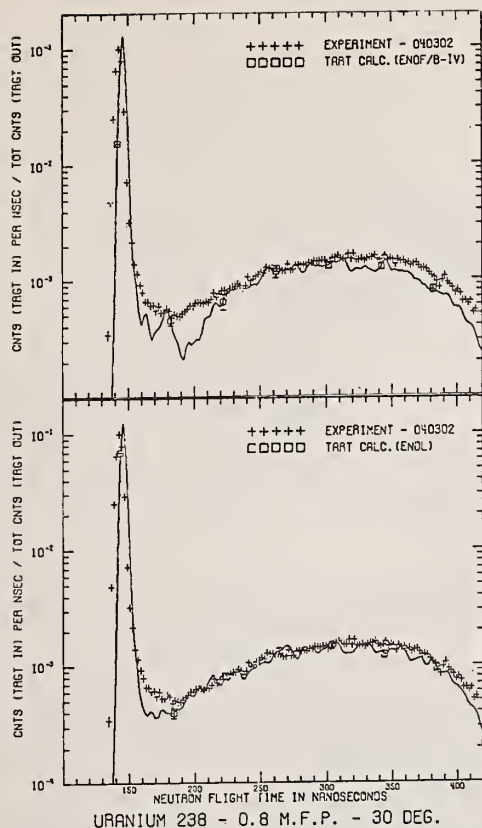


Fig. 2 Comparison between the high energy measurements and calculations for the 0.8 m.f.p.  $^{238}\text{U}$  sphere at  $30^\circ$ .

#### Comparison With Calculations

Table 1 presents a comparison of the measured and calculated integrals for the high energy time-of-flight spectra shown in figs. 2 and 3. The integral above 12 MeV (<164 ns) is a measure of the non-elastic cross section while the integral from 2 to 12 MeV (400 to 164 ns) is a measure of the high energy neutron emission cross section from  $\sigma(n,n')$ ,  $\sigma(n,2n)$ , and  $\bar{\nu}_{sf}$ . Table 1 shows that the ENDF/B-IV non-elastic cross section is correct while that of ENDL appears to be slightly high. In the 2-12 MeV region ENDL gives better agreement with measurements than ENDF/B-IV. The ENDF/B-IV discrepancy for the 2-12 MeV region increases from -16% to -20% in going from 0.8 to 2.8 m.f.p.

Table 1 Comparison of measured<sup>a</sup> and calculated integrals for the  $30^\circ$  high energy emission spectra shown in figs. 2 and 3. 2 and 12 MeV correspond to flight times of 400 and 164 ns, respectively. See figs. 2 and 3 for units on the integrals.

m.f.p.	Measured		ENDF/B-IV		ENDL	
	2-12	>12	2-12	>12	2-12	>12
0.8	0.263	0.644	0.224	0.643	0.243	0.630
2.8	0.324	0.233	0.260	0.232	0.286	0.216

- a. The absolute error on the measured integrals is  $\pm 5\%$ . The error on the ratio of two integrals is  $\pm 3\%$ .
- b. These calculations agree with previous calculations by Howerton.<sup>9</sup>

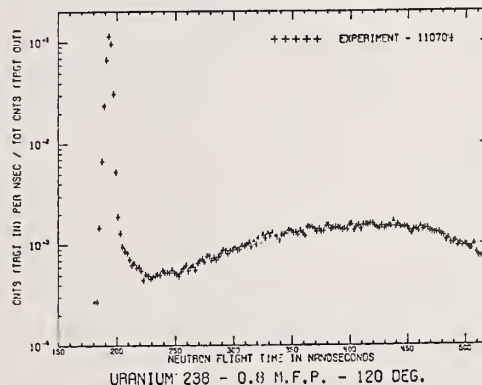
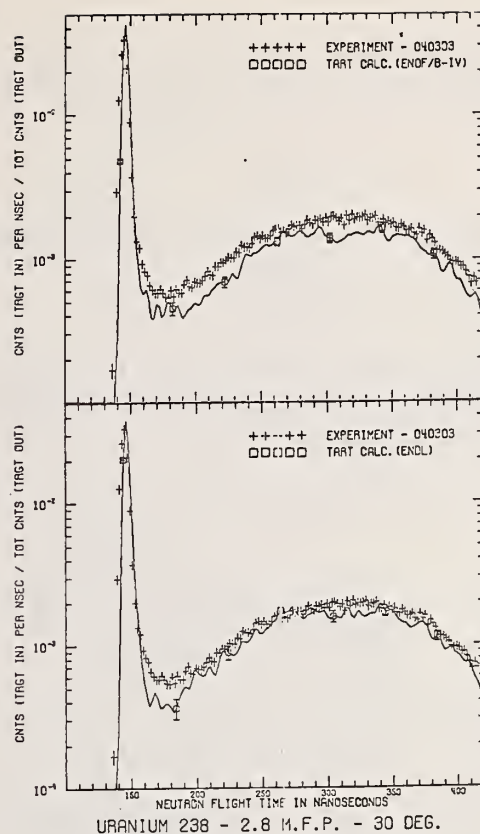


Fig. 3 Comparison between the high energy measurements and calculations for the 2.8 m.f.p. sphere at  $30^\circ$ . The 0.8 m.f.p. data at  $120^\circ$  are presented without calculations.

Table 2 presents the integrals of the 100 ns low energy spectra of figs. 4 and 5 between 10 and 934 keV. Table 2 and figs. 4 and 5 show that the best overall agreement is achieved using ENDF/B-IV cross sections. This agreement is further illustrated by comparison of ENDF/B-IV calculations with the higher resolution 10 ns measurements shown in fig. 6. At 2.8 m.f.p. ENDL yields the correct integral by overestimating the higher energy and underestimating the lower energy neutrons.

Table 2 Comparison of measured<sup>a</sup> and calculated integrals for the emission spectra shown in figs. 4 and 5 between 10 and 934 keV. See figs. 4 and 5 for units.

	0.8 m.f.p. ( $\times 10^{-7}$ )	2.8 m.f.p. ( $\times 10^{-6}$ )
Measured	9.40	3.70
ENDF/B-IV	10.0	3.75
ENDL	8.57	3.65

a. The absolute error on the measured integrals is  $\pm 10\%$  and arises from the uncertainty in the  $^6\text{Li}$  glass efficiency. The error on the ratio of the two measured integrals is  $\pm 5\%$ .

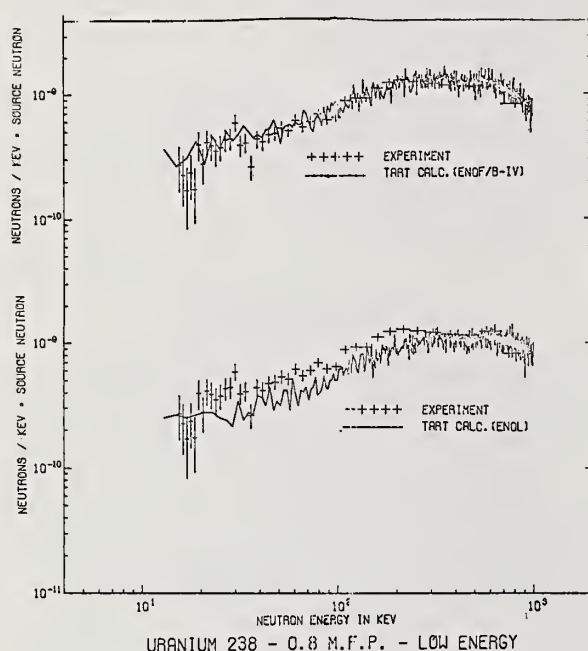


Fig. 4 Comparison between the low energy 100 ns measurements and calculations for the 0.8 m.f.p. sphere.

### Conclusions

Neither library yields satisfactory agreement with both low and high energy spectra. However, ENDL should yield the most reliable estimate of tritium breeding and total fissions in a CTR blanket since it yields the best agreement for the 2.8 m.f.p. high energy spectra and gives the correct number of low energy neutrons for the 2.8 m.f.p. sphere. Agreement with the 2.8 m.f.p. measurements is emphasized since the blanket is fueled with a thick layer of  $^{238}\text{U}$ . Also, because of multiple collisions, the total number of low energy neutrons is more important than exact spectral shape. On the other hand, the breeding of Pu comes mainly from neutron capture below 1 MeV. Since ENDF/B-IV yields the correct number and spectral shape for neutrons between 10 and 934 keV it should yield the most reliable estimate of Pu breeding.

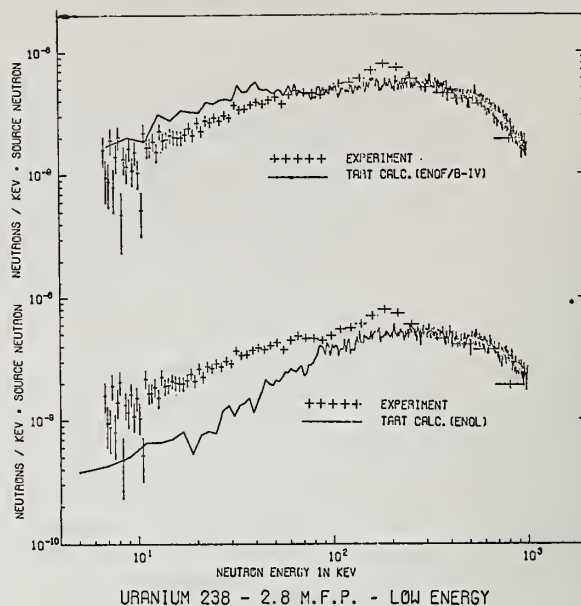


Fig. 5 Comparison between the low energy 100 ns measurements and calculations for the 2.8 m.f.p. sphere.

An earlier calculation<sup>1</sup> of the tritium breeding using ENDL cross sections yielded 1.26 tritons per 14-MeV neutron into the blanket. Since then, ENDL has been revised<sup>6</sup> by decreasing the fission cross section and increasing the  $(n,3n)$  cross section in order to preserve the non-elastic cross section. The predictions shown in figs. 2-5 and tables 1 and 2 were calculated with this latest revised ENDL library. As expected, this revised library yielded a lower tritium breeding ratio of 1.11. The corresponding total fissions using revised ENDL is 0.864, and the Pu breeding using ENDF/B-IV is 2.23.

The present measurements do not cover the energy range between 1 and 2 MeV. Since the various libraries predict percentages from 15 to 25% for neutrons between 1-2 MeV in the sphere calculations, it is clear that these neutrons contribute significantly to total fissions and tritium breeding, and measurements in this energy range would provide additional checks on the various libraries.



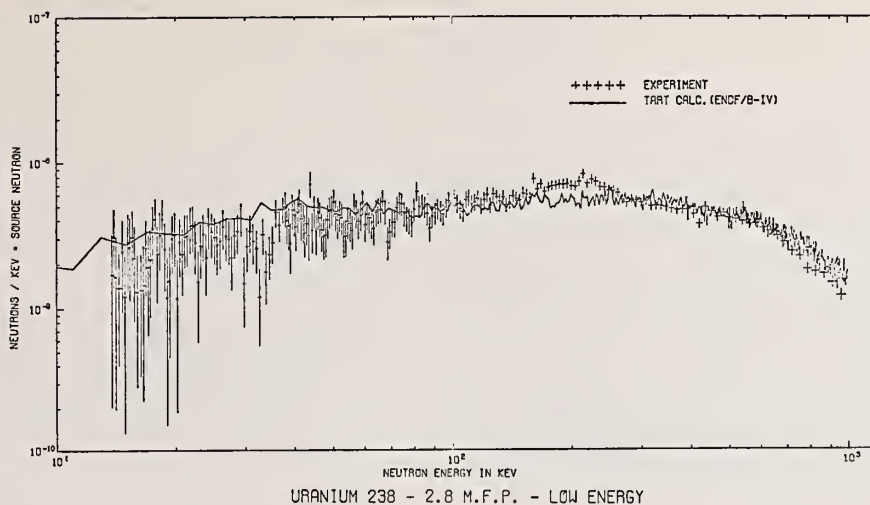


Fig. 6 Comparison between the low energy 10 ns measurements and calculations for the 2.8 m.f.p. sphere.

#### References

1. R. C. Haight and J. D. Lee, Proceedings of the First Topical Meeting on the Technology of Controlled Nuclear Fusion, April 16-18, 1974, San Diego CA (p.271)
  2. R. J. Howerton and M. H. MacGregor, Evaluated Neutron Reaction Data for  $^{238}\text{U}$ , UCRL-51427 (1973) unpublished.
  3. C. Wong et al., Livermore Pulsed Sphere Program: Program Summary Through July 1971, UCRL-51144, Rev. 1, (1972) unpublished.
  4. C. Wong et al., Livermore Pulsed Sphere Program: Low Energy Measurements on Carbon, Iron and Concrete, UCRL-51144, Addendum (1973) unpublished.
  5. R. J. Howerton, Testing of ENDF/B-IV-P Evaluations with SDT-10 Benchmark Pulsed Spheres, UCRL-75693 (Preprint) May 10, 1974.
  6. R. J. Howerton (private communication).
- \*Work performed under the auspices of the Energy Research and Development Administration.

# REACTIVITIES FOR TWO-COMPONENT FUSION CALCULATIONS\*

George H. Miley and Harry H. Towner  
Nuclear Engineering Program  
University of Illinois  
Urbana, Illinois 61801

Tables and graphs of fusion reactivities ( $\langle\sigma v\rangle$ ) are readily available for fusion in thermalized (Maxwellian) plasmas using common fuels. However, plans to construct the Two-Component Torus (TCT) have created a need for reactivities to characterize fusion via high-energy beams interacting with low-temperature target plasmas. Such reactivities are derived in the present paper for a variety of fuels including  $D\rightarrow T$ ,  $D\rightarrow^3\text{He}$ ,  $D\rightarrow D$ ,  $T\rightarrow T$ ,  $T\rightarrow^3\text{He}$ , and  $p\rightarrow^{11}\text{B}$ . Some examples of the use of these reactivities in two-component calculations are also described.

(Fusion Reactivities; Two-Component Torus (TCT); Fusion Energy Multiplication; Advanced Fusion Fuels; Fusion Cross Sections; Doppler Effect)

## Introduction

With the steadily increasing research in fusion, a need has developed for a convenient collection of both fusion cross sections and reactivities (i.e.  $\langle\sigma v\rangle$  values). Averaged reactivities are employed in the computation of fusion rates which, for species 1 and 2, are by definition given as  $n_1 n_2 \langle\sigma v\rangle_{1,2}$ . The average indicated must be over the appropriate energy distribution of the reacting species. Until recent years, most of the interest was directed towards fusion in thermalized plasmas that could be accurately represented by a Maxwellian ion distribution function. Thus plots of reactivities averaged over Maxwellian distributions are reasonably available<sup>1,2</sup>, at least for the more common fusion fuels such as D-T, D-D, and D- $^3\text{He}$ . Plans to construct a Two-Component Torus (TCT)<sup>3</sup> have generated a need for reactivities which describe fusion between high-energy beams and a target Maxwellian plasma, the dominant fusion process in the TCT. This requirement motivated the present work.

## Reactivity Calculations

In general, the reactivity is defined as:

$$\langle\sigma v\rangle = \int_{\vec{v}_1} \int_{\vec{v}_2} f_1(\vec{v}_1) f_2(\vec{v}_2) |\vec{v}| \sigma(|\vec{v}|) d\vec{v}_1 d\vec{v}_2 \quad (1)$$

where  $f_1(\vec{v}_1)$  and  $f_2(\vec{v}_2)$  are the velocity distributions of the two fusing species (normalized to unity),  $\vec{v} = \vec{v}_1 - \vec{v}_2$  is the relative velocity of the two species, and  $\sigma(|\vec{v}|)$  is the fusion cross section for the reactants. For the normal Maxwellian plasma with equal ion temperatures, T, this expression reduces to:

$$\langle\sigma v\rangle = \frac{4}{\sqrt{2\pi m_1}} \left( \frac{\mu}{m_1 kT} \right)^{3/2} \int_0^\infty dE E \sigma(E) \exp\left(-\frac{\mu E}{m_1 kT}\right). \quad (2)$$

Here the energy variable, E, is given as  $m_1 v^2/2$  where v is the relative velocity, while the reduced mass of the two fusing ions is given by  $\mu$ . For completeness, we have evaluated this "Maxwellian" reactivity and it is shown in Fig. 1. Since these results are based on the same cross sections that are employed later for beam-target reactivities, this provides a means of

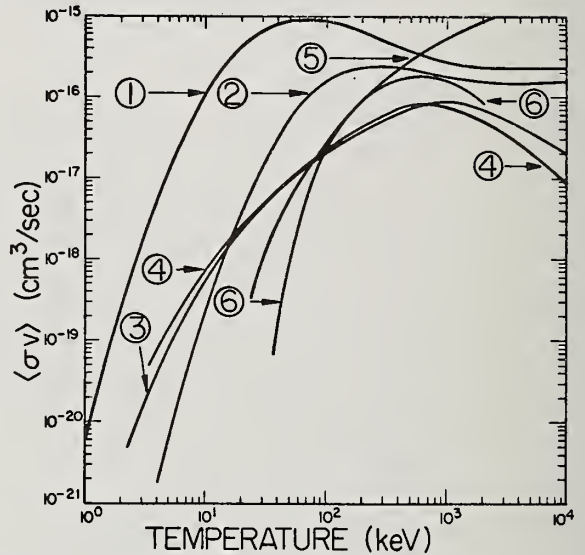


Fig. 1. Reactivities for fusion in a Maxwellian plasma of temperature  $T_i \equiv T$ . Here the curves correspond to: 1.  $T(d,n)^4\text{He}$ ; 2.  $^3\text{He}(d,p)^4\text{He}$ ; 3.  $D(d,p)T$ ; 4.  $T(t,2n)^4\text{He}$ ; 5.  $T(^3\text{He},x)^4\text{He}$  (where  $x=p+n$ , or  $d$ , or  $p$  and  $y = ^4\text{He}$  or  $^5\text{He}$ ); and 6.  $^{11}\text{B}(p,2^4\text{He})^4\text{He}$ .

comparing the present cross section set to that used by others.<sup>1,2</sup> In general, the agreement is good although some slight differences are observed.

The first five reactions shown were evaluated using a fit to experimental cross section data developed by Duane<sup>4</sup>, namely:

$$\sigma(E) = [E\{\exp(A1\sqrt{E})-1\}]^{-1} [A2/\{1+(A3xE-A4)^2\}+A5]. \quad (3)$$

Here E refers to the relative energy of the incident ion in eV and the values of the constants A1 through A5 are tabulated in Refs. 4 and 5. The cross section for the  $p\text{-}^{11}\text{B}$  reaction was obtained by fitting the data of Jarmie and Seagrave<sup>6</sup> in energy segments as described in Ref. 5. These fits, shown in Fig. 2, are thought to be accurate to within a few percent over the energy range involved. All of the cross sections exhibit a characteristic resonance; and compared to the

\*Work performed under auspices of E.R.D.A.

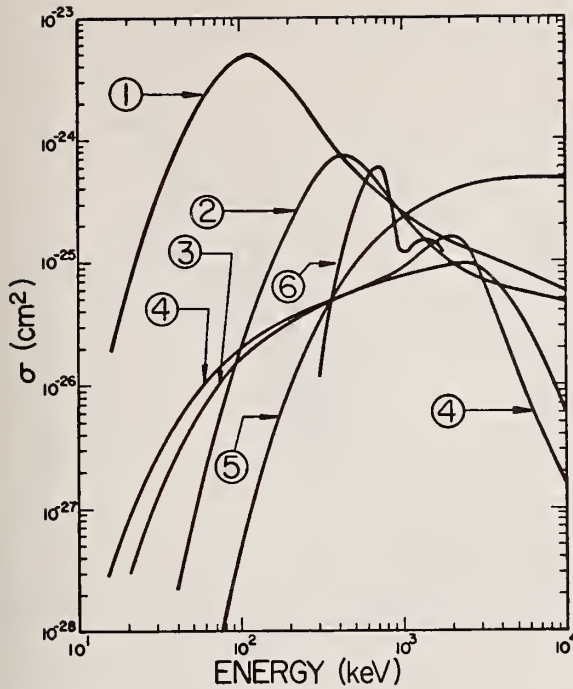


Fig. 2. Fusion cross sections. The curve numbers correspond to reactions listed in Fig. 1.

"standard" D-T cross section, several of the fuels such as p-<sup>11</sup>B and D-<sup>3</sup>He have a narrower resonance width.

While various measurements for the common reactions seem to be in reasonable agreement, there are some noticeable discrepancies in data reported for T-T, T-<sup>3</sup>He, and particularly for p-<sup>11</sup>B. However, the absolute accuracy of the original data used is not certain, so this must be viewed as an unevaluated data set. Tabular presentations from computer print outs of the reactivities and cross section shown in Figs. 1 and 2 are given in Ref. 5 if a more accurate determination is desired.

In the two-component system, fusion occurs as injected high-energy ions slow down in the target plasma. Thus, it is convenient to define an "instantaneous" reactivity corresponding to the reaction between a beam species at velocity  $\vec{v}_0$  and the target plasma at temperature T. As shown later, average fusion rates can then be calculated by integrating the instantaneous reactivity over the slowing down distribution of the injected beam.

In this case, the velocity distribution for the target ions (say species 2) is described by a Maxwellian distribution. That is:

$$f_2(\vec{v}_2) = \frac{\beta^3}{\pi^{3/2}} \exp[-(\beta \vec{v}_2)^2] \quad (4)$$

where  $\beta^2 = m_2/(2T_B)$ . Here the temperature of the target (or background) ions is given by  $T_B$  (in energy units) and their mass as  $m_2$ .

Since the beam is assigned an instantaneous velocity  $\vec{v}_0$ , we have, by definition

$$f_1(\vec{v}_1) = \delta(\vec{v}_1 - \vec{v}_0) \quad (6)$$

where  $\vec{v}_0$  is the velocity of the injected beam particles.

After changing the integration variables in Eq. (1) from  $\vec{v}_1$  and  $\vec{v}_2$  to  $\vec{v}_1$  and  $\vec{v}$ , the instantaneous two-component reactivity becomes:

$$\langle \sigma v \rangle_b = \frac{\beta^3}{\pi^{3/2}} \int_{\vec{v}_1} \delta(\vec{v}_1 - \vec{v}_0) d\vec{v}_1 \int_{\vec{v}} \sigma(|\vec{v}|) |\vec{v}| \times \exp(-\beta^2(v^2 + v_0^2 + 2\vec{v}_1 \cdot \vec{v})) d\vec{v}. \quad (7)$$

Here the subscript b is added to distinguish this reactivity from the previous case for Maxwellian fusion [Eq. (2)]. By using spherical coordinates and letting  $\vec{v}_1$  lie in the z direction, the integration over  $\vec{v}_1$  and  $\phi$  can be completed. Then Eq. (7) simplifies to:

$$\langle \sigma v \rangle_b = \frac{2\beta^3}{\sqrt{\pi}} \int_{v=0}^{\infty} \sigma(v) v^3 \times \int_0^{\pi} \exp(-\beta^2(v^2 + v_0^2 + 2vv_0 \cos \theta)) \sin \theta d\theta dv \quad (8)$$

Finally, performing the  $\theta$  integration, the following form for the beam-target reactivity is obtained:

$$\langle \sigma v \rangle_b = \frac{2\beta}{\sqrt{\pi}} \frac{1}{v_0} \int_{v=0}^{\infty} \sigma(v) v^2 \exp(-\beta^2(v^2 + v_0^2)) \times \sinh(2\beta^2 v_0 v) dv. \quad (9)$$

Results from the numerical evaluation of this reactivity, using the cross sections described earlier, are illustrated in Figs. 3a and 3b. Additional results and tabulations may be found in Ref. 5. The  $\langle \sigma v \rangle_b$  curves display a shape characteristic of the resonance behavior of the fusion cross sections. The width (in energy) of the curves is somewhat larger than for the corresponding cross section per se due to the integration over target velocities. However, these reactivities are much more sharply peaked than the normal Maxwellian reactivities of Fig. 1 since the latter involve a second integration over a broad velocity distribution.

For clarity, curves are only shown for two target plasma temperatures,  $T_1 = 0$  and 50 keV. (Results for intermediate temperatures are given in Ref. 5). As described later the temperature effect on  $\langle \sigma v \rangle_b$  is of importance to energy multiplication calculations, and it can be likened to a Doppler effect, i.e. as  $T_B$  increases, the reactivity curves broaden in energy width. This can be understood physically by observing that in the region below the peak in the cross section, the relative ion velocities, on the average, are below the optimum for a maximum reaction rate. Hence when



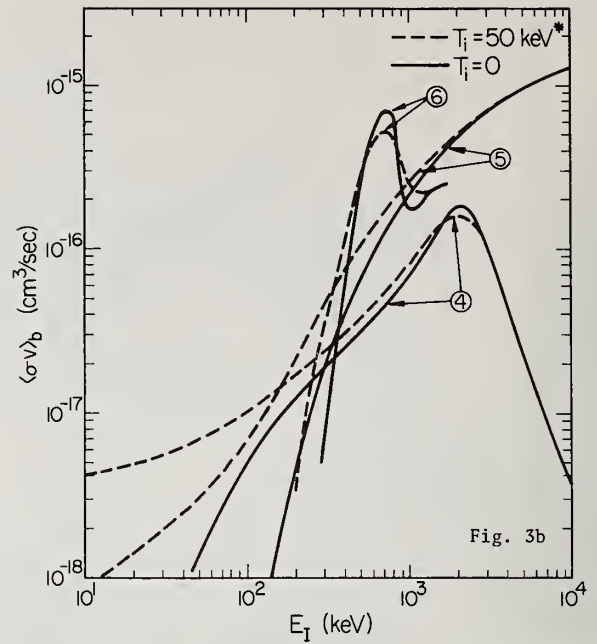
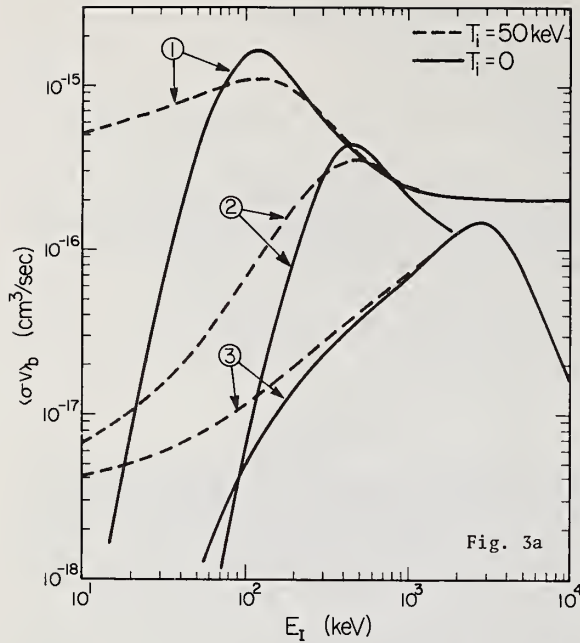


Fig. 3. Instantaneous two-component reactivities. The curve numbers correspond to reactions listed in Fig. 1 except now the first symbol represents the target, e.g.  $T(d,n)^4\text{He}$  indicates D injected into T. (Curves for  $T_i \neq 0$  assume 50 keV except reaction 6 where  $T_i = 100$  keV.)

the target temperature, i.e. velocity increases, the relative ion velocity moves closer to the optimum. Just the reverse effect occurs for energies above the peak.

In the limit where the injection energy is much larger than the background temperature, the relative velocity essentially reduces to the velocity of the injection ion. As a result, the  $\langle \sigma v \rangle_b$  values become temperature independent for large injection energies.

Finally, it should be noted that the maximum values for the two-component reactivities are of the same order of magnitude as that obtained in the usual Maxwellian case. This is important since large power densities are desirable from an economic point of view.

Indeed, Jassby<sup>7</sup> has shown that two-component systems potentially can achieve quite high power densities.

#### Energy Multiplication Calculations

To illustrate the use of these results, the calculation of fusion energy multiplication for two-component operation will be considered. Two types of operation can be envisioned: normal injection into a target plasma or, alternately, injection followed by magnetic compression designed to "clamp" the beam ions at high energies. In the first case the energy multiplication ratio is designated as an F-value while, to distinguish clamping, the term G-value is commonly used in that case. We will briefly consider both.

**F-Value Calculations.** The F-value, defined as the ratio of the total fusion energy produced via beam-target interactions to the energy injected into the plasma, can be written as:

$$F = \frac{n_B Q_f}{E_I} \int_0^{\tau_{SD}} \langle \sigma v \rangle_b dt = \frac{n_B Q_f}{E_I} \int_{E_I}^{E_{th}} \frac{\langle \sigma v \rangle}{|dE/dt|} dE \quad (10)$$

where it is recognized that  $\langle \sigma v \rangle_b$  varies with time, i.e. with the energy of the injected ions as they slow down. Here  $n_B$  is the target ion density,  $Q_f$  is the energy released per fusion reaction, and  $\tau_{SD}$  is the thermalization time, i.e. the time required for an ion injected at energy  $E_I$  to reach the average background plasma energy  $E_{th}$  (for numerical evaluation  $E_{th}$  has arbitrarily been taken as  $2kT_B$ ). The transformation to an energy integration is convenient since it introduces  $|dE/dt|$ , the time rate of energy loss of injected beam ions, which is easily evaluated. This formulation neglects the energy spread or dispersion of the injected ions during slowing, but, as noted later, for most cases this is a reasonable approximation.

F-values calculated in this fashion are shown for  $D \rightarrow T$ , i.e. for deuterium injected into a pure tritium target in Fig. 4. [Here and in subsequent sections the convention  $x \rightarrow y$  indicates that species  $x$  is injected into a target plasma of species  $y$ .]

In evaluating Eq. (10) the Fokker-Planck slowing-down model of Sivukhin<sup>8</sup> was used to represent the energy loss rate  $|dE/dt|$ . The curves shown assume a hot electron background plasma but cold ions ( $T_i \sim 0$ ). As originally discussed by Dawson, et al.<sup>9</sup>, the results for  $D \rightarrow T$  are quite favorable and can be achieved with less demanding confinement times than Maxwellian-fusion plasmas with equivalent energy multiplication. For breakeven operation ( $F = 1$ ), for example, TCT operation

requires  $E_I$  of order of 120 keV at  $T_e \sim 5$  keV. However, to reach the Lawson breakeven point (corresponding to a recirculation of the output power at 33% conversion efficiency and reinjection at 100% efficiency),  $F = 2$  is required making considerably higher electron temperatures necessary. For economic electrical production, an energy multiplication approaching 10 is desirable, necessitating higher background temperatures to achieve additional Maxwellian fusion<sup>10</sup>. Still for near-term experiments or for special purpose reactors where high power densities (regardless of recirculation rates) are the goal<sup>7</sup>, two-component operation appears to be quite attractive.

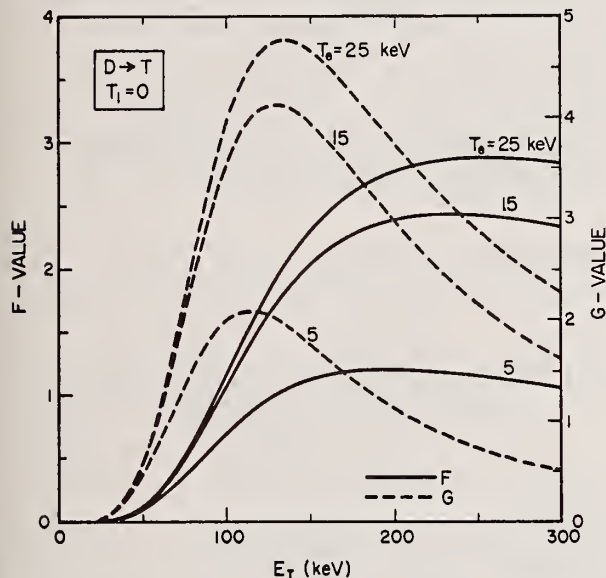


Fig. 4. Energy multiplication for injection of a deuterium beam of energy  $E_I$  into a tritium target plasma of density  $\sim 1 \times 10^{14} \text{ cm}^{-3}$  with electron temperature  $T_e$  and cold ions ( $T_i = 0$ ).

The effect of ion temperature on the F-value has been discussed elsewhere<sup>11</sup> and is illustrated in Fig. 5 for D-T over the range of injection energies expected for early TCT experiments. In this region it is observed that the F-values increase slowly with increasing  $T_i$ . The reason can be explained with reference to Eq. (10). As  $T_i$  increases, the ion drag is reduced, giving a longer thermalization time which is a positive effect. However, the increase in  $\langle \sigma v \rangle_b$  with  $T_i$  for lower energies (cf Figs. 3a and 3b) due to the Doppler effect noted earlier dominates, and the increase in F observed is mainly due to this.

Energy dispersion during thermalization also represents a small correction to the F-value curves of Fig. 5, and an estimate of this effect is shown in Fig. 6. Again a slight increase in F-value is indicated which can be rationalized as follows. To a first approximation the beam dispersion is roughly symmetrical around the average energy. Thus, at energies below the peak in the F-value, the contribution from the high-energy "wing" of the dispersion will outweigh the contribution from the low-energy wing due to the positive slope of the F-value curve in this

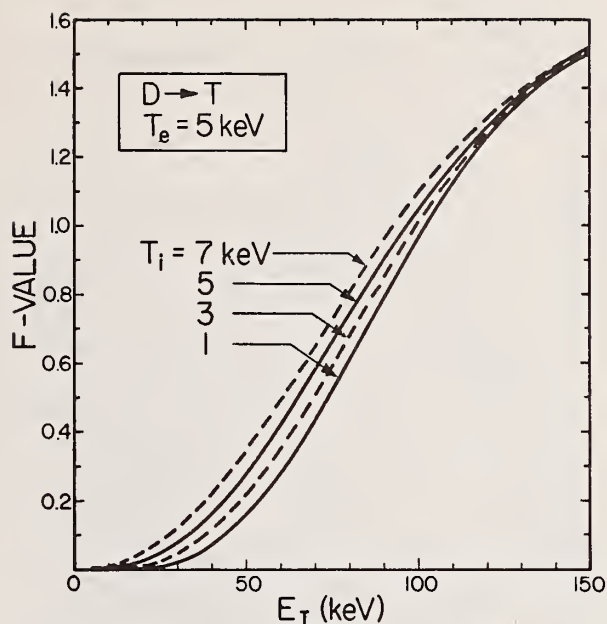


Fig. 5. Illustration of the effect of ion temperature on F-values for D-T.

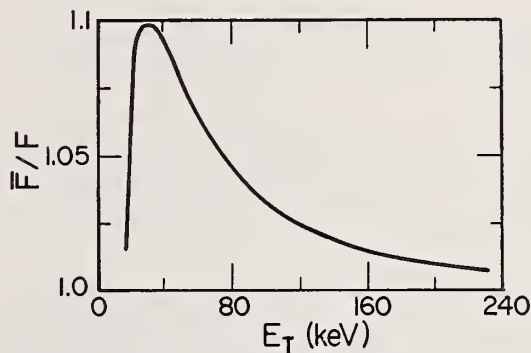


Fig. 6. Ratio of  $\bar{F}$ , the energy multiplication including dispersion, to  $F$ , the value based on the mean energy during slowing. The example shown is for D-T where  $T_e = T_i = 3$  keV at a target density of  $3 \times 10^{13} \text{ cm}^{-3}$ .

region.

In realistic situations, several other corrections must also be included, e.g. small decreases in the F-value are expected due to charge exchange and trapped electron losses under conditions typical of those expected for TCT.

Similar calculations have been carried out for other fuels<sup>11</sup> and the results for D-<sup>3</sup>He shown in Fig. 7 are typical. It is obviously difficult to obtain energy multiplications approaching unity in this case. This is characteristic of non D-T fuels<sup>12</sup>, and although energy breakeven for  $F < 1$  is possible [for example  $F = 0.23$  would provide breakeven with 90% injection and direct conversion efficiencies<sup>13</sup>], attainment of economic operation in this fashion appears as a formidable task. Thus there is a strong incentive to attempt to



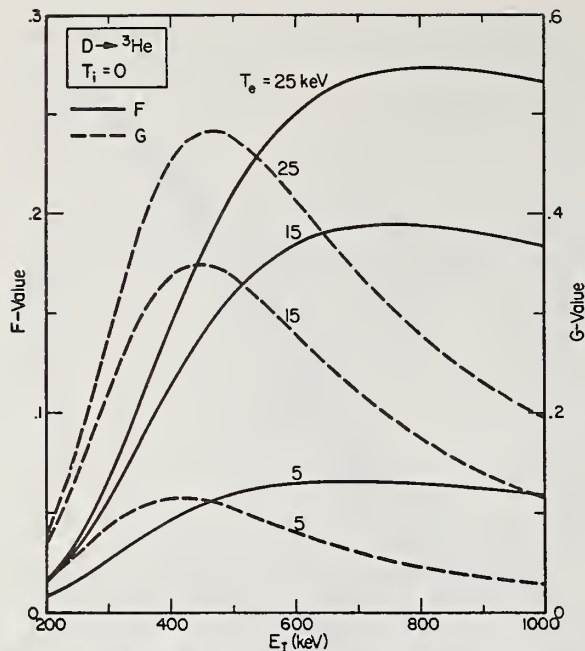


Fig. 7. Energy multiplication for injection of D into pure  $^3\text{He}$  at a target density of  $1 \times 10^{14} \text{ cm}^{-3}$ .

increase the energy multiplication by some technique such as energy clamping<sup>14</sup> or possibly colliding beam techniques<sup>15</sup>.

**Clamping.** In energy clamping magnetic compression or other techniques are employed to supply energy to the beam ions to make up for energy losses due to coulombic drag against the target plasma. In this fashion these ions can be held at high energies, i.e. near the optimum energy for fusion reactions for extended periods of time.

Energy multiplication for the clamped case is defined as the G-value. To illustrate its calculation it is assumed that clamping maintains the high-energy ions for a time long compared to the slowing down time. In that case, the energy associated with injection per se can be neglected compared to the energy required for clamping, and to a good approximation:

$$G \approx \frac{n_B Q_f \langle \sigma v \rangle_b E_I}{|dE/dt|_{E=E_I}} \quad (11)$$

The ions are assumed to be clamped at energy  $E_I$  so both the reactivity and  $|dE/dt|$  are evaluated at that energy.

As seen from Fig. 7, maximum G-values are roughly double the maximum F-values for D-He<sup>3</sup>. Another important advantage of this approach is that the injection energy requirements are almost halved. On the other hand, the large recirculating power associated with clamping must be handled very efficiently to achieve reasonable overall plant performance.

Referring back to Fig. 4, we see that maximum G-values for D-T exceed maximum F-values by factors of order of 1.7. This is somewhat lower than for D-<sup>3</sup>He because the resonance in the fusion cross section for

D-T reactions is less sharply peaked. Even larger factors in  $(G/F)_{\text{max}}$  are obtained for a very sharply peaked cross section such as p-<sup>11</sup>B.

As with normal two component fusion, various small corrections to the G-values shown in the earlier figures should be considered. For example, the effect of the ion temperature is illustrated in Fig. 8 for D-T operation. As might be expected in light of Eq. (11), the temperature effect on the G-value closely follows the Doppler change in  $\langle \sigma v \rangle_b$ . Thus, as in the

case of F-values (Fig. 5), the G-value increases somewhat with increasing  $T_i$  for lower injection energies.

However, now the transition to a negative effect occurs at a somewhat lower injection energy than in the F-value case. This happens because the F-value includes an extra integration over energy [see Eq. (10)]. In that case an ion injected at an energy above the cross-over point in the  $\langle \sigma v \rangle_b$  curve can still provide a net increase in F-values if the positive contribution as the ion slows down through the lower energy region outweighs the initial negative contribution.

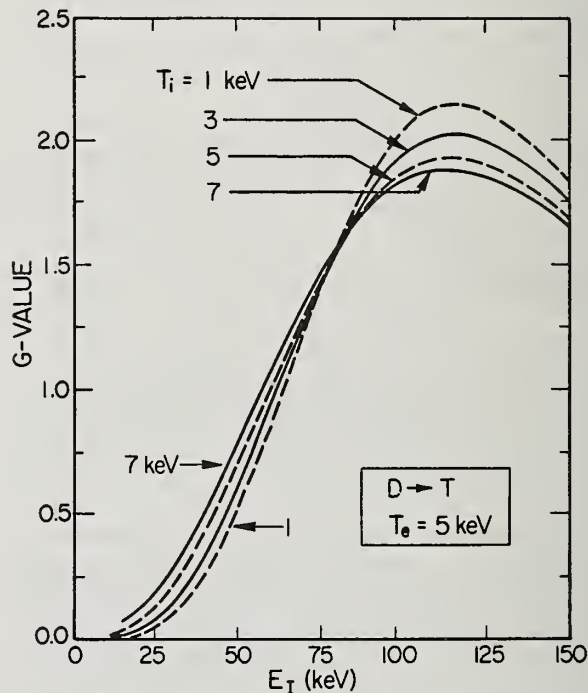


Fig. 8. Illustration of the effect of ion temperature on G-values for D-T.

Ultimately we are interested in obtaining maximum G-values. Unfortunately, in the region of the peak of these curves, the Doppler effect represents a negative contribution. The decrease in G-values is not large however, and, as stressed earlier, various additional small effects must be considered before a final assessment is possible.

### Conclusions

In conclusion, the beam-target plasma reactivities  $\langle \sigma v \rangle_b$  presented in Figs. 3a and 3b have been shown to be extremely useful in two-component fusion calculations. In such cases they replace the conven-



tional Maxwellian reactivities of Fig. 1. Applications of these reactivities to energy multiplication calculations for both normal and clamped two-component operation have been demonstrated and are thought to give reasonably accurate results. However, a number of small corrections such as involved with the ion temperature, energy dispersion and charge exchange during slowing, etc. have been noted that must be included for precision calculations.

Due to space limitations, the reactivities shown here were not complete, but an extensive listing of figures and tables has been included in Ref. 5.

The authors wish to acknowledge the assistance of N. Ivich in compilation of the cross sections and reactivities.

#### References

1. C. F. Barnett, W. B. Gauster, and J. A. Ray, "Atomic and Molecular Collision Cross Sections of Interest in Controlled Thermonuclear Research," ORNL-3113 Rev. Oak Ridge National Laboratory, (1964).
2. S. L. Green, Jr., "Maxwell Averaged Cross Sections For Some Thermonuclear Reactions On Light Isotopes," UCRL-70522, Lawrence Livermore Laboratory, (1967).
3. "TCT - Two Component Torus Joint Conceptual Design Study," Princeton Plasma Physics Laboratory and Westinghouse Electric Corporation, (1974).
4. B. H. Duane, "Fusion Cross Section Theory," in BNWL-1685, Battelle N.W. Laboratories, (1972), p. 57.
5. G. Miley, H. Towner and N. Ivich, "Fusion Cross Sections and Reactivities," AEC Report COO-2218-17, NE Program, Univ. of Illinois, (1974).
6. N. Jarmie and R. Seagrave (eds.), "Charged Particle Cross Sections," LA-2014, Los Alamos Scientific Laboratory, (1957).
7. D. L. Jassby, "Utilization of Fusion Neutrons From Beam-Driven Tokamak Reactors," TM-280, Princeton Plasma Physics Laboratory, (Nov. 1974).
8. D. V. Sivukhin, Reviews of Plasma Physics, (Consultants Bureau, New York, 1966), vol. 4, pp. 93-128.
9. J. M. Dawson, H. P. Furth, F. H. Tenney, Phys. Rev. Lett., 26, 1156 (1971).
10. R. W. Conn, W. A. Houlberg, and J. Kesner, "Parametric Studies of Driven Tokamaks," UWFD-106, Univ. of Wisconsin, (June 1974).
11. H. Towner, G. Miley, D. Jassby, and F. Tenney, Bull. Am. Phys. Soc., Ser. II, 19, 876 (1974).
12. C. Bathke, H. Towner and G. Miley, Trans. Am. Nucl. Soc., 17, 41 (1973).
13. G. Miley and H. H. Towner, "Energy Multiplication in Two-Component Plasmas," in AEC Report COO-2218-18, NE Program, Univ. of Illinois (1974).
14. D. L. Jassby and H. P. Furth, "Two-Energy-Component Fusion Reactors With Sustained Suprathermal-Ion Energy," MATT-1048, Princeton Plasma Physics Laboratory, (May 1974).
15. R. M. Kulsrud and D. L. Jassby, "Neutralized Colliding - Beam Toroidal Fusion Reactors," MATT-1114, Princeton Plasma Physics Laboratory (Jan. 1975).

E. Melkonian, J. P. Felvinci, and W. W. Havens, Jr.

Columbia University

New York, N.Y. 10027

The levels in  $^{238}\text{U}$  show unusual clusterings of large and small levels as evidenced by runs statistics and sequential correlation of values of  $\Gamma_n^\circ$ . Also,  $\Gamma_n^\circ$  is found to show significant correlation with  $\Gamma_\gamma$ . These effects are interpreted in terms of a model which assumes that excitation states are built upon persistent states of collective vibration and that an entering neutron seeks to form those states involving minimum change of particle motion.

( $^{238}\text{U}$ , resonance levels,  $\Gamma_n^\circ$ ,  $\Gamma_\gamma^\circ$ , collective motion, level densities, correlations)

We have previously reported our observations (1-3) of variations in the fission fragment energy distributions from level to level in the low neutron energy fission of  $^{233}\text{U}$  and  $^{235}\text{U}$ . In addition, we noted that many of the resonance levels, previously assumed to be single, turned out to consist of several levels corresponding to different sets of quantum numbers. In interpreting these results, we were able to form a reasonably consistent model based on two hypotheses: 1) there exist well-defined persistent collective vibrational states of the compound nucleus formed by the addition of a low energy neutron, with its about 6 Mev of binding energy, in contrast to earlier assumptions that the addition of that much energy destroys all correlations between particle motions, and 2) the collective vibrational states most likely to be formed upon the addition of a neutron are those requiring the minimum change of the internal structure of the target nucleus. The sequences of resonance levels, and the corresponding level densities, then correspond to energies left after subtraction of the collective motion energy. Where several collective states with the required quantum numbers, but different energies, exist, the possibility arises that several sequences of levels be present with different level spacings and neutron widths.

Since these ideas are not necessarily restricted to fissile nuclei, we considered other nuclides for similar effects. In particular, we examined  $^{238}\text{U}$  whose properties are important to determining breeding ratios and Doppler effects in fast breeder reactors. Rahn et al.<sup>(4)</sup> (hereafter referred to as I) have determined the resonance parameters of  $^{238}\text{U}$  to 4 Kev and have separated the levels into s-wave and p-wave on the bases of the Dyson-Mehta theory and other statistical tests. Considering only the s-wave levels of I from here on and assuming that the reduced neutron width distribution corresponds to only one Porter-Thomas distribution, one would expect to find various magnitudes of neutron widths distributed randomly with increasing neutron resonance energy. A glance at Fig. (1) based on the table of s-wave parameters of I ap-

pears to show large neutron energy regions with unusually large values of  $\Gamma_n^\circ$  and similar regions devoid of large levels. For a quantitative estimate of this observation, a Wald-Wolfowitz runs statistic test was applied to the s-wave levels of I. The first 120 levels (to 2.4 keV) have a probability of only 0.4% that they were randomly selected from a single Porter-Thomas distribution. The energy region from 1.26 to 2.2 keV (44 levels) has an unusually small number of runs and gives a similar probability of 0.1%. The probability to 3 keV is 1%. Above 3 keV, consistency with the P-T distribution is observed, but this is the energy region where the selection of pure s-wave levels could not be carried out so well. Another type of calculation, that of the correlation coefficient between successive pairs of the reduced neutron widths ( $\Gamma_n^\circ$ ), gives  $0.32 \pm 0.08$  to 2.4 keV, again indicating clustering of levels of similar magnitudes in deviation from the P-T distribution.

The absorption of a neutron by  $^{238}\text{U}$  occurs in the state  $J = 1/2^+$ ,  $K = 1/2$ , denoted by  $(1/2^+, 1/2)$ . Under the present hypotheses the energy levels are not based on the ground state of  $^{239}\text{U}$  but on collective vibrational states. Two such possible Nillson states are  $1/2 + [620]$  at 688 keV, observed by both Sheline et al.<sup>5</sup> and Bollinger and Thomas<sup>6</sup>, and  $1/2 + [600]$  calculated to be at about 2 MeV by Gustafson.

Level density calculations based on the residual energy left after subtraction of these values of collective energy give spacings of 20 ev and 200 ev respectively<sup>3</sup>. The 20 ev spacing is close to the measured value of 20.8 ev of  $\langle D \rangle$  for  $^{238}\text{U}$ , while the 200 ev figure is about the spacing of the regions with levels of large  $\Gamma_n^\circ$ . It is assumed that  $\Gamma_n^\circ$  is enhanced for those levels corresponding to the levels built upon the 2 MeV collective state.

Since there appears to be two classes of levels, depending upon coincidence or not with the levels based on the 2 MeV collective state, it becomes possible that  $\Gamma_\gamma$  might be different for the two classes. Figure 2 shows the 71 values of  $\Gamma_\gamma$  given in I for the s-wave

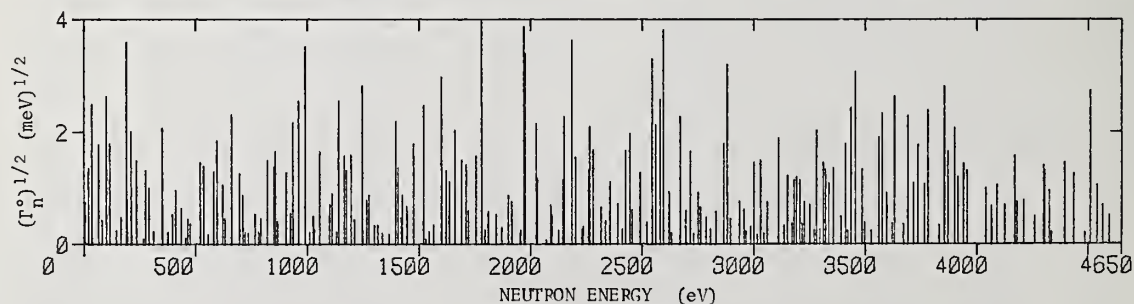


Figure 1. Magnitudes of  $(\Gamma_n^\circ)^{1/2}$  versus level energy, for levels selected as s-wave by Rahn, et al.<sup>4</sup>

levels of  $^{238}\text{U}$  plotted against  $\Gamma_n^0$ . An upward trend is apparent. Calculation of the correlation coefficient gives  $\rho = 0.53 \pm 0.09$ . Removal of levels with large  $\Gamma_\gamma$  or  $\Gamma_n^0$  drops the value of  $\rho$  to  $0.24 \pm 0.15$ , consistent with no or very small correlation. Removal of the same levels and application of the runs statistics as outlined above increases the probability of a single Porter-Thomas family to 20%. The result given is significant statistically, but it assumes that there is no bias in the determination of  $\Gamma_\gamma$ .

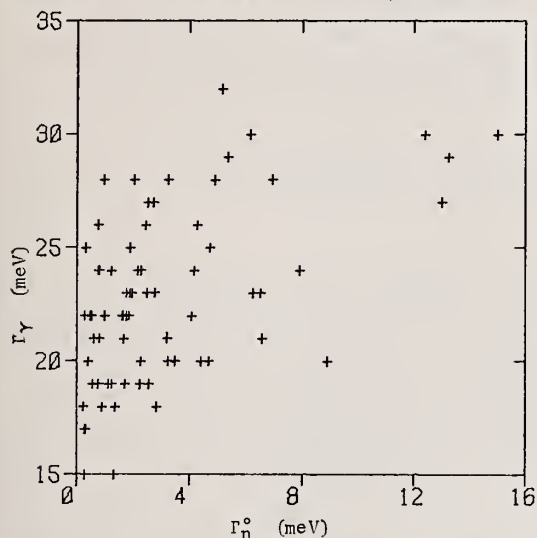


Figure 2.  $\Gamma_\gamma$  versus corresponding values of  $\Gamma_n^0$  for the 71 levels for which  $\Gamma_\gamma$  were given by Rahn, et al.<sup>4</sup>

The effects noted above are statistically significant and lend support to the suggestion of the presence of factors other than those assumed previously. Taken together with the contents of ref. 3, they lend support to the hypotheses presented above.

\* Research supported in part by the U.S.A.E.C.

#### References:

1. E. Melkonian and G.K. Mehta, Physics and Chemistry of Fission, Vol. II, 355 (1965): IAEA, Vienna.
2. J.P. Felvinci and E. Melkonian, Proceedings of the Third Conference of Neutron Cross Sections and Technology. - CONF - 710301, Vol. 2, 855 (1971).
3. J.P. Felvinci and E. Melkonian, Transactions of the ANS, 19, 420, (1974).
4. J.P. Felvinci, E. Melkonian and W.W. Havens, Jr. Paper GB 11, and D. Cacuci, J.P. Felvinci and E. Melkonian, paper EB8, Conference on Nuclear Cross Sections and Technology, (Washington, D.C.) (1975).
5. F. Rahn, H.S. Camarda, G. Hacken, W.W. Havens, Jr., H.I. Liou, J. Rainwater, M. Slagowitz, and S. Wynchank, Phys. Rev. C 6, 1854 (1972).
6. R.K. Sheline, W.N. Shelton, T. Udagawa, E.T. Journey and H.T. Motz. Phys. Rev. 151, 1011 (1966).
7. L.M. Bollinger and C.E. Thomas. Phys. Rev. C 6, 1322 (1972).



CROSS SECTION AND METHOD UNCERTAINTIES: THE APPLICATION OF SENSITIVITY ANALYSIS  
TO STUDY THEIR RELATIONSHIP IN CALCULATIONAL BENCHMARK PROBLEMS\*

C. R. Weisbin, E. M. Oblow, J. Ching, J. E. White  
R. Q. Wright, and J. Drischler

Oak Ridge National Laboratory  
Oak Ridge, Tennessee 37830

Sensitivity analysis is applied to the study of an air transport benchmark calculation to quantify and distinguish between cross-section and method uncertainties. The boundary detector response was converged with respect to spatial and angular mesh size,  $P_k$  expansion of the scattering kernel, and the number and location of energy grid boundaries. The uncertainty in the detector response due to uncertainties in nuclear data is 17.0% (one standard deviation, not including uncertainties in energy and angular distribution) based upon the ENDF/B-IV "error files" including correlations in energy and reaction type. Differences of approximately 6% can be attributed exclusively to differences in processing multigroup transfer matrices.

(Air transport; benchmark; sensitivity; profiles; uncertainties)

## I. Introduction

The complete ORNL cross section sensitivity and uncertainty analysis system (FORSS)<sup>1</sup> has been applied to estimate the overall uncertainty and the contribution of individual components in several calculational benchmark transport problems. Only relatively simplified geometries were considered so that uncertainties due to spatial modelling were considerably reduced. Since the availability of evaluated uncertainties and their correlations in energy and reaction type is limited in ENDF/B-IV but do exist for N and O, this paper describes the analysis of an air transport benchmark problem including the estimation of the effects of uncertainties in nuclear data.

Cross-section sensitivity studies of radiation transport in air have been underway for several years. The most recent and complete analysis is that of Bartine *et al*<sup>2</sup> which includes preliminary estimates of the uncertainty in cross section over broad energy ranges based on simplified assumptions about data correlations. The present work extends this type of analysis by incorporating the final, and very detailed, ENDF/B-IV uncertainty files including covariance as a function of energy and reaction type. It then attempts to go further by quantifying other types of uncertainties introduced in the analysis procedure.

Section II presents the problem characteristics pointing out the differences between the specifications used in ref. 2 and those for the present study. Section III describes the sensitivity methodology<sup>2,3</sup> used in conjunction with the point-energy discrete ordinates technique<sup>4</sup> to attempt to converge<sup>5</sup> the results with respect to the energy grid used. Section IV reviews the formulation for processing large multigroup covariance matrices<sup>6</sup> with special emphasis placed on display techniques and bulk data management schemes. Differences due to divergent cross-section processing techniques<sup>7</sup> are treated, in Section V, by successive runs with different processed sets and with projections based upon sensitivity theory. Section VI presents the results of folding covariance matrices with sensitivity profiles to estimate uncertainties due to nuclear data. The effects of using different transport methods are assessed only briefly in Section VII by comparing the results from Discrete Ordinates and Moments Method techniques. Section VIII summarizes the results and conclusions of the entire study.

## II. Benchmark Problem Definition

The source geometry approximates a point source at the center of a sphere of air of radius  $r_0$ . A uniformly distributed, isotropic source is contained within a region, characterized by radius  $r_s$ , sufficiently small with respect to the dimension of the transport media,  $r_0$ . A detector with a flat energy response,  $\Sigma_D = 1.0 \text{ cm}^{-1}$ , is distributed in a zone from  $r_D$  to  $r_0$ . The geometry is shown in Fig. 1.

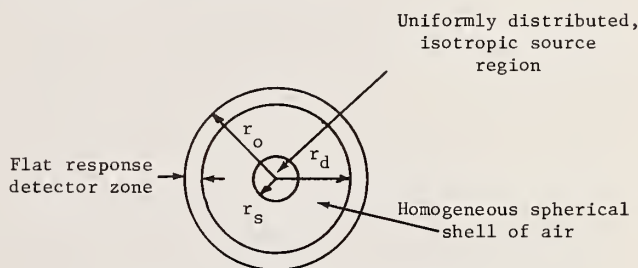


Fig. 1. Geometric Model Employed

$$r_D = 1990 \text{ m}$$

$$r_s = 12.5 \text{ m}$$

$$r_0 = 2000 \text{ m}$$

$$\rho_{14N} = 4.25 \times 10^{-5} \text{ (atoms/barn-cm)}$$

$$\rho_{16O} = 1.13 \times 10^{-5} \text{ (atoms/barn-cm)}$$

In order to standardize the source description in a form which is both general for fission and fusion devices and useful for recalculation with other methods and group structures, an analytic representation was chosen. The source spectrum was obtained by superposition of a Gaussian energy distribution around 14 MeV and a Watt fission spectrum peaked around 1 MeV. More precisely, the source spectrum was represented analytically in terms of a Gaussian

$$G(E) = G_0 e^{-\frac{1}{2}[(E-E_0)/(\Delta E)]^2} \quad (1)$$

and a Watt fission spectrum

$$F(E) = F_0 e^{-E/\alpha} \sinh[(\beta E)^{1/2}] \quad (2)$$

\*Research performed by Union Carbide Nuclear Division under contract with the United States Energy Research and Development Administration.

where  $E$  is the neutron energy in MeV,  $E_0 = 14$  MeV,  $\Delta E = 1$  MeV,  $\alpha = 1$  MeV,  $\beta = 2$  MeV<sup>-1</sup>,  $G(E)$  and  $F(E)$  are in units of source neutrons/sec-MeV-cm<sup>3</sup>, and the constants  $G_0$  and  $F_0$  are determined by normalizing the total source strength to unity over the energy range of interest with half of the neutrons coming from each of the distributions. That is

$$\int_E \int_{r_s} G(E) dE dV = \int_E \int_{r_s} F(E) dE dV = 0.5 \quad (3)$$

A graph of the source spectrum is presented in Fig. 2. The transport characteristics of the media are illustrated in Fig. 3 which presents the macroscopic total cross section for air between 100 keV and 15 MeV. The quantity of interest is the flux everywhere in the system and, in particular the response of a flat detector of unit cross section in the zone at 2000 meters.

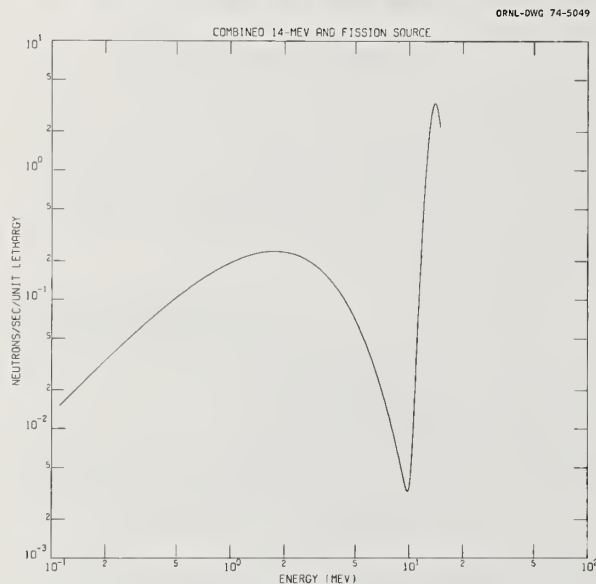


Fig. 2. Air Transport Benchmark Source Spectrum

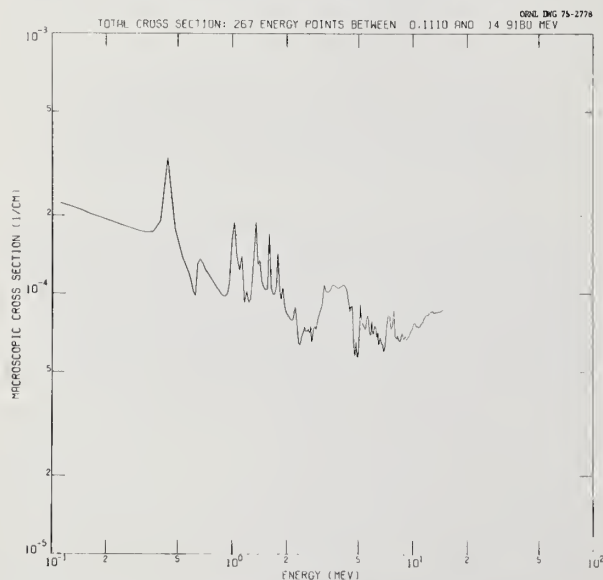


Fig. 3. Macroscopic Total Cross Section for Air Between 100 keV and 15 MeV.

The problem specifications presented above differ significantly in several important respects from the problem analyzed in ref. 2. In the earlier work, the quantity of interest was the total (neutron and gamma ray) tissue dose at 2000 meters from a prototypical thermonuclear source. This work focuses primarily on total integrated boundary flux (i.e., the response of the flat detector) arising from a hypothetical 14-MeV Gaussian source with an equal fission component. The number densities in ref. 2 were  $3.664 \times 10^{-5}$  for N and  $9.74 \times 10^{-6}$  for O, markedly different from those taken for this work and presented in Fig. 1. Finally, the problem was solved earlier in a 101-33 coupled neutron and gamma-ray energy group structure, using ENDF/B-III MAT 1133, Mod 3 for <sup>14</sup>N and MAT 1134, Mod 1 for <sup>16</sup>O. This work finalized on a 266-group optimized structure, selected using MAT 4133 Mod 3 and MAT 4134 Mod 1 while the complete uncertainty analysis using this multigroup structure was based on cross-section sets from ENDF/B IV, MAT 1275 for <sup>14</sup>N and MAT 1276 for <sup>16</sup>O.

### III. Energy Grid Selection and Converged Solutions

The key element in the creation of a fine-energy structure solution to the benchmark problem was the selection of a fine-structure energy grid. The point-energy processing code MOMANS<sup>4</sup> and a point-energy version of the SWANLAKE<sup>8</sup> sensitivity code was used for this purpose. The great speed and flexibility in generating processed neutron cross sections and sensitivity results on a pointwise energy grid make it possible to converge transport results as a function of the number and location of energy boundaries.

The convergence procedure is described as follows. First, an integral flux parameter was chosen for the problem defined in Section II above, the result of interest was the total boundary detector response. The response at the outer boundary in a shielding situation was found to usually ensure equal or better convergence of the total flux versus distance throughout the rest of the shield system. Next, a fine point-energy solution of the benchmark problem was obtained using a point energy grid. These results were then analyzed with the point-energy sensitivity code to select an initial few-point energy grid (~40 points) to begin convergence tests. This initial grid was chosen by constructing a cumulative probability function for the sensitivity profile as a function of energy and then selecting energy boundaries invoking an equal total importance criteria.<sup>5</sup> That is, the group boundaries are selected so that the reaction rate, biased by an importance function, is divided equally among the energy groups. In the terminology of sensitivity theory, each energy group is chosen to be equally sensitive in absolute magnitude to all the multigroup cross-section data. Hence, any error introduced in subsequent approximations of the weighting flux in the multigroup averaging process would be spread more uniformly over the entire energy range. This initial grid is not equally spaced in lethargy as was the starting grid.

The second phase of the benchmark calculation consisted of convergence tests to ensure high accuracy of the final flux results within the limitations of computer storage and run time. Thus, the few point grid (41 points) was used as energy boundaries and successive multigroup runs were made with ANISN to attempt to converge the solution with respect to spatial and angular mesh interval size and  $P_0$  expansion of the scattering kernel. When 1% or better convergence was achieved on this scale, additional energy boundaries (in multiples of the number in the original few-point grid) were added uniformly and point discrete ordinates calculations performed to try to converge the results in energy. This latter procedure was carried out until either 1% con-



vergence was achieved or cross-section core storage requirements were exceeded. Finally, the optimized energy bounds were used as the multigroup structure for computation of forward and adjoint fluxes for use in the analysis presented in subsequent sections.

With the following notation:

- $P_L$  - Legendre expansion of the scattering kernel  
 $S_N$  - Discrete angles at which the angular flux is calculated  
 $I_m$  - Spatial intervals used in problem solution  
 $J_k$  - Number of energy groups employed for solution  
 $E$  - Relative error given by

$$\frac{F(\text{run of interest}) - F(\text{best converged run})}{F(\text{best converged run})} \times 100$$

$F$  - Boundary detector response

(or mathematically)

$$\int_{111 \text{ keV}}^{15 \text{ MeV}} \int_{r_d}^{r_o} \phi_o(E, r) dE dV$$

and the initial problem parameters set as  $P_3$ ,  $S_{16}$ ,  $I_{82}$ ,  $J_{40}$ , Tables I through IV indicates the type of convergence achieved.

Table I.  $P_L$  Convergence for Legendre Expansion of Scattering Kernel

$P_L$	$P_1$	$P_2$	$P_3$	$P_5$
$F$	2.490	2.760	2.774	2.772
$E(\%)$	-10.17	-0.43	-0.07	0

Table II.  $S_N$  Convergence for Angular Flux Quadrature

$S_N$	$S_8$	$S_{12}$	$S_{16}$	$S_{20}$	$S_{24}$
$F$	2.503	2.714	2.774	2.831	2.861
$E(\%)$	-12.51	-5.14	-3.04	-1.02	0

Table III.  $I_m$  Convergence for Spatial Intervals

$I_m$	$I_{43}$	$I_{82}$	$I_{121}$	$I_{201}$	$I_{281}$
$F$	2.557	2.774	2.855	2.900	2.910
$E$	-12.13	-4.67	-1.89	-0.34	0

Table IV.  $J_k$  Convergence for Number of Energy Groups (Number Points -1)

$J_k$	$J_{40}$	$J_{78}$	$J_{116}$	$J_{154}$	$J_{192}$	$J_{266}$
$F$	2.774	2.493	2.305	2.452	2.481	2.454
$E$	13.04	1.59	-6.07	-0.08	1.10	0

The final results of the convergence test indicated that good convergence of the response ( $<5\%$ ) could be achieved with the following parameter set:  $P_3$ ,  $S_{24}$ ,  $I_{201}$ , and  $J_{266}$ . The convergence of the final set of problem parameters was examined by reducing the specifications jointly ( $P_2$ ,  $S_{20}$ ,  $I_{121}$ ,  $J_{192}$ ) and observing the convergence to within 1%. The numerical values for the energy group bounds and spatial intervals are not given here due to space limitations; they can be found in ref. 15. Figures 4 and 5 illustrate the converged scalar flux spectrum at 2000 meters and the adjoint spectrum at the center of the sphere.

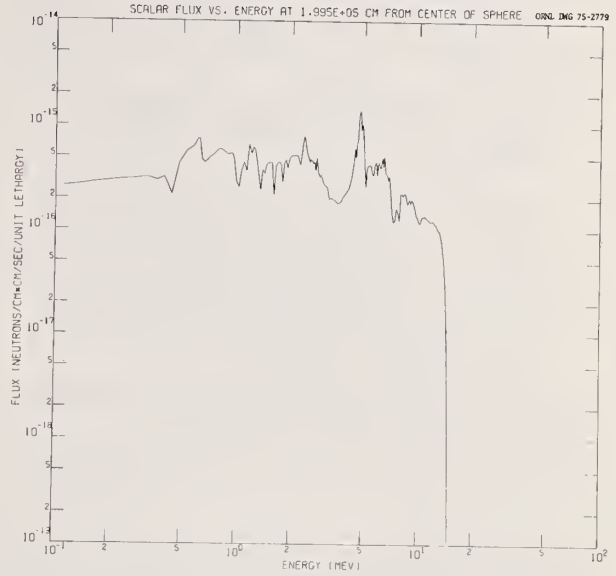


Fig. 4. Total Scalar Flux Spectrum at 2000 Meters - Air Transport Benchmark Problem.

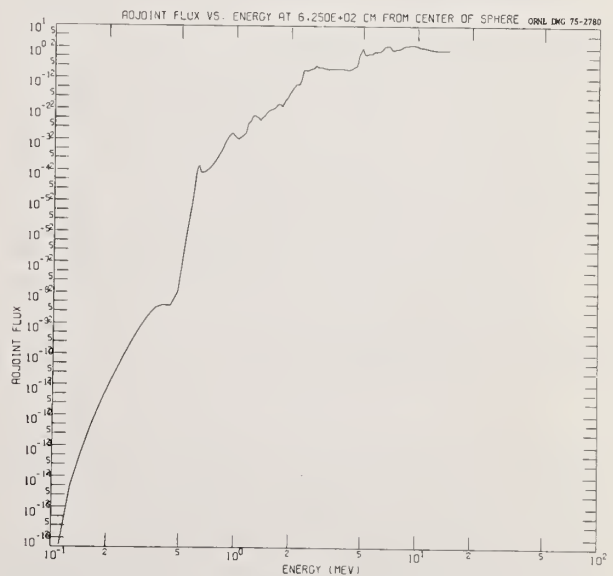


Fig. 5. Adjoint Spectrum at the Center of the Sphere - Air Transport Benchmark Problem



#### IV. Processing Uncertainty Files

##### A. Formulation of Multigroup Covariance Matrices

Only recently have standard formats and procedures been established within the ENDF/B system<sup>10</sup> for the processing of evaluated and correlated energy-dependent uncertainty information into a multigroup covariance matrix formulation. These covariance matrices were established to permit systematic sensitivity investigations<sup>11,12</sup> to determine, in a credible fashion, what cross-section measurements, evaluation, or processing methods most need further refinement.

Some of the guiding principles behind the formulation of uncertainty files for microscopic cross sections are designed to:

1. Provide a unique format for the estimated uncertainties which is flexible, but not unwieldy.
2. Permit the information to be processed at the same time as the cross-section data without imposing an undue burden on cross-section processing codes.
3. Promote the use of the file by implementation of a format to which experimental uncertainties could be readily translated.

With this in mind, the types of covariance representations permitted<sup>10</sup> in ENDF/B-IV include:

LB=0 absolute components only correlated over each  $E_k$  interval

$$\text{Cov}(X_i, Y_j) = \sum_k P_{j;k}^{i;k} F_{XY,k} \quad (4)$$

LB=1 fractional components only correlated over each  $E_k$  interval

$$\text{Cov}(X_i, Y_j) = \sum_k P_{j;k}^{i;k} F_{XY,k} X_i Y_j \quad (5)$$

LB=2 fractional components correlated over all  $E_k$  intervals

$$\text{Cov}(X_i, Y_j) = \sum_{k,l} P_{j;k}^{i;k} F_{XY,k} F_{XY,l} X_i Y_j \quad (6)$$

LB=3 fractional components correlated between  $E_k$  and  $E_l$  intervals

$$\text{Cov}(X_i, Y_j) = \sum_{k,l} P_{j;l}^{i;k} F_{X,k} F_{Y,l} X_i Y_j \quad (7)$$

where  $X_i$  and  $Y_j$  represent cross sections  $X$  and  $Y$  evaluated at energies  $i$  and  $j$ , respectively, the  $F$ 's ( $F_{XY,k}$ ,  $F_{XY,k'}$ ,  $F_{X,k}$ , and  $F_{Y,l}$ ) represent uncertainty coefficients, taken directly from the ENDF/B file, describing the correlation between cross sections  $X$  and  $Y$  for a specific energy interval. These fractional components are defined with respect to assumed normal distribution of cross-section uncertainties; furthermore, multiple sections (e.g.,  $F_{XY,k}^n$ ) may be provided

to identify specific types of experimental uncertainties associated with the complete covariance matrix. The  $F_{XY,k}$  and  $F_{XY,k'}$  are taken from a single table of energy-dependent correlation information for reactions  $X$  and  $Y$ . The  $F_{X,k}$  and  $F_{Y,l}$  indicates that the covariance data for these reactions are taken from two independent tables, one for  $X$  and one for  $Y$ . The  $P_{j,k}^{i,k'}$  is zero except for the case when energy  $i$  is contained within energy interval  $k$  and energy  $j$  is contained within energy interval  $k'$ .  $\text{Cov}(X_i, Y_j)$  is then the covariance between cross section  $X$  and energy  $i$  and cross section  $Y$  at energy  $j$ . There is a fifth law (LB=4), but since it can be described as combinations of the first four, no data has yet been cast in this form for ENDF/B-IV.

This type of formulation (sums of quantities separable in  $X$  and  $Y$ ) has the very desirable characteristic that if one assumes a flux model uncorrelated to the cross sections of interest, the multigroup covariance matrices are reduced to combinations of single integrals involving group fluxes and cross sections which can be calculated easily. In particular, for

LB=0,

$$\text{Cov}(X_G, Y_H) = \frac{\sum_n \sum_k F_{XY,k}^n \phi_{G,k}^n \phi_{H,k}^n}{\phi_G \phi_H}$$

LB=1,

$$\text{Cov}(X_G, Y_H) = \frac{\sum_n \sum_k F_{XY,k}^n \phi_{G,k}^n X_{G,k}^n \phi_{H,k}^n Y_{H,k}^n}{\phi_G \phi_H}$$

LB=2,

$$\text{Cov}(X_G, Y_H) = \sum_n \left[ \left( \sum_k F_{XY,k}^n \phi_{G,k}^n X_{G,k}^n \right) \times \left( \sum_{k'} F_{Y,k'}^n \phi_{H,k'}^n Y_{H,k'}^n \right) \right] / \phi_G \phi_H \quad (10)$$

LB=3

$$\text{Cov}(X_G, Y_H) = \sum_n \left[ \left( \sum_k F_{X,k}^n \phi_{G,k}^n X_{G,k}^n \right) \left( \sum_{k'} F_{Y,k'}^n \phi_{H,k'}^n Y_{H,k'}^n \right) \right] / \phi_G \phi_H \quad (11)$$

The derivation of Eqs. (8-11) are fully described in ref. 10; the notation used here is:

$\text{Cov}(X_G, Y_H)$  = Multigroup covariance between reaction X group G as it relates to reaction Y, group H.

$\phi_G$  = Multigroup flux for user group G.

$X_{G,k}^n$  = Multigroup cross section for reaction X for a super-group (G,k) constructed from the union of energy bounds for interval k (taken from subsection n) and those which were user input.  $\phi_{G,k}^n$  is the flux for this group.

## B. Implementation

The PUFF processing system<sup>13</sup> based on the MINX<sup>14</sup> multigroup processing code was developed specifically to read the ENDF/B-IV "error" files and construct multigroup covariance matrices according to Eqs. (8-11). For detailed programming considerations, the reader is referred to Appendix A of ref. 15.

The salient features are noted below:

1. Multigroup cross sections and fluxes are computed for a group structure which is the union between the user group structure and all energies used in the error file description for all the reactions and materials of interest. This supergroup structure obviously can get very large quite rapidly as the size of the problem considered and the level of detail available in the files expand.
2. The large number of fluxes and cross sections required have been appropriately labelled for subsequent automated retrieval. (Note that most processing codes normally do not preserve group flux values.)
3. All programming reflects variable dimensioning storage allocation.
4. All new coding is transparent to the MINX user not interested in processing error files. There is a single input flag which is 0/1; no error processing required/process errors. All other input is identical to a normal multigroup processing run. It should also be noted that with just a single additional input flag, the error processing input is quite user-oriented.

## C. Results for Processed Uncertainty Files

Several quantities related to uncertainties in multigroup cross sections have been derived from the pointwise ENDF/B "error" file. Clearly, of interest, is the covariance matrix

$$\text{Cov}(X_G, Y_H) = \langle (X_G - \bar{X}_G) (Y_H - \bar{Y}_H) \rangle \quad (12)$$

for reaction X, group G as it relates to reaction Y group H, and the associated quantity, the relative covariance matrix.

$$\text{Rel Cov}(X_G, Y_H) = \text{Cov}(X_G, Y_H) / X_G Y_H \quad (13)$$

In this notation, the standard deviation is given by:

$$\text{Std. Dev}(X_G) = \sqrt{\text{Cov}(X_G, X_G)} \quad (14)$$

and the analogous relative quantity, the relative standard deviation, is

$$\text{Rel Std. Dev}(X_G) = \frac{\text{Std. Dev}(X_G)}{X_G} \quad (15)$$

It is reasonable to expect that the covariance matrix of energy-dependent cross sections is strongly diagonal, i.e., the magnitude of the matrix elements tend to be small for groups G and H significantly displaced from each other in energy. However, the greater number of off-diagonal terms makes it difficult to say, a priori, that only the diagonal elements need be considered.

The correlation matrix is a quantity constructed by dividing the relative covariance matrix for  $X_G$  and  $Y_H$  by the respective relative standard deviations.

$$\text{Corr}(X_G, Y_H) = \frac{\langle (X_G - \bar{X}_G) (Y_H - \bar{Y}_H) \rangle}{\sqrt{\langle (X_G - \bar{X}_G)^2 \rangle \langle (Y_H - \bar{Y}_H)^2 \rangle}} \quad (16)$$

The correlation matrix is bounded by unity, i.e.,

$$|\text{Corr}(X_G, Y_H)| \leq 1 \quad (17)$$

When  $\text{Corr}(X_G, Y_H) = 0$ , the group cross sections are said to be totally uncorrelated; when  $|\text{Corr}(X_G, Y_H)| = 1$ , the group cross sections are termed fully correlated.

Figures 6 through 8 illustrate some of the processed correlation matrices and standard deviations obtained for nitrogen and oxygen. Appendix B of ref. 15 presents a complete set of correlation matrices (and standard deviations) for all energies and reaction types for N and O. These graphs are given in 22 groups for clarity of presentation. The actual matrices used in the section on results correspond to the problem described in this paper (266 groups). Figure 6 presents the correlation matrix for elastic scattering (reaction 2) as a function of energy as well as the standard deviation for <sup>14</sup>N. Several points are immediately noteworthy. First, the standard deviation has not appreciably changed from its description in ref. 2 (this is true for all reactions for N and O); the cross section is reasonably well known at lower energies (~3%) and only slightly less so at higher energies (~5-8%). The cross section is not fully correlated, as assumed in ref. 2 (with only the limited information available at that time) and there is some structure clearly evident. Above 1 MeV, the correlation matrix tends to become more diagonal with increasing energy; at lower energies (< 600 eV) the full correlation assumption appears valid.

Figure 7 illustrates the same type of behavior exhibited in the (n,α) cross section. Where the standard deviation curve goes outside the plot frame, the uncertainty has become inordinately large. This typically is the case for a reaction near threshold. The standard deviation is of the order of (20-30%) and is not fully correlated. It is the diagonal elements that are primarily important for the descrip-



tion of the inelastic (reaction 4), capture (reaction 102), and (n,p) (reaction 103) cross sections above 600 eV. Below this energy, both capture and (n,p) are fully correlated functions of energy. Figure 8 illustrates the correlation matrix as a function of energy for cross section covariance. The "deep" hole indicates the anti-correlation between elastic and (n, $\alpha$ ) below 10 MeV (to preserve the total cross section, if the elastic cross section increases, the (n, $\alpha$ ) would decrease etc.). The "grand canyon" has significant structure and is not uniformly -1 across the entire energy range as assumed in ref. 2.

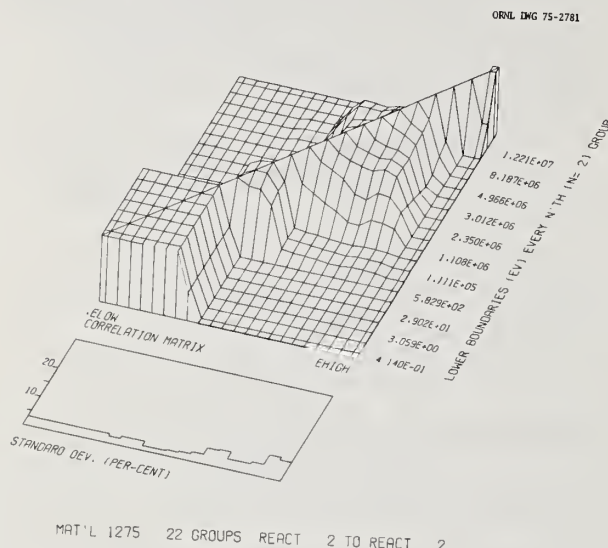


Fig. 6. Correlation Matrix and Standard Deviation for the Elastic Scattering Cross Section

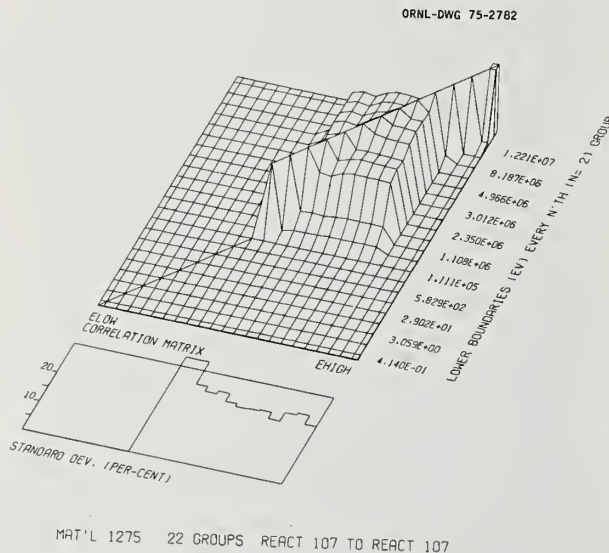


Fig. 7. Correlation Matrix and Standard Deviation for the (n, $\alpha$ ) Cross Section

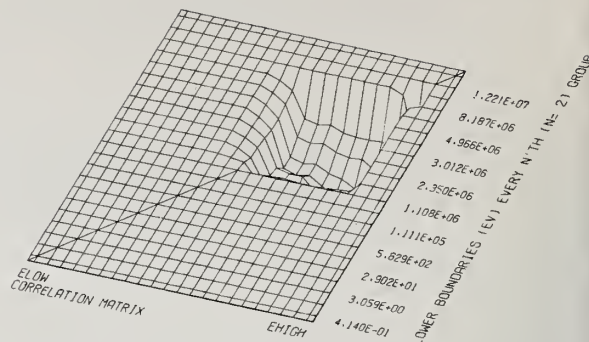


Fig. 8. Correlation Matrix as a Function of Energy Between the Elastic and (n, $\alpha$ ) Cross Section

The process of folding these covariance matrices with sensitivity profiles is described in Section VI.

#### V. Uncertainties Introduced in the Averaging of Multigroup Cross Section

The neutron multigroup cross sections used in the energy grid selection phase of the study were processed using the XLACS module of the AMPX system<sup>17</sup> while those used in the final analysis of the 266-group benchmark were obtained with the MINX<sup>14</sup> code. Both programs are available at ORNL and the choice was made primarily for expediency. However this, and more fundamental interest, does raise the question of consistency and validity of different multigroup processing techniques. Significant differences due to a wide variety of distinct physical approximations in flux modeling and methods of numerically group averaging have already been reported for fast reactor situations.<sup>7</sup>

To investigate the potential impact of cross-section processing methods uncertainties, the benchmark was repeated using MINX (M) multigroup data, XLACS (X) multigroup data, and pointwise cross sections used in conjunction with the point-ANISN (PA) technique.<sup>4</sup> The integrated boundary fluxes obtained were .925 (PA), .835 (M), and .784 (X) neut/sec. The volume of the detector zone is that corresponding to the last of the 201 spatial intervals. The point-ANISN results are expected to be on the high side because the points on the chosen grid emphasize minima in the total cross section and do not use averages of  $\sigma_T$ . This approach tends to increase the response for deep penetration problems compared with that obtained using multigroup methods. Approximately, six percent differences in the integrated boundary flux can be attributed exclusively to differences in multigroup processing techniques. Using a linear perturbation theory estimate,  $\Delta R/R$  is estimated by:



$$(\Delta R/R)_X = \sum_{X,G} P_{X,G} (\Delta \sigma/\sigma)_{X,G} \quad (18)$$

$$(\Delta R/R) = \sum_X (\Delta R/R)_X \quad (19)$$

$P_{X,G}$  = relative sensitivity coefficient,  
reaction X group G

$(\Delta \sigma/\sigma)_{X,G}$  = relative difference in multigroup  
cross sections for reaction X, group G

$(\Delta R/R)_X$  = projected change in response due to  
a change in multigroup cross section  
type X

We find that essentially all the 6% difference comes in the processing of multigroup transfer matrices. Differences arising from processing integrated cross section (e.g.,  $\sigma_{el}$ ,  $\sigma_{in}$ ) lead to changes in response which are less than .2% most of this coming from the linearization approximation in MINX.

#### VI. Folding Nuclear Data Covariance Matrices with Sensitivity Profiles

The 266-group forward and adjoint fluxes computed in section III have been combined to generate sensitivity profiles<sup>2</sup> for all important reaction cross sections in air. A complete set of illustrations can be found in ref. (15); one of the most important, the profile for (n, $\alpha$ ), is presented in Fig. 9. The complete set of profiles were then folded with the relative covariance matrices generated in section IV according to the following equation:

$$\left(\frac{\Delta R}{R}\right)^2 = \sum_{X,Y,G,H} P_{X,G} \text{Rel. Cov. } (X_G, Y_H) P_{Y,H} \quad (20)$$

with the following definitions

$P_{X,G}$  - relative sensitivity profile for reaction X,  
group G

$\left(\frac{\Delta R}{R}\right)^2$  - relative variance due to nuclear data uncertainties in integrated reaction cross sections

Tables V and VI present the results of this folding process. The summation has been partitioned in thirds to distinguish the contribution from a given reaction Z, how it correlates with all other reactions, and the contributions from all terms not involving reactions Z. The individual reactions are enumerated below:

Reaction Number	Reaction Type
2	$\sigma_{el}$
4	$\sigma_{in}$
102	$\sigma_{n,\gamma}$
103	$\sigma_{n,p}$
107	$\sigma_{n,\alpha}$

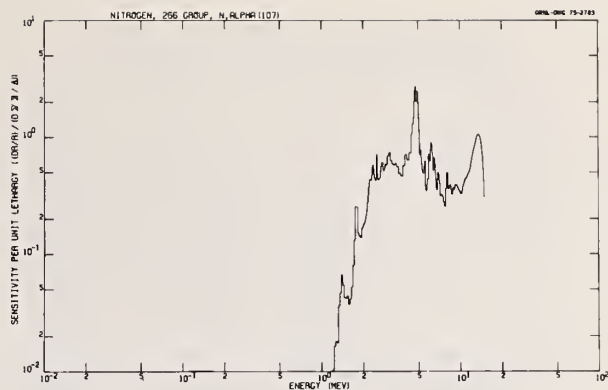


Fig. 9. Sensitivity Scattering for (n, $\alpha$ ) Scattering Cross Section

Table V. Components to the Variance of the Integrated Boundary Fluence due to Nuclear Data Uncertainties in <sup>14</sup>N (MAT 1275)

Variance Component	ENDF/B IV	Uncorrelated	Fully Correlated
React 2 + 2	4.518+1	1.038+0	2.182+2
React 2 + others	-2.147+2	-5.506+0	2.168+3
All react 2	-1.696+2	-4.468+0	2.386+3
Not react 2	4.532+2	1.326+1	5.387+3
React 4 + 4	7.805+1	4.835+0	5.211+2
React 4 + others	-5.294+1	-3.807+0	2.983+3
All react 4	2.512+1	1.028+0	3.504+3
Not react 4	2.585+2	7.761+0	4.269+3
React 102 + 102	4.675-4	2.657-5	4.664-3
React 102 + others	0	0	1.203+1
All react 102	4.675-4	2.657-5	1.204+1
Not react 102	2.836+2	8.789+0	7.761+3
React 103 + 103	1.916+1	9.377-1	1.578+2
React 103 + others	-1.368+1	-6.514-1	1.899+3
All react 103	5.486+0	2.863-1	2.057+3
Not react 103	2.781+2	8.502+0	5.716+3
React 107 + 107	3.812+2	9.379+0	1.439+3
React 107 + others	-1.985+2	-4.838+0	3.811+3
All react 107	1.826+2	4.541+0	5.250+3
Not react 107	1.010+2	4.247+0	2.523+3
Relative standard deviation <sup>14</sup> N cross section uncertainties (%)	1.684+1	2.964+0	8.816+1

Table VI. Components to the Variance of the Integrated Boundary Fluence due to Nuclear Data Uncertainties in  $^{16}\text{O}$  (MAT 1276)

Variance Component	ENDF/B IV	Uncorrelated	Fully Correlated
React 2 $\rightarrow$ 2	1.723+0	7.356-2	1.365+1
React 2 $\rightarrow$ others	-2.473+0	-2.080-1	7.410+1
All react 2	-7.502-1	-1.344-1	8.775+1
Not react 2	5.385+0	4.319-1	1.006+2
React 4 $\rightarrow$ 4	3.490+0	3.435-1	3.224+1
React 4 $\rightarrow$ others	-2.275+0	-2.119-1	9.136+1
All react 4	1.215+1	1.317-1	1.236+2
Not react 4	3.420+0	1.858-1	6.471+1
React 103 $\rightarrow$ 103	4.179-2	5.016-3	2.438-1
React 103 $\rightarrow$ others	-4.248-2	-3.833-3	1.306+1
All react 103	-6.889-4	1.184-3	1.331+1
Not react 103	4.635+0	2.963-1	1.750+2
React 107 $\rightarrow$ 107	2.427+0	1.222-1	1.487+1
React 107 $\rightarrow$ others	-1.304+0	-6.997-2	7.609-1
All react 107	1.123+0	5.223-2	9.097+1
Not react 107	3.512+0	2.453-1	9.734+1
Relative standard deviation from $^{16}\text{O}$ cross section uncertainties (%)	2.152+0	5.455-1	1.372+1

Since covariance matrices for all the integrated reaction cross sections (including those quantities served) were explicitly given in the ENDF/B-IV file, we have chosen to consider each of the partials as the independent reaction cross section; thus, the total cross section appears only implicitly in Tables V and VI.

Assuming no correlation between the N and O uncertainty files, the relative standard deviation due to all integrated reaction cross section uncertainties is 17.0%. The importance of the  $^{14}\text{N}$  (n, $\alpha$ ) cross section is clearly evident, as it was in earlier studies. Just as clear is the relative unimportance of  $^{16}\text{O}$  cross sections. The  $^{14}\text{N}$  elastic cross section is anti-correlated with other reactions diminishing the contribution to the variance from the uncertainties in the elastic scattering cross section considered by itself. As a function of energy, the "Uncorrelated" case corresponds to no correlation between cross sections in different energy groups; correlation between reactions for a given energy group is still included. "Fully Correlated" corresponds to the case of unity everywhere in the correlation matrix. These latter two cases are included simply to give the reader a feeling for the sensitivity of the estimated overall uncertainty due to two extreme kinds of correlation evaluation.

#### VII. Comparison of Transport Methods

The point and multigroup discrete ordinates results obtained above have been compared to fluxes calculated using the moments method technique. This latter procedure was one of the earliest methods applied to deep penetration radiation transport problems in simplified geometry of uniform composition. Modern moments method<sup>18</sup> and flux reconstruction<sup>19</sup> programs are very fast (the 267 energy point air problem, including cross section preparation, runs in less than three minutes on the ORNL 360/91) and compute the infinite medium spectrum, the age, higher moments (up to 20,0), and the flux at all spatial and energy points in the system including all cross section detail.

We have found that the total integrated fluxes agree to within 1% at all space points out to 1000 meters. At 1500 meters, differences of the order of 7% are observed. The fluxes right at the boundary cannot be easily compared since the moments technique applies only to infinite media. However, for higher energy groups (e.g., 12.2-14.9 MeV), where the angular flux is primarily outward directed, the two techniques give fluxes at 2000 meters which at 11 agree to within 7%. Finally, detailed comparisons of flux spectra at individual space points were inconclusive due to non-physical structure in the moments method fluxes at specific energy points due primarily to failure of a particular reconstruction scheme. In general, however, the moments method spectra agree well with the benchmark results. The agreement is spatial behavior, with the flux averaged over broad energy bins is also good.

#### VIII. Conclusions

Sensitivity analysis is applied to the study of an air transport benchmark calculation to quantify and distinguish between cross section and method uncertainties. The boundary detector response was converged with respect to spatial and angular mesh size,  $P_L$  expansion of the scattering kernel, and the number and location of energy grid boundaries. The uncertainty in the detector response due to uncertainties in nuclear data is 17.0% (one standard deviation, not including uncertainties in energy and angular distribution) based upon the ENDF/B-IV "error files". Differences of approximately 6% can be attributed exclusively to differences in processing multigroup transfer matrices.

#### Reference

- <sup>1</sup>E. G. Silver, E. M. Oblo, J. M. Kallfelz, C. R. Weisbin, D. E. Bartine, G. F. Flanagan, and F. R. Mynatt, "Generalized Reactor Sensitivity Program at ORNL," Trans. Am. Nucl. Soc. **18**, 341 (June 1974).
- <sup>2</sup>D. E. Bartine, E. M. Oblo, and F. R. Mynatt, "Radiation Transport Cross-Section Sensitivity Analysis - A General Approach Illustrated for a Thermonuclear Source in Air," Nucl. Sci. Eng., **55**, 147-167 (1974).
- <sup>3</sup>E. M. Oblo, D. E. Bartine, and F. R. Mynatt, "General Sensitivity Theory for Radiation Transport," ORNL-TM-4110 (March 1973).
- <sup>4</sup>J. Ching, H. Goldstein, and E. M. Oblo, "Application of a Discrete-Energy Discrete-Ordinates Technique to the Study of Neutron Transport in Iron," ORNL-TM-4235 (December 1974).
- <sup>5</sup>E. Oblo, J. Ching, and J. Drischler, "Selection of Group Energy Boundaries Using Sensitivity Theory," Trans. Am. Nucl. Soc. **17**, 547 (1973).
- <sup>6</sup>F. G. Perey, G. deSaussure, and R. B. Perez, "Estimated Data Covariance Files for Evaluated Cross Sections - Examples for  $^{235}\text{U}$  and  $^{238}\text{U}$ ," Proceedings of ANS Topical - Advanced Reactors: Physics, Design, and Economics, September, 1974, to be published.
- <sup>7</sup>C. R. Weisbin, N. M. Greene, H. Henryson, II, R. J. LaBauve, C. Durston, D. E. Cullen, and R. B. Kidman, "Fast Reactor Cross-Section Processing Codes - Is There a Dollars Worth of Difference Between Them?" Proceedings of ANS Topical - Advanced Reactors: Physics, Design, and Economics, September, 1974, to be published.

<sup>8</sup>D. E. Bartine, F. R. Mynatt, and E. M. Oblow, "SWANLAKE, A Computer Code Utilizing ANISN Radiation Transport Calculations for Cross-Section Sensitivity Analysis," ORNL-TM-3809 (May 1973).

<sup>9</sup>W. W. Engle, Jr., "A Users Manual for ANISN, A One-Dimensional Discrete Ordinates Transport Code with Anisotropic Scattering," K-1693, Computing Technology Center, Oak Ridge Gaseous Diffusion Plant (1967).

<sup>10</sup>F. Perey, Format Modifications 73-7, minutes of the CSEWG meeting, December 1973 (enclosures 6 and 12).

<sup>11</sup>F. G. Perey, "The Estimated Data Covariance Files of ENDF/B - Their Uses," minutes of the CSEWG meeting, June 17-19, 1974 (enclosure 10).

<sup>12</sup>H. Henryson, II *et al.*, "Variational Sensitivity Analysis - Theory and Application," Proceedings of ANS Topical - Advanced Reactors: Physics, Design, and Economics, September, 1974, to be published.

<sup>13</sup>C. R. Weisbin, "PUFF, An ENDF/B-IV Error File Processing Code," ORNL Quarterly Report to the Defense Nuclear Agency (April 1974).

<sup>14</sup>C. R. Weisbin, P. D. Soran, R. E. MacFarlane, D. R. Harris, R. J. LaBauve, J. S. Hendricks, and J. E. White, "MINX, A Multigroup Interpretation of Nuclear Cross Sections from ENDF/B," Los Alamos Scientific Laboratory (to be published); see also, Trans. Am. Nucl. Soc., 16, 127 (1973).

<sup>15</sup>C. R. Weisbin, E. M. Oblow, J. Ching, J. E. White, R. Q. Wright, and J. Drischler, "Cross Section and Method Uncertainties: The Application of Sensitivity Analysis to Study Their Relationship in Computational Benchmark Problems," Oak Ridge National Laboratory report ORNL-TM-4847 (to be published).

<sup>16</sup>F. G. Perey, "Tedium Isotopes for MF=33," correspondence to the Error Quantity Subcommittee of the CSEWG (May 29, 1974).

<sup>17</sup>N. M. Greene and F. R. Mynatt, "The AMPX Modular Code System for Generating Coupled Neutron-Gamma Multigroup Cross-Section Sets," Trans. Am. Nucl. Soc., 15, 568 (1972); see also N. M. Greene *et al.*, "AMPX: A Modular Code System for Generating Coupled Multigroup Neutron-Gamma Libraries from ENDF/B," ORNL-TM-3706 (to be published).

<sup>18</sup>C. R. Weisbin, H. Goldstein, and L. J. Lidofsky, Trans. Am. Nucl. Soc., 12, 402 (1969); see also "A New Moments Solution to the Neutron Transport Equation," NYO-268, Pegram Nuclear Physics Lab. (1969).

<sup>19</sup>P. D. Soran, "Reconstruction of Neutron Spatial Distribution from Spatial Moments," Columbia University Doctoral Thesis, 1971.

#### Acknowledgments

The authors take great pleasure in acknowledging the efforts of D. K. Trubey in making the moments method technique operational and getting appropriate solutions for this problem. F. G. Perey and P. G. Young made significant contributions in the review and application of the ENDF/B-IV error files. Virginia Glidewell and Susan Pierce deserve many thanks for preparing the manuscript in the appropriate format and having it available ahead of schedule.



Cross sections for the (n,2n) and (n,3n) reactions have been measured for several nuclides between 6 and 15 MeV using a large liquid scintillator to count the neutrons directly. Measurements were made relative to fission cross section of  $^{238}\text{U}$  for  $^{56}\text{Fe}$ ,  $^{59}\text{Co}$ ,  $^{76}\text{Se}$ ,  $^{78}\text{Se}$ ,  $^{80}\text{Se}$ ,  $^{82}\text{Se}$ ,  $^{89}\text{Y}$ ,  $^{93}\text{Nb}$ ,  $^{103}\text{Rh}$ ,  $^{169}\text{Tm}$ ,  $^{175}\text{Lu}$ ,  $^{181}\text{Ta}$ ,  $^{197}\text{Au}$ ,  $^{209}\text{Bi}$ ,  $^{238}\text{U}$ , and for the natural elements Pt and W. The relative accuracy was generally in the range 5 to 10 %. The present results are compared with previous measurements.

(Nuclear reactions  $^{56}\text{Fe}$ ,  $^{59}\text{Co}$ ,  $^{76,78,80,82}\text{Se}$ ,  $^{89}\text{Y}$ ,  $^{93}\text{Nb}$ ,  $^{103}\text{Rh}$ ,  $^{169}\text{Tm}$ ,  $^{175}\text{Lu}$ ,  $^{181}\text{Ta}$ ,  
W, Pt,  $^{197}\text{Au}$ ,  $^{209}\text{Bi}$ ,  $^{238}\text{U}$ (n,2n) ;  $^{238}\text{U}$ (n,3n) ;  $E_n = 8 - 15$  MeV ; measured  $\sigma(E_n)$ ).

## Introduction

The activation technique generally used to measure (n,2n) and (n,3n) cross sections depends on the determination, after neutron bombardment, of the activity produced in a sample and is therefore limited to nuclides which leave a suitably active residual isotope.

The large scintillator method used in the present experiment depends on the detection of the emitted neutrons and thus can be used for any nuclide, provided that several grams of material are available for a sample. The present work uses essentially the same technique as Mather and Pain<sup>1</sup>. The main difference is the energy range covered which was from threshold to 15 MeV in the present work, as compared to the energies of 12.4 and 14.3 MeV for Mather's measurements.

## Experimental Method

A description of the principle of the method and details of the experimental set up and of corrections are given elsewhere<sup>2</sup>. The experiment relies on two properties of the neutron detector, a large loaded liquid scintillator : its high neutron efficiency and the relatively long lifetime in the scintillator for neutrons before capture. This gives identification of an (n,2n) event by two separate pulses in the scintillator within the 30  $\mu\text{s}$  following the event.

### Detection of (n,2n) and (n,3n) events (fig. 1)

About 10 to 15 grams of the sample to be measured are placed at the center of the scintillator and irradiated by a collimated neutron beam. Neutrons are produced by the  $\text{D(d,n)}^3\text{He}$  reaction, using a gaseous target and the 14 MeV tandem Van de Graaff accelerator pulsed at a frequency of 2.5 MHz (pulse width  $\sim 2$  ns). An electrostatic beam sweeper is used to keep only three bursts each 60  $\mu\text{s}$ .

After each group of three bursts, a 30  $\mu\text{s}$  counting gate is opened on the output of the liquid scintillator. The number of gates containing 0, 1, 2, ... pulses are recorded during a run. These data are corrected for the two sources of background in the scintillator :

- The natural background, measured for the same number of counting gates with the accelerator beam off.
- The accelerator dependant background, measured with the beam on and the sample out for the same number of incident neutrons.

The data are also corrected for the detection dead time (120 ns), for the detector efficiency ( $\sim 75\%$ ), and for the possibility of two (n,n') or (n,n) events occurring in the same counting gate, being then indistinguishable from a (n,2n) event.

These corrections give the number of gates containing 2 or 3 neutrons, i.e. the number of (n,2n) and (n,3n) events, for non fissionable materials.

In the case of fissionable materials, it is necessary to subtract the fission events of neutron multiplicity 2 or 3. The total number of fissions can be calculated from the higher measured multiplicities ( $\geq 4$ ) using fission multiplicity distributions previously determined with a fission chamber<sup>3</sup>. These distributions and the calculated number of fissions thus enable one to deduce the number of fission events of multiplicity 2 or 3.

### (n,2n) and (n,3n) cross section determinations

A relative incident neutron flux measurement allows the (n,2n) and (n,3n) cross-sections to be normalized on a reference cross section.

In the case of fissionable materials, (n,2n) and (n,3n) cross sections can be directly obtained relative to fission cross section, since the number of fission events occurring during the measurement is also determined. Because of the lack of accurately determined (n,2n) cross sections, a fission cross section was also chosen as reference for non fissionable materials, the fission cross section of  $^{238}\text{U}$ .

### Relative flux measurement (fig. 1)

The flux monitor consists of a small liquid scintillator located 1.5 meter behind the sample, in the collimated neutron beam. Monoenergetic incident neutrons in the energy range 6-15 MeV are produced using the  $\text{D(d,n)}^3\text{He}$  reaction. With the pulsing system adopted, it is possible, by the time-of-flight technique, to separate the monoenergetic neutrons, the only neutrons which induce (n,2n) or (n,3n) reactions, from deuteron break-up neutrons as well as from neutrons induced by (d,n) reactions on the target materials. This technique provides very precise relative flux measurement for (n,2n) and (n,3n) reactions.

A relative determination of the efficiency of the monitor versus neutron energy, using the results of a Monte-Carlo code calculation, allows, in the case of  $^{238}\text{U}$ , an accurate determination of the apparent fission cross section and of the fission neutron multiplicities. This calibration is necessary since, in contrast to (n,2n) or (n,3n) events, fission events may be induced by the secondary neutrons.

## Results

### Standards

The large liquid scintillator efficiency was determined using a  $^{252}\text{Cf}$  source and assuming a value of  $\bar{\nu} = 3.732 \pm 0.000$  for the average number of prompt neutrons emitted per spontaneous fission.

The standard fission cross section of  $^{238}\text{U}$  used for the normalization of the results was taken from the evaluation of Sowerby et al.<sup>4</sup>.

## Error derivation

The errors quoted are standard errors derived by quadratic addition of the statistical errors of the experimental data and the errors of the corrections. The uncertainties of the standards,  $\bar{\nu}$  for  $^{252}\text{Cf}$  and the fission cross section of  $^{238}\text{U}$ , have not been included.

## (n,2n) and (n,3n) cross sections

The final (n,2n) cross sections for 17 non fissionable materials between threshold and 15 MeV are given in table I. Also listed are the (n,2n) and (n,3n) cross sections of  $^{238}\text{U}$  and the fission cross section of  $^{238}\text{U}$  used as a standard.

(n,2n) cross sections of  $^{56}\text{Fe}$  and  $^{175}\text{Lu}$  were derived from measurements on the natural elements, using the results of the calculations by Pearlstein<sup>47</sup> to subtract the contribution of the other isotopes. Enriched isotopes were used for the measurements on selenium. The calculations of Pearlstein were, here also, used in order to correct for the contribution of the non measured  $^{74}\text{Se}$  and  $^{77}\text{Se}$  isotopes present in small amount in the samples.

## Discussion

The present measurements are compared to previously published results in figure 2. The values of Ashby et al.<sup>5</sup> at 14.1 MeV for  $^{56}\text{Fe}$ ,  $^{209}\text{Bi}$ ,  $^{197}\text{Au}$ ,  $^{181}\text{Ta}$  and the values of Mather et al.<sup>1</sup> at 12.4 and 14.3 MeV for  $^{89}\text{Y}$ ,  $^{93}\text{Nb}$ ,  $^{103}\text{Rh}$ ,  $^{169}\text{Tm}$ ,  $^{197}\text{Au}$  and  $^{238}\text{U}$ , also obtained with the large liquid scintillator method, are in relatively good agreement with the present results. By contrast, results obtained by the activation technique are generally more scattered, partly due to the variety of standards used for detector calibration and for flux determination.

Nevertheless, the agreement between the results obtained by the two techniques is rather good for  $^{56}\text{Fe}$ ,  $^{76}\text{Se}$ ,  $^{82}\text{Se}$ ,  $^{89}\text{Y}$  (ref. 45),  $^{197}\text{Au}$ ,  $^{209}\text{Bi}$  and  $^{238}\text{U}$ .

The lack of agreement between the two techniques for  $^{103}\text{Rh}$ ,  $^{175}\text{Lu}$ ,  $^{181}\text{Ta}$  is probably due to the measurement in the activation method of only one isomer for each of the nuclei  $^{102}\text{Rh}$ ,  $^{174}\text{Lu}$  and  $^{180}\text{Ta}$ ; whereas the large liquid scintillator method has the advantage of measuring the total (n,2n) cross sections.

In the case of  $^{93}\text{Nb}$ , earlier measurements of the (n,2n) cross section by the activation method have not been plotted in the figure, since they are now proved<sup>46</sup> to be measurements of only the 10.15 days isomeric state of  $^{92}\text{Nb}$ .

For  $^{169}\text{Tm}$ , although two activation measurements are approximatively a factor 2 lower, a recent compilation<sup>46</sup> of experimental data has proved the consistency of the results obtained by the two techniques.

In the case of  $^{59}\text{Co}$ , results of activation measurements are too widely scattered for a valuable comparison to be possible.

Results for the 4 measured isotopes of Se are compared in fig.2. Such measurements are useful for studying the dependence of (n,2n) cross sections on the number of neutrons for isotopes of a given element and should help in calculating more precise (n,2n) cross sections.

## Conclusion

The major experimental difficulty encountered in the present work was the presence of secondary neutrons accompanying the monoenergetic neutrons of the  $\text{D(d,n)}^3\text{He}$  reaction used to produce incident neutrons. However this difficulty was overcome by the use of pulsed beam which allowed one to measure the incident neutron spectrum and at the same time to maintain a sufficiently high neutron flux.

As far as we know, the present results are the only ones to cover the entire energy range from threshold to 15 MeV. They show the value of the large liquid scintillator method for providing (n,2n) and (n,3n) cross sections over a large energy range.

## References

1. D S Mather et al., AWRE Report 047/69 (1969)  
AWRE Report 072/72 (1972)
2. J Frehaut, G Mosinski, Rapport CEA-R-4627 (1974)
3. M Soleilhac et al., J. Nucl. Energy 23 (1969) 257
4. M G Sowerby et al., AERE Report R7273 (1973)
5. V J Ashby et al., Phys. Rev. 111 (1958) 616
6. R Wenusch et al., Nucl. Sci. Abstracts 17(1963)3475
7. P Hille et al., Data taken in Nucl. Phys. 65 (1965) 257
8. N Flerov et al., Atomnaya Energiya 5 (1958) 657
9. L Rosen, L Stewart, Phys. Rev. 107 (1957) 824
10. E Feicht, H. Vonach, Nukleonik 10 (1967) 58
11. V Lebedev, Data taken in ref. 10
12. A Adam et al., Nucl. Phys. 49 (1963) 489
13. S Okumura, Nucl. Phys. A93 (1967) 74
14. Gabbard, Data taken in Euratom Report EUR 122.e (1963)
15. E Veigold, R N Glover, Nucl. Phys. 32 (1962) 106
16. A Paulsen, H Liskien, J. Nucl. Energy 19 (1965) 907
17. P Decowski et al., Nucl. Phys. A112 (1968) 513
18. M Bormann et al., J. Phys. Radium 22 (1961) 602
19. J Cabé et al., Euratom Report EANDC 49 (1963) 82
20. B Granger et al., Euratom Report EANDC 49 (1963) 83
21. W Dilg et al., Nucl. Phys. A118 (1968) 9
22. D R Nethaway, Nucl. Phys. A190 (1972) 635
23. R G Wille, R W Fink, Phys. Rev. 118 (1960) 242
24. D G Vallis, AWRE Report 076/66 (1966)
25. R Rieder, H Munzer, Acta Phys. Austria 23 (1966) 42
26. H A Tewes et al., UC34-WASH (1960) 1028
27. R J Prestwood, B P Bayhurst, Phys. Rev. 121 (1961) 1438
28. H K Vonach et al., EANDC E 89 "U" (1968) 37
29. A K Hankla et al., Bull. Am. Phys. Soc. 13 (1968) 1421
30. S K Mangal et al., Nucl. Phys. 69 (1965) 158
31. J Karolyi et al., Nucl. Phys. A122 (1968) 234
32. R Vos et al., Bull. Am. Phys. Soc. 18 (1973) 775
33. A Poularikas et al., J. Inorg. Nucl. Chem. 13 (1960) 196
34. M Bormann et al., Nucl. Phys. A115 (1968) 309
35. J D Knight et al., Phys. Rev. 112 (1958) 259
36. E R Graves et al., Data taken in ref. 35
37. J A Phillips, AERE NP/R 2033 (1956)
38. A Daroczy et al., Proc. Conf. on Neutron Physics, Kiev 1 (1971) 228
39. G P Antropopov et al., Atomnaya Energiya 5 (1958) 456
40. J L Perkin et al., J. Nucl. Energy 14 (1961) 69



41. P V Rao, R W Fink, Phys. Rev. 154 (1967) 1023  
 42. S S Hasan et al., Nucl. Phys. A181 (1972) 101  
 43. W Lu and al., Phys. Rev. 1C (1970) 350  
 44. A Paulsen, R Wiedera, Z. Physik 238 (1970) 23

45. C Philis, Rapport CEA-R-4636 (1975)  
 46. C Philis, P G Young, to be published as Rapport CEA  
 47. S Pearlstein, Nuclear Data B, Section A, 3 (1967) 3

$E_n$ MeV	$\Delta E_n$ keV	$\sigma_f$ mb	$\sigma(n, 2n)$ , mb									
		$^{238}\text{U}$		$^{56}\text{Fe}$	$^{59}\text{Co}$	$^{76}\text{Se}$	$^{78}\text{Se}$	$^{80}\text{Se}$	$^{82}\text{Se}$	$^{89}\text{Y}$	$^{93}\text{Nb}$	$^{103}\text{Rh}$
9.44	115	960									$56 \pm 21$	
9.93	110	952							$109 \pm 6$		$404 \pm 27$	$103 \pm 13$
10.42	100	948						$65 \pm 5$	$325 \pm 16$		$607 \pm 39$	$361 \pm 24$
10.91	95	952			$19 \pm 6$		$17 \pm 5$	$257 \pm 14$	$518 \pm 26$		$800 \pm 45$	$593 \pm 31$
11.40	90	957			$127 \pm 10$		$148 \pm 9$	$457 \pm 24$	$689 \pm 36$		$947 \pm 54$	$837 \pm 48$
11.88	85	965		$39 \pm 8$	$232 \pm 15$	$116 \pm 12$	$352 \pm 21$	$635 \pm 36$	$814 \pm 44$	$53 \pm 8$	$1133 \pm 65$	$1011 \pm 58$
12.36	85	978		$108 \pm 10$	$368 \pm 24$	$252 \pm 24$	$522 \pm 38$	$844 \pm 61$	$970 \pm 68$	$215 \pm 12$	$1215 \pm 65$	$1194 \pm 64$
12.85	80	999		$220 \pm 16$	$508 \pm 30$	$434 \pm 36$	$693 \pm 50$	$936 \pm 67$	$1044 \pm 73$	$450 \pm 21$	$1286 \pm 71$	$1257 \pm 69$
13.33	75	1031		$326 \pm 23$	$601 \pm 37$	$607 \pm 48$	$828 \pm 60$	$1036 \pm 73$	$1147 \pm 80$	$668 \pm 41$	$1380 \pm 72$	$1314 \pm 68$
13.80	75	1086		$415 \pm 26$	$711 \pm 41$	$743 \pm 56$	$970 \pm 69$	$1137 \pm 81$	$1132 \pm 80$	$846 \pm 35$	$1300 \pm 70$	$1364 \pm 72$
14.28	70	1163		$413 \pm 29$	$626 \pm 46$	$798 \pm 60$	$971 \pm 70$	$1109 \pm 79$	$1134 \pm 81$	$837 \pm 61$	$1358 \pm 98$	$1396 \pm 101$
14.76	65	1216		$521 \pm 36$	$742 \pm 53$	$873 \pm 65$	$1018 \pm 74$	$1136 \pm 82$	$1172 \pm 84$	$981 \pm 71$	$1444 \pm 104$	$1458 \pm 105$

$E_n$ MeV	$\Delta E_n$ keV	$\sigma_f$ mb	$\sigma(n, 2n)$ , mb										$\sigma(n, 3n)$ mb
		$^{288}\text{U}$	$^{169}\text{Tm}$	$^{175}\text{Lu}$	$^{181}\text{Ta}$	$^{197}\text{Au}$	$^{209}\text{Bi}$	Nat. Pt	Nat. W	$^{238}\text{U}$		$^{238}\text{U}$	
7.93	150	952					$131 \pm 15$	$208 \pm 26$	$238 \pm 27$	$1081 \pm 110$			
8.44	140	962	$68 \pm 34$	$180 \pm 37$	$310 \pm 28$	$44 \pm 22$	$382 \pm 36$	$404 \pm 36$	$690 \pm 46$	$1178 \pm 113$			
8.94	125	964	$377 \pm 27$	$686 \pm 50$	$808 \pm 47$	$288 \pm 20$	$810 \pm 51$	$614 \pm 48$	$1032 \pm 55$	$1313 \pm 113$			
9.44	120	960	$978 \pm 87$	$1220 \pm 110$	$1382 \pm 112$	$738 \pm 65$	$1191 \pm 98$	$1059 \pm 74$	$1510 \pm 99$	$1361 \pm 139$			
9.93	110	952	$1232 \pm 69$	$1482 \pm 83$	$1560 \pm 84$	$1027 \pm 57$	$1563 \pm 86$	$1338 \pm 78$	$1729 \pm 101$	$1378 \pm 114$			
10.42	100	948	$1567 \pm 87$	$1709 \pm 96$	$1795 \pm 97$	$1378 \pm 75$	$1837 \pm 100$	$1505 \pm 88$	$1755 \pm 101$	$1407 \pm 92$			
10.91	95	952	$1661 \pm 107$	$1872 \pm 125$	$1850 \pm 115$	$1589 \pm 101$	$1948 \pm 124$	$1619 \pm 85$	$1800 \pm 94$	$1389 \pm 142$			
11.40	90	957	$1715 \pm 79$	$1802 \pm 105$	$1860 \pm 103$	$1691 \pm 76$	$1936 \pm 110$	$1794 \pm 101$	$2014 \pm 113$	$1478 \pm 111$			
11.88	85	965	$1799 \pm 96$	$1878 \pm 103$	$1877 \pm 96$	$1816 \pm 94$	$1935 \pm 101$	$1953 \pm 111$	$2011 \pm 114$	$1360 \pm 125$		$-4 \pm 46$	
12.36	85	978	$1953 \pm 84$	$2060 \pm 120$	$2051 \pm 113$	$2012 \pm 83$	$2131 \pm 119$	$2028 \pm 108$	$2087 \pm 112$	$1449 \pm 113$		$109 \pm 43$	
12.85	80	999	$2093 \pm 86$	$2101 \pm 124$	$2143 \pm 117$	$2166 \pm 87$	$2125 \pm 121$	$2062 \pm 113$	$2124 \pm 117$	$1374 \pm 105$		$209 \pm 68$	
13.33	75	1031	$2131 \pm 123$	$2134 \pm 109$	$2137 \pm 119$	$2197 \pm 123$	$2165 \pm 122$	$2070 \pm 107$	$2206 \pm 114$	$1207 \pm 109$		$337 \pm 60$	
13.80	75	1086	$2172 \pm 88$	$2195 \pm 115$	$2219 \pm 119$	$2287 \pm 90$	$2350 \pm 130$	$2094 \pm 111$	$2122 \pm 112$	$906 \pm 115$		$507 \pm 91$	
14.28	70	1163	$1916 \pm 139$	$2071 \pm 151$	$2101 \pm 151$	$2037 \pm 147$	$2144 \pm 155$	$2124 \pm 158$	$2146 \pm 154$	$908 \pm 184$		$502 \pm 116$	
14.76	65	1216	$2053 \pm 147$	$2252 \pm 161$	$2229 \pm 159$	$2215 \pm 158$	$2348 \pm 168$	$2221 \pm 164$	$2269 \pm 177$	$749 \pm 182$		$647 \pm 128$	

Table I. Experimental results for the (n,2n) cross section of  $^{56}\text{Fe}$ ,  $^{59}\text{Co}$ ,  $^{76}\text{Se}$ ,  $^{78}\text{Se}$ ,  $^{80}\text{Se}$ ,  $^{82}\text{Se}$ ,  $^{89}\text{Y}$ ,  $^{93}\text{Nb}$ ,  $^{103}\text{Rh}$ ,  $^{169}\text{Tm}$ ,  $^{175}\text{Lu}$ ,  $^{181}\text{Ta}$ ,  $^{197}\text{Au}$ ,  $^{209}\text{Bi}$ , Pt, W,  $^{238}\text{U}$ , and for the (n,3n) cross section of  $^{238}\text{U}$ . Cross sections are normalized on the fission cross section of  $^{238}\text{U}$  as evaluated by Sowerby et al<sup>4</sup>.

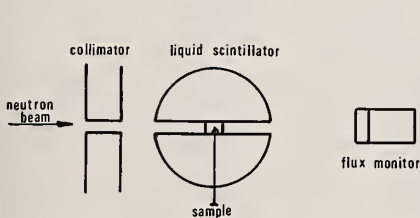


fig. 1a Experimental set up

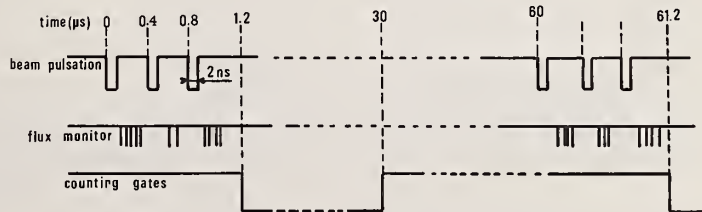


fig. 1b Time sequence of gated data collection



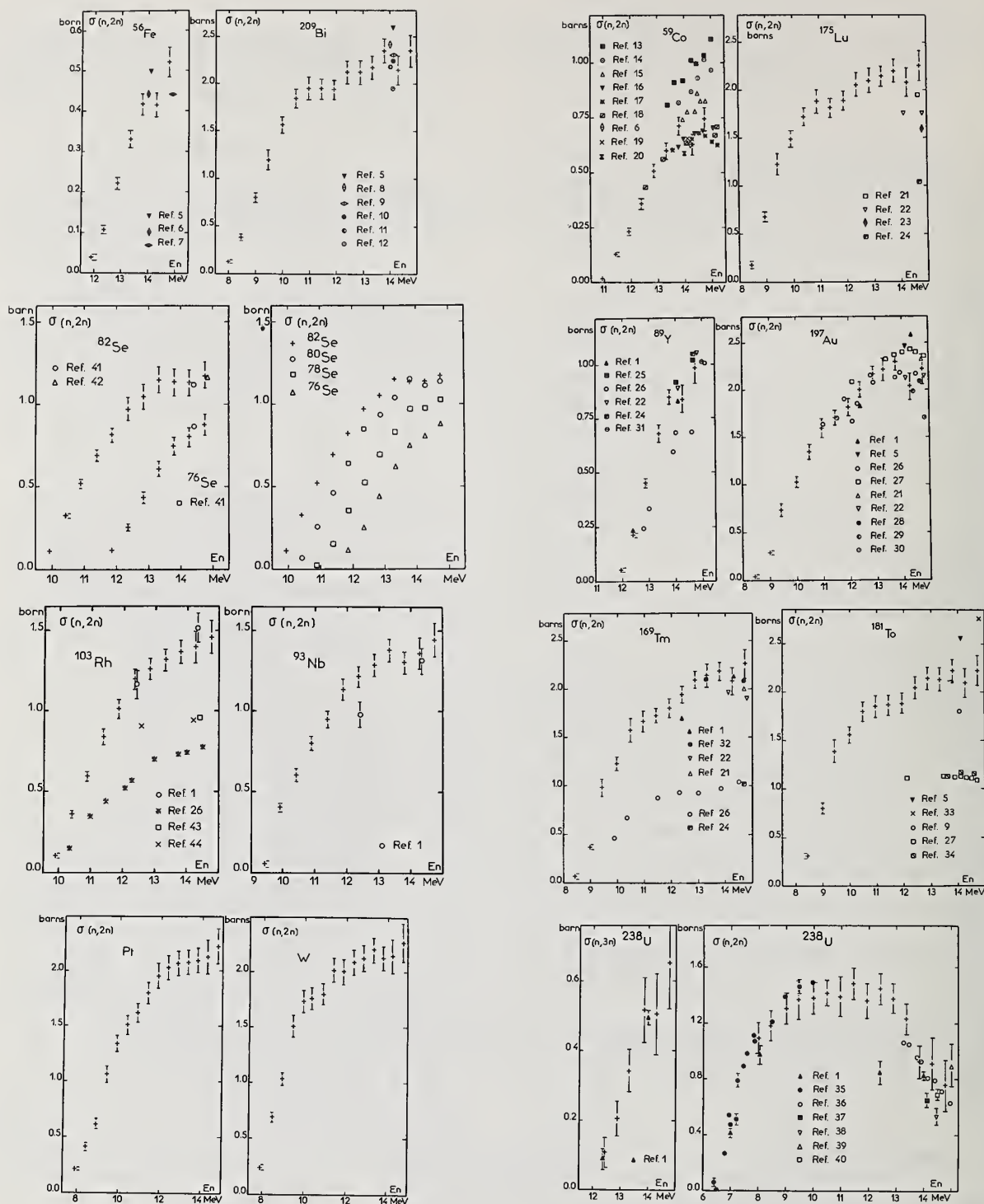


Fig. 2. Values of  $(n,2n)$  and  $(n,3n)$  cross sections obtained in the present experiment, (+) symbols, plotted against incident neutron energy and compared with previously published results.

Measurements have been made of the differential elastic and inelastic scattering cross sections, at 28 angles each, for 9, 9.21, 9.6, 10, 10.25, 10.74, 11, 11.22, 11.79, 12, 13, 14, 14.5, and 15 MeV neutrons incident upon natural carbon. The measurements were made with the TUNL FN tandem accelerator and a high-precision goniometer time-of-flight spectrometer. Monte Carlo simulation has been used to correct the differential cross sections for multiple scattering. Absolute uncertainties are typically 5%. These data partially fill the 9-15 MeV gap in the C elastic and inelastic scattering data set required for the CTR program.

[NUCLEAR REACTIONS C(n,n), C(n,n'), E = 9-15 MeV; measured  $\sigma(E_n, \theta)$ ]

### Introduction

Detailed knowledge of the energy-dependent differential cross sections for the scattering of fast neutrons by carbon is required for accurate calculations of neutron transport in the blanket and shield of prototype fusion reactors.

### Experimental Apparatus

Differential cross-section experiments were performed using the TUNL neutron time-of-flight (TOF) facility which is shown in Fig. 1. The details of the facility are described in BB12 of the conference proceedings; thus, only a brief description will be given here. The TUNL FN tandem accelerator provided a beam of deuterons which was preacceleration pulsed and bunched into bursts with a time dispersion of approximately 1.5 nsec. The average beam current at the target was about 2  $\mu$ A at a pulse repetition rate of 2 MHz. Neutrons were produced via the D(d,n)<sup>3</sup>He reaction in a deuterium gas cell. The gas cell was a thin-wall stainless steel, tantalum-lined cylinder 3.0 cm in length and isolated from the accelerator vacuum system by a 3.5  $\mu$ m thick molybdenum foil. The cell contained deuterium gas at a pressure of 2 atm.

Figure 2 illustrates the scattering geometry. The 99.98%-pure carbon sample was a right circular cylinder with 1.9 cm diam. and 2.54 cm height. The sample was suspended with its axis vertical and located a distance of 9.3 cm from the center of the gas cell. The neutron detector was an 8.9 cm diam x 5.08 cm thick NE 218 scintillator which was coupled to a Phillips 58DVP phototube and could be positioned at distances of 1.5 to 4.0 m from the scatterer. The detector was housed in a 7300 kg shield composed of Cu, paraffin, and Li<sub>2</sub>CO<sub>3</sub>. The detector was also shielded from direct neutrons from the source by a tungsten shadow bar 62 cm long. A second neutron detector was housed in a cylindrical copper shield which was suspended above the scattering plane. This detector viewed the primary neutron source directly and served the purpose of normalizing the neutron fluence for the carbon and polyethylene scatterers throughout the course of the experiment.

A block diagram of the electronics is shown in Fig. 3. Fast timing signals from the main and monitor detectors and the beam pulse pick-off were converted to logic signals by constant-fraction pulse-height discriminators. The time difference between the detector pulses and the delayed pick-off pulses, as measured by time-to-amplitude converters (TAC), determined the flight times of the neutrons. The linear signals from both detectors were used for lower-level discrimination to reject pulses with amplitudes smaller than a predetermined value

and for pulse-shape discrimination (PSD) to reject detected  $\gamma$  rays from the time spectra. The PSD, TOF, and routing pulses were fed through a computer interface to four ADC's. The experimental information was stored and processed by an on-line computer (DDP-224) for on-line display and analysis. Neutron TOF, gamma TOF, and PSD cross-over timing spectra were stored and displayed for both the monitor and main detector systems. The TOF spectra could be displayed simultaneously for on-line diagnostic purposes. The computer also provided for on-line calculations of peak yields, background subtraction, TOF energy calculations, kinematic energy calculations, plus a host of other calculations and diagnostics.

### Experimental Procedure

In order to obtain absolute cross sections, comparisons must be made of the scattering from the nuclei in question and some standard. The accuracy with which this comparison can be made is a major source of uncertainty in the determination of differential cross sections. The principal source of this uncertainty arises because the neutrons scattered from the standard usually have an energy much different from those scattered by the nuclei being studied, and hence, the comparison depends on the relative efficiency of the neutron detector at widely separated neutron energies. This relative efficiency has been difficult to measure in the past with an accuracy better than  $\pm 5\%$ .

Measurements of the <sup>2</sup>H(d,n)<sup>3</sup>He cross-section angular distributions at a number of bombarding energies between 2 and 10 MeV have provided a technique for measuring the energy dependence of the neutron detector efficiency with improved accuracy. The relative efficiency of the neutron detector used in the work reported here was determined by measuring the angular distributions of neutrons from the <sup>2</sup>H(d,n)<sup>3</sup>He reaction at deuteron bombarding energies of 4.0, 6.2, 9, and 10 MeV. These are energies for which the absolute cross sections are quoted with errors of 1-3%. The scattering geometry, PSD, and neutron energy thresholds of the main and monitor detectors were maintained in the same geometrical and electronic configurations during the efficiency and scattering cross section measurements. The PSD electronics was tested and maintained with the continuous neutron and gamma ray spectra generated by a Pu-Be source, while the energy thresholds were placed on the Compton edge which resulted from <sup>137</sup>Cs gamma rays interacting in the scintillators. The relative efficiency of the main detector was determined for neutrons with energies between 2.0 and 13 MeV. The efficiency curve exhibited systematic structure between 7 and 9 MeV when calculated from the absolute cross sections of Schulte, *et al.*<sup>1)</sup>, and lesser systematic structure between 11 and 13 MeV when calculated from the absolute cross sections of Thornton<sup>2)</sup>. This structure was also observed by experimenters in another TUNL group. A series of n-p scattering experiments which overlapped the above energy

\*Partially supported by USAEC

<sup>†</sup>Visiting scientist from Tübingen U.

<sup>††</sup>Visiting scientist from Frankfurt U.

<sup>\*\*</sup>Visiting scientist from Tulane U.



regions were performed to determine the relative efficiency over the 6-9 and 10-13 MeV regions. No systematic structure was observed in the relative efficiency curve by this time-consuming method. The experimental uncertainty on each data point was  $\pm 1-3\%$ , and the fitted curve (Fig. 4) through the points defined the energy dependence of the efficiency to better than  $\pm 2\%$ .

For the scattering cross-section measurements, the cylindrical sample was suspended with its axis aligned with the center of rotation of the detector-collimator system and perpendicular to the reaction plane. The position of the sample was carefully monitored by observation with a leveling telescope. Neutron TOF spectra were obtained with the sample in place and with the sample removed for a fixed number of monitor counts. In addition, sample-in gas-out spectra were taken to complete the background subtraction process. During the course of an angular-distribution measurement, the energy thresholds and PSD of the main and monitor detectors were periodically checked. The course of a measurement proceeded from the forward to the backward angles in  $10^\circ$  increments and then reversed to obtain the  $5^\circ$  incremental angles. This technique served as an additional monitor of the experimental stability. The differential cross sections measured in this experiment were normalized to the accurately known n-p scattering differential cross sections of Hopkins and Breit<sup>3)</sup>. This was accomplished by measuring the number of neutrons scattered by a thin polyethylene  $(CH_2)_n$  scatterer at a laboratory angle sufficient to give separations of the carbon elastic and inelastic and n-p scattering peaks. At energies  $> 13$  MeV it was necessary to perform an additional scattering experiment on a cylindrical carbon scatterer (containing the same number of C nuclei as the polyethylene) so as to correct for overlap of the n-p and C scattering peaks. One of these time spectra with background subtracted is shown in Fig. 5. The well-defined but kinematically broadened n-p scattering peak is seen to be clearly separated from the two peaks resulting from elastic and inelastic scattering by carbon. One polyethylene scattering spectrum was obtained near the beginning of an angular distribution and the second near the end. The normalization constants derived after correcting the yields for dead time in the counting electronics were always found to be consistent with the counting statistics. Additional uncertainties in sample flux-attenuation calculations and n-p scattering cross-section values increase the over-all uncertainty in normalization to 2-3%.

In addition to providing normalization, the polyethylene scattering spectra provided a means of verifying the scattering angle of the neutron detector. The relative positions of the n-p, the carbon elastic, and inelastic scattering peaks depend very sensitively on scattering angle; consequently, comparison of TOF and kinematic peak positions allowed the average scattering angle, with respect to the incident neutron beam, to be determined to within  $\pm 0.3^\circ$ .

#### Data Corrections

The measurements were corrected for background, dead time in the electronic counting systems, and for the effects of finite geometry. The finite sample size and source size corrections were performed using Monte Carlo simulation techniques. The Monte Carlo calculations were performed with an IBM S/370-135 computer using a modified version of the Oak Ridge code. The calculations corrected for the anisotropy of the flux from the primary neutron source, finite source size, angular resolution, multiple scattering, and attenuation in the carbon and polyethylene scatterers. The first two corrections for source anisotropy and size affect the normalization, and depend upon the relative sizes of the scattering sample and the polyethylene sample used to obtain the normalization. The normal-

ization correction factors due to this effect were calculated with the Monte Carlo code to be 1.01.

The remaining finite sample effects which may alter the shape of an angular distribution were also obtained by Monte Carlo calculations. The code simulated the effects of the finite source, detector, and sample geometry and, by iteration, found a single scattering angular distribution which would provide a calculated laboratory angular distribution in agreement with the measured distribution. Sufficient neutron histories were run so that uncertainties in the calculated cross sections due to Monte Carlo statistics were  $< \pm 1\%$  and the calculations stopped when the calculated cross sections were within  $\pm 1\%$  of the least-squares fit to the measured cross sections. A typical Monte Carlo calculation involving 20,000 (forced collision) neutron histories in each of 3 iterations typically required 18 min of computer time. This particular code executes twice as fast on the IBM S/370-135 as on a CDC 6600.

#### Experimental Results

Measurements were made of the differential elastic and inelastic scattering cross sections of natural carbon at 28-30 angles each (in  $5^\circ$  increments) over the angular range  $25-160^\circ$  for incident neutron energies of 9.0, 9.21, 9.60, 10.0, 10.25, 10.74, 11.0, 11.22, 11.79, 12.0, 13.0, 14.0, 14.5, and 15 MeV. These energies were selected in order to probe the structure in the total cross section of carbon. Particular care was taken to probe the minima of the angular distributions in  $2.5^\circ$  increments for a number of cases. The results are displayed in Figs. 6 and 7. The curves through the experimental points are the least-squares fit (LSF) to a sum of Legendre polynomials. The polynomial coefficients and their uncertainties were computed using the LSF technique described by Cziffra and Moravcsik<sup>4)</sup>. The calculations were terminated: (1) when the uncertainty in the highest-order coefficient exceeded the coefficient, (2) when chi-square divided by the number of degrees of freedom reaches a minimum, and (3) when the inclusion of the next higher-order polynomial does not change the integrated cross section by more than its uncertainty. The experimental uncertainties associated with each data point are a propagated combination of relative and normalization errors. The internal consistency of the data sets is illustrated by the completeness with which the polynomial fits intersect nearly all of the data points. The extrapolated zero degrees elastic scattering cross sections are  $> \sigma_{\text{wick}}$  for all energies. Extrapolations of the Legendre polynomial fit to zero degrees agrees to within 1-7% with the recent small angle scattering performed at the USA-BRL at  $E_n=9.5, 11, \text{ and } 14 \text{ MeV}$ <sup>5)</sup>. However, the 7% disagreement emphasizes the need for more detailed small angle scattering measurements over the entire energy range of this experiment.

#### References

1. R.L. Schulte, M. Cosack, A.W. Obst, and J.L. Weil, Nucl. Phys. **A192**, 609 (1972).
2. S.T. Thornton, Nucl. Phys. **A136**, 25 (1969).
3. J.C. Hopkins and G. Breit, Nucl. Data Tables **A9**, 137 (1971).
4. P. Cziffra and M.J. Moravcsik, UCRL-8523, 1959 (unpublished).
5. C.E. Hollandsworth and W.P. Bucher, private communication.



# Cyclo-Graaff Laboratory

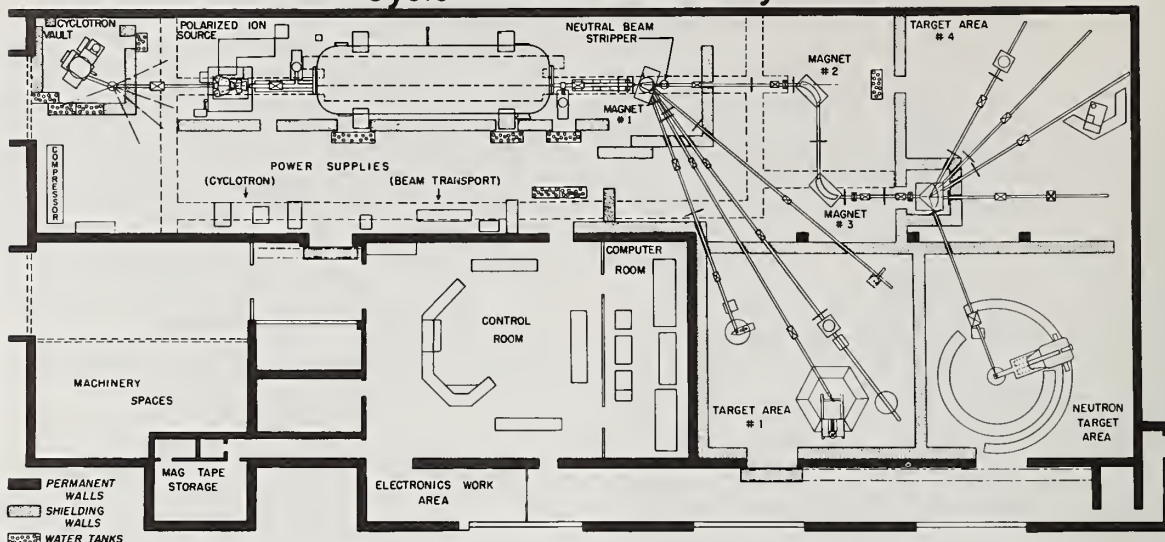


Fig. 1 Plan view of the Cyclo-Graaff Laboratory.

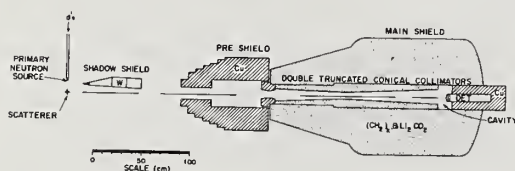


Fig. 2 The experimental scattering geometry used in the differential cross section measurements.

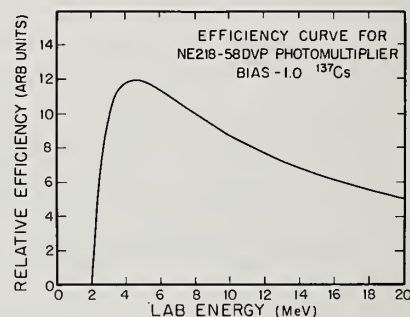


Fig. 4 Relative efficiency curve of the main neutron detector. The curve is an empirical fit to the experimental data.

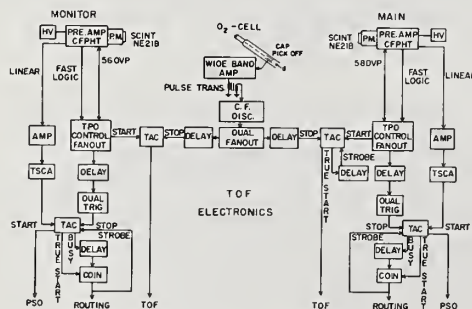


Fig. 3 Block diagram of the experimental electronics.

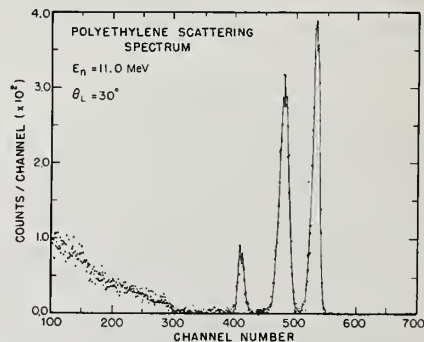


Fig. 5 Neutron TOF spectra showing 11 MeV neutrons scattered from a 5 mm dia. polyethylene cylinder.

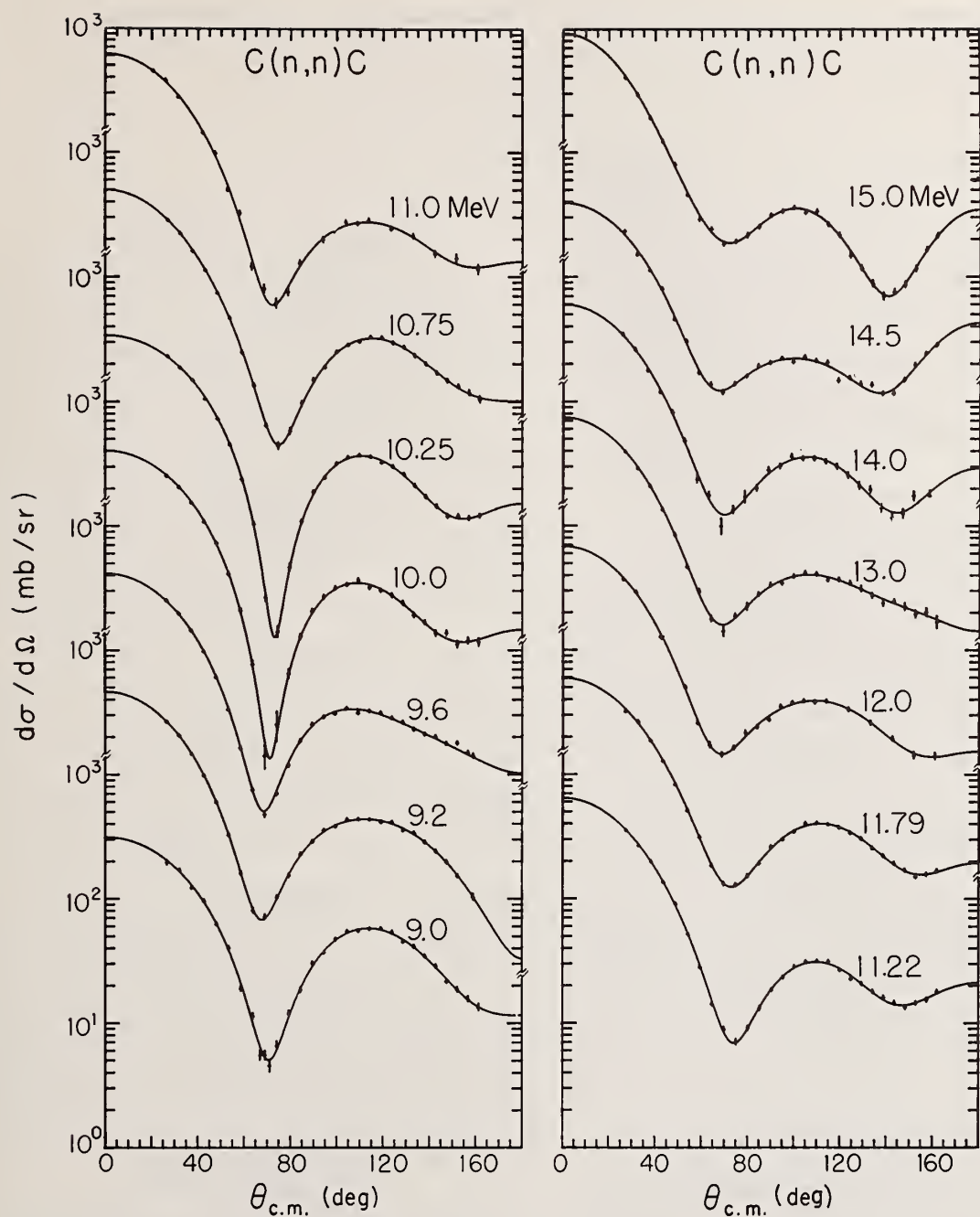


Fig. 6. The angular distribution for the elastic scattering of 9-15 MeV neutrons from carbon.

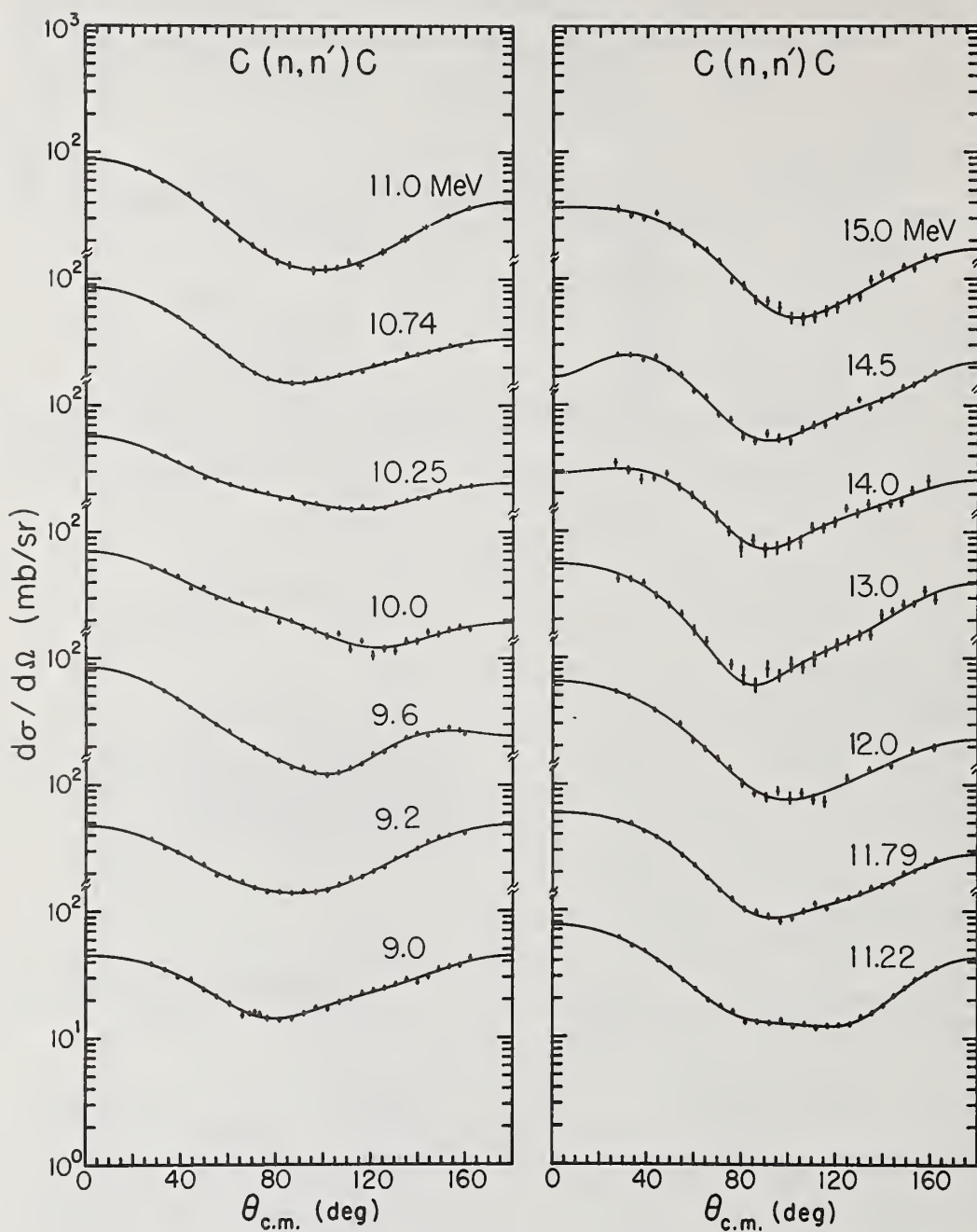


Fig. 7. The angular distribution for the inelastic scattering ( $Q = -4.43$  Mev) of 9-15 MeV neutrons from carbon.



M.A. Etemad

Atomic Energy Organization of Iran  
Nuclear Research Center, Tehran, Iran

Fast neutron inelastic scattering cross sections have been measured for the elements Al, Ti, V, Mn, Fe, Ni, Nb, Pb and Bi by the time-of-flight technique. The measurements were made in the energy range of 2 to 4.5 MeV in steps of 0.25 MeV and at a scattering angle of  $125^\circ$ . The experimental results are compared to the excitation functions calculated on the basis of the Hauser-Feshbach formalism and corrected for the effects of the level width fluctuations.

(Neutrons, Inelastic-Scattering, MeV Range 2 to 4.5, Measurements, Time-of-flight, Hauser-Feshbach)

### 1. Introduction

The accurate knowledge of cross sections for neutron inelastic scattering is important in many fields of nuclear science and technology. In fast reactors inelastic scattering processes largely determine the neutron spectrum, but also in thermal reactors inelastic scattering contributes substantially to the slowing down of neutrons. For the efficient design of neutron shields for all kinds of reactors and also for many types of accelerators one has to know the cross sections for inelastic neutron scattering and the spectrum of the gamma radiation resulting from the subsequent de-excitation of levels. Uncertainties in these cross sections will directly affect the safety and economy of reactors. Accordingly, neutron inelastic cross sections are frequently requested for reactor core and shielding calculations<sup>1</sup>. A study of the list of neutron inelastic cross sections available at present<sup>2</sup> shows clearly that there are still large regions, both in energy and mass number, for which there exist no or few experimental data.

In those cases where no experimental data are available or the existing data are uncertain, calculations of the cross sections based on well established theories will constitute a good basis for the evaluation of the requested cross sections. However, to check the reliability of the models for cross section predictions and in order to estimate the confidence level of the calculated data a systematic study of the inelastic scattering process based on experimental information for a rather large number of elements and over a wide range of energy is necessary.

The present investigation was undertaken to perform a systematic study of neutron inelastic scattering cross sections for a number of elements between Al and Bi over a wide energy range. Neutron inelastic scattering processes have been observed in the elements: Al, Ti, V, Mn, Fe, Ni, Nb, Pb,  $Pb_r$  (radiogenic lead) and Bi in the energy region from 2 to 4.5 MeV at energy steps of 250 KeV. Scattering samples of natural isotopic abundance were used. The experimental results have been compared with those calculated using the Hauser-Feshbach<sup>3</sup> formalism properly corrected for the level width fluctuation and resonance interference effects according to Moldauer<sup>4</sup>.

### Experimental Techniques

The inelastic scattering measurements were performed using the Studsvik 6 MV Van de Graaff accelerator. By using a klystron bunching system in the top terminal of the accelerator pulses shorter than 2 ns at a repetition rate of 1 MHz could be obtained. A neutron time-of-flight spectrometer, with a flight path of 300 cm, was used to record the neutron inelastic scattering spectra. This spectrometer used a neutron detector consisting of a fast organic scintillator with a diameter of 10 cm and a thickness of 5 cm, viewed by a fast photomultiplier.

Neutrons for the scattering measurements were produced by the T(p,n) reaction using a gas target with a length of 3.0 cm. The target cell was filled with tritium gas to a pressure of about 1 atmosphere. The total energy spread of the neutron beam was  $\pm 50$  KeV in the energy range of this work. The scattering samples consisted of cylinders of 5 cm height, 2.5 cm outer diameter and 0.95 cm inner diameter. The target flux was monitored by a direction sensitive neutron long counter positioned at a distance of 300 cm from the target and at an angle of  $72^\circ$  relative to the direction of the charged particle beam. The experimental set up of the present measurements is explained more fully elsewhere<sup>5</sup>.

The inelastic neutron scattering measurements were performed at energies between 2.0 and 4.5 MeV, in steps of 0.25 MeV. The cross sections were measured at only one scattering angle of  $125^\circ$ . This has been shown to be sufficient since the neutron inelastic scattering angular distribution functions are either isotropic or only slightly anisotropic but symmetric around  $90^\circ$  in the C.M. system. To check this, neutron inelastic angular distributions were studied at 3.02 MeV neutron energy and at five different angles;  $30^\circ$ ,  $60^\circ$ ,  $90^\circ$ ,  $125^\circ$  and  $150^\circ$ <sup>5</sup>. The angular distribution functions could be well described by second order Legendre polynomial expansion. Then the total inelastic cross sections were found by multiplying  $4\pi$  by differential cross sections at  $125^\circ$ .

The inelastic cross sections were determined relative to the well known n-p cross sections which has been compiled by Horsley<sup>6</sup>. Thus scattering from hydrogen in the form of a polythene sample was measured for each incident neutron energy at a scattering angle of  $30^\circ$ . The size of the polythene sample was 3 cm in height, 0.95 cm outer diameter and 0.65 cm inner diameter. The method of data analysis and the measurements of neutron detector efficiency curve are discussed in detail elsewhere<sup>5</sup>. The experimental cross sections have been corrected for the effects of the neutron source anisotropy, attenuation of the neutron flux in the scatterer, finite geometry of target-scatterer system and the multiple scattering of neutrons, using Monte Carlo techniques<sup>7</sup>.

### Theoretical Analysis

The inelastic scattering process is mainly characterized by compound nucleus formation in the neutron energy range of the present investigation, i.e. 2.0 to 4.50 MeV. According to the Hauser-Feshbach(H-F)<sup>3</sup> formalism, the angular distributions and the total inelastic scattering cross sections can be calculated provided that the transmission coefficients and the level characteristics (such as spins and parities) of the target nuclei are known. According to Moldauer<sup>4</sup>, the H-F cross section formula must be corrected for the effects of level width fluctuations and resonance interference. Thus a "corrected" transmission coefficient has been

\* Work has been performed at AB. Atomenergi, Studsvik during author's stay in Sweden.

introduced which is a function of a parameter  $Q$ . This parameter which takes into account the resonance interference contribution is depended on the properties of the compound nucleus. In the limit of strongly overlapping resonances its value goes to zero while in the case of isolated resonances  $Q$  approaches unity.

The transmission coefficients used to calculate the neutron inelastic cross sections were obtained from optical model calculations using a local optical potential and a set of generalized optical model parameters. These parameters are derived by Holmqvist and Wiedling<sup>8</sup> on the basis of more than 100 neutron elastic scattering angular distributions measured at Studsvik. These generalized parameters were found to be independent of incident neutron energy but were a function of mass number. The usefulness of these parameters has been further investigated by Etemad<sup>9</sup> who has compared the calculated neutron elastic scattering cross sections for 12 elements, in the energy range of 1.5 to 8.5 MeV, with the available measured cross sections. The neutron inelastic cross sections were calculated on the basis of H-F formalism with and without Moldauer corrections. In the former case calculations were performed for the two limiting cases of  $Q$  equal to zero and one. Information on the properties of the energy levels of the studied elements, used in H-F calculations, is given in a previous report<sup>5</sup>.

### Results

The results of the present neutron inelastic scattering measurements are shown in Figs. 1-9 where the total (integrated) inelastic cross sections are plotted against incident neutron energy. The numerical values of the cross sections are given in a previous report<sup>5</sup>. Included in the figures are also cross sections measured by other experimenters. The results of the theoretical calculations are given by three curves in the Figs. 1-9. The solid curves represent the H-F calculations while the dashed and dashed-dotted curves are those corrected for the level width fluctuations and resonance interference effects with the value of  $Q$  taken to be zero and one, respectively. For the elements Al, V, Fe and Nb, the available experimental data in the literature were adequate to compare the experimental results with the theoretical predictions from threshold to 4.5 MeV. In such cases, comparisons have also been made with the excitation functions recommended by the evaluated nuclear data file ENDF/B-III (dotted curves).

All cross sections given in this work are determined for 100% of the individual isotopes except in the case of element Ti. For this element, the integrated cross sections are given per atom of the natural Ti. The total errors of the inelastic cross sections measured in this work are shown in the figures representing the excitation functions and they are in general of the order of 10-15%.

### Discussions

Since it will be too lengthy, for this report, to discuss the results of the present work in detail, the discussions will be limited to some general remarks. The results of this work are, however, discussed more fully elsewhere<sup>5</sup>.

An overall comparison of the experimental and theoretical results reported in this work indicates that the calculation of neutron inelastic scattering cross sections based on Hauser-Feshbach formalism and properly corrected for the level width fluctuation and resonance interference effects will in general give a good description of these cross sections. At low energies where there are few channels open for the decay of the compound nucleus the corrections according to the Moldauer theory are more important and can not be

neglected. At higher energies where inelastic transitions to many states of the target nucleus will be energetically possible these corrections are small and pure H-F calculations seem to be adequate. The results of the cross section calculations according to Moldauer theory indicate that the excitation functions calculated with the parameter  $Q$  equal to zero agree better with the measured excitation functions.

This type of calculations is very sensitive to the level properties of the target nucleus. Accordingly, proper knowledge of the level energies and their spins and parities is necessary for realistic calculations. Some of the discrepancies between experimental and calculated cross sections in this work can be due to the lack of such information.

### Acknowledgement

The present work has been performed at the Neutron Physics Section of AB. Atomenergi, Studsvik, during author's stay in Sweden. The author wishes to express his appreciation for the support and assistance he received from the AB. Atomenergi, Studsvik.

### References

1. WRENDA 73, INDC(SEC) - 32/U
2. CINDA 74, LAEA, Vienna, 1974.
3. HAUSER, W. and FESHBACH, H., Phys. Rev. 87 (1952) 366.
4. MOLDAUER, P.A., Phys. Rev. 135B (1964) 642.
5. ETEMAD, M.A., AB. Atomenergi, Studsvik, Sweden, Report AE-481, 1973.
6. HORSLEY, A., Nuclear Data A2 (1966) 243.
7. HOLMQVIST, B., et al., Arkiv Fysik 34 (1967) 481.
8. HOLMQVIST, B. and WIEDLING, T., AB. Atomenergi, Studsvik, Sweden, Report AE-430, 1971.
9. ETEMAD, M.A., AB. Atomenergi, Studsvik, Sweden, Report AE-485, 1975.
10. CHIEN, J.P. and SMITH, A.B., Nucl. Sci. Eng. 26 (1966) 500.
11. TOWLE, J.H. and GILBOY, W.B., Nucl. Phys. 39 (1962) 300.
12. HOLMQVIST, et al., Nucl. Phys. A146 (1970) 321.
13. TOWLE, J.H., Nucl. Phys. A117 (1968) 657.
14. SMITH, A.B., et al., Phys. Rev. C1 (1970) 581.
15. BARROWS, A.W. et al., Nucl. Phys. A107 (1968) 153.
16. HOPKINS, J.C. and SILBERT, M.G., Nucl. Sci. Eng. 19 (1964) 431.
17. GILBOY, W.B. and TOWLE, J.H., Nucl. Phys. 64 (1965) 130.
18. MONTAGUE, J.H. and PAUL, E.B., Nucl. Phys. 30 (1962) 93.
19. BARNARD, E. et al., Nucl. Phys. A118 (1968) 321; (PEL-180).
20. ROGERS, V.C., et al., Nucl. Sci. Eng. 45 (1971) 297.
21. TOWLE, J.H., et al., Nuclear Data for Reactors, Paris 17-21 October, 1966. Conf. Proc. IAEA, Vienna, 1967. Vol. 1, p. 367.
22. COLES, R.E., AWRE - 0 - 66/71, 1971.
23. CRANBERG, L. et al., Phys. Rev. 159 (1967) 969.
24. TANAKA, S. et al., Nucl. Phys. A179 (1972) 513.



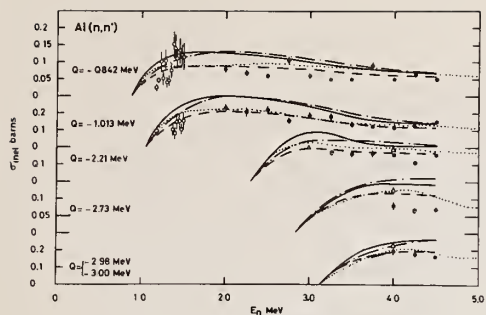


Fig. 1 Excitation functions for Al.

(●) Present measurement,  
 (○) Ref. 10 (△) Ref. 11  
 (—) H - F (---) Q = 0  
 (-.-) Q = 1 (.....) ENDF/B-III

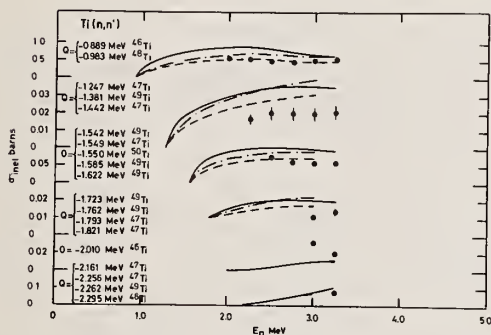


Fig. 2 Excitation functions for Ti.

(●) Present measurement,  
 (—) H - F, (---) Q = 0,  
 (-.-) Q = 1

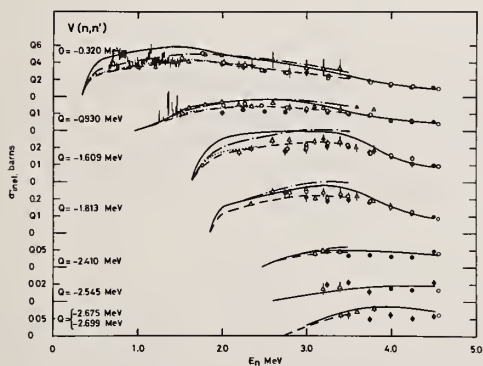


Fig. 3 Excitation functions for V.

(●) Present measurement,  
 (○) Ref. 12, (△) Ref. 13,  
 (□) Ref. 14, (—) H - F,  
 (---) Q = 0, (-.-) Q = 1,  
 (.....) ENDF/B-III

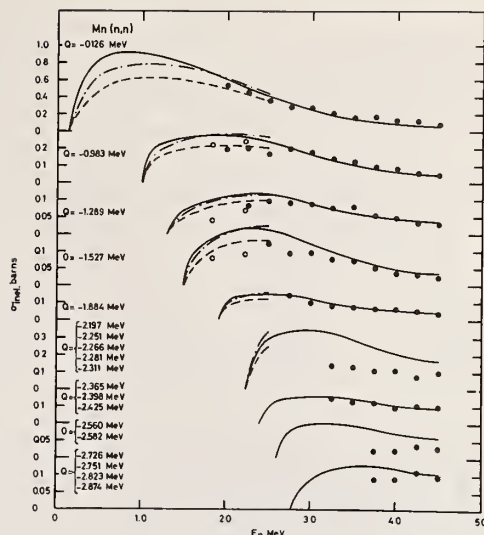


Fig. 4 Excitation functions for Mn.

(●) Present measurement,  
 (○) Ref. 15, (—) H - F,  
 (---) Q = 0, (-.-) Q = 1

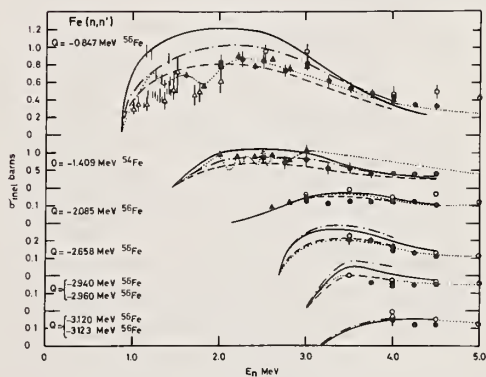


Fig. 5 Excitation functions for Fe.

(●) Present measurement,  
 (○) Ref. 16, (△) Ref. 17,  
 (□) Ref. 18, (◇) Ref. 19,  
 (—) H - F, (---) Q = 0,  
 (-.-) Q = 1, (.....) ENDF/B-III



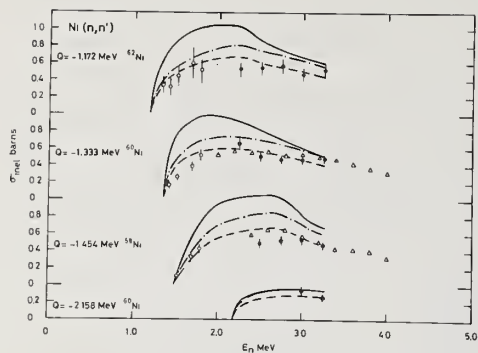


Fig. 6 Excitation functions for Ni.

(●) Present measurements,  
 (○) Ref. 20, (△) Ref. 21,  
 (—) H - F, (---) Q = 0,  
 (-.-) Q = 1

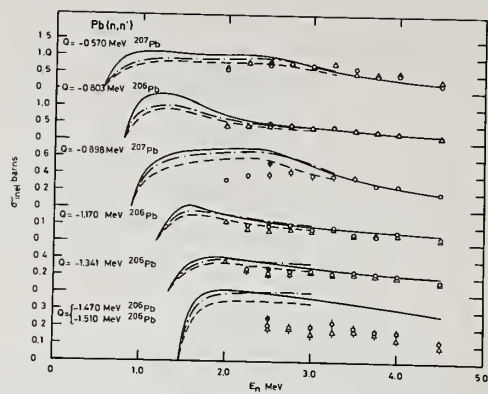


Fig. 8 Excitation functions for Pb.

(○) Present measurement - Pb sample  
 (△) Present measurement - Pb<sub>r</sub> sample  
 (●) Ref. 23, (—) H - F,  
 (---) Q = 0, (-.-) Q = 1

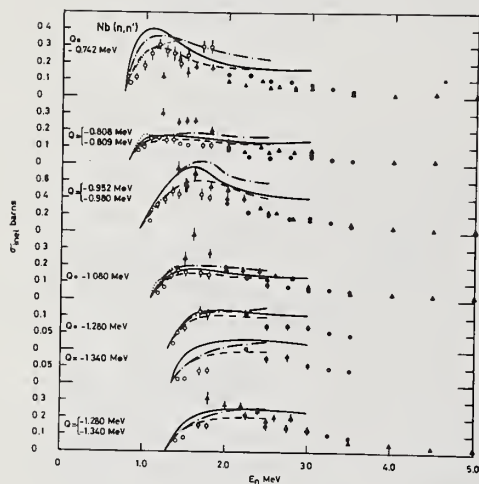


Fig. 7 Excitation functions for Nb.

(●) Present measurement,  
 (○) Ref. 20, (▲) Ref. 22,  
 (—) H - F, (---) Q = 0,  
 (-.-) Q = 1, (.....) ENDF/B-III

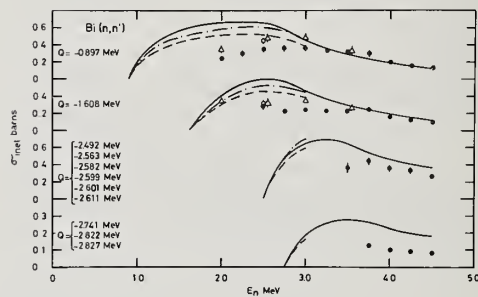


Fig. 9 Excitation functions for Bi.

(●) Present measurement,  
 (○) Ref. 23, (△) Ref. 24,  
 (—) H - F, (---) Q = 0,  
 (-.-) Q = 1

Photoneutrons from the target of the Yale LINAC were polarized by elastic scattering from a cylinder of graphite. The polarized neutrons were observed at angles of  $50^\circ$  and  $130^\circ$  and their energies determined with a time-of-flight resolution of  $0.75 \text{ ns.m}^{-1}$ . The absolute polarization of the neutrons was measured in a true double-scattering experiment; this polarized source then was used to measure the analyzing powers of the reactions  ${}^4\text{He}$ ,  ${}^6\text{Li}$ ,  ${}^9\text{Be}$ , and  ${}^{16}\text{O}$  over wide ranges of energy and angle. These reactions are of interest from three viewpoints i) the design of fission and fusion power reactors ii) absolute neutron standards and iii) fundamental theory. General, multi-level R-function analyses and phase-shift analyses of the observed analyzing powers were made in all cases. Differential and total cross sections were predicted and compared with currently available measurements.

(NUCLEAR REACTIONS:  ${}^4\text{He}(\bar{n},n)$ ;  ${}^6\text{Li}(\bar{n},n)$ ;  ${}^9\text{Be}(\bar{n},n)$ ;  ${}^{12}\text{C}(\bar{n},n)$  and  ${}^{16}\text{O}(\bar{n},n)$ ;  $E=2$  to  $5 \text{ MeV}$ ;  $\theta_{\text{lab}}=20^\circ$  to  $150^\circ$ ; measured  $\bar{p}(E,\theta)$  absolutely for  ${}^{12}\text{C}(n,\bar{n})$  reaction then determined  $A(E,\theta)$  for other reactions; R-function and phase-shift analyses.)

### Introduction

In this paper, we present the results obtained at the Yale Electron Accelerator Laboratory in an extensive program of studies of the polarization of fast neutrons elastically scattered from selected light nuclei. The objectives of the work are the measurement of absolute values of the neutron polarizations over wide ranges of energy and angle, the interpretation of the results in terms of the R-matrix theory of nuclear reactions and the determination of definitive sets of phase-shifts. It is possible not only to shed light on those results deduced from earlier analyses of total and differential cross sections but also to uncover new information concerning those states that do not make themselves felt in the more conventional work.

The importance of polarization measurements stems from the fact that polarization is a consequence of interference effects between the various amplitudes associated with a particular reaction. In the case of neutron-nucleus scattering, such effects can arise in a number of ways, for example: i) in the make-up of the hard-sphere scattering at energies where many different partial wave amplitudes are allowed, ii) from the interference between certain resonance and hard-sphere scattering, iii) from resonance-resonance interference and iv) from interference due to distant levels (which may be interpreted in terms of an optical model).

We have taken the results of our analyses of the polarization data and have predicted the total and differential cross sections. In all cases, good agreement with published work is obtained. This approach is the inverse of that taken in those analyses prior to this work.

The reactions that we have studied are of interest from both pure and applied points of view.

### Experimental Method

The basic method used in these studies involves the polarization of an initially unpolarized flux of neutrons by elastic scattering from a suitable light nucleus (in this case,  ${}^{12}\text{C}$ ). The state of polarization of the flux scattered at a given angle is measured using a true double-scattering method in which the polarized flux is scattered again from an identical  ${}^{12}\text{C}$  target at an identical scattering angle.

The left-right asymmetry in the doubly scattered flux is measured and, after taking into account the (known) energy-loss at the first scattering, the results are analyzed to give the absolute polarization  $\bar{p}$  of the flux.<sup>1</sup> Having established the polarization of the source, the analyzing powers of other nuclei can be obtained simply by replacing the second scatterer with an appropriate target.<sup>2,3</sup>

The initial flux of unpolarized neutrons is generated via the  $(\gamma,n)$  reaction in a heavy nucleus and therefore the primary spectrum is Maxwellian with a maximum intensity at an energy of about  $1 \text{ MeV}$ . The intensity decreases rapidly at energies above  $5 \text{ MeV}$ ; this is a necessary feature in making measurements of polarization that results from elastic scattering of neutrons in light nuclei.<sup>1</sup> The pulsed nature of the LINAC makes it possible to measure the neutron energies with good resolution (typically  $0.7 \text{ ns.m}^{-1}$ ). We have also developed a generalized neutron spin-precession method that is well-suited for use with such a continuous energy spectrum of neutrons; this method greatly reduces the systematic errors that would otherwise occur in the experiment.<sup>4</sup>

Photoneutrons from a Pb-U target are generated by bombardment with  $50 \text{ MeV}$  electrons at a rate of  $270 \text{ s}^{-1}$ . The pulse width is typically  $20 \text{ ns}$  and the peak current  $5$  to  $10 \text{ A}$ . In order to measure the  $\bar{n}$ - ${}^{12}\text{C}$  polarization absolutely, a fraction of the photoneutrons is scattered from a flat plate of graphite  $15 \text{ cm}$  long x  $7.5 \text{ cm}$  wide x  $1.5 \text{ cm}$  thick placed at a reaction angle of  $50^\circ$ . The angular resolution of the arrangement is  $\pm 7^\circ$ . The polarized neutrons travel along a  $27\text{-m}$  flight path (passing through the solenoid) and scatter from a second graphite plate (identical to the first) into two plastic scintillators (each  $12.5 \text{ cm}$  dia x  $15 \text{ cm}$  thick) which are placed at  $\pm 50^\circ$ . These detectors each subtend an angle of  $\pm 7^\circ$  at the second target. The neutron time-of-flight spectra are stored in an on-line computer; the channel widths are typically  $6 \text{ ns}$ . At  $2 \text{ MeV}$ , the overall resolution is about  $50 \text{ keV}$ .

Having determined the "point" polarization of the  ${}^{12}\text{C}(n,\bar{n})$  reaction, the experiment is repeated using cylinders of graphite, each  $10 \text{ cm}$  dia x  $1 \text{ cm}$  thick, in place of the thin plates. The flux of polarized neutrons incident on the second scatterer is in excess of  $0.5 \times 10^6$  neutrons/ $100 \text{ cm}^2\text{-hour}$  between  $2$  and  $5 \text{ MeV}$ . At a reaction angle of  $50^\circ$ , the source polarization in the range  $2.1$  to  $3.4 \text{ MeV}$  is greater than  $50\%$  (negative) and from  $4.4$  to  $5 \text{ MeV}$ , it increases from  $30\%$  to  $50\%$  (positive).

A typical layout of the experiment when used to measure the analyzing power of a light nucleus is shown in Fig. 1. Here, the first reaction angle is  $130^\circ$  (chosen to increase the source polarization

\*Work supported by U.S.A.E.C.

†Now at A.N.U. Canberra, Australia.

††Now at A.N.L. Argonne, Ill. U.S.A.

between 1 and 2MeV) and the analyzer under study is a liquid oxygen target, viewed by an array of scintillation counters:

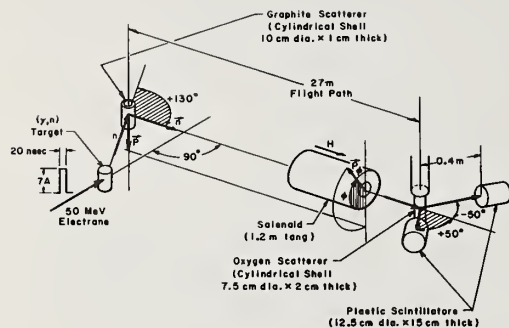


Figure 1.

Arrangement for measuring the analyzing power in  $\bar{n}$ - $^{16}\text{O}$  scattering in the energy range 1 to 4MeV.

The essential points in obtaining the analyzing power when using the generalized spin-precession solenoid are:

The integrated magnetic field required to precess a neutron of measured energy  $E_n$  through  $180^\circ$  is

$$\int H \cdot dl = 2.37 \times 10^5 \times \sqrt{E_n(\text{MeV})} \text{ Oe-cm}$$

and the angle of precession,  $\phi$ , of a non-relativistic neutron of measured energy  $E_\phi$  is

$$\phi = \pi \sqrt{E_n/E_\phi}$$

The product of the polarization  $p$  of the source and the analyzing power  $A$  of the second scatterer is

$$pA = \pm(1-R_\pm)/(R_\pm - \cos\phi)$$

where + and - refer to the right and left detector, respectively and

$$R_\pm = [N_\pm(H)/N_\pm(O)] [C(O)/C(H)]$$

where  $N_\pm(H)$  and  $C(H)$  are the corresponding detector count rates and monitor count rate with the field on and  $N_\pm(O)$  and  $C(O)$  the corresponding rates with the field off. It is now straightforward to deduce  $pA$  independently of the monitor rates. Details of the method are given in Ref. 4. The advantages of this method are well-illustrated in Fig. 2 which shows the time-of-flight spectra of neutrons (doubly-scattered from  $^{12}\text{C}$ ) observed in the left detector ( $-50^\circ$ ) with and without the magnetic field:

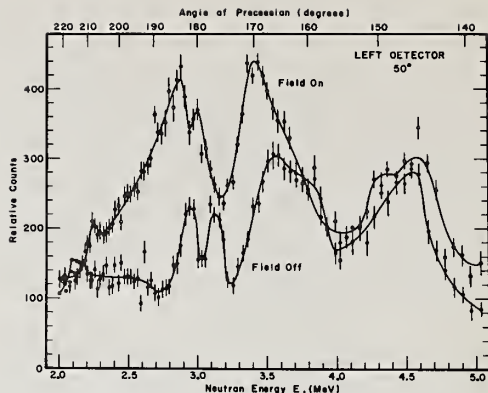


Figure 2.

Spectra of neutrons observed in a single detector at  $-50^\circ$  in a  $^{12}\text{C}$  double-scattering experiment, with and without the solenoidal field on. The field is set to precess a 3MeV neutron through  $180^\circ$ . The precisely determined angles of precession are also given.

The neutron energy-loss that occurs at the first ( $^{12}\text{C}$ ) scatterer can be put to advantage in those cases where it is necessary to reduce the number of high energy neutrons that are generated above the threshold for inelastic scattering. This method was successfully used in the studies of  $\bar{n}$ - $^6\text{Li}$  and  $\bar{n}$ - $^9\text{Be}$  scattering (primary reaction angle equal to  $130^\circ$ ).

#### Phase-shift and R-matrix Analyses

The measured polarizations were analyzed using iterative grid search techniques to give definitive sets of phase-shifts and R-matrix parameters. The inclusion of partial waves higher than d-waves did not alter the quality of the fits significantly. Expressions for the differential cross section, polarization and total cross section used are:

$$\sigma(\theta) = (1/k^2) \sum_{L=0}^{\infty} B_L P_L(\cos\theta)$$

$$\sigma(\theta)p(\theta) = (1/k^2) \sum_{L=1}^{\infty} C_L P_L^1(\cos\theta)$$

$$\sigma_T = (4\pi/k^2) \sum_{L=0}^{\infty} [L \sin^2 \delta_L^- + (L+1) \sin^2 \delta_L^+]$$

where  $P_L(\cos\theta)$  and  $P_L^1(\cos\theta)$  are the Legendre and associated Legendre polynomials. Values for the expression  $B_L$  and  $C_L$  in terms of phase-shifts have been derived by Blatt and Biedenharn and Simon and Welton.<sup>5,6</sup>

The elastic scattering of neutrons from spin-zero nuclei is the simplest application of R-matrix theory.<sup>7</sup> Only one channel is open so that

$$R_{1J} = \sum_{\lambda} \gamma_{\lambda 1J}^2 / (E_{\lambda 1J} - E)$$

where  $\gamma_{\lambda 1J}^2$  and  $E_{\lambda 1J}$  are the reduced widths and energies and the states are denoted by  $\lambda$ , and, also

$$R_{1J} = (f_1 - B_{1J})^{-1}; f_1(E) = a u_1^{-1}(a) (du_1/dr)_a$$

where  $a$  is the channel radius,  $u_1$  is the radial part of the wave function and  $B_{1J}$  is the boundary condition. The collision function  $U_{1J}$  can be expressed in terms of a single, real phase-shift,  $\delta_{1J}$  thus

$$U_{1J} = \exp(2i\delta_{1J})$$



The phase-shifts are related to the R-function as follows

$$\delta_{1J} = -\phi_1 + \arctan \left\{ P_1 R_{1J} / [1 - R_{1J}(S_1 - B_{1J})] \right\}$$

where  $S_1$ ,  $P_1$  and  $\phi_1$  are the well-known shift function, penetrability, and hard-sphere phase-shift. We define the resonance energy  $E_R$  as the energy at which the resonant phase-shift is an odd integral multiple of  $\pi/2$ . The width of the resonance is

$$\Gamma_{\lambda 1J} = 2P_{1J} \gamma_{\lambda 1J}^2$$

Distant levels are taken into account using the method given in Ref. 8, i.e.

$$R_{1J}^\infty = R_{01J} + R_{1J}^E$$

A fit was made to the polarization measurements by minimizing the quantity

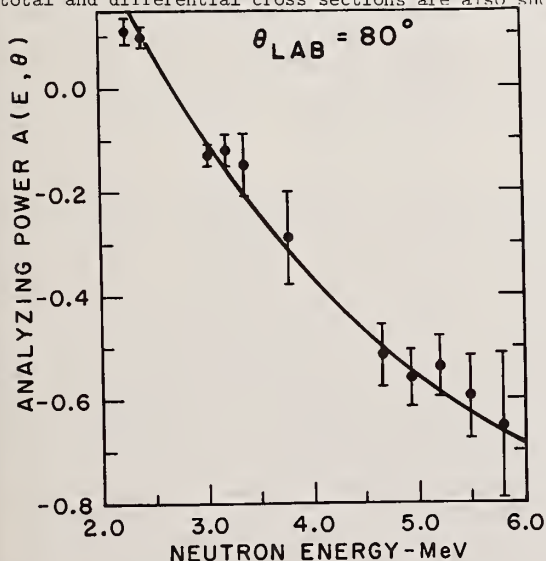
$$S = \sum_{j=1}^M \sum_{i=1}^N \frac{[P_{\text{cal}}(\theta_i, E_j) - P_{\text{exp}}(\theta_i, E_j)]^2}{[\Delta P(\theta_i, E_j)]^2}$$

where  $N$  is the number of angles (between 4 and 9, depending on the experiment) and  $M$  is the total number of energy points used. The optimum R-matrix parameters derived from this procedure, were used to predict the differential and total cross sections, and additional polarizations throughout the entire energy range up to about 5 MeV.

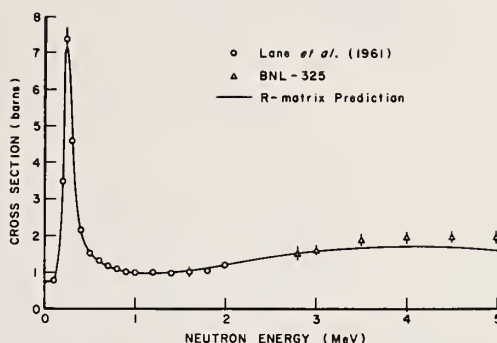
Details of the analysis of the polarization data in the case of  $\bar{n}$ - $^6\text{Li}$  scattering are given in a recent paper.<sup>3</sup> This is a complex problem because the target nucleus no longer has spin zero and the  $(n, \alpha)$  channel must be properly taken into account.

### Results

Typical examples of our measured polarizations (or analyzing powers) and various R-function fits are shown in the following figures. Some predicted total and differential cross sections are also shown:



The measured (absolute) analyzing power for the reaction  $^6\text{Li}(\bar{n}, n)$  at  $\theta_{\text{lab}} = 80^\circ$  in the energy range 2 to 6 MeV. The curve is in good agreement with the predictions of Ref. 9.



The Neutron Total Cross Section of  $^6\text{Li}$   
Figure 4.

The neutron total cross section of  $^6\text{Li}$  predicted from an R-matrix fit to the measured (absolute) analyzing power. The calculation also predicts the  $(n, \alpha)$  cross section using the Thomas approximation for the R-matrix. The points shown above are taken from Refs. 10.

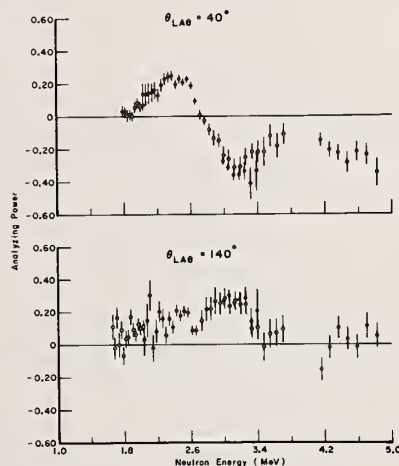


Figure 5.

The measured (absolute) analyzing power for the reaction  $^6\text{Li}(\bar{n}, n)$  at  $\theta_{\text{lab}} = 40^\circ$  and  $140^\circ$  in the energy range 1.6 to 4.8 MeV. The open and closed circles refer to measurements made with the primary reaction angle of the source equal to  $130^\circ$  and  $50^\circ$  respectively.

## Conclusions

The power of this new method of measuring absolute neutron polarizations in light nuclei has now been amply demonstrated. The results have been analyzed within the framework of standard R-matrix theory and have been incorporated into the existing body of data on these nuclei to give information of unprecedented completeness for neutron-induced reactions.

## References

1. R. J. Holt, F. W. K. Firk, R. Nath and H. L. Schultz, Phys. Rev. Lett. **28**, 114(1972) and Nucl. Phys. **A213**, 147(1973).
2. G. T. Hickey, F. W. K. Firk, R. J. Holt and R. Nath, Nucl. Phys. **A225**, 470(1974).
3. R. J. Holt, F. W. K. Firk, G. T. Hickey and R. Nath, Nucl. Phys. **A237**, 111(1975).
4. R. Nath, F. W. K. Firk, R. J. Holt and H. L. Schultz, Nucl. Instr. **98**, 385(1972).
5. J. Blatt and L. Biedenharn, Rev. Mod. Phys. **24**, 258(1952).
6. A. Simon and T. Welton, Phys. Rev. **90**, 1036(1953).
7. A. M. Lane and R. G. Thomas, Rev. Mod. Phys. **30**, 257(1958).
8. F. W. K. Firk, J. E. Lynn and M. C. Moxon, Proc. Phys. Soc. **82**, 477(1963).
9. R. L. Walter and T. Stambach, Nucl. Phys. **A180**, 225(1972).
10. R. O. Lane, A. J. Elwyn and A. Langsdorf, Jr., Phys. Rev. **136**, B1710(1964) and BNL-325(1958).
11. R. B. Schwartz, R. A. Schrack, and H. T. Heaton, II, "MeV Total Neutron Cross Sections" National Bureau of Standards, (1974).

## Appendix

The following R-matrix parameters were obtained in a preliminary fit to our measured analyzing power of the  $^{16}\text{O}(\bar{n},n)$  reaction. The total neutron cross section data given in Ref. 11 were also used in the fitting procedure. Interaction radius =  $1.4(A+1) = 4.3\text{fm}$

l J S	$E_{\lambda l J S}$ (MeV)	$\gamma_{\lambda l J S}^2$ (MeV)	$R_{\lambda l J S}^{\infty}$	$B_{\lambda l J S}$
0 1 1	-0.885	0.4	0	0
0 2 2	-0.555	0.4	0	0
1 0 2	0.7	2.4	0.4	-0.7
1 1 1	-	-	0.4	0
1 2 1	2.75	0.2	0	-0.4
1 1 2	-	-	0.2	0
1 2 2	2.75	1.0	0	-0.4
1 3 2	-	-	0.2	0
2 1 1	-	-	-	0
2 2 1	-	-	-	0
2 3 1	0.63	0.6	0	-1.9
2 0 2	-	-	-	0
2 1 2	-	-	-	0
2 2 2	-	-	-	0
2 3 2	-	-	-	0
2 4 2	2.71	0.8	0	-1.4

The narrow state at 0.82MeV was ignored in the overall fit.

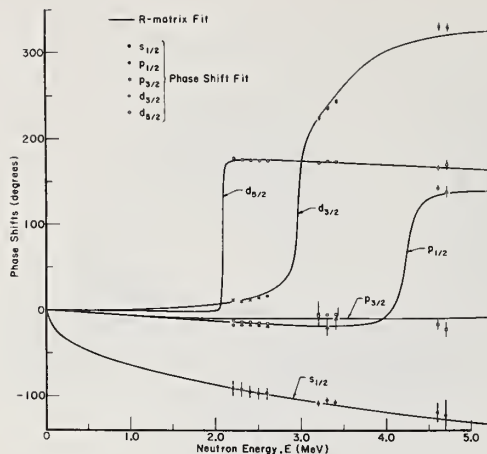


Figure 6.

A phase-shift analysis of the measured absolute polarization for the reaction  $^{12}\text{C}(n,\bar{n})$  the source polarization, together with the phase-shifts derived from the R-matrix fit.

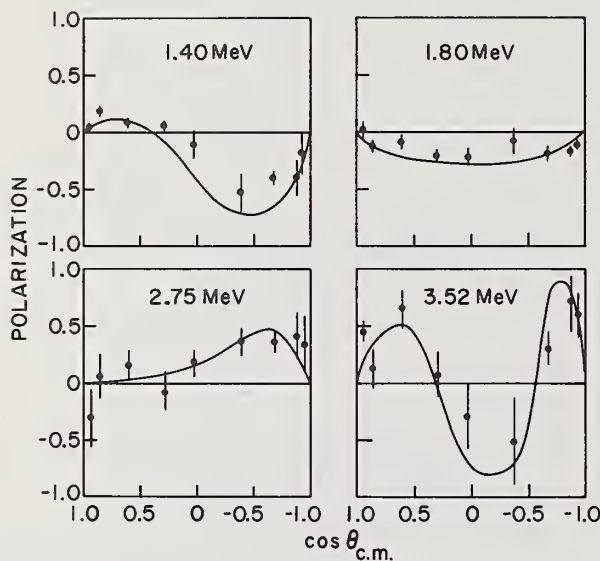


Figure 7.

Four typical R-function fits to the measured analyzing power for the reaction  $^{16}\text{O}(\bar{n},n)$ . Measurements of this kind were made as a continuous function of energy between 1 and 5MeV.

W. E. Kinney and F. G. Perey  
Oak Ridge National Laboratory  
Oak Ridge, Tennessee 37830

The ORNL program to measure neutron elastic and inelastic scattering cross sections for 26 nuclides from C to  $^{238}\text{U}$  in the 4–8.5 MeV energy range is summarized. Data acquisition and reduction techniques are reviewed and typical results given. The nuclides investigated are tabulated.

(Neutron, scattering, cross section, elastic, inelastic, differential)

### Introduction

A program to measure neutron elastic and inelastic scattering cross sections in the 4–8.5 MeV incident neutron energy range was started in 1965 at the ORNL Van de Graaff facility. The program concluded with the publication of the final report in June, 1974, bringing to 26 the number of nuclides investigated. The data acquisition and reduction techniques employed in the program are first discussed. Typical results are given and the results summarized.

### Data Acquisition

Conventional time-of-flight techniques were used in the data acquisition. Neutrons were produced by the  $\text{D(d,n)}^3\text{He}$  reaction on both the 3.0 and 5.5 MeV Van de Graaffs. The deuteron beam was pulsed at 2 MHz and bunched to  $\sim 1.5$  nsec. Deuterium was circulated at  $\sim 1.5$  atm pressure in one of several gas cells from 1 to 4 cm in length and diameter  $\sim 1.5$  cm. Energy resolutions varied from  $\pm 0.03$  to  $\pm 0.17$  MeV depending on the cell length and incident deuteron energy.

The scattering samples, nominally  $\sim 1$  mole of material in the form of solid right circular cylinders, were suspended 10–30 cm from the gas cell. The diameters were  $\sim 1/3$  total mean-free-path to prevent multiple scattering from becoming excessive. The scattered neutrons were detected in NE-213 liquid scintillators optically coupled to XP-1040 photomultipliers. The scintillators were 12.5 cm in diameter. Both 2.5 and 5.0 cm thicknesses were used. A single detector was used in earlier work. Later, three detectors with an angular separation of  $\sim 7^\circ$  were employed. The detectors were mounted on a coordinate system with flight path variable to  $\sim 6$  m and angle to  $\sim 150^\circ$ . Three paraffin shields were employed: a fore shield to attenuate source neutrons, an intermediate shield to decrease the contribution of room and air scattering in the source vicinity, and a detector shield. The source neutron production was monitored by a separate time-of-flight system using a 5 cm diameter by 2.5 cm thick NE-213 detector viewed by a 56-AVP photomultiplier placed  $\sim 4$  m from the gas cell at an angle of  $\sim 55^\circ$ .

Standard electronics supplied the flight time and pulse height for each event to a PDP-7 computer which up-dated the spectra. The electronic bias was set at  $\sim 700$  keV to ensure good pulse shape discrimination against  $\gamma$ -rays. Detector efficiencies were measured by (n,p) scattering from a 6 mm diameter polyethylene sample and also the  $\text{D(d,n)}^3\text{He}$  neutron production at  $0^\circ$ <sup>1</sup>.

When sufficient data were accumulated at a desired experimental configuration (generally to achieve better than 3% statistics in the elastic peak), the data were written on magnetic tape for later processing.

### Data Reduction

Neutron peak areas were first extracted from the monitor spectra on the PDP-7 with the aid of a light pen. The monitor areas, time-of-flight spectra, and geometric parameters were then sent to an

IBM/360 computer where sample-out spectra were normalized to sample-in by the ratios of their monitor areas and subtracted from the sample-in spectra. The resulting spectra were converted from counts vs time-of-flight spectra to center-of-mass cross section vs energy spectra. The energy spectra were then smoothed and written on magnetic tape for further processing by the PDP-7. Figure 1 shows the initial time-of-flight spectrum with its converted energy spectrum for  $^{54}\text{Fe}$  at an incident neutron energy of 6 MeV at  $90^\circ$ .

Peak areas were extracted from the energy spectra on the PDP-7 with the aid of its light pen. Generally, three areas corresponding to best, low, and high estimates of the background were extracted for each peak. The high and low estimates were treated as 95% confidence limits in including stripping uncertainties with other uncertainties in the error analysis. The peak areas and continuum information, if any, were written on magnetic tape for final processing by the IBM/360.

Finite sample corrections were made according to semi-analytic recipes<sup>2</sup>. Corrections to elastic data were typically 5–10% at forward angles and 40–80% in the first minimum. Anisotropic results were fit by least squares to a Legendre series to obtain angle-integrated cross sections.

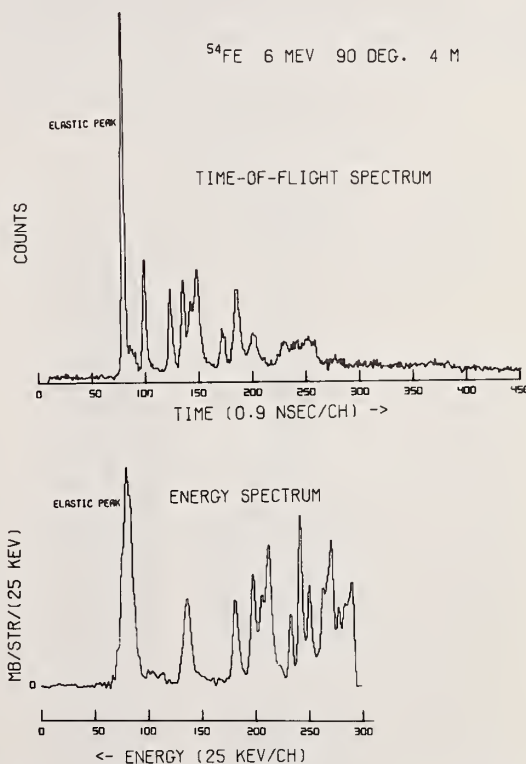


Fig. 1. A typical time-of-flight spectrum for  $^{54}\text{Fe}$  with its transformed energy spectrum. The sample-out spectrum has not been subtracted from the time-of-flight spectrum and the energy spectrum has been offset. The energy spectrum terminates at  $\sim 1$  MeV scattered neutron energy— $\sim$  channel 350 in the time-of-flight spectrum.

\*Research performed at Oak Ridge National Laboratory operated by Union Carbide Corporation for the Energy Research and Development Administration.



The nuclides studied are summarized in Table I, below. Most were chosen to satisfy, at least partially, requests to NCSAG.

Elastic scattering differential cross sections were measured for all samples except  $^{206}\text{Pb}$  and  $^{207}\text{Pb}$  since their elastic scattering cross sections are expected to be essentially the same as those for  $^{208}\text{Pb}$ . The data were reported in both graphical and tabular form and were compared with the results of others and with the then-current ENDF/B evaluations. A typical graphical presentation of elastic scattering data is shown in Figure 2 where data for natural nickel and  $^{60}\text{Ni}$  are compared. The curves are Legendre fits to the natural nickel results. The degree of agreement among the data is gratifying and lends confidence to the reproducibility achievable with our data acquisition and reduction techniques. It is to be noted that the 6.44–8.56 MeV  $^{60}\text{Ni}$  data were taken roughly a year earlier than the other data and were reduced by different experimentalists.

Differential cross sections for inelastic scattering to discrete levels or groups of levels in the residual nucleus (the predominant isotope in the case of natural samples) were measured for all samples except  $^{238}\text{U}$ . Comparisons were made with the results of others but no other data existed for 12 of the samples. Comparisons with then-current ENDF/B evaluations, when available, were also made.

Level densities and spacings are such for 14 of the nuclides investigated that, with our experimental energy resolutions, maxima in the inelastic scattering cross sections could not be uniquely identified with the excitation of specific groups of levels for excitation energies above a few MeV. In these cases, the data were reduced as inelastic scattering to a continuum. Considerable structure indicating preferential excitation of some levels was found in the continua for all nuclides lighter than W thus casting doubt on the adequacy of treating continuum inelastic scattering by a simple evaporation model in those cases. An example of continuum structure is shown in Figure 3 where data for  $^{60}\text{Ni}$  are given.

Table I  
Summary of Results

Element or Isotope	Maximum Inelastic Discrete Level $E_x$ , MeV	ORNL Report
C	4.43	4441 (12/69)
N	5.10	4805 (2/74)
O	6.131	4780 (4/72)
Na	5.78 + continuum	4518 (8/70)
Mg	6.00	4550 (6/70)
Al	5.825	4516 (10/70)
Si	6.887	4517 (7/70)
S	6.76	4539 (6/70)
Ca	6.58	4519 (4/70)
Ti	3.86 + continuum	4810 (10/73)
V	3.08 + continuum	4551 (10/70)
Cr, $^{52}\text{Cr}$	3.49 + continuum	4806 (1/74)
$^{54}\text{Fe}$	4.58 + continuum	4907 (2/74)
Fe	4.116 + continuum	4515 (6/70)
Co	2.585 + continuum	4549 (6/70)
Ni, $^{60}\text{Ni}$	4.613 + continuum	4523 (4/70)
		4807 (1/74)
$^{63}\text{Cu}$ , $^{65}\text{Cu}$	1.72 + continuum	4908 (2/74)
Y	3.87 + continuum	4552 (12/70)
W	continuum	4803 (5/73)
$^{206}\text{Pb}$	2.634 + continuum	4909 (6/74)
$^{207}\text{Pb}$	4.386 + continuum	"
$^{208}\text{Pb}$	5.254 + continuum	"
$^{238}\text{U}$	—	4804 (6/73)

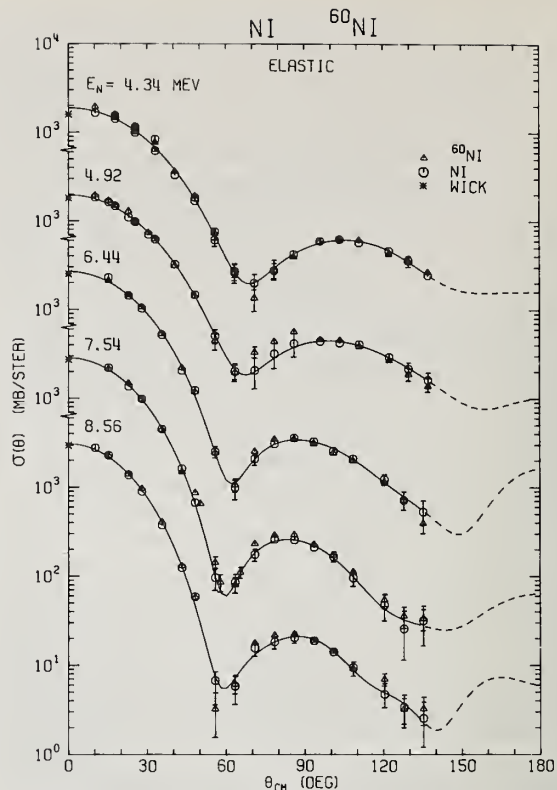


Fig. 2. Our natural nickel and  $^{60}\text{Ni}$  elastic differential elastic scattering cross sections with Legendre fits to the natural nickel data. WICK is Wick's Limit.

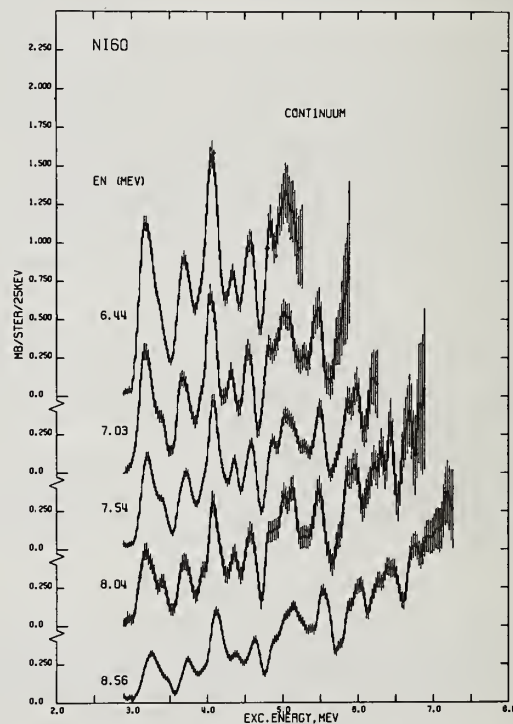


Fig. 3.  $^{60}\text{Ni}$  angle-averaged cross sections for inelastic scattering to the continuum as a function of excitation energy for incident neutron energies,  $E_N$ , from 6.44 to 8.56 MeV. The structure is typical of that found in the continua for nuclides lighter than W.

Our differential cross sections were integrated over angle by fitting anisotropic angular distributions to a Legendre series or by averaging distributions which were isotropic within experimental uncertainties. The angle-integrated data were plotted vs incident neutron energy and compared with the results of others and with then-current ENDF/B evaluations. Typical of these results is Figure 4 where  $^{52}\text{Cr}$  and natural

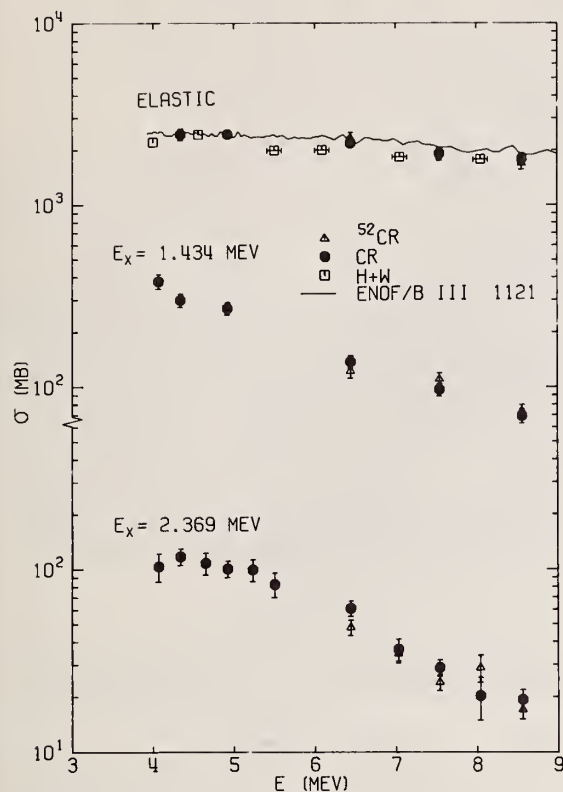


Fig. 4. Natural chromium and  $^{52}\text{Cr}$  angle-integrated elastic scattering cross sections and cross sections for inelastic scattering to levels in  $^{52}\text{Cr}$  per atom of natural chromium as a function of incident neutron energy,  $E$ . Results of Holmqvist and Wiedling (H + W)<sup>3</sup> and the ENDF/B III 1121 curve are also shown.

chromium data are compared with the results of Holmqvist and Wiedling<sup>3</sup> and with the ENDF/B III 1121 evaluation.

Our data were generally in agreement or consistent with the results of others in our opinion. We considered eight of the then-current ENDF/B evaluations to be an adequate-to-good representation of neutron elastic and inelastic scattering data in the 4–9 MeV energy range while nine were found to be deficient in some respects. All the materials for which evaluations existed have been re-evaluated.

### Summary of Results

Table I summarizes the nuclides investigated. The second column lists the maximum excitation energy for which inelastic scattering to discrete levels was extracted and also whether inelastic scattering to a continuum was included. The ORNL report number and date of publication are given in column 3. All results have been sent to the National Neutron Cross Section Center for inclusion in CSISRS.

### Acknowledgement

This program reflects the work of many. We gratefully acknowledge the contributions of J. W. McConnell, A. M. Marusak, J. A. Biggerstaff, M. V. Harlow, C. O. LeRigoleur, J. K. Dickens, P. H. Stelson, E. Hungerford, C. M. Perey, and the staff of the ORNL Van de Graaff Laboratory.

### References

1. W. E. Kinney, "Neutron Elastic and Inelastic Scattering from  $^{56}\text{Fe}$  from 4.60 to 7.55 MeV", ORNL-TM-2052, January, 1968
2. W. E. Kinney, *Nucl. Instr. and Methods*, 83, 15 (1970)
3. B. Holmqvist and T. Wiedling, "Neutron Elastic Scattering Cross Sections: Experimental Data and Optical Model Cross Section Calculations", AE-366, Aktiebolaget Atomenergi (1969)

FAST NEUTRON CAPTURE AND ACTIVATION CROSS SECTIONS  
W. P. Poenitz  
Argonne National Laboratory  
9700 South Cass Avenue, Argonne, Illinois 60439, U.S.A.

Fast neutron capture cross sections were measured in the energy interval from 0.02 to 0.7 MeV using white source neutron time-of-flight techniques and from 0.3 to 3.0 MeV using monoenergetic neutrons. Target materials were Co, Ni, Zn, Cu, Nb, Ho, Ta, Au and  $^{238}\text{U}$ . A 1300 l liquid scintillator was used as a capture  $\gamma$ -ray detector. Flat efficiency neutron detectors and/or the standard capture cross section of Au were used for the neutron flux determination. Fast neutron capture and activation cross sections were calculated in terms of the statistical model. The Hauser-Feshbach formalism and a gamma cascade model previously described<sup>1</sup> were used.

(Fast neutron capture, Co, Ni, Cu, Zn, Nb, Ho, Ta, Au,  $^{238}\text{U}$ , theory and experiment).

### Introduction

Fast neutron capture and activation cross sections are of considerable interest to fission and fusion reactor evaluators in connection with neutron absorption losses,  $\gamma$ -ray production and after-heat problems. These important applications have led to a large number of measurements, applying a variety of experimental techniques. In the present measurements, a large liquid scintillator<sup>2</sup> was used for the detection of the prompt capture  $\gamma$ -rays. The neutron flux was measured with a Grey Neutron Detector<sup>3</sup> and most of the cross section values were normalized with the standard capture cross section of Au. Measurements for elemental samples of Co, Ni, Zn, Cu, Nb, Ho, Ta, Au and  $^{238}\text{U}$  were carried out in various energy ranges depending on the specific interest in a material.

The basic formalism for the theoretical calculation of fast neutron capture cross sections in terms of the statistical model was developed more than two decades ago<sup>4-5</sup>. This formalism was applied in many systematic calculations of capture cross sections<sup>6-10</sup>. The agreement between different theoretical results and between theoretical and experimental values was not always satisfactory. Discrepancies up to a factor of 2 were found<sup>8-10</sup>. Other theoretical calculations resulted in a relatively good description of the experimental values<sup>7-10</sup>. There are many publications dealing with the calculation of activation cross sections at thermal neutron energy, however, only a few concerning the calculation of fast neutron activation cross sections<sup>11-13</sup>. In view of the difficulties to measure most of the important activation and capture cross sections of fission product nuclei, further study of fast neutron activation and capture cross sections appears desirable.

### Experimental Techniques

The  $^7\text{Li}(p,n)^7\text{Be}$  reaction was utilized as a neutron source. A pulsed and bunched proton beam was accelerated by the Argonne Tandem-Dynamitron. The repetition rates were 0.5, 1 or 2 MHz and the pulse width was 1-2 nsec. The targets consisted of metallic lithium with thicknesses between 0.04 and 0.1 MeV for the production of "monoenergetic" neutrons and about 0.5 MeV for white-spectrum measurements. A 4 $\pi$  neutron shield surrounding the source was used in order to reduce the  $\gamma$ -ray and neutron background of the detectors. A conical opening in the shield provided a collimated neutron beam.

The capture  $\gamma$ -ray detector was a 1300-liter iron tank filled with a liquid scintillator. The scintillation light was viewed by twelve AVP 57 multipliers. The time resolution of the detector was 3-4 nsec and the  $\gamma$ -energy resolution was 26 per-

cent for  $^{60}\text{Co}$  (FWHM). The threshold for the detection of  $\gamma$ -rays was set in the range 0.8-3.0 MeV in order to eliminate the detection of  $(n,n'\gamma)$  and  $(n,\gamma n')$  processes. The tank was shielded by 10-20 cm of lead, 60 cm of concrete and partially by 2-4 cm of low-background iron.

The samples consisted of metallic discs with a diameter of 8.9 cm. With exception of the Ho sample, which contained 2 percent Er, all samples were at least 99.5 percent pure. The samples were placed in the flight-path 2.5 m from the source. This was sufficient to separate by time-of-flight the low-energy neutron group of the source reaction up to 2.5 MeV primary neutron energy.

The Grey Neutron Detector<sup>3</sup> was used as a neutron monitor for measurements with monoenergetic neutrons. However, some absolute values for the capture cross section of Au were obtained by using the Black Neutron Detector<sup>14</sup>. A 1 mm-thick lithium glass detector was used as a neutron flux monitor in the white spectra measurements.

The data were recorded with an on-line computer system. The time-of-flight spectra from the capture  $\gamma$ -ray detector and from the Li-glass detector were recorded as well as the energy spectrum coincident with the neutron peak in the time-of-flight channel. A corresponding energy spectrum coincident with an equally spaced interval adjacent to the neutron peak was utilized for background subtraction.

Corrections were applied for the capture of neutrons scattered elastically or inelastically within the sample, the efficiencies for the capture and the neutron detector, scattering of neutrons in air, and the neutron flux attenuation in the samples. The dominant uncertainty is due to the extrapolation of the capture  $\gamma$ -ray energy spectra to zero pulse height. This uncertainty limits the accuracy of the present measurements to 7 percent at best.

In the case of some low energy resonance cross section measurements of Ni, only an average correction was applied for the capture of scattered neutrons. The statistics and background contribute in this case appreciably to the uncertainty of the data.

### Experimental Results

#### Low Energy Measurements for Ni and $^{238}\text{U}$

The capture cross sections of Ni and  $^{238}\text{U}$  are of interest as structural and as fertile materials in reactor design. These cross sections were measured in the lower keV range relative to the capture cross section of Au using a white spectra neutron source. The data are shown in Figs. 1 and 2. The  $^{238}\text{U}$  data were averaged over 4, 10 and 20 keV intervals, eliminating most of the structure which exists in both the  $^{238}\text{U}$  capture and the Au



reference cross sections. The Ni capture cross section has many very narrow resonances and hence the widths observed in the measurements are given by the experimental resolution. In order to improve the statistics of the results the data were further averaged with a resolution of about 3 nsec/m.

#### Intermediate Energy Range

The white spectra measurements on Ni revealed some structure at several hundred keV. Thus, the white spectra measurements were extended to the 0.35-0.75 MeV range. Neighboring elements were included in these measurements. Fig. 3 shows the data obtained for Co, Ni, Cu and Zn. Ni shows a very pronounced structure with fluctuations exceeding 30 percent above 0.5 MeV. Also shown in this figure are data for the total cross section of Co and Ni. These data were obtained from an evaluated data file<sup>15</sup> and averaged with the same resolution as those for the capture cross section. The structure obtained for the capture cross sections is very similar to that of the total cross sections, however, differences in the amplitudes at some energies are apparent.

#### MeV Energy Range

Measurements with monoenergetic neutrons were

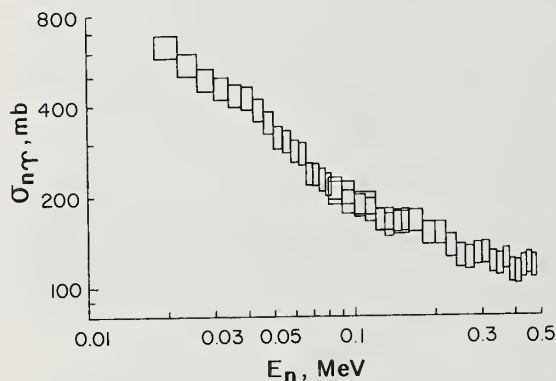


Fig. 1. Capture Cross Section of  $^{238}\text{U}$ .

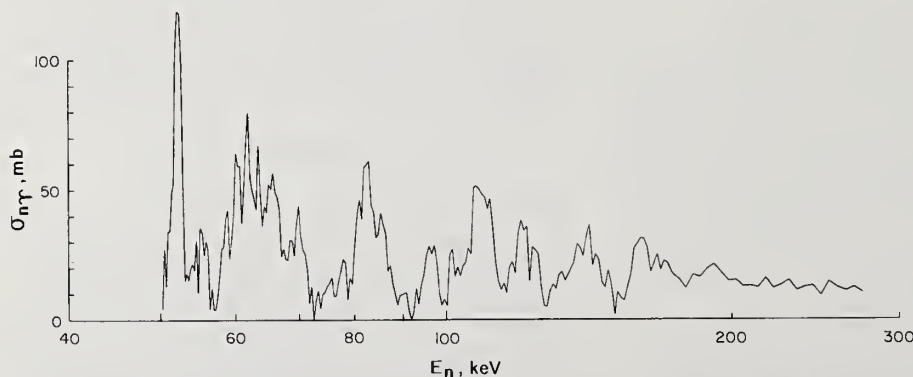


Fig. 2. Capture Cross Section of Ni obtained with white neutron source measurements.

carried out between 0.3 and 3.0 MeV for Ni, Cu, Zn, Nb, Mo, Ta, Au, and  $^{238}\text{U}$ . The results are shown in Fig. 4. The size of the symbols shows the uncertainty of the measurement. All values were normalized at 0.5 MeV to a capture cross section of 138 mb for Au which was obtained in an evaluation of a consistent set of data for several standard cross sections<sup>16</sup>.

#### Model Calculations

In the energy range of the present measurements, the statistical theory should apply and the neutron capture or activation cross section were derived from

$$\sigma_1(E) = \frac{1}{2(2I+1)} \frac{\pi}{k^2} \sum_{l=0}^{\infty} \sum_{j=|l-\frac{1}{2}|}^{l+\frac{1}{2}} T_n(lj, E) \cdot \frac{\sum_{j=|j-I|}^{j+I} (2J+1) T_c(J, E) \cdot R \cdot B_i(J, E)}{T_Y(J, E) + \sum_n T_n(l', j', E, E_m)}$$

The sum in the denominator is over all neutron exit channels.  $R$  is a correction for replacing the average over the ratios in above formula with the ratio of the averages.  $T_c$  and  $T_n$  are given by  $2\pi\langle\Gamma\rangle/\langle D\rangle$  where a difference is made between the total radiation width  $\langle\Gamma\rangle$  and the capture width  $\langle\Gamma\rangle$ . The  $B_i(J, E)$  are the probabilities for the occupation of a low lying level by the  $\gamma$ -cascades. Thus, if  $i$  denotes an isomeric state,  $\sigma_i$  is the appropriate activation cross section. The total capture cross section is obtained for setting all  $B_i=1$ . All other notations in above formula are as commonly used.

Following the experimental situation and a previously used model<sup>1</sup>, both the target and the compound nucleus are assumed to consist of discrete low lying levels with known spin energy and parity and at higher energies of a level continuum described by a level density formula. The fermi-gas model with modifications for shell and pairing energy was used in the present calculations.

Partial  $\gamma$ -radiation widths obtained from the single-particle model by Weisskopf<sup>17</sup> were commonly used in the calculation of total radiation widths and  $\gamma$ -cascade behavior. However, Axel<sup>18</sup>, derived a different expression for the  $\gamma$ -width from the inverse cross section,  $\sigma_Y$ , thus suggesting the giant resonance energy dependence for the partial widths.

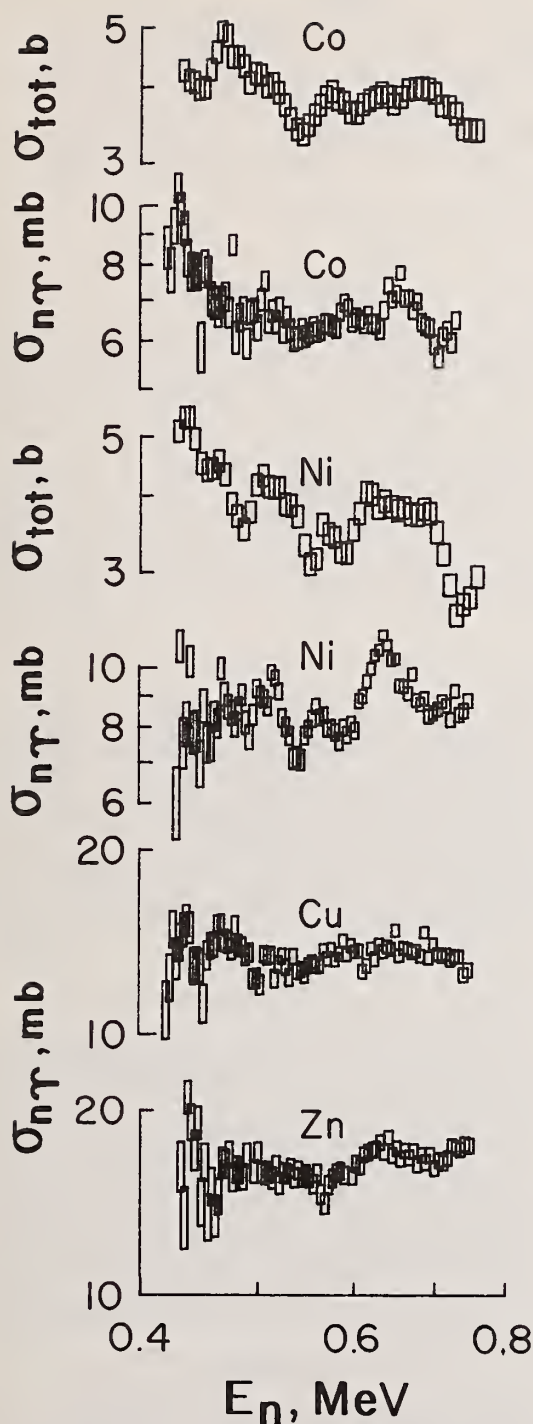


Fig. 3. Total and Capture Cross Sections of Co, Ni, Cu and Zn.

The neutron transmission coefficients for the discrete levels were calculated with the optical model code ABACUS<sup>19</sup>. Neutron transmission coefficients to levels in the continuum of the target nucleus were calculated with the assumption of a completely absorbing nucleus.

Gamma and capture transmission coefficients were calculated by summing over all transitions to discrete levels and integrating over the level density in the continuum. Weisskopf, Axel and Pigmy resonance transitions were used optionally.

The calculation of the low level occupation probabilities was carried out with a  $\gamma$ -cascade model previously described<sup>1</sup>. However, the Axel and Pigmy resonance transition probabilities were included as an option to the single-particle transition probabilities.

Model calculations are discussed here for the capture and activation of <sup>181</sup>Ta. Ta is of specific interest as a test example for the present calculations because the daughter nucleus, <sup>182</sup>Ta, has an isomeric state with a high spin value (10<sup>-</sup>) and thus a very small activation cross section for this isomeric state. Experimental values for the activation cross section exist up to 1.6 MeV<sup>20</sup>.

Capture cross sections are very insensitive to the neutron transmission coefficients. As a result, the difference between spherical model and deformed model calculations result in negligible differences for Ta<sup>9</sup>. Brzosko et al.<sup>21</sup> calculated  $\gamma$ -ray spectra and fast neutron capture cross sections for a number of elements including Ta using the Axel transition probabilities. They suggested that Ta requires a Pigmy resonance contribution as well as all the other considered elements, though the  $\gamma$ -ray spectrum does not show the anomalous bump in the 5-6 MeV range.

Fig. 5 shows the results from the present calculations in comparison with the present experimental results for the capture cross section and the measurements by Cox<sup>20</sup> for the isomeric state. All curves labeled with A are for parameters in the level density formulas and transition probabilities applicable to a wide range of nuclei. The only normalization used is the value for  $\langle \Gamma \rangle / \langle D \rangle$  which was obtained from experimental values in the eV-energy range<sup>22</sup>. The improvement obtained for the capture cross section by using Axel instead of Weisskopf is similar as recently reported by Gardner<sup>23</sup>, however, the difference between the inclusion or exclusion of 1 percent Pigmy resonance is much smaller than obtained by Brzosko et al.<sup>21</sup>. The most satisfactory result of the present calculations is the good agreement obtained for the isomeric cross section which is about two orders of magnitude smaller than the capture cross section. Inclusion of quadrupole radiation in the  $\gamma$ -ray cascades changes the isomeric cross section very little, however, increasing the spin cut-off factor in the level density formula to a value desirable for a deformed nucleus<sup>24</sup> improves the agreement for the capture cross section but increases the isomeric cross section excessively.

#### Conclusions

Experimental measurements of fast neutron capture cross sections on stable nuclei provide a basis for the calculation of capture and activation cross sections. The agreement obtained for calculated cross sections gives confidence in calculations for unstable isotopes which are difficult to measure. An example is <sup>94</sup>Nb in which results were recently reported<sup>13</sup>.

Acknowledgment. This work was supported by the U.S. Energy Research and Development Agency.

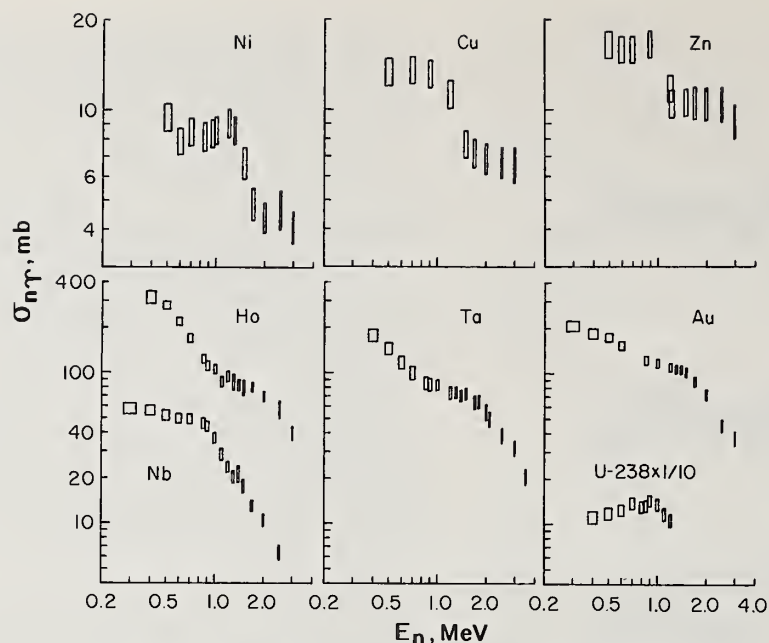


Fig. 4. Results obtained with monoenergetic neutrons.

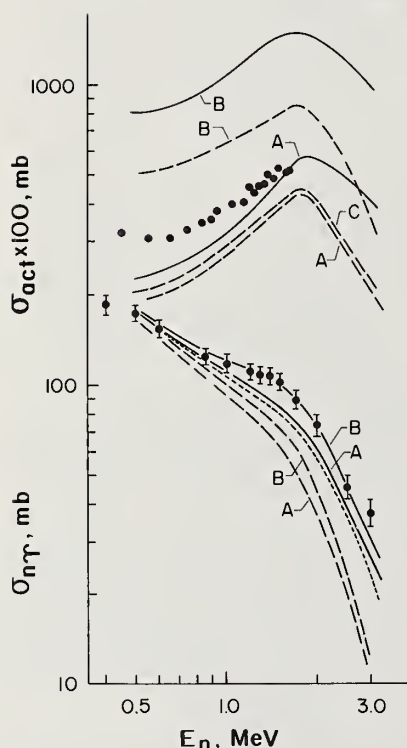


Fig. 5. Comparison of experimental values and theoretical calculations. All solid curves were obtained with Axel and 1 percent Pigmy resonance transitions, the dotted curve is for Axel only, and all dashed curves are for Weisskopf. Curves labeled B assume larger spin cut-off factors, curve C includes 2 percent quadrupole transition.

#### References

1. W. P. Poenitz, *Z. f. Physik* **197**, 262 (1966).
2. F. Reines et al., *Rev. Sci. Instr.* **25**, 1061 (1954).
3. W. P. Poenitz, *Nucl. Instr. Methods* **58**, 39 (1968).
4. B. Margolis, *Phys. Rev.* **88**, 327 (1952).
5. A. M. Lane, J. E. Lynn, *Proc. Phys. Soc.* **A70**, 557 (1957).
6. V. Benzi and M. V. Bortolani, *Conf. on Nucl. Data*, Vol. I, 537, IAEA (1967).
7. V. Benzi et al., *Comitato Nazionale Energia Nucleare*, RT/ I(69)44 (1969).
8. J. L. Cook, *Conf. on Nucl. Data*, Vol. I, 549, IAEA (1967).
9. M. P. Fricke et al., *Conf. on Nucl. Data*, Vol. II, 281, IAEA (1970).
10. F. Schmittroth, *hanford Eng. Dev. Lab.*, ENDF-195 (1973).
11. J. Csikai et al., *Nucl. Phys.* **41**, 316 (1963).
12. H. A. Grench et al., *Nucl. Phys.* **A94**, 157 (1966).
13. W. P. Poenitz, *Argonne National Laboratory*, ANL/NDM-8 (1974).
14. W. P. Poenitz, *Nucl. Instr. Methods* **109**, 413 (1973).
15. A. B. Smith, *Argonne National Laboratory*, ANL/NDM-1 and priv. com. (1974).
16. W. P. Poenitz, *Conf. on Neutron Standards*, USAEC CONF-701002 (1970).
17. J. M. Blatt, V. F. Weisskopf, *Theoretical Nuclear Physics*, John Wiley & Sons, N.Y. (1952).
18. P. Axel, *Phys. Rev.* **126**, 671 (1962).
19. E. H. Auerbach, *Brookhaven National Laboratory*, BNL-765 (1962).
20. S. A. Cox, *Phys. Rev.* **133**, B378 (1964).
21. J. S. Brzosko et al., *Can. J. Physics* **47**, 2849 (1969).
22. S. F. Mughabghab, D. I. Garber, *Brookhaven National Laboratory*, BNL-325, 3rd Ed. (1973).
23. D. G. Gardner, *Bull. Am. Phys. Soc.*, Vol. 19, No. 9, 1017 (1974).



# SCATTERING OF NEUTRONS BY NITROGEN AND OXYGEN FROM 5.0 TO 9.3 MeV

D. L. Bernard

University of Southwestern Louisiana  
Lafayette, Louisiana 70501

and

M. C. Taylor

Columbia Scientific Industries Corporation  
Austin, Texas 78762

Angular distributions of neutrons scattered elastically and inelastically from nitrogen-14 and oxygen-16 have been measured at neutron energies of 5.04, 6.25 and 9.29 MeV. Neutron flux attenuation and multiple scattering corrections were made using a modified version of an existing computer code. Special consideration was given in the modification of the code to developing an angular resolution function to treat the effects on multiple scattering corrections due to the solid angle subtended by the scattering sample at the neutron producing target. Graphs and tabulated results are presented as center of mass differential scattering cross sections versus the cosine of the center of mass scattering angle.

(Differential cross sections; neutron cross sections; neutron time-of-flight spectroscopy; angular distributions)

## Introduction

Neutron scattering cross-sections for elements such as nitrogen and oxygen have important applications in the area of neutron transport calculations with air as the transport medium. Furthermore, such applications require accurate cross-section values to obtain meaningful results.

Several research groups have devoted considerable efforts to measuring neutron scattering data with oxygen and nitrogen scatterers. Particular efforts have been made at ORNL by J. L. Fowler, et al.<sup>1</sup> and Dickens and Perey<sup>2</sup> and Perey and Kinney<sup>3</sup>, the latter group being primarily concerned with the nitrogen nonelastic discrepancy below 9 MeV. Gamma-ray production cross-sections for nitrogen have been measured by V. J. Orphan et al.<sup>4</sup>

A fast neutron spectrometer system was built for determining neutron differential cross-sections with several scatterers including oxygen and nitrogen. However, only the oxygen and nitrogen data are presented here. Neutron bombarding energies at which data were measured are 5.04 MeV, 6.25 MeV and 9.29 MeV. Data were also measured at 10.0 MeV; however, due to the abnormally high gamma ray background yields, the gamma rejection electronics did not function as desired, thus making the accuracy of these data points questionable.

The differential scattering cross-sections were determined by normalizing the measured angular distributions to known n-p cross-sections at the appropriate incident neutron energies. The cross-sections were then corrected for neutron flux attenuation and multiple scattering in the samples using an analytical computer code modified with target-detector angular resolution functions.

## Experimental Method

The Tandem Van de Graaff of the University of Texas Center for Nuclear Studies was used as the basic accelerator system. A pulsed negative ion source was designed and assembled onto a 100 keV Cockroft-Walton accelerator built by Columbia Scientific Industries and University of Texas personnel. The resulting injector system provided a pulsed beam of protons to be accelerated to the desired energy by the Tandem accelerator.

A low background neutron producing target was developed and used in conjunction with a neutron

detector, shield assembly, angular distribution goniometer, and automatic scattering sample changer. Details of the design of the Van de Graaff pulsed beam facility used in this work are presented elsewhere<sup>5</sup>. Only a brief description will be given here including pertinent instrumental developments made since the last publication.

## The Pulsed Ion Source

A McKibben<sup>6</sup> type direct extraction negative ion source was designed and assembled on a 100 keV Cockroft-Walton accelerator. Power for the ion source extraction high voltage as well as that of the 100 keV for acceleration was transported by a specially fabricated insulated coaxial cable. All isolation transformers and power supplies were placed in oil filled containers at ground potential. This allowed for removal of considerable weight from the terminal of the Cockroft-Walton injector. Furthermore, confined quarters for the injector did not allow use of a large air insulated terminal in relation to standard designs. Consequently, high voltage safety in the region of the injector terminal was enhanced by this arrangement.

Negative ions from the injector were chopped into bursts of 25 nanosecond duration by R. F. sweeping the beam across a slit. The chopped beam then entered a klystron buncher which compressed the bursts. The 100 keV pulsed-bunched beam then entered the tandem accelerator. Neutron spectra were measured by conventional methods of fast neutron time-of-flight electronics. From the measured full-width-half-maximum (FWHM) of the  $T(p,n)^3\text{He}$  neutron group produced at the target end of the beam tube, beam pulse widths of 1 to 2 nanoseconds were verified. Average beam currents of 0.5 microampere to 1.0 microampere with peak currents of 0.3 milliamperes were obtained.

## The Neutron Producing Target

Considerable effort was put into developing a monoenergetic primary neutron beam. Only one beam collimator was used in the beam tube within the target room area in order to minimize target room background. This was fabricated with isotopically pure Silicon-28, as the (p,n) threshold of Silicon-28 is about 15 MeV. The beam was stopped in a tritium gas cell at the end of which was a 20 mil Silicon-28 disc. The gas cell was 3 cm long and pressurized at 1 atmosphere. The entrance foil of the gas cell was made of 1/10 mil Havar.

## Neutron Detector and Shield Assembly

The neutron detector consisted of a 58AVP photo-multiplier optically coupled to an NE218 liquid scintillator 12.5 cm diameter by 15.2 cm long. With this type of scintillator, pulse shape discrimination could be employed to reject gamma rays. The detector was housed in 2.54 cm thick lead rings. Surrounding the lead rings was a  $\text{LiCO}_3$ -paraffin shield. The collimator throat of the shield was made of research-grade graphite. The detector-shield assembly was located on a mobile angular distribution carriage which permitted measuring neutron flight paths of 3.5 meters. Figure 1 shows schematically the arrangement of neutron producing target, sample holder and angular distribution carriage. A layer of  $\text{LiCO}_3$ -paraffin blocks lined the wall nearest the tritium gas cell to minimize the occurrence of neutron reactions with the concrete material of the wall.

In addition to the main neutron detector, a stationary neutron detector was used to monitor the primary neutron beam. Neutron time-of-flight electronics was also used with this detector.

The best time resolution obtained with the main detector was 2.5 nanoseconds due in large part to the relatively large thickness of the scintillator. Time resolutions of 1.25 to 1.50 nanoseconds were obtained consistently with the monitor detector which used a 2 cm thick scintillator, and this represents more realistically the neutron beam resolution.

## Angular Distribution Measurement

Angular distributions of neutrons elastically scattered from oxygen-16 ( $\text{H}_2\text{O}$  sample) were measured for 5.04 and 6.25 MeV incident neutron energies. The oxygen differential cross-sections as a function of the cosine of the scattering angle in the center-of-mass system of coordinates are plotted in Figure 2. The solid curve represents data corrected for flux attenuation and multiple scattering. The points with error bars represent uncorrected data. Both data points and curve have been corrected for detector efficiency. The corrected data are presented in Table I.

The presence of hydrogen in the sample permitted absolute differential cross-section determinations using known n-p cross-sections<sup>7</sup>. The scatterer used for these measurements consisted of distilled water in a thin walled polyethylene cylindrical container 2.54 cm diameter by 3.81 cm long. An empty polyethylene container of the same dimensions was used for measuring background spectra.

Figure 3 shows elastic and inelastic neutron scattering angular distributions for 6.25 MeV neutrons incident on hydrazine ( $\text{NH}_2\text{NH}_2$ ). The hydrazine was contained in a thin walled polyethylene cylinder 3.81 cm diameter by 5.08 cm long. The container was epoxy sealed to minimize exposure of hygroscopic hydrazine to room air. The angular distributions were normalized to the n-p differential cross sections at this energy and were corrected for detector efficiency. The solid curve represents the differential cross-sections corrected for flux attenuation and multiple scattering within the sample. The corrected data including experimental errors are tabulated in Tables 2 and 3.

The same hydrazine sample was used to measure neutron angular distributions at 9.29 MeV incident energies. Figure 3 shows the differential cross sections and the cross sections (curve) corrected for

flux attenuation and multiple scattering. The cross sections and their experimental errors are tabulated in Tables 4 and 5.

## Data Corrections

### Flux Attenuation and Multiple Scattering Corrections

Flux attenuation corrections were made using the method of Levin<sup>8</sup>. They ranged from 10% to 12% for scattering yields from oxygen and nitrogen.

Multiple scattering corrections were made using a method originally developed by Blok and Jonker<sup>9</sup> and applied to neutron scattering by Walt and Barschall<sup>10</sup>, Meier et al.<sup>11</sup>, Wills et al.<sup>12</sup>, J. D. Reber and J. D. Brandenberger<sup>13</sup> and W. Galati<sup>14</sup>. The method was modified by including an angular resolution function for deconvoluting the data to remove effects of the finite width of the scatterer and neutron detector. These corrections were generally between 10% and 15%. Occasionally, there were angles at which a 60% correction was required.

Flux attenuation and multiple scattering corrections were incorporated into a computer code and run on the University of Southwestern Louisiana Univac 70/46 computer.

## References

1. J. L. Fowler, C. H. Johnson, F. X. Hass and R. M. Feezel, Proceedings of the Third Conference on Neutron Cross Sections and Technology, Knoxville.
2. J. K. Dickens and F. G. Perey, Nucl. Science and Eng. **36**, 280 (1969).
3. F. G. Perey and W. E. Kinney, Nucl. Science and Eng. **46**, 428 (1971).
4. V. J. Orphan, C. G. Hoot, and V. V. Verbinshi, Trans. Amer. Nucl. Soc. **16**, 348 (June, 1973).
5. D. L. Bernard, et al., IEEE Trans. Nucl. Sci. **NS-18**, 90 (1971).
6. G. P. Lawrence, R. K. Beauchamp, and J. L. McKibben, Nucl. Instr. and Meth. **32** (1965) 357.
7. J. C. Hopkins and G. Breit, Nucl. Data, Sect. A: 137-45 (Mar., 1971).
8. L. Cranberg and J. S. Levin, LASL Report No. LA-2177, Jan. 1959 (see Appendix II by J. S. Levin).
9. J. Blok and C. C. Jonker, Physica **18**, 809 (1952).
10. M. Walt and H. H. Barschall, Phys. Rev. **93**, 1062 (1954).
11. R. W. Meier, P. Scherrer, and A. Trumpp, Helv. Phys. Acta. **27**, 577 (1954).
12. J. E. Wills, et al., Phys. Rev. **109**, 891 (1958).
13. J. D. Reber and J. D. Brandenberger, Phys. Rev. **103**, 1077 (1967).
14. W. Galati, Ph.D. Dissertation, University of Kentucky, 1969 (unpublished).



Table I. Differential cross sections of neutrons elastically scattered from oxygen-16 at 5.05 MeV and 6.25 MeV bombarding energies. The errors are rms absolute errors consisting of systematic and statistical uncertainties. The uncertainty in scattering angle is estimated to be  $\pm 0.5^\circ$ . The scattering angle,  $\cos\theta$  and  $\sigma(\theta)$  are in the center of mass system. All cross sections are in mb/steradian and have been corrected for sample attenuation, multiple scattering and detector efficiency.

$\theta$ (degrees)	$\cos\theta$	$E_n=5.04$ MeV $\sigma(\theta) \pm \Delta\sigma(\theta)$	$E_n=6.25$ MeV $\sigma(\theta) \pm \Delta\sigma(\theta)$
21.2	0.932	717.8 $\pm$ 70.5	3429.4 $\pm$ 150.2
31.8	0.849	580.6 $\pm$ 56.5	1608.5 $\pm$ 80.1
42.3	0.739	324.1 $\pm$ 26.6	1000.6 $\pm$ 50.0
52.8	0.605	98.3 $\pm$ 9.2	340.2 $\pm$ 17.5
63.1	0.452	88.8 $\pm$ 8.2	14.1 $\pm$ 1.0
73.4	0.285	80.6 $\pm$ 7.9	10.1 $\pm$ 1.0
83.6	0.112	43.9 $\pm$ 4.2	27.2 $\pm$ 2.7
93.6	-0.063	36.5 $\pm$ 3.6	177.3 $\pm$ 8.5
103.6	-0.235	81.2 $\pm$ 7.9	260.9 $\pm$ 13.0
113.4	-0.397	112.9 $\pm$ 10.6	222.9 $\pm$ 10.5
123.1	-0.547	117.9 $\pm$ 10.2	150.4 $\pm$ 7.5
132.8	-0.679	100.5 $\pm$ 9.8	134.1 $\pm$ 6.5
142.3	-0.792	105.4 $\pm$ 9.6	14.6 $\pm$ 1.0
151.8	-0.881	112.0 $\pm$ 10.1	88.0 $\pm$ 4.5

Table 2. Differential cross sections of neutrons elastically scattered from nitrogen-14 at 6.25 MeV bombarding energy. See caption of Table I.

$\theta$ (degrees)	$\cos\theta$	$\sigma(\theta) \pm \Delta\sigma(\theta)$
21.2	0.932	827.9 $\pm$ 40.2
31.8	0.849	408.4 $\pm$ 40.8
42.3	0.739	49.4 $\pm$ 2.9
52.8	0.605	129.1 $\pm$ 7.2
63.1	0.452	157.8 $\pm$ 11.6
73.4	0.286	99.1 $\pm$ 5.6
83.6	0.112	73.9 $\pm$ 2.9
93.6	-0.063	69.6 $\pm$ 4.2
103.6	-0.235	66.4 $\pm$ 3.9
113.4	-0.397	75.1 $\pm$ 6.0
123.1	-0.547	50.4 $\pm$ 3.0
138.8	-0.679	51.5 $\pm$ 4.0
142.3	-0.792	95.9 $\pm$ 9.0
151.8	-0.881	31.1 $\pm$ 3.1

Table 3. Differential cross sections of neutrons inelastically scattered from nitrogen-14 at 6.25 MeV bombarding energy. See caption of Table I.

$Q = -2.311$ MeV			$Q = -3.945$ MeV		
$\theta$ (deg.)	$\cos\theta$	$\sigma(\theta) \pm \Delta\sigma(\theta)$	$\theta$ (deg.)	$\cos\theta$	$\sigma(\theta) \pm \Delta\sigma(\theta)$
43.3	0.728	37.1 $\pm$ 2.5	44.7	0.711	6.9 $\pm$ 0.4
53.9	0.728	5.5 $\pm$ 0.3	55.6	0.566	1.1 $\pm$ 0.2
64.4	0.431	3.2 $\pm$ 0.3	66.3	0.402	7.7 $\pm$ 0.4
74.8	0.262	8.1 $\pm$ 0.5	76.8	0.228	6.4 $\pm$ 0.4
85.1	0.086	2.2 $\pm$ 0.2	87.2	0.049	0.5 $\pm$ 0.2
95.1	-0.089	4.7 $\pm$ 0.4	97.3	-0.127	3.6 $\pm$ 0.2
105.1	-0.259	11.4 $\pm$ 0.5	107.2	-0.295	10.8 $\pm$ 1.0
114.8	-0.419	6.4 $\pm$ 0.3	116.8	-0.451	8.3 $\pm$ 0.9
124.4	-0.566	1.5 $\pm$ 0.2	126.3	-0.592	1.3 $\pm$ 0.2
133.9	-0.694	14.9 $\pm$ 1.5	135.6	-0.714	4.8 $\pm$ 0.3
143.3	-0.802	5.4 $\pm$ 0.5	144.7	-0.816	4.3 $\pm$ 0.4
152.6	-0.888	9.8 $\pm$ 0.9	153.6	-0.896	9.4 $\pm$ 0.9

Table 4. Differential cross sections of neutrons elastically scattered from nitrogen-14 at 9.29 MeV bombarding energy. See caption of Table I.

$\theta$ (degree)	$\cos\theta$	$\sigma(\theta) \pm \Delta\sigma(\theta)$
42.6	0.736	185.0 $\pm$ 15.2
53.1	0.600	51.0 $\pm$ 3.1
73.8	0.279	18.5 $\pm$ 1.5
83.9	0.105	10.8 $\pm$ 1.0
94.1	-0.072	60.2 $\pm$ 4.5
103.9	-0.242	83.0 $\pm$ 5.2
113.8	-0.404	27.4 $\pm$ 2.5
123.5	-0.552	18.0 $\pm$ 1.5

Table 5. Differential cross sections of neutrons inelastically scattered from nitrogen-14 at 9.29 MeV bombarding energy. See caption of Table 1.

$Q = -2.311$ MeV			$Q = -3.945$ MeV		
$\theta$ (deg.)	$\cos\theta$	$\sigma(\theta) \pm \Delta\sigma(\theta)$	$\theta$ (deg.)	$\cos\theta$	$\sigma(\theta) \pm \Delta\sigma(\theta)$
43.1	0.730	20.0 $\pm$ 1.2	43.5	0.725	26.0 $\pm$ 1.2
53.6	0.592	13.3 $\pm$ 1.0	54.2	0.585	14.0 $\pm$ 1.4
74.5	0.267	6.0 $\pm$ 0.6	75.1	0.257	2.2 $\pm$ 1.0
84.7	0.092	16.0 $\pm$ 1.6	85.4	0.081	3.0 $\pm$ 1.0
94.8	-0.084	33.1 $\pm$ 2.9	95.4	-0.095	7.2 $\pm$ 0.5
104.7	-0.254	32.2 $\pm$ 3.0	105.4	-0.265	10.8 $\pm$ 1.0
114.5	-0.415	0.7 $\pm$ 0.5	115.1	-0.424	1.6 $\pm$ 1.0
124.2	-0.561	2.0 $\pm$ 1.0	124.7	-0.569	1.0 $\pm$ 0.5

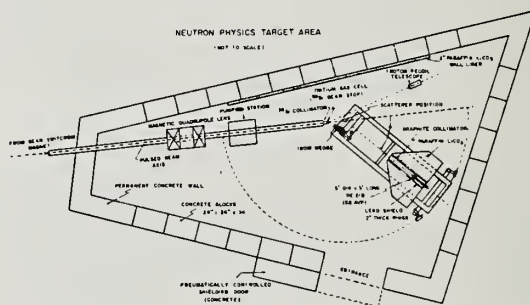


Figure 1. A schematic diagram of the arrangement of apparatus in the Tandem accelerator target room used for neutron cross section measurements.



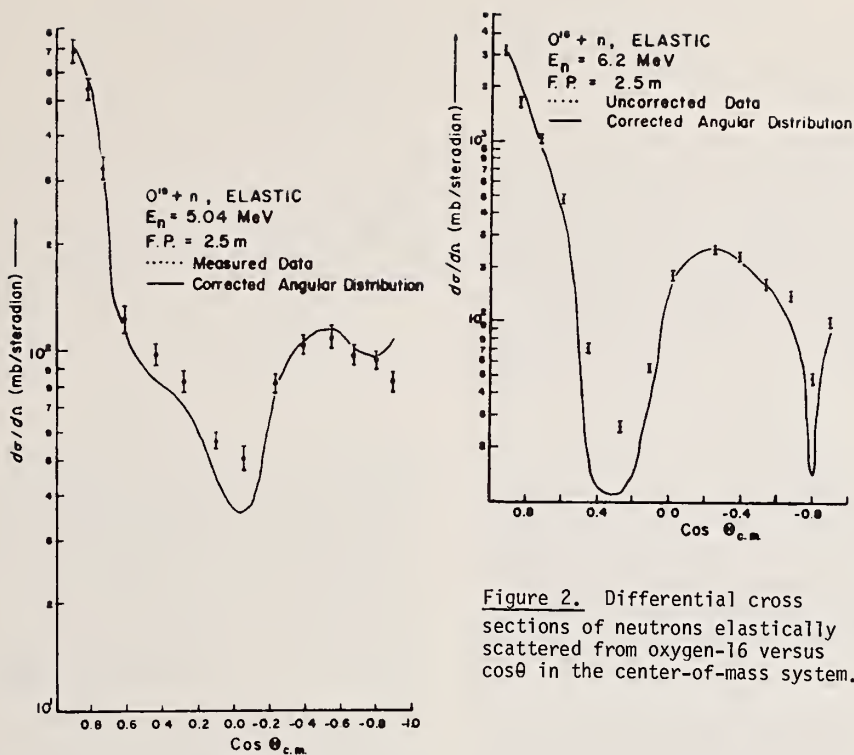
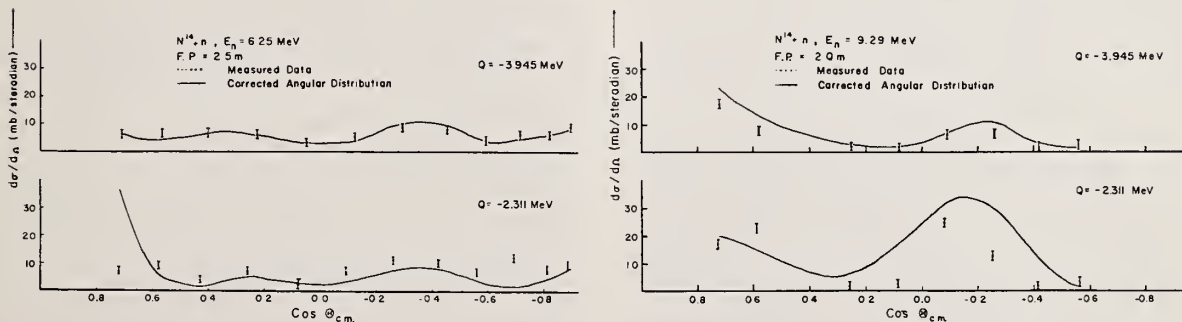
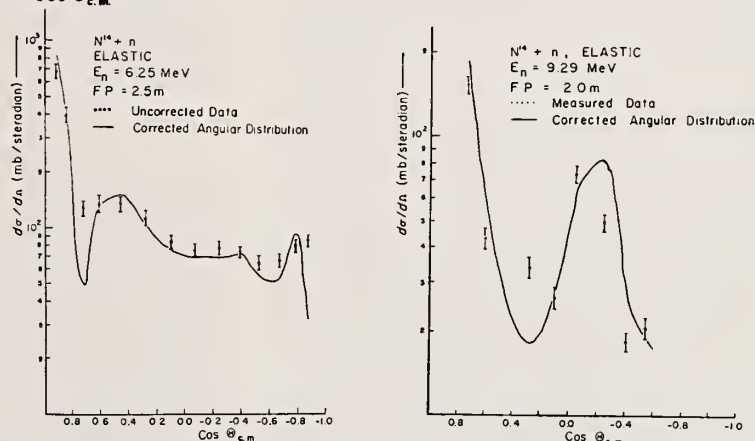


Figure 2. Differential cross sections of neutrons elastically scattered from oxygen-16 versus  $\cos\theta$  in the center-of-mass system.

Figure 3. Differential cross sections of neutrons scattered from nitrogen-14 versus  $\cos\theta$  in the center-of-mass system.



By the application of a new technique, absolute cross sections for the small-angle elastic scattering of neutrons by U have been accurately determined at various energies in the range 7-14-MeV. The data show less strong forward-peaking at small angles than previously reported results. In addition, measurements of the small-angle scattering by Pb were also carried out over the same energy range; and the results, while in conflict with some previous reported measurements, are, apart from normalization, in excellent agreement with optical model calculations based on the energy independent, non-local potential of Perey and Buck.

(Fast Neutrons; Scattering; Pb; U; Small Angles)

### Introduction

There have been many conflicting measurements<sup>1-5</sup> of the scattering of fast neutrons through small angles by heavy nuclei. Several important questions of a fundamental nature, which concern the strength of the electric dipole moment of the neutron, the nature of the fission process, and the possible existence of long-range nuclear forces, have been raised by reported anomalies in the scattering at small angles, and these questions still remain to be clearly resolved. One reason for this conflict of results is that, even though measurements at small angles are difficult, a higher precision is required. Another problem lies in the interpretation of existing data, which in general is available only at isolated energies and with large uncertainties in the normalizations. As a result many investigators have relied, in the interpretation of their data, on specialized nuclear models which fit only the shape of angular distribution data at a single energy.

It is the purpose of this paper to present results which contribute to the resolution of the above problem. Absolute measurements of the elastic scattering of neutrons by Pb and <sup>238</sup>U were carried out to high accuracy for angles in the interval 3 to 15 degrees and over the range of energies from 7 to 14 MeV. This energy range spans a large body of existing data and, in addition, is sufficiently wide to provide a good test for optical model predictions of differential scattering cross sections at small angles.

### Experimental Technique

A detailed description of the experimental arrangement for the U measurements (shown in figure 1) has been reported elsewhere<sup>6</sup>. Basically, it can be characterized as a four-fold shielded detector configuration that involves shielding (collimating channels) along the entire beam path(s) from scatterer to detector. The distinguishing difference between the conventional shielded-detector geometry and the configuration applied here is that with the latter the transverse dimensions of the collimating channels are small compared to those of the scattering sample, and the scattering is therefore defined by the acceptance profiles of the channels rather than the size of the scatterer. The main advantages of this technique are high counting rates and the near elimination of background due to air scattering. For the U measurements, as well as for other small-angle measurements at this laboratory, Pb was used as a standard of reference at each measured point. The absolute cross sections for Pb were, in turn, determined by a set of auxiliary

measurements which were carried out in a ring-type geometry. Corrections for air scattering are important at small angles in ring geometry and were found to be most accurately determined by analytical means.

### Measurements

Both time-of-flight and pulse-shape discrimination techniques were employed in the measurements. Deuterons from the BRL Tandem Van de Graaff were pulsed at a repetition rate of 2MHz and bunched to 1.5 nsec FWHM. The energy spreads of neutrons produced by means of the  $d(D,N)^3\text{He}$  reaction in a gas cell were typically 120 and 260 KeV for neutron energies of 14.0 and 7.0 MeV, respectively. Over each angular distribution measurement the deuteron energy was adjusted to compensate for slight changes in the neutron emission angle and thereby yield a constant neutron energy. The high counting rates inherent in each of the scattering geometries permitted the use of relatively thin scattering samples (75% transparency), and thus the greater uncertainties inherent in large multiple scattering corrections were avoided.

Correction to the data were made for multiple scattering, air scattering, finite geometry and other effects.<sup>6</sup> In calculating the effects of both multiple scattering (by Monte Carlo techniques) and air scattering, constraints due to neutron flight time requirements were imposed. The error flag assigned to each data point includes that due to counting statistics (0.5 to 2.5%), uncertainties in the corrections, and other experimental uncertainties such as in the detector efficiency and in the transmission of the scatterer.

### Results

In Figure 2 the data, less Schwinger scattering, is displayed in the C.M. system. These data are well represented (see curves of Figure 2) by the functional relationship

$$\ln \sigma(\theta, E) = A(E) + B(E)\mu + C(E)\mu^2 \quad (1)$$

where  $\mu = 1 - \cos\theta$ ,  $A(E)$  is a polynomial of 4th order in  $E$ , and  $B(E)$  and  $C(E)$  are quadratic in  $E$ . It was verified that the form of the angular dependence of Equation (1) is sufficiently general so as not to preclude good fits (i.e.,  $< 0.5\%$ ) to a variety of optical model calculations over the range 0-15°. The percent deviations of Equation (1) from both the data and Wick Limits are plotted in Figure 3 for Pb. For U, the arrows in Figure 2 indicate Wick Limits.

The present data can be clearly compared with those of other workers at neighboring energies by the curves generated from Equation (1). It is seen that the present results for both Pb and U disagree with the data of references 1 and 2 on which were based reports of anomalous scattering. The shape of the angular distribution of Adam et al<sup>3</sup> at 14.7 MeV for U, which indicates some anomalous peaking around 5°, is only in fair agreement with the corresponding curve. While good statistical agreement is obtained with the data of Benenson et al<sup>4</sup> for Pb, we do not support their claim that the optical model parameters of Rosen et al<sup>7</sup> best describe the data (see figure 4). The 14.1 MeV cross sections for Pb and U which were measured over the angular range 5-150° by Coon et al<sup>8</sup> are in excellent agreement with our measurements.

### Conclusions

In Figure 4 it is seen that the present data strongly disagree with the optical model predictions of Rosen et al.<sup>7</sup> However, the parameters of Fu and Perey<sup>9</sup>, which are based on the energy independent, non-local optical model potential of Perey and Buck<sup>10</sup>, are apart from normalization, in excellent agreement; i.e. the shapes of the angular distributions agree to within ±2% (see Figure 5). For U, similar agreement is obtained with the theoretical calculations of Palla<sup>11</sup> which take into account the nuclear deformation. It is concluded that, to within ±2%, no anomalies exist in the scattering of 7-14 MeV neutrons by Pb or U.

### References

1. G.V. Anikin and I.I. Kotukhov, *Yad. Fiz.* **12** 1121 (1970) [*Sov. J. Nucl. Phys.* **12** 614 (1971)].
2. Yu. V. Dukarevich and A.N. Dyumin, *Zh. Eksp. Teor. Fiz.* **44** 130 (1963) [*Sov. Phys. - JEPT* **17** 87 (1973)].
3. A. Adam et al., *Acta. Phys.* **25** 261 (1968).
4. R. E. Benenson et al., *Nucl. Phys.* **A212** 147 (1973).
5. For other references to small-angle scattering results see N.S. Lebedeva and V.M. Morozov, *Atomnaya Energiya* **28** 310 (1970).
6. W. Bucher et al., *Nucl. Inst. and Meth.* **111**, 237 (1973).
7. L. Rosen et al., *Ann. of Phys.* **34** 96 (1965).
8. J.H. Coon et al., *Phys. Rev.* **111** 250 (1958).
9. C.Y. Fu and F.G. Perey, *Ornl-4765*, Oak Ridge National Lab. (1972).
10. F. Perey and B. Buck, *Nucl. Phys.* **32** 353 (1962).
11. G. Palla, *Phys. Lett.* **35B** 477 (1971).

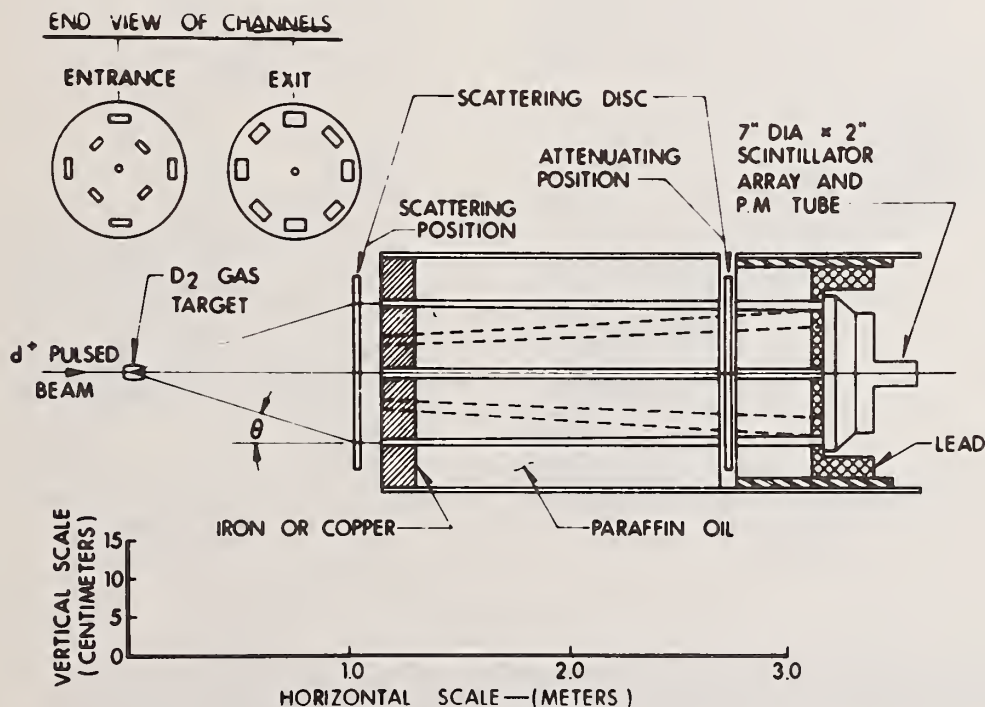


FIG. 1. Schematic diagram of experimental arrangement showing 3 of 9 channels. Note expanded vertical scale.



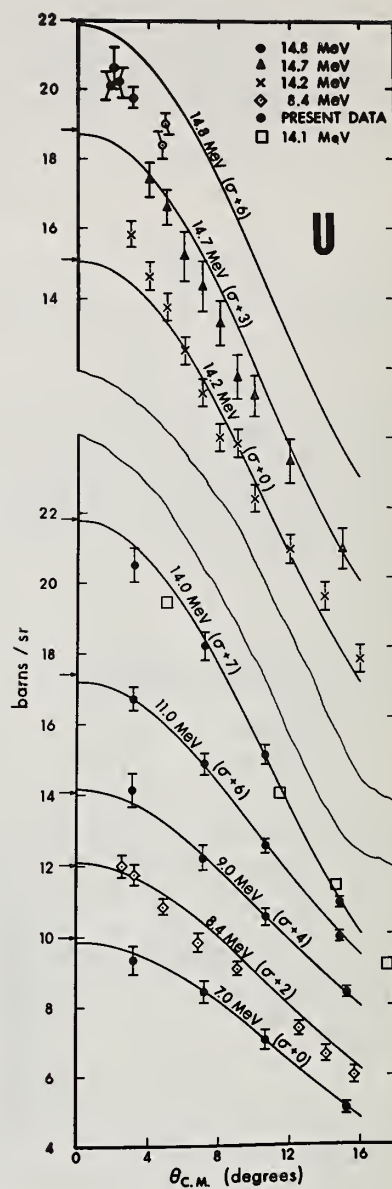
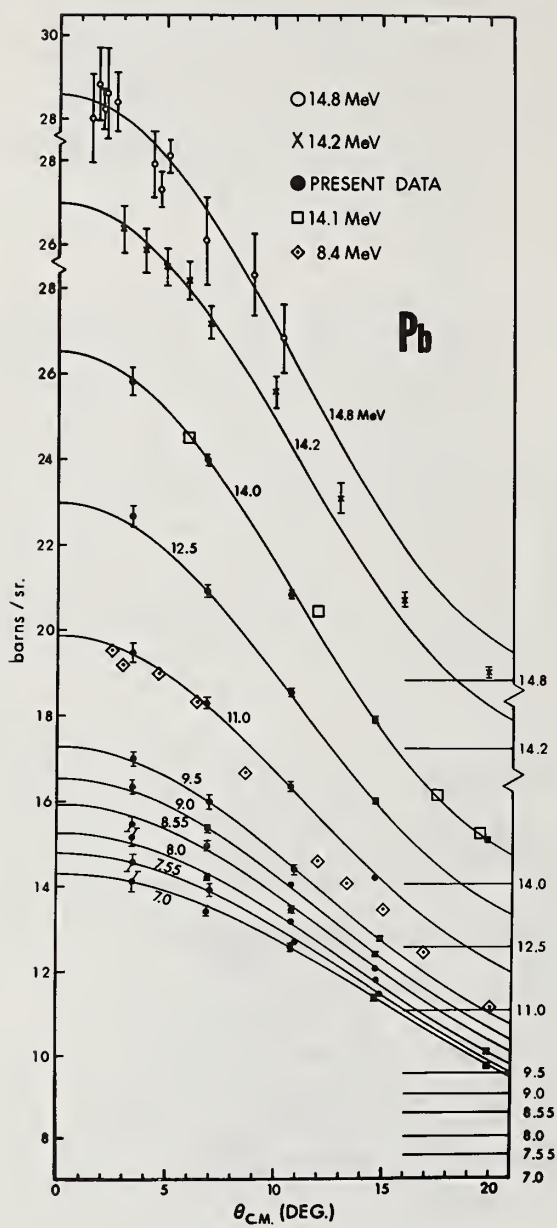


FIG. 2. Neutron scattering from Pb and U. The data at 8.4, 14.1, 14.2, 14.7, and 14.8 are from refs. 1, 8, 2, 3, and 4, respectively. The scale for the Pb cross sections is displaced by the amount  $E(\text{MeV})$  in b/sr.; the displacements for U are as indicated on each curve.

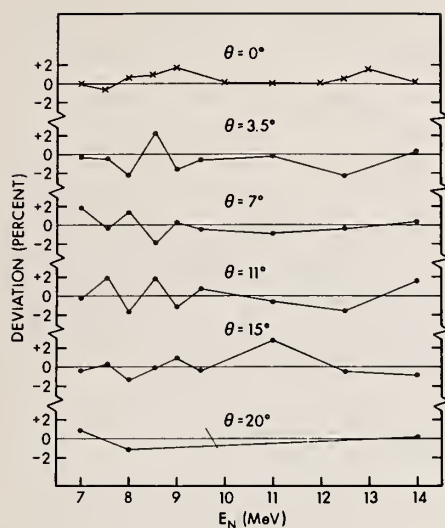


FIG. 3. Percent deviations of Eq. (1) from the data points and, at zero degrees, from the energy-averaged Wick Limit values.

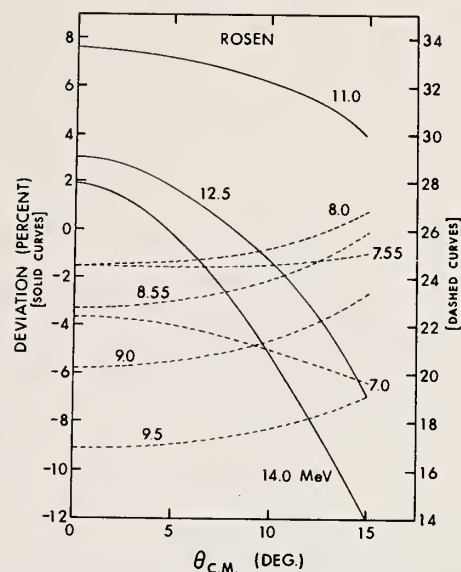


FIG. 4. Percent deviations of predictions of optical Model of Rosen et al.<sup>7</sup> from present data.

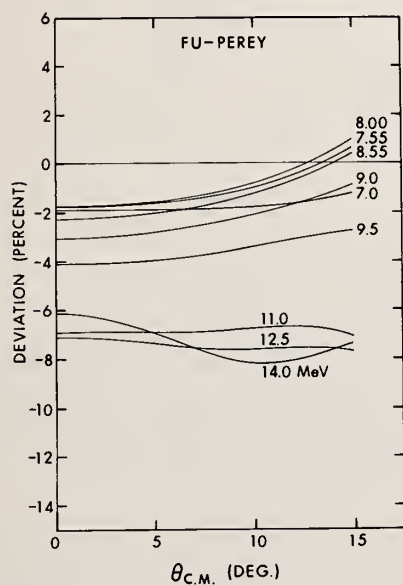


FIG. 5. Percent deviations of predictions of optical model of Fu and Perey<sup>9</sup> from present data.

ELASTIC AND INELASTIC DIFFERENTIAL NEUTRON SCATTERING CROSS SECTIONS FOR  $^{238}\text{U}$  FROM 0.9 - 2.7 MeV\*  
 J. J. Egan, G. H. R. Kegel, G. P. Couchell, A. Mittler, B. K. Barnes, W. A. Schier, D. J. Pullen, P. Harihar,  
 T. V. Marcella, N. B. Sullivan, and E. Sheldon  
 Lowell Technological Institute  
 Lowell, Massachusetts 01854,  
 and  
 A. Prince,  
 Brookhaven National Laboratory  
 Upton, Long Island, New York 11973

Differential cross sections have been measured via the time-of-flight method for neutrons scattered at  $90^\circ$  from the ground and first two excited states, at 45 and 148 keV, of  $^{238}\text{U}$  in the bombarding energy range 0.9 to 2.7 MeV. The  $^7\text{Li}(p,n)^7\text{Be}$  reaction was the neutron source. The LTI 5.5 MeV Van de Graaff accelerator in conjunction with a Mobley bunching system generated proton pulses with durations as short as 320 picoseconds (fwhm). The excellent timing characteristics of this system enabled the three states in  $^{238}\text{U}$  to be resolved up to 2.7 MeV. Above 1.5 MeV the present results for the  $2^+$  state at 45 keV are 2 to 2.5 times larger than the ENDF/IV cross sections. However, the present results are in good agreement with theoretical calculations which incorporate both direct interaction and compound nucleus contributions to the cross sections.

(NUCLEAR REACTIONS  $^{238}\text{U}(n,n)$ ,  $(n,n')$ ,  $E = 0.9 - 2.7$  MeV; measured  $\sigma(E_n, 90^\circ)$  for ground, 45, 148 keV states. Time-of-flight. Compared with calculated excitation functions.)

### Introduction

The purpose of this paper is to report measurements of the differential neutron scattering cross sections for the ground and first two excited states, at 45 keV ( $2^+$ ) and 148 keV ( $4^+$ ), in  $^{238}\text{U}$  for bombarding energies up to 2.7 MeV. Previously published data on the  $2^+$  state have been subject to large uncertainties in the region above 1.1 MeV due to the inability to resolve this state from the ground state. The  $4^+$  state has been resolved only up to 1.5 MeV. Estimates of the level cross sections at higher energies have been obtained from theoretical calculations and from analysis of data on the combined neutron groups.

In the present work these levels have been resolved up to 2.7 MeV. The differential cross sections at  $90^\circ$  will be presented and compared with theoretical calculations which include contributions from direct interaction and compound nucleus mechanisms.

### Experimental Methods

The data were taken at the Lowell Technological Institute Van de Graaff accelerator laboratory. The 5.5 MV type CN machine with terminal pulsing and Mobley bunching system routinely produces proton pulses of 320 ps at a 5 MHz repetition rate. We have recently achieved pulse widths as short as 280 ps, as determined by the full width at half maximum of the prompt gamma-ray peak in a time-of-flight spectrum measured by a scintillation detector with premium timing characteristics.

The scattering data were taken using the time-of-flight technique with the  $^7\text{Li}(p,n)^7\text{Be}$  reaction as the neutron source. The scattered neutron groups due to incident neutrons which leave  $^7\text{Be}$  in its first excited state were not in the time region of interest, and hence presented no problem in these measurements. Before each data point was taken, a new target was made in place in the proton beam by an evaporator system incorporated in the target assembly. Target thickness was monitored during the evaporation process by the main neutron detector, which will be described later.

Figure 1 depicts the experimental arrangement. The scattering sample was a circular disk of depleted uranium 0.25-in. thick by 1.5-in. diameter. For measurements at  $90^\circ$  the plane of the disk was oriented at  $45^\circ$  to the beam direction in order to minimize

the spread in flight times arising from neutrons scattering from different parts of the sample.

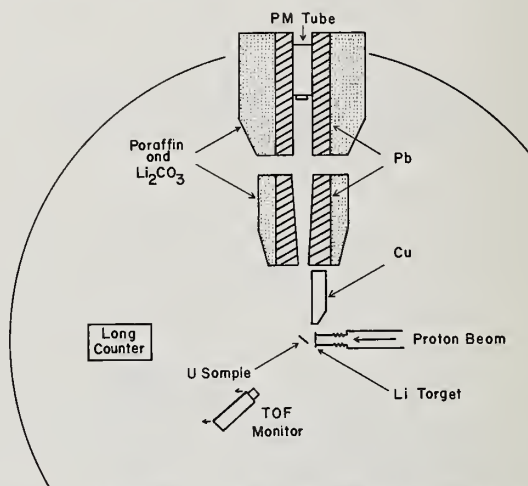


Fig. 1. Schematic diagram of the experimental arrangement.

The main neutron detector consisted of a 0.25-in. thick by 4.5-in. diameter NE102 plastic scintillator mounted on an RCA 8854 photomultiplier tube. The detector is shielded by two massive shields containing a paraffin and lithium carbonate mixture. The shields are lined with thick lead annuli. A massive copper shadow bar intercepts the direct target neutrons. The flight path for this experiment was 2.82 m.

The normalization of the data was accomplished by monitoring the prompt gamma rays produced by proton induced reactions in  $^7\text{Li}$  with the time-of-flight (TOF) monitor detector, which consists of a 0.25-in. thick by 1.5-in. diameter Pilot U plastic scintillator mounted on an RCA C31024 photomultiplier tube. This detector has extremely good time resolution. It was also used to monitor the proton beam pulse width.

An on-line computer system sampled the gamma-ray peak width in the TOF monitor spectrum at two minute intervals and automatically inhibited data acquisition whenever the beam pulse width became larger than a



predetermined value (usually this was set at 350 ps). A standard long counter calibrated against a recoil proton telescope served as an auxiliary monitor.

The associated electronic system consisted of commercially available NIM modules with the addition of a "walk" correction circuit which subtracted a fraction of the linear signal of the main neutron detector from the output of the time-to-amplitude converter (TAC) in order to minimize time jitter due to signals of different sizes at the TAC input. The electronic system was adjusted for optimum time resolution before each data point was taken.

Efficiency curves for the main detector were taken before and after each data point. These were obtained by measuring the  ${}^7\text{Li}(p,n){}^7\text{Be}$  angular distribution and normalizing to the known relative cross section. The absolute efficiency was not needed because we removed the sample and brought the main detector to  $0^\circ$  (we also moved the target to the sample position, and the TOF monitor back an equal distance) in order to measure the incident flux. Hence the incident and scattered flux were measured with the same detector.

Figures 2 and 3 show the time-of-flight spectra of the scattered neutrons at 0.9 and 2.0 MeV respectively. The run times for these spectra were approximately 48 hours. The excellent resolution at 2 MeV attests to the good long term stability of our system. The full width at half maximum of the elastic neutron group is 0.8 ns for the spectrum at 2.0 MeV.

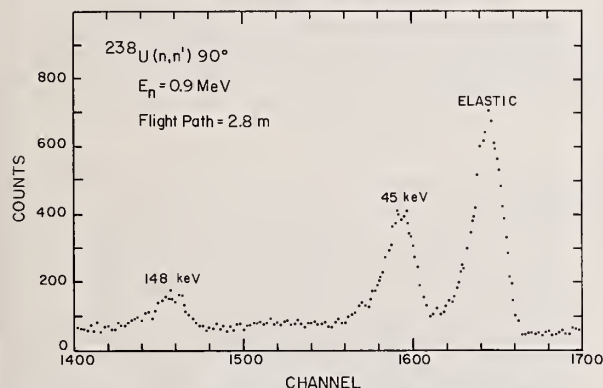


Fig. 2. The time-of-flight spectrum for 0.9 MeV incident neutrons scattered from  ${}^{238}\text{U}$  at  $90^\circ$ .

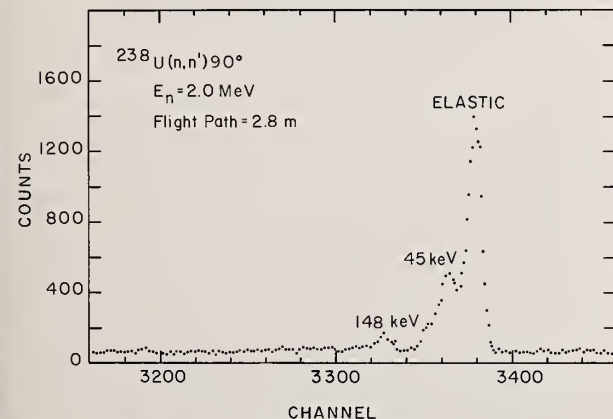


Fig. 3. The time-of-flight spectrum for 2.0 MeV incident neutrons scattered from  ${}^{238}\text{U}$  at  $90^\circ$ .

## Results and Analysis

The results of the experiment are shown on Figs. 4, 5, and 6. Figure 4 shows the elastic differential cross section at  $90^\circ$ . Figures 5 and 6 show the inelastic differential cross sections for the 45 and 148 keV levels respectively. The solid curves represent theoretical calculations and the dashed curve is the ENDF/IV evaluation for comparison. The upper solid curve is the sum of the direct and compound nucleus curves. The data shown in these figures have been corrected for neutron attenuation and multiple scattering using the Monte Carlo code MCN.<sup>1</sup>

As early as 1970, Prince<sup>2</sup> indicated that previous estimates of the inelastic cross sections above 1.5 MeV may be too low due to a direct excitation of the rotational levels by inelastic scattering. Indeed some earlier cross section compilations<sup>3</sup> list the inelastic cross sections as zero for both the  $2^+$  and  $4^+$  states above 1.5 and 1.8 MeV respectively. Prince's 1970 calculation indicated that the direct interaction contributes significantly to the cross sections and becomes the dominant component above 1.5 MeV.

The elastic scattering data in Fig. 4 agree with the ENDF/IV evaluation up to 1.5 MeV and are somewhat lower than ENDF/IV at higher energies. Presumably this is due to the inability to separate out the 45 keV state in earlier experiments. The calculations underestimate the cross section somewhat in the 1.5 to 2.0 MeV region. At other energies there is good agreement between data and theory.

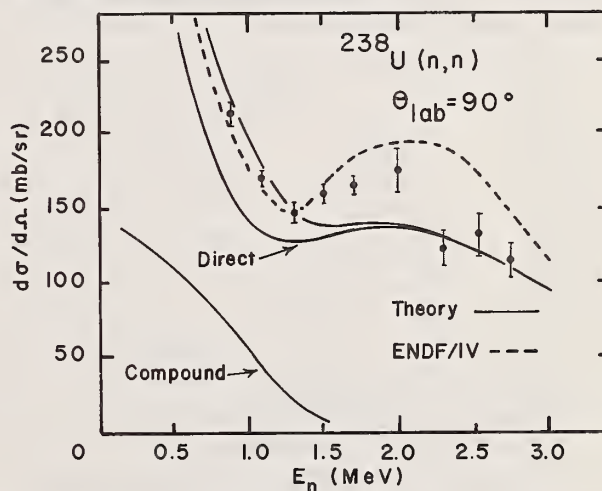


Fig. 4 The lab differential elastic neutron scattering cross section at  $90^\circ$  for  ${}^{238}\text{U}$ . The upper solid curve is the sum of the compound nucleus plus direct interaction theoretical calculations.

The data for the  $2^+$  state at 45 keV in Fig. 5 are a factor of 3 times higher than ENDF/IV above 2 MeV. The theoretical calculations are slightly low in this region, but the overall agreement with the theory is not unreasonable.

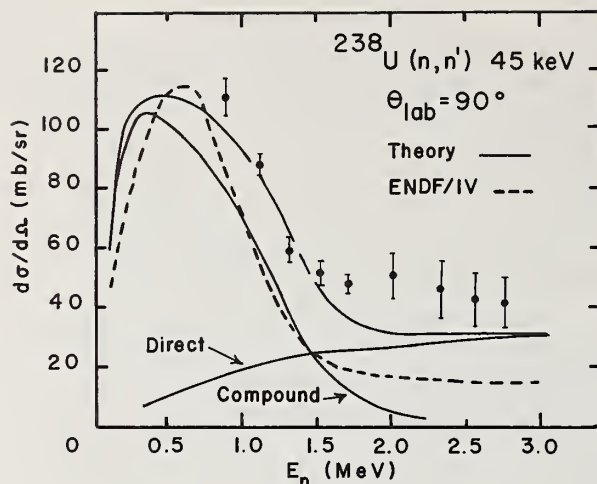


Fig. 5. The lab differential inelastic scattering cross section at  $90^\circ$  for the  $2^+$  45 keV state in  $^{238}\text{U}$ . The upper solid curve is the sum of the compound nucleus plus direct interaction theoretical calculations.

The data for the  $4^+$  state at 148 keV in Fig. 6 are significantly higher than ENDF/IV, especially above 2 MeV. The theoretical calculations are consistently high, but again the agreement between the data and the calculations is reasonable.

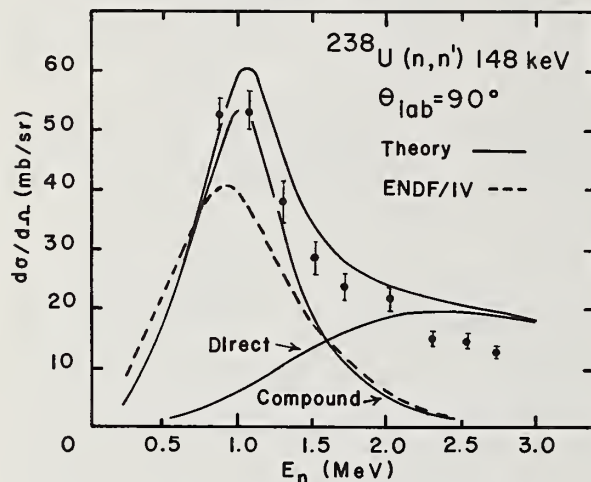


Fig. 6. The lab differential inelastic scattering cross section at  $90^\circ$  for the  $4^+$  148 keV state in  $^{238}\text{U}$ . The upper solid curve is the sum of the compound nucleus plus direct interaction theoretical calculations.

The theoretical calculations shown were accomplished using the coupled channel code JUPITOR-1<sup>4</sup> for the direct interaction contribution, and the code COMNUC-3 for the compound nucleus contribution. The JUPITOR calculations coupled the  $0^+$ ,  $2^+$ , and  $4^+$  levels using a non-spherical energy dependent optical model potential with spin-orbit coupling. The COMNUC Hauser-Feshbach calculations were made using transmission coefficients obtained from a spherical optical potential. These compound nucleus calculations included as possible exit channels compound elastic scattering,

inelastic scattering to discrete as well as continuum levels, radiative capture ( $n,\gamma$ ), and fission ( $n,f$ ). New compound nucleus calculations are currently in progress using transmission coefficients obtained from the non-spherical optical potential used in the JUPITOR calculations. Indications are that these new calculations will increase the compound nucleus cross section by about ten percent.

The ENDF/IV compilation lists the angular distributions for inelastic scattering to the  $2^+$  and  $4^+$  states as isotropic. The theoretical calculations indicate that these angular distributions are not isotropic. We are currently making measurements of these angular distributions in order to check the predictions of the theory. In light of this, one must exercise caution in determining  $\sigma_{n,n'}$ , the integrated cross section, from our  $90^\circ$  measurements. Simply multiplying our results by  $4\pi$  may lead to gross errors.

In conclusion, our data confirm the theoretical prediction that the inelastic cross sections for the 45 and 148 keV states are much more significant at energies above 1.5 MeV than ENDF/IV and previous cross section compilations indicate. And, of theoretical interest, the contribution to inelastic scattering due to direct interaction becomes very important at energies above 1.5 MeV for the first two excited states of  $^{238}\text{U}$ .

#### Acknowledgement

The authors wish to thank G. D. Turner and Charles Forest of the Los Alamos Scientific Laboratory for performing the Monte Carlo calculations used in the finite sample corrections.

#### References

\*This work supported in part by the National Science Foundation.

1. E. D. Cashwell, J. R. Neergaard, W. M. Taylor, and G. D. Turner, LASL Report LA-4751 (1972).
2. A. Prince, *Nuclear Data for Reactors Vol. II* (International Atomic Energy Agency, Vienna 1970) p. 825.
3. I. Langer, J. J. Schmidt, D. Woll, KFK Report KFK-750, EUR 3715e, EANDC (E)-88 "u" p. 605 (1968).
4. T. Tamura, ORNL Report ORNL 4152 (1967).

ABSOLUTE MEASUREMENTS OF NEUTRON RADIATIVE CAPTURE CROSS SECTIONS  
FOR  $\text{Na}^{23}$ ,  $\text{Cr}$ ,  $\text{Mn}^{55}$ ,  $\text{Fe}$ ,  $\text{Ni}$ ,  $\text{Rh}^{103}$ ,  $\text{Ta}$ ,  $\text{U}^{238}$  IN THE keV ENERGY RANGE

C. LE RIGOLEUR, A. ARNAUD, J. TASTE

C.E.N. CADARACHE

13.115 Saint-Paul-lez-Durance (France)

The absolute measurements of several neutron radiative capture cross sections in the keV energy range are presented. The total energy weighting technique was used. Absolute neutron flux were done. Special care was given to the correction arising from the neutron sensitivity of the gamma detector.

(Absolute radiative capture cross sections - keV energy range -  
 $\text{Na}^{23}$ ,  $\text{Cr}$ ,  $\text{Mn}^{55}$ ,  $\text{Fe}$ ,  $\text{Ni}$ ,  $\text{Rh}^{103}$ ,  $\text{Ta}$ ,  $\text{U}^{238}$ )

### Experiment

The capture gamma ray detector was used with fast time of flight technique and with the total energy weighting technique in order to make the detection efficiency for a capture independant of the gamma ray cascade. This efficiency was absolutely determined.

The neutron flux was measured with a  $\text{B}^{10}\text{Ina}$  (Tl) detector or with a  $\text{Li}^6$  glass scintillator. The absolute efficiency of these detectors was determined from a standard detector.

Details on total energy weighting technique, experimental set-up and neutron flux detectors are given in Ref. 1-2-3-4.

The usual corrections for neutron scattering and self-shielding, gamma attenuation in the sample, non linearity of the weighting function ... have been applied. Special care was given to the correction arising from the neutron sensitivity of the gamma detector.

Neutron scattered by the sample may be captured by the gamma detector. This time dependant background depends of the mass and thickness of the sample, angular distribution of scattered neutrons, energy and shape of the incident neutron flux. To cope with this serious problem we have first calculated the time probability that a neutron scattered at angle  $\theta$  and energy E be captured by the gamma detector. Then and for each experimental run we have calculated the capture yield arising from neutrons scattered by the sample. We have assumed an isotropic angular distribution

in the center of mass system. Multiple scattering in the sample was taken into account. These calculations were checked experimentally measuring the gamma detector response using a carbon sample.

For iron this correction is very large. There is a large resonance scattering cross section at 27.7 keV and an important resonance capture cross section in fluorine at 27.07 keV.

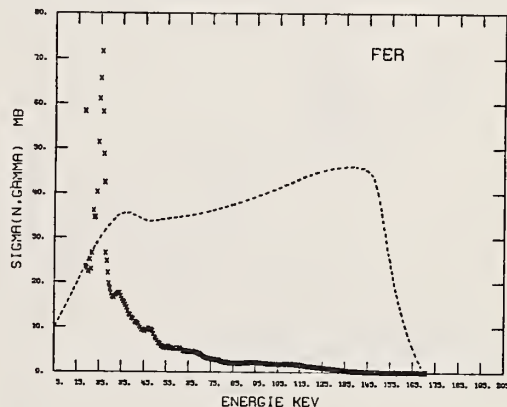


Fig. 1.

\*\* Contribution of scattered neutrons in the capture detector for iron sample.  
-- Incident neutron flux.

On Fig. 1. is shown the calculated contribution of scattered neutron. This contribution has the same order of magnitude than the capture yield from the iron sample

### Results $^{23}\text{Na}$ (20 - 160 keV)

The metallic sodium sample were sealed in Al containers with two thin windows (.1 mm and .03 mm). The background from the aluminum

.../...



This work				CAPTURE CROSS SECTION MEASUREMENTS		Other measurements on Na	
En LAB (keV)	Atom/Barn	$\lambda \gamma \pm \Delta \lambda \gamma$ BARN x eV	$\sigma \frac{\Gamma_n \Gamma_\gamma}{eV}$	$\lambda \gamma \pm \Delta \lambda \gamma$ BARN x eV	En LAB (keV)	$\sigma \frac{\Gamma_n \Gamma_\gamma}{eV}$	En LAB (keV)
35.45	0.01599	$38.41 \pm 1.50$	0.3048				
35.39	0.01963	$36.51 \pm 2.24$	0.306				
35.38	0.03225	$39.50 \pm 2.16$	0.313				
35.30	0.03707	$38.66 \pm 1.60$	0.307				
<u>35.38 <math>\pm</math> 0.19</u>		<u>38.77 <math>\pm</math> 1.5</u>	<u>0.307 <math>\pm</math> 0.012</u>	<u>35.8 <math>\pm</math> 4 (a)</u>	35.0 (b)	<u>0.394 <math>\pm</math> 0.048 (b)</u>	<u>35.39 (c)</u>
53.62	0.01599	$38.51 \pm 2.5$	0.4607				
53.26	0.01963	$34.89 \pm 5.0$	0.4169				
53.33	0.03225	$39.54 \pm 3.2$	0.4730				
53.36	0.03707	$38.05 \pm 3.9$	0.4547				
<u>53.39 <math>\pm</math> 0.35</u>		<u>37.74 <math>\pm</math> 2.5</u>	<u>0.4513 <math>\pm</math> 0.030</u>	<u>34.16 <math>\pm</math> 4 (a)</u>	52.2 (b)	$\frac{\Gamma_n}{\Gamma_\gamma} = 700 \text{ eV}$ <u>0.987 (b)</u>	<u>53.15 (d)</u>
118.32	0.01963	$32.118 \pm 1.55$	0.852				
117.88	0.03707	$33.245 \pm 1.58$	0.882				
<u>118.10 <math>\pm</math> 1.2</u>		<u>32.68 <math>\pm</math> 1.50</u>	<u>0.867 <math>\pm</math> 0.040</u>		114.7 (b)	<u>1.50 <math>\pm</math> 0.37 (b)</u>	117.61 (c)
132.95	0.01963	$10.045 \pm 1.2$	0.299				
132.70	0.03707	$10.48 \pm 1.2$	0.312				
<u>132.8 <math>\pm</math> 1.4</u>		<u>10.26 <math>\pm</math> 1.2</u>	<u>0.305 <math>\pm</math> 0.035</u>		129.5 (b)	<u>0.29 <math>\pm</math> 0.07 (b)</u>	
144.06	0.01963	$11.57 \pm 0.85$	0.406				
144.08	0.03707	$8.55 \pm 0.6$	0.276				
<u>144.07 <math>\pm</math> 1.6</u>		<u>10.06 <math>\pm</math> 2.0</u>	<u>0.341 <math>\pm</math> 0.064</u>		139.1 (b)	<u>0.71 <math>\pm</math> 0.18 (b)</u>	

TABLE I

a) Capture cross section measurements by activation  
(Le Rigoleur et al - ref 5-6)

b) Capture cross section measurements with a large liquid  
scintillator detector at RPI (R. W. Hockenbury et al - ref 7)

c) Transmission measurements at Saclay (P. Ribon et al - ref 8)

d) Transmission measurements at Columbia University  
(F. Rahn et al - ref 9)

containers, important at 119.8 and 145 keV, was determined with an empty can. The results are shown in table I. There are large discrepancies between our results and those of R.P.I.

Cr, Ni (15 - 65 keV)

Fe (15 - 165 keV)

Only one sample thickness was used for Cr (0.0182 atom/barn) and Ni (0.0185 atom/barn) but two for Fe (0.00824 and 0.0166 atom/barn).

Our data are shown on Fig. 2-3-4 and complete the results already published (Ref. 3-4).

Up to now no detail comparison has been done with other data.

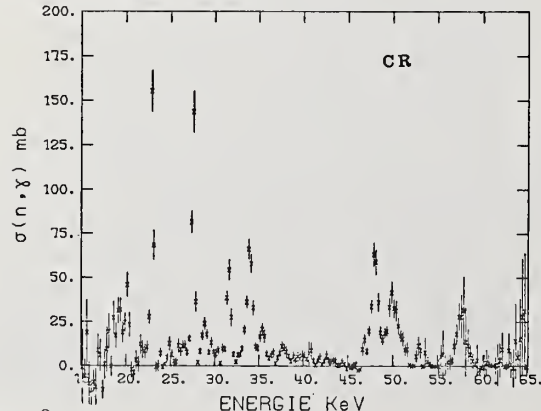


Fig. 2.

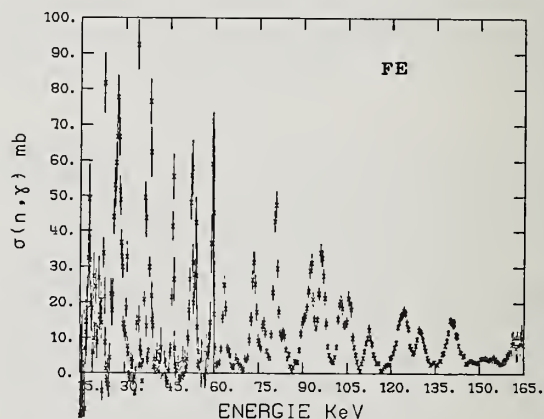


Fig. 3.

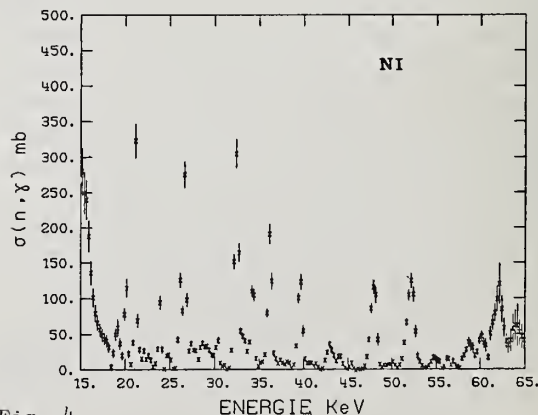


Fig. 4.

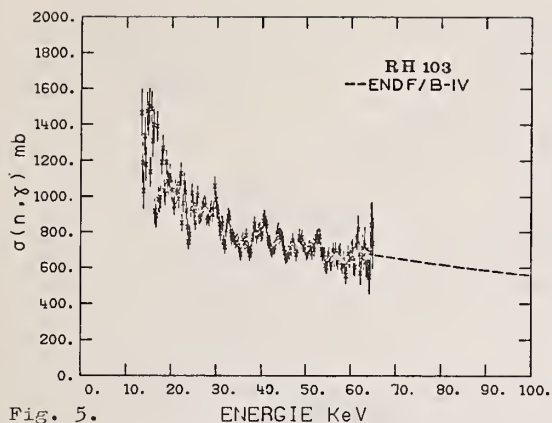


Fig. 5.

Rh<sup>103</sup> (15 - 350 keV)

The thickness of the metallic sample was 0.0062 atom/barn and its diameter 20 mm. Our data are shown on Fig. 5-6. Below 65 keV our data are in good agreement with ENDF/B-IV but are 20-25 % lower above 100 keV. On Fig. 7. is also shown an evaluation (Ref. 12.) which has been completed recently and the agreement with our data is better. We must notice that our data were not taken into account in this last evaluation.

Ta (10 - 160 keV)

The thickness of the metallic sample was 0.00463 atom/barn and its diameter 25 mm. Our data are shown on Fig. 8-9. Below 30 keV our data are in rather good agreement with ENDF/B-IV but 20-25 % higher above.

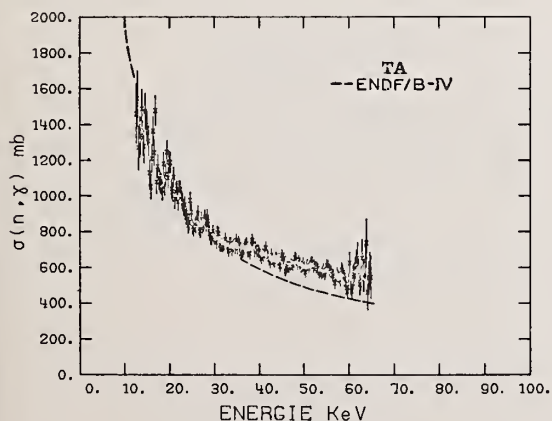


Fig. 8

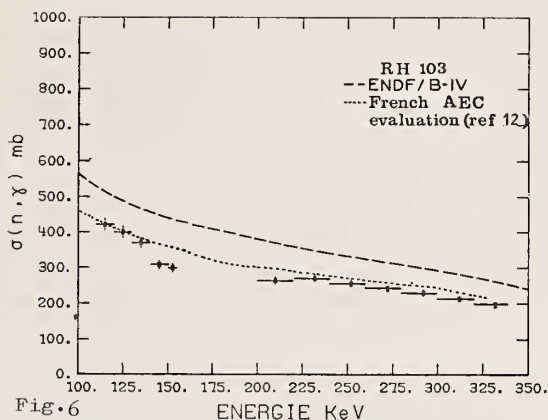


Fig.6

Mn<sup>55</sup> (15 - 500 keV) (Fig. 7.)

Two metallic samples were used in these measurements (0.0113 and 0.0198 atom/barn). Our data averaged over 10 keV below 100 keV and 20 keV above agree with the results of SPITZ et al (Ref. 10.) obtained with the time of flight technique but are 25 % lower than those of STUPEGIA obtained by the activation technique (Ref. 11.).

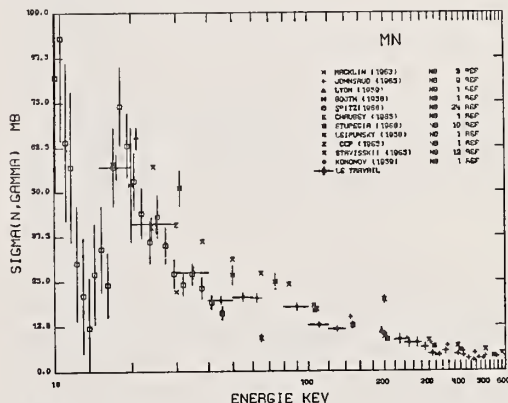


Fig. 7

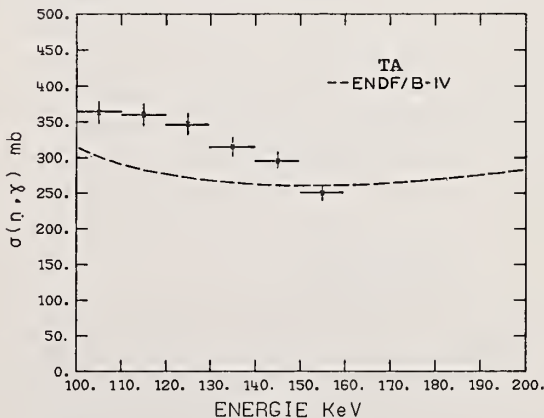


Fig. 9

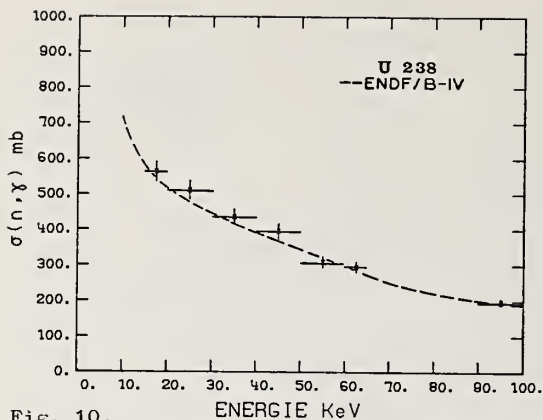


Fig. 10.

$^{238}\text{U}$  (15 keV - 550 keV)

We used a metallic sample (410 ppm of  $^{235}\text{U}$ ). The thickness of the sample was 0.003388 atom/barn and its diameter 16.2 mm. Because of the rather poor statistic we have averaged our results over 10 keV below 100 keV and 20 keV above 100 keV. Our data are shown on Fig. 10 and 11. Below 100 keV our data are 6-8 % below those of ORELA, between 10 % and 20 % higher than those of MOXON and agree within  $\pm 5$  % with those of FRIESNHAHN. Between 120 keV and 250 keV our results are smaller than any other measurements. If we compare with the data of RYVES our results are 15 % smaller at 160 keV, 6 % smaller at 238 keV, but in better agreement around 500 keV.

All these authors are referenced in Ref. 13. Consequently our results are in a rather good agreement with ENDF/B-IV below 100 keV and above 300 keV. Between 100 and 300 keV they are up to 15 % smaller. The gamma absorption correction in the sample is very high 18 % and the associated error on the cross section is estimated to 3 %. Additional work must be done on this correction and new experiments are planned in the 200 keV range. Consequently our data on  $^{238}\text{U}$  are preliminary data.

#### Conclusions

The present measurements are believed to give absolute capture cross sections within 4-8 % (1 standard deviation and all errors added quadratically). For some elements the ENDF/B-IV evaluated data are not in our expe-

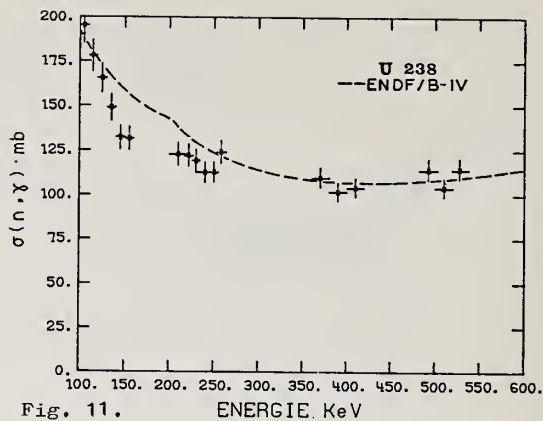


Fig. 11.

rimental error bars.

#### References

- 1) R.L. MACKLIN and J.H. GIBBONS  
Phys. Rev. 159 (1967) 1007.
- 2) C. LE RIGOLEUR, A. ARNAUD  
Proceedings of a meeting hold at Karlsruhe  
KFK 2046 - NEACRP U-61 - NEANDC U-98
- 3) C. LE RIGOLEUR et al - CEA N-1661
- 4) C. LE RIGOLEUR et al - CEA N-1662
- 5) C. LE RIGOLEUR et al - Journal of Nuclear  
Energy - A/B - 1966 - Vol 20, p. 67 to 73
- 6) EANDC (E) 140U for renormalization of  
Ref. 5
- 7) R.W. HOCKENBURY et al - Phys. Rev. -  
178-4, 1746 (1969)
- 8) P. RIBON et al  
Conf. PARIS CN 23/72, 1966
- 9) F. RAHN et al  
Phys. Rev. 8 - 1827 (1973)
- 10) L.M. SPITZ et al  
Nuclear Physics A 121 (1968) 655 - 672
- 11) D.C. STUPEGIA et al  
Journal of Nuclear Energy  
Vol 22 - N° 5 - p 267 (1968)
- 12) P. RIBON et al - to be published
- 13) G. DE SAUSSURE and R.B. PEREZ  
Atlanta meeting - to be published.